Ultrafast Pulse Metrology

Johannes Blöchl

München 2025

Ultrafast Pulse Metrology

Johannes Blöchl

Dissertation
an der Fakultät für Physik
der Ludwig–Maximilians–Universität
München

vorgelegt von
Johannes Blöchl
aus Freyung

München, den 15. September 2025

Erstgutachter: Prof. Dr. Matthias F. Kling
Zweitgutachter: Prof. Dr. André Staudte
Tag der mündlichen Prüfung: 11. November 2025

Zusammenfassung

Die Untersuchung ultraschneller Licht-Materie-Wechselwirkung erfordert präzise Kontrolle und Metrologie ultrakurzer Laserpulse, experimenteller Aufbauten und zugehöriger Parameter. Verbunden mit jüngsten Entwicklungen in der Attosekundenphysik entstehen neue Anforderungen an die Lasertechnologie, deren Charakterisierung, aber auch an die erforderlichen experimentellen Methoden. Diese Anforderungen werden beispielsweise von der Skalierung der Energien hoher Harmonischer hin zum sogenannten Wasserfenster – dem Energiebereich zwischen den Kohlenstoff und Sauerstoff K-Kanten (284 bis 543 Elektronenvolt) – oder von der Entwicklung von Petahertzelektronik angetrieben. Darüber hinaus eröffnen sich neue Perspektiven für die Untersuchung elementarer Prozesse.

Im Rahmen dieser Arbeit werden die zugrundeliegenden physikalischen und experimentellen Aspekte moderner Attosekundenphysik genauer untersucht. Beginnend mit einer auf Petahertzelektronik basierenden Messmethode zur Bestimmung der Träger-Einhüllenden-Phase (CEP) im Einzelschussexperiment wird gezeigt, dass mit einem einfachen experimentellen Aufbau und dem Ausnutzen elementarer Elektronendynamik in Gas und Plasma eine robuste und vielseitige Messmethode erzielt werden kann, die durch ihre Einsetzbarkeit bei verschiedenen Wellenlängen überzeugt.

Des Weiteren wird unter Ausnutzung von solitonischer Propagationsdynamik in Wellenleitern gezeigt, dass sich Laserpulse im kurzwelligen Infrarotbereich simultan spektral verbreitern und zeitlich komprimieren lassen. Damit werden die komplizierte Lichtfeldsynthese sowie die Notwendigkeit dispersiver Optiken und die damit verbundenen Einschränkungen umgangen. Hierbei liegt ein Augenmerk auf der Stabilität von Ausgangsleistung und CEP und der damit einhergehenden Wellenformstabilität. Die zeitliche Charakterisierung zeigt eine Wellenform von der Dauer eines einzelnen optischen Zyklus, bestehend aus Spektralkomponenten zweier optischer Oktaven. Diese Bandbreite ermöglicht es, Subzyklen-Elektronendynamik zu kontrollieren, was sich als spektraler Effekt in der feldaufgelösten Messmethode äußert. Die Vermessung dieses Effekts erlaubt eine in-situ CEP Kalibrierung. Die demonstrierte spektrale Verbreiterung setzt dabei neue Maßstäbe in der Erzeugung hochintensiver ultrakurzer Pulse, besonders hinsichtlich der erzielten Spitzenleistung von 0,26 Terawatt, der hohen mittleren Leistung und der ausgezeichneten Stabilität.

Solche Systeme eignen sich hervorragend zur Erzeugung hoher Harmonischer mit hohen Energien. Durch die hohe mittlere Leistung kann das Interaktionsvolumen gesteigert werden, um die schlechte Konversionseffizienz zu kompensieren. Die dadurch entstehende höhere thermische Belastung des experimentellen Aufbaus und der Filter erfordert neue Wege, dieser standzuhalten. Gleichzeitig ist eine präzise Stabilisierung der zeitlichen Verfahrstufe vonnöten, um die hohe zeitliche Auflösung in Experimenten zu gewährleisten. Daher wurde eine Methode entwickelt, die sowohl die Filterung von treibendem Laser und erzeugten Harmonischen erlaubt als auch der Stabilisierung des zeitlichen Versatzes zweier Pulse eines Interferometers dient. Es wird abschließend demonstriert, dass damit zum einen der hohen mittleren Leistung standgehalten wird, zum anderen aber auch ein stabiles Interferometer über die Dauer typischer Messkampagnen erzielt werden kann.

Abstract

The investigation of ultrafast light-matter interaction requires precise control and metrology of ultrashort laser pulses, experimental setups, and related parameters. Connected with recent developments in attosecond physics, new requirements arise for laser technology, its characterization, and the necessary experimental methods. These requirements are driven, for example, by the scaling of the energies of high-harmonics toward the so-called water window – the energy range between the carbon and oxygen K-edges (284 to 543 electron volts) – or by the development of petahertz electronics. In addition, new perspectives for the investigation of elementary processes open up.

In the context of this work, the underlying physical and experimental aspects of modern attosecond physics are examined in more detail. Starting with a measurement method based on petahertz electronics to determine the carrier-envelope phase (CEP) in a single-shot experiment, it is demonstrated that a robust and versatile measurement method can be achieved with a simple experimental setup. This method takes advantage of elementary electron dynamics in gas and plasma and is distinguished by its applicability across various wavelengths.

Furthermore, by utilizing solitonic propagation dynamics in waveguides, it is demonstrated that laser pulses in the short-wave infrared range can be simultaneously spectrally broadened and temporally compressed. This approach circumvents complicated light-field synthesis, as well as the need for dispersive optics and the associated limitations. Attention is given to the stability of output power and the CEP, along with the resulting waveform stability. Temporal characterization reveals a waveform with a duration of a single optical cycle, consisting of spectral components spanning two optical octaves. This bandwidth enables the control of sub-cycle electron dynamics, which manifests as a spectral effect in the field-resolved measurement method. Measuring this effect allows for in-situ CEP calibration. The demonstrated spectral broadening sets new standards in the generation of high-intense ultrashort pulses, particularly regarding the achieved peak power of 0.26 terawatts, high average power, and excellent stability.

Such systems are particularly well-suited for generating high-energy high-harmonics. The high average power allows for an increased interaction volume to compensate for the poor conversion efficiency. However, this results in a higher thermal load on the experimental setup and on the filters, necessitating new approaches to withstand it. At the same time, precise stabilization of the temporal delay line is essential to ensure high temporal resolution in experiments. Therefore, a method has been developed that allows for the filtering of the driving laser and the generated harmonics while also stabilizing the temporal delay between two pulses in an interferometer. It is ultimately demonstrated that this method can withstand high average power and achieve a stable interferometer throughout the duration of typical measurement campaigns.

Contents

List of Figures

List of Tables

Acronyms

ADK	Ammosov-Delone-Krainov
ATI	above-threshold ionization
BBO	β-barium borate
CaF_2	Calcium fluoride
CEP	carrier-envelope phase
CW	continuous wave
DFG	difference frequency generation
FFT	fast Fourier transform
FROG	frequency-resolved optical gating
FS	fused silica
FWHM	full-width at half-maximum
GDD	group delay dispersion
HCF	hollow-core fiber
HH	high-harmonic
HHG	high-harmonic generation
HORUS	**H**igh-power **O**PCPA system for high **R**epetition rate **U**ltrafast **S**pectroscopy
IR	infrared
MIR	mid infrared
NIR	near infrared
OAP	off-axis parabolic mirror
OPA	optical parametric amplifier
OPCPA	optical parametric chirped-pulse amplifier
PAP	parametric asymmetry plot
PID	proportional–integral–derivative
PPT	Perelomov-Popov-Terent'ev
PSD	position sensitive detector
SHG	second harmonic generation
SPI	statistical photoionization

SPM	self-phase modulation
SWIR	short-wave infrared
SXR	soft X-ray
Ti:Sa	Titanium:Sapphire
TIA	transimpedance amplifier
Tiptoe	**T**unneling **I**onization with a **P**erturbation for the **T**ime-domain **O**bservation of an **E**lectric field
TOD	third-order dispersion
UHV	ultra-high vacuum
UV	ultraviolet
VIS	visible
XUV	extreme ultraviolet
YAG	Yttrium Aluminium garnet
Yb:YAG	Ytterbium doped Yttrium Aluminium garnet
ZnSe	Zinc Selenide

Publications

Publications related to this thesis

- **Johannes Blöchl**, Maximilian F. Kuthe, Hartmut Schröder, Abdallah M. Azzeer, Thomas Nubbemeyer and Matthias F. Kling. *Multi-millijoule hollow-core fiber compression of short-wave infrared pulses to a single cycle.* Opt. Express, **Vol. 33**, No. 13: pp. 28071–28080, 2025. URL `http://dx.doi.org/10.1364/OE.564364`.

- **Johannes Blöchl**, Maximilian F. Seeger, Hartmut Schröder, Minjie Zhan, Alexander Guggenmos, Thomas Nubbemeyer, Matthias F. Kling and Boris Bergues. *Ionization effects in single-shot carrier-envelope phase detection with gas-gap devices.* Applied Physics Letters, **Vol. 126**, No. 13: p. 131106, 2025. ISSN 0003-6951. URL `http://dx.doi.org/10.1063/5.0246794`.

Patent applications related to this thesis

Johannes Blöchl, Maximilian F. Kuthe, Fritz Keilmann, Thomas E. Nubbemeyer and Matthias F. Kling. German patent application DE 10 2025 119 843.8, *Verfahren zum Abtrennen, Ausrichten und Überlagern von Komponenten eines ersten und eines zweiten Lichtstrahls und Interferometer.* assignee: Ludwig-Maximilians-Universität München and Max-Planck-Gesellschaft zur Förderung der Wissenschaften e.V., patent filed 21.05.2025.

Other publications

- Weiwei Li, Zilong Wang, Judit Budai, Lázár Tóth, **Johannes Blöchl**, Thomas Nubbemeyer, Péter Dombi and Matthias F. Kling. *Petahertz sampling of Fano resonances in a hybrid metal-dielectric nanostructure.* in preparation.

- **Johannes Blöchl**, Johannes Schötz, Boris Bergues and Matthias F. Kling. *From Ultrafast Light-Induced Currents to Spatially-Resolved Field Sampling.* In Luca Argenti, Michael Chini and Li Fang (Editors), *Proceedings of the 8th International Conference on Attosecond Science and Technology*, pp. 177–186. Springer International Publishing, Cham, 2024. ISBN 978-3-031-47938-0 URL `https://doi.org/10.1007/978-3-031-47938-0`.

- Kai-Fu Wong, Weiwei Li, Zilong Wang, Vincent Wanie, Erik Månsson, Dominik Hoeing, **Johannes Blöchl**, Thomas Nubbemeyer, Abdallah Azzeer, Andrea Trabattoni, Holger Lange, Francesca Calegari and Matthias F. Kling. *Far-Field Petahertz Sampling of Plasmonic Fields.* Nano Letters, **Vol. 24**, No. 18: pp. 5506–5512, 2024. PMID: 38530705, URL `http://dx.doi.org/10.1021/acs.nanolett.4c00658`.

- Maximilian F. Seeger, Dominik Kammerer, **Johannes Blöchl**, Marcel Neuhaus, Vladimir Pervak, Thomas Nubbemeyer and Matthias F. Kling. *49 W carrier-envelope-phase-stable few-cycle 2.1μm OPCPA at 10 kHz*. Opt. Express, **Vol. 31**, No. 15: pp. 24821–24834, 2023. URL http://dx.doi.org/10.1364/OE.493326.

- Johannes Schötz, Ancyline Maliakkal, **Johannes Blöchl**, Dmitry Zimin, Zilong Wang, Philipp Rosenberger, Meshaal Alharbi, Abdallah M. Azzeer, Matthew Weidman, Vladislav S. Yakovlev, Boris Bergues and Matthias F. Kling. *The emergence of macroscopic currents in photoconductive sampling of optical fields*. Nature Communications, **Vol. 13**, No. 1: p. 962, 2022. ISSN 2041-1723. URL http://dx.doi.org/10.1038/s41467-022-28412-7.

- **Johannes Blöchl**, Johannes Schötz, Ancyline Maliakkal, Natālija Šreibere, Zilong Wang, Philipp Rosenberger, Peter Hommelhoff, Andre Staudte, Paul B. Corkum, Boris Bergues and Matthias F. Kling. *Spatiotemporal sampling of near-petahertz vortex fields*. Optica, **Vol. 9**, No. 7: pp. 755–761, 2022. URL http://dx.doi.org/10.1364/OPTICA.459612.

- Johannes Schötz, Lennart Seiffert, Ancyline Maliakkal, **Johannes Blöchl**, Dmitry Zimin, Philipp Rosenberger, Boris Bergues, Peter Hommelhoff, Ferenc Krausz, Thomas Fennel and Matthias F. Kling. *Onset of charge interaction in strong-field photoemission from nanometric needle tips*. Nanophotonics, **Vol. 10**, No. 14: pp. 3769–3775, 2021. URL http://dx.doi.org/doi:10.1515/nanoph-2021-0276.

Conference contributions

- Weiwei Li, Zilong Wang, Judit Budai, Lázár Tóth, **Johannes Blöchl**, Thomas Nubbemeyer, Péter Dombi and Matthias F. Kling. *Petahertz sampling of Fano resonances in a hybrid metal-dielectric nanostructure*. Abstract submitted to UltrafastX 2025.

- **Johannes Blöchl**, Johannes Schötz, Boris Bergues and Matthias F. Kling. *Spatiotemporal sampling of near-petahertz vortex fields*. In *CLEO 2023*, p. FF2B.5. Optica Publishing Group, 2023. URL http://dx.doi.org/10.1364/CLEO_FS.2023.FF2B.5.

- Maximilian F. Seeger, Dominik Kammerer, **Johannes Blöchl**, Thomas Nubbemeyer and Matthias F. Kling. *35W Carrier-Envelope-Phase-Stable Few-Cycle Mid-Infrared OPCPA at 10 kHz*. In *CLEO 2023*, paper STu4H.3. Optica Publishing Group, 2023. URL http://dx.doi.org/10.1364/CLEO_SI.2023.STu4H.3.

- **Johannes Blöchl**, Johannes Schötz, Ancyline Maliakkal, Natālija Šreibere, Zilong Wang, Philipp Rosenberger, Peter Hommelhoff, Andre Staudte, Paul B. Corkum, Boris Bergues and Matthias F. Kling. *Spatio-temporal sampling of near-infrared vortex beams*. Poster contribution to ATTOFEL 2022, URL https://www.ucl.ac.uk/~ucapaem/attofel2022.html.

Chapter 1

Introduction

When plucking the string of an instrument, the resulting tone has a distinct pitch. To determine its precise value, one has to listen for a moment – due to the elementary property of waves with precise frequencies[1], namely their temporal extension. In contrast, when clapping one's hands once, a short tone is emitted, but it does not favor a distinct pitch; rather, it is a superposition of many frequencies. Now, when walking through a crowded street, many audible frequencies are present as well, but they do not form a short tone. The reason is the missing phase relation between each individually emitted frequency – its control is crucial in the generation of a temporally short wave. Since light is an electromagnetic wave, the very same principle applies. The generation of short light pulses thus requires the generation of many frequency components and their temporal alignment. Such pulses are highly desirable, as they promise to enhance the resolution in time-resolved experiments. Similar to a camera, where the fastest resolvable feature depends on the exposure time, the investigation of ultrafast physical phenomena in the time domain requires pulses of comparable or shorter duration, possibly combined with nonlinearities. Therefore, the generation of short pulses, their characterization, and the design of experimental methods form a cohesive triad for the investigation of ultrafast effects.

Driven by seminal achievements in laser technology [1, 2], such as the availability of the required femtosecond (10^{-15} s) laser pulses [3], their waveform or power stability, wide spectral coverage, or the high peak power, many ultrafast phenomena became accessible for investigation. In particular, the observation of electronic motion with unprecedented precision [4–7], photoisomerization [8], electron dynamics [9, 10], or nanoplasmonics [11–13] has been pioneered in the last decades. In addition, petahertz electronics, i.e., the generation and manipulation of electronic signals at petahertz frequencies, emerged from the manipulation of charge-carriers with light-fields [14–18]. All of these experiments are connected through coherent charge-carrier manipulation, therefore, the precise knowledge and control of the waveform driving the interaction is compulsory. In particular, the waveform stability of few- to single-cycle laser pulses can be related to the stability of their carrier-envelope phase (CEP), or global phase, which in turn becomes one of the key parameters. Thus, the CEP measurement is essential and profits from recent developments in petahertz electronics [18, 19] that have demonstrated the capabilities of light-field controlled charge-carrier dynamics in detecting the global phase [20–24], even spatially resolved [25]. In addition, even the measurement of the electric field of light has become feasible through novel techniques in petahertz electronics [26–34]. All of these approaches benefit from the electric current measurement of laser-field induced charge migration or separation, which opens up a new perspective for compact and simple measurement devices [18].

[1] Strictly speaking, an instrument does not emit a pure sinusoidal wave but has overtones as well.

The aforementioned requirement of short pulses is closely related to techniques for spectral broadening and temporal compression of laser pulses. Hollow-core fibers (HCFs) were pioneered by Nisoli et al. [35,36] and have become one of the workhorses for spectral broadening of lasers [37], along with multi-pass cells [38]. Whereas the generation of new spectral components in fibers and their compression was initially decoupled [35–37] and dispersive mirrors were used for temporal compression [39, 40], more powerful methods based on solitonic propagation are available [41, 42]. These methods are based on waves that do not alter their shape along propagation, so-called solitons, which were discovered in water centuries ago [41, 43]. In optics, a soliton is a wavepacket for which nonlinear and diffractive or dispersive effects balance [41], in particular regarding dispersive effects from wave-guiding. Soliton propagation was described in solid glass fibers [44, 45] and experimentally observed a few years later in 1980 by Mollenauer et al. [46]. Interestingly, they observed the compression of picosecond pulses solely by their nonlinear propagation through a fiber – soliton self-compression. Such compression is accompanied by a gain in spectral bandwidth. These effects are known to exist in HCFs as well, but since the dispersion landscape there is different, solitons have not been observed in hollow fibers for quite some time. Thus, it is not surprising that solitons were first observed in photonic bandgap fibers [47] and antiresonant fibers [48–50], with peak powers reaching the gigawatt range [41]. In HCFs, soliton propagation was observed in 2019 when Travers et al. demonstrated the capabilities of precisely tuned waveguide parameters in generating solitons reaching the ultraviolet (UV) [51]. This work profits from the length scale capabilities of stretched fibers [52] that allow the enhancement of the required waveguide effects by increasing the fiber length [41, 51]. The pulse compression approach using solitons is appealing compared to light field synthesis [3, 53–56] due to the reduced complexity of the setup, but at the cost of a coupling between pulse compression and the generation of spectral bandwidth.

Petahertz electronics, in combination with soliton dynamics, promise to bring a new quality to the coherent control of waveforms and field-driven processes. With the accompanying sub-cycle precision, they form new branches of modern attosecond physics and align next to the long-term workhorse, high-harmonic generation (HHG). Historically, attosecond physics has emerged from the first milestone, the observation of high-harmonics (HHs) [57, 58] and their energy plateau [59]. The generated radiation was found to be emitted during very short times only, shorter than the optical half-period of light. Explained by the three-step [60] or the Lewenstein model [61], HHG became controllable and has served as the backbone for ultrafast science. Due to the high energy of the emitted photons in HHG, both single-photon ionization of outer- and inner-shell electrons can be driven, and even sidebands shifted by the laser photon energy can be observed in pump-probe experiments [62]. The isolation of a single HH emission event by amplitude gating [63] enabled the measurement of the light wave with attosecond streaking [64]. The time resolution in all these experiments stems from two key parameters: First, the strong nonlinearity of the HHG process, resulting in broadband and attosecond short pulses, which set the physical limit on the achievable resolution; and second, the stability of the interferometric measurements, manifesting an experimental challenge.

Latest advances have led to the demand for higher cut-off energies towards the water window, the range between the carbon and oxygen K-edges from 284 to 543 electron volts (eV) [65]. Such high energies can only be generated by HHG under certain constraints regarding the peak intensity, atomic species of the target or driving wavelength. In particular, the scaling of the cut-off energy $\mathcal{E}_{\mathrm{cutoff}} \propto I_{\mathrm{P}}$ and $\mathcal{E}_{\mathrm{cutoff}} \propto \lambda^2$ [60] renders the use of long wavelength λ drivers and high ionization potential I_{P} targets attractive. This scaling law is accompanied by a drastic decrease in conversion efficiency, which scales between λ^{-4} [66] and $\lambda^{-5} \rightarrow \lambda^{-7}$ [67–70]. Consequently, the scaling of the conversion efficiency

drastically reduces the expected photon flux, demanding more powerful laser sources to compensate for this trend by an increasing volume of high intensity in which the signal is generated. Preferably, the repetition rate of the laser system is in a multi-kilohertz range, or even higher, such that experiments may profit from high statistics. Thus, a third requirement for modern attosecond science, precisely controlled high-intense laser pulses, is manifested.

Soliton dynamics directly promise to address the third requirement, whereas petahertz metrology ensures the control and measurement of multi-octave spanning supercontinua and the corresponding waveforms in time with unprecedented parameters. Regarding the high peak intensity solitons can provide, a combination of this methodology with experimental apparatuses from classic HHG-based attosecond science may start a new era for time-resolved spectroscopy in the water-window. Difficulties arising from adapting the experiments to the new parameters, however, must first be overcome. In particular, the second requirement, the stability of the delay line, must be ensured for maximal precision. If successful, charge-carrier dynamics in hitherto rarely explored energetic regions can be investigated, opening new prospects for the investigation of petahertz electronic effects, thus pushing petahertz metrology.

In this thesis, I will present novel solutions to propel modern attosecond science. In particular, I will demonstrate that light-field controlled charge-carrier dynamics in gas and plasma enable the detection of the CEP of ultrashort laser pulses by detecting the electric currents generated on a petahertz scale. Characterization of this petahertz electronics based CEP detection method proves its long-term reliability and also demonstrates a large wavelength independence of the detector – a major advantage compared to other methods. In addition, I will present a spectral broadening scheme of a short-wave infrared (SWIR) laser system based on soliton self-compression that provides highly stable and intense laser pulses at a high repetition rate – a fundamental prerequisite for modern attosecond science. Their characterization with a petahertz electronics technique reveals a CEP-stable single-cycle optical waveform, and the stability is used to characterize the spectral response of the measurement technique by exploiting its CEP-dependent characteristics. Consequently, an intrinsic absolute phase calibration is possible. The achievable peak power sets a new milestone for laser systems of this class. These results additionally form a foundation for high-flux HHG in the water window range. An experimental apparatus for HHG is adapted and thoroughly studied. Especially the novel interferometric stabilization scheme the apparatus is equipped with supports operation at high average power and a long-term interferometric stability on the sub-100 as scale. For diagnostics of the generated extreme ultraviolet (XUV) radiation, a spectrometer is adapted and its data reveals that the generation of high cut-off energies is feasible. The future combination of all the presented results constitutes a highly powerful and versatile machinery for attosecond science and petahertz metrology.

The following chapters are organized as follows: In Chapter 2, I will introduce the basic concepts of laser pulses in time, space, and frequency domain, followed by a discussion of strong-field ionization and of the formation of laser-induced currents. After presenting the signal scaling of such currents in saturated ionization, I provide details on the propagation of lasers through waveguides and corresponding nonlinear effects. I will conclude the chapter with a short review of the interference pattern in Mach-Zehnder interferometers.

In Chapter 3, I will present the results on the single-shot detection of the CEP of a Titanium:Sapphire (Ti:Sa) laser system, investigate the achievable performance, and demonstrate the applicability of the current sampling approach to a SWIR laser system.

Design considerations for a soliton-based spectral broadening system in the SWIR range will be presented in Chapter 4. Subsequently, experimental data of its implementation regarding various parameters are presented, identifying the cutting-edge parameter

set the system provides. As first application of the multi-octave spanning spectrum generated, the spectral response of the measurement technique is investigated, allowing for an in-situ absolute phase calibration.

Finally, in Chapter 5, I present an attosecond beamline adapted to the requirements caused by using a high-power SWIR laser. The focus will be on the filter method separating the laser from the generated HHs, which simultaneously serves as means for active stabilization of the delay line for pump-probe experiments. The latter is of outermost importance for precise time-resolved experiments, as it fundamentally limits the achievable resolution.

Chapter 2

Theoretical background on ultrafast lasers and light-matter interaction

The study of the interaction of light with matter requires a theoretical background in basic models of coherent optical radiation and its interaction with atoms and molecules. Starting with the field representation of a laser pulse in time and frequency, I will introduce expressions for the peak power and, after a discussion of Gaussian beams in space, the peak intensity, both of which are critical for describing strong-field interaction. Subsequently, I will present different ionization models for atoms and molecules, which serves as a basis for the discussion of the signal formation of laser-induced currents. Afterwards, I will review the concept of HHG, a necessary requirement for Chapter 5 and for the motivation of Chapter 4. Thereafter, effects of saturation of ionization in laser-driven electric current generation are considered. This discussion serves as background for the results presented in Chapter 3 and is part of our corresponding publication [71]. Hereafter, I will start with a discussion of methods for the sampling of optical laser fields, which is an essential prerequisite for Chapter 4, where the results on hollow-core fiber spectral broadening and compression are presented. Therefore, a theoretical discussion of the propagation of laser light through waveguides and the corresponding nonlinear effects is also given in this chapter. Finally, I will present a short description of the interference pattern in Mach-Zehnder interferometers, which will be required in Chapters 4 and 5.

2.1 Description of laser pulses in time, frequency and space

Maxwell's equations [72] describe light as an electromagnetic wave with the electric and magnetic components E and B, respectively [73]. The electric field in time, $E(t)$, can be expressed as a superposition of its frequency components via the inverse Fourier transform [74–76]

$$E(t) = \frac{1}{\sqrt{2\pi}} \int_{\mathbb{R}} |E(\omega)| \exp\left[i\omega t - i\varphi(\omega)\right] \mathrm{d}\omega = \mathcal{IFT}\left[|E(\omega)|e^{-i\varphi(\omega)}\right] \tag{2.1}$$

with the spectral amplitude $|E(\omega)|$. The spectrum $E(\omega) = |E(\omega)|e^{-i\varphi(\omega)}$, however, is a complex quantity which is not to be confused with the spectral intensity introduced below. The spectral phase $\varphi(\omega)$ aligns the Fourier components with respect to each other, where a flat $\varphi(\omega)$ corresponds to the shortest possible pulse in time, with most energy confined in the main peak. Within this thesis, the sign convention is chosen such that negative times are earlier than positive ones.

This model is appealing since any linear propagation through material can be expressed as a phase term by the relation

$$\varphi(\omega) = \frac{n(\omega)\omega x}{c}, \tag{2.2}$$

where the linear refractive index n of the material light propagates through is directly connected to the phase term by the distance x at the speed of light $c \approx 3 \times 10^8 \,\frac{\mathrm{m}}{\mathrm{s}}$. The refractive index of a material can be approximated by Sellmeier equations [77,78], reducing the complexity of individual materials to few experimentally determinable constants, as presented in the literature for common optical materials such as fused silica (FS) [79] or Calcium fluoride (CaF_2) [80]. Series expansion of the spectral phase $\varphi(\omega)$ in terms of its derivatives $\varphi^{(k)}(\omega)$ around the central frequency ω_0,

$$\varphi(\omega) = \sum_{k=0}^{\infty} \frac{1}{k!} \frac{\partial^k \varphi(\omega)}{\partial \omega^k}\bigg|_{\omega=\omega_0} (\omega-\omega_0)^k = \sum_{k=0}^{\infty} \frac{1}{k!} \varphi^{(k)}(\omega_0)(\omega-\omega_0)^k \tag{2.3}$$

$$= \varphi_0 + \mathrm{GD}(\omega-\omega_0) + \frac{1}{2}\mathrm{GDD}(\omega-\omega_0)^2 + \tag{2.4}$$

$$+ \frac{1}{6}\mathrm{TOD}(\omega-\omega_0)^3 + \mathcal{O}((\omega-\omega_0)^4), \tag{2.5}$$

defines the commonly used expressions group delay (GD), group delay dispersion (GDD) and third-order dispersion (TOD). The symbol $\mathcal{O}$ denotes the Landau-O-symbol. The higher-order terms, in particular the group delay dispersion, or second-order dispersion, require careful treatment since they have significant impact on the shape of $E(t)$. The central frequency is related to the cycle time $T = \frac{1}{f} = \frac{2\pi}{\omega} = \frac{\lambda_0}{c}$, with f being the central frequency and λ_0 the central wavelength.

For illustration, a field that has a Gaussian envelope, a so-called Gaussian pulse, is defined by

$$E(t) = E_0 \exp\left[-2\ln(2)\frac{t^2}{\tau_{\mathrm{fwhm}}^2}\right] \cos(\omega t - \varphi_{\mathrm{CEP}}) \tag{2.6}$$

with the peak amplitude of the field envelope E_0, the full-width at half-maximum (FWHM) pulse duration of the intensity envelope τ_{fwhm} and the offset between the carrier wave and the envelope, φ_{CEP}. The latter, also referred to as global phase, or CEP, is an important parameter describing the symmetry of the system with a single number. Note that, despite being introduced here in the context of Gaussian pulses, the notion CEP is used for various pulse shapes with a well-defined envelope. For illustration of the role of CEP and the second-order dispersion, see Fig. 2.1.

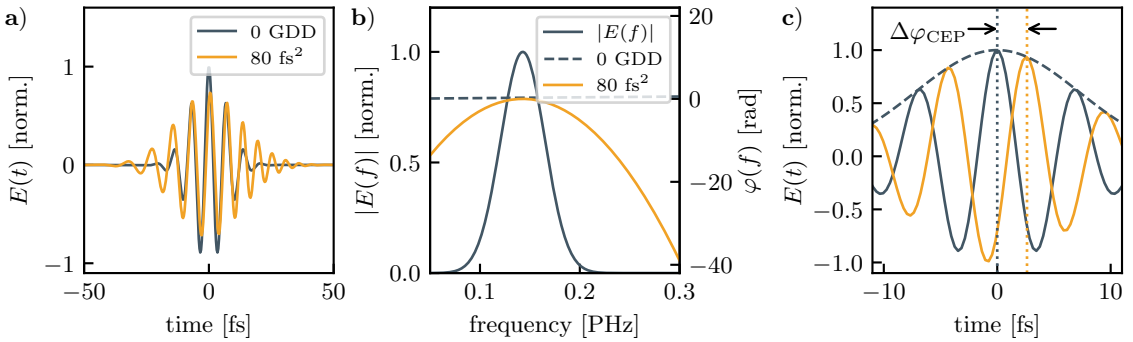

Figure 2.1: a) Gaussian pulse in time, $\tau_{\mathrm{fwhm}} = 12\,\mathrm{fs}$, $\lambda_0 = 2.1\,\mu\mathrm{m}$, compressed and with a GDD of $80\,\mathrm{fs}^2$. **b)** Spectral amplitudes and phase corresponding to a). **c)** Carrier waves with different CEPs (0 and $\frac{3\pi}{4}$).

The intensity of the pulse can be derived via the energy flux given by the Poynting vector $\boldsymbol{S}$ and calculating the temporal average

$$I = \frac{1}{T}\int_0^T \mathrm{d}t|\boldsymbol{S}| = \frac{1}{T}\int_0^T \mathrm{d}t\epsilon_0 c|E(t)|^2, \tag{2.7}$$

where I used $\boldsymbol{S} = \boldsymbol{E} \times \frac{1}{\mu_0}\boldsymbol{B}$ and $|B| = \frac{|E|}{c}$ [73]. Assuming a sinusoidal wave of amplitude E_0, this integral evaluates to $I = \frac{1}{2}\epsilon_0 c|E_0|^2$. Experimentally, the accessible quantities are the pulse energy and duration, which convert to a peak intensity $I_0 = P_0/A$ with the area A and the peak power P_0 by

$$P_0 = 0.94\frac{\mathcal{E}}{\tau_{\mathrm{fwhm}}} \quad \text{(Gaussian)} \quad \text{and} \tag{2.8a}$$

$$P_0 = 0.88\frac{\mathcal{E}}{\tau_{\mathrm{fwhm}}} \quad (\mathrm{sech}^2), \tag{2.8b}$$

where $\mathcal{E}$ is the pulse energy, see Appendix A.1 for a derivation.

A common model for the representation of the laser beam in space is the Gaussian beam, according to which the electric field as a function of space reads

$$E(r,\phi,z) = E(r,z) = E_0\frac{w_0}{w(z)}\cdot\exp\left(-\frac{r^2}{w^2(z)}\right)\exp\left(-ik\frac{r^2}{2R(z)}\right)\cdot\exp\left(-i(kz-\zeta(z))\right), \tag{2.9}$$

with the wavefront curvature $R(z)$, the beam radius $w(z)$ where $w(z=0) = w_0$, and the Gouy phase $\zeta(z)$. The following relations hold:

$$w(z) = w_0\sqrt{1+\left(\frac{z}{z_{\mathrm{R}}}\right)}, \tag{2.10}$$

$$z_{\mathrm{R}} = \frac{w_0^2\pi}{\lambda}. \tag{2.11}$$

Here, z_{R} is the Rayleigh-length, the characteristic length scale of a focus. Along that length, the phase of the light field changes according to the expression for the Gouy phase

$$\zeta = \arctan\left(\frac{z}{z_{\mathrm{R}}}\right). \tag{2.12}$$

The laser beam intensity I is the power per area, therefore the energy content in a pulse with a given intensity distribution in space $I(t,x,y)$ can be calculated as

$$\mathcal{E} = \int \mathrm{d}t \int \mathrm{d}x\,\mathrm{d}y\, I(t,x,y) = 2\pi\int \mathrm{d}t\int_0^\infty \mathrm{d}r\, r\cdot I(t,r). \tag{2.13}$$

The latter equality holds only if the beam is radially symmetric. If $I(t,\cdot)$ can be written in terms of its peak value I_0, $I(t,\cdot) = I_0 f(t,\cdot)$, the expression for the peak intensity as a function of pulse energy and f is

$$I_0 = \frac{\mathcal{E}}{\int f(t,\cdot)\,\mathrm{d}t\,\mathrm{d}A}. \tag{2.14}$$

For an intensity shape that can be written as $f(t,x,y) = g(t)\cdot h(x,y)$, the integrals can be evaluated separately which yields

$$I_0 = \frac{P_0}{\int \mathrm{d}A h(x,y)}, \tag{2.15}$$

according to Eq. (2.8). The remaining integral can be evaluated for a Gaussian pulse in space (Eq. (2.9)) at $z = 0$

$$\int \mathrm{d}A h(x,y) = 2\pi \int_0^\infty \mathrm{d}r\, r \exp\left[-\frac{2r^2}{w_0^2}\right] = 2\pi \left[-\frac{w_0^2}{4}\exp\left(-\frac{2r^2}{w_0^2}\right)\right]\Bigg|_0^\infty = \frac{w_0^2\pi}{2}. \tag{2.16}$$

Finally, the expression for the peak intensity of a Gaussian pulse in the focus is

$$I_0 = \frac{2P_0}{w_0^2\pi}. \tag{2.17}$$

The intensity has been defined in the time domain. According to Eq. (2.1), an equivalent expression for the intensity in frequency space can be defined. Importantly, spectrometers typically measure the spectral intensity as a function of wavelength, $I_\lambda(\lambda)$. To convert the data to frequency space $f = \frac{c}{\lambda}$, it is essential to consider the Jacobi determinant. It is directly defined by the requirement of similar energy content in the spectrum, independent of its representation. The energy content is

$$\mathcal{E} = \int_0^\infty I_\lambda(\lambda)\,\mathrm{d}\lambda \tag{2.18}$$

with the integral transformation $\frac{\mathrm{d}\lambda}{\mathrm{d}f} = -\frac{c}{f^2}$, the expression reads

$$\int_0^\infty I_\lambda(\lambda)\,\mathrm{d}\lambda = \int_\infty^0 \left(-\frac{c}{f^2}\right)\cdot I_\lambda\left(\frac{c}{f}\right)\mathrm{d}f = \int_0^\infty \left(\frac{c}{f^2}\right)\cdot I_\lambda\left(\frac{c}{f}\right)\mathrm{d}f = \int_0^\infty I_f(f), \tag{2.19}$$

which results in the conversion rule $I_\lambda \cdot \frac{c}{f^2} = I_f$.

2.2 Strong-field ionization of atoms and molecules

The removal of bound electrons from atoms, molecules or solids by light has been the subject of studies for more than a century [81–83]. If the photon energy is high enough, a single photon is sufficient to remove an electron as described by the photoelectric effect [83]. In the case of photon energies lower than the binding energy of the weakest bound electron, however, several photons are required to provide enough energy to overcome the potential barrier or to tunnel through it. There are two distinct processes involved: tunneling ionization, which is the case for high field strengths and low frequencies, and multiphoton ionization, the case for low field strengths or high frequencies [84]. To distinguish between them, the Keldysh parameter γ was introduced [84]. It is defined as (following Refs. [84–86])

$$\gamma = \frac{\omega\sqrt{2m_\mathrm{e}I_\mathrm{P}}}{eE} \qquad \text{SI units} \tag{2.20a}$$

$$\gamma = \frac{\omega\sqrt{2I_\mathrm{P}}}{E} \qquad \text{atomic units} \tag{2.20b}$$

with the ionization potential I_P and the electron mass m_e. For $\gamma \gg 1$, multiphoton behavior is expected, whereas for $\gamma \ll 1$ tunneling ionization is present. The multiphoton ionization process can be described by the absorption m photons of energy $\mathcal{E}_\mathrm{Ph}$ as required to overcome the potential barrier I_P, $m = \lceil I_\mathrm{P}/\mathcal{E}_\mathrm{Ph}\rceil$. If more than m photons are absorbed, the electron has significant kinetic energy upon the exit of the atom, which constitutes above-threshold ionization (ATI). Tunneling ionization, on the other hand, describes the removal of an electron from the atom through a suppressed potential barrier due to the laser field. In that case, the electron can tunnel through the residual barrier, marking

tunneling ionization, or is directly liberated as in the case of barrier-suppression ionization [87–89].

For such processes to occur, a high photon flux within a given interval of time is required and can be provided by pulsed lasers. In this context, the latter is typically treated as classical electromagnetic field (or just as electric field component) as introduced in Sec. 2.1, and the process is referred to as strong-field ionization. In the following, I assume that the ionization rate $w(t)$, which describes the rate at which electrons are emitted, can be expressed as a function of the electric field $E(t)$, $w(E(t))$.

2.2.1 Tunnel ionization

Over the years, various models for strong-field ionization have been introduced, starting with models for static electrical fields, such as Fowler-Nordheim-Tunneling [90], or AC fields in Hydrogen(-like) atoms, such as Keldysh [84], Perelomov-Popov-Terent'ev (PPT) [91–93] or its static approximation, Ammosov-Delone-Krainov (ADK) [94] theory. For an overview, Ref. [95] is recommended. Those models have proven their reliability in modeling ionization processes in noble gas atoms, and extensions to diatomic molecules are available [96]. Empirical simplifications are proven to be accurate [89] and models for nonadiabatic tunneling even cover sub-cycle ionization dynamics [86].

In the case of strong and slowly oscillating fields, tunnel ionization can be imagined as a laser field perturbing the Coulomb potential of the atom, which results in a barrier the bound electron can tunnel through, see Fig. 2.2. For single atomic species, such as

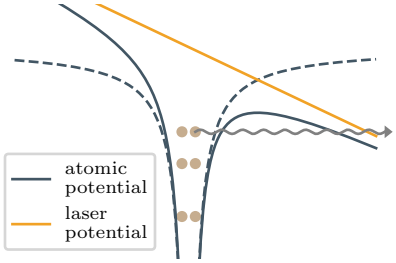

Figure 2.2: Schematic drawing of tunnelionization: A laser field perturbs the Coulomb potential binding the electrons (dots) such that one of them can tunnel through the suppressed barrier. The tunneling process is indicated by the wiggly line.

Hydrogen, Helium, Argon or Neon, and even for di-atomic molecules, analytic expressions for the tunneling ionization rate are available [84, 86, 89, 91–94, 96]. For long-wavelength drivers, as in the SWIR range, I use the static ionization rate of Ref. [89]. In this context, the ionization rate as a function of field amplitude E is given by (in atomic units)

$$w(E) = \frac{C_l^2}{2^{|m|}|m|!}\frac{(2l+1)(l+|m|)!}{2(l-|m|)!}\frac{1}{\kappa^{2\frac{Z}{\kappa}-1}}\left(\frac{2\kappa^3}{E}\right)^{2\frac{Z}{\kappa}-|m|-1}\exp\left(-\frac{2\kappa^3}{3E}\right). \tag{2.21}$$

Here, m, l are angular momentum quantum numbers, C_l are coefficients describing the amplitude of the electron wavefunction in the tunneling region, see Ref. [89]. Their values are tabulated in Ref. [96, Table 1 and 2] for selected atoms and diatomic molecules. The parameter κ is a short hand notation for $\kappa = \sqrt{2I_\mathrm{P}}$, Z is the charge seen by the active electron [89]. I use this ionization model to calculate the spectral response of the field measurements as presented in Sec 2.5. Since SI units[1] are used in the rest of the thesis, the conversion laws from SI to atomic units from Ref. [97] are helpful:

$$[E] = 1\,\text{a.u.} = 5.14220826 \times 10^{11}\,\frac{\text{V}}{\text{m}} \tag{2.22}$$

$$[I] = 1\,\text{a.u.} = 3.50944758 \times 10^{16}\,\frac{\text{W}}{\text{cm}^2}. \tag{2.23}$$

[1] Système international d'unités

High-harmonic generation Closely related to tunneling ionization is the process of high-harmonic generation. Following Refs. [4, 60], HHG can be described by the semi-classical three-step-model, see Fig. 2.3. The first step is tunneling of an electron out of the atom during the peak of electric field (panel a) in Fig. 2.3). In the next step (panel b)), the free electron is accelerated in the field and, due to the oscillatory manner, driven back to the parent atom. There, it can finally recollide whereby a higher energetic photon is emitted (panel d)).

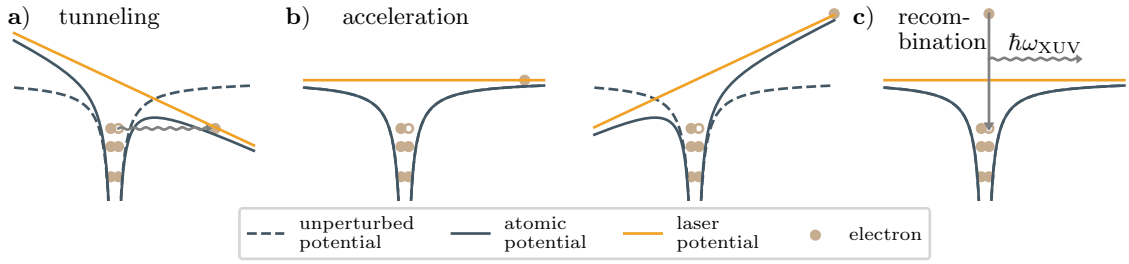

Figure 2.3: High-harmonic generation according to the three step model [60]. **a)** Tunnel ionization of an electron, **b)** acceleration of the classic electron in the electric field, **c)** recombination and emission of a high energetic photon.

The emitted energy depends on the trajectory in the electric field, which, in the scope of the three-step-model, is the velocity at the returning point. In Fig. 2.4, the returning trajectories are plotted. Those are the electrons emitted shortly after the peak of the field [4, at $\approx T/20$ after the peak]. The maximum energy of the emitted photon scales with the kinetic energy of the electron, that is, the ponderomotive potential (see Appendix A.2) and the ionization potential I_P according to the cut-off law $E_\mathrm{cutoff} = I_\mathrm{P} + 3.17U_\mathrm{P}$ [60]. Therefore, the cut-off energy increases with wavelength according to a $\propto \lambda^2$ scaling law. Other models suggest a slightly enhanced cut-off law of the form $E_\mathrm{cutoff} = I_\mathrm{P} \cdot F\frac{I_\mathrm{P}}{U_\mathrm{P}} + 3.17U_\mathrm{P}$ with $F\frac{I_\mathrm{P}}{U_\mathrm{P}} \approx 1.3$ for $I_\mathrm{P} \ll U_\mathrm{P}$ [61]. Therefore, a slightly higher cut-off energy can be expected in such a case.

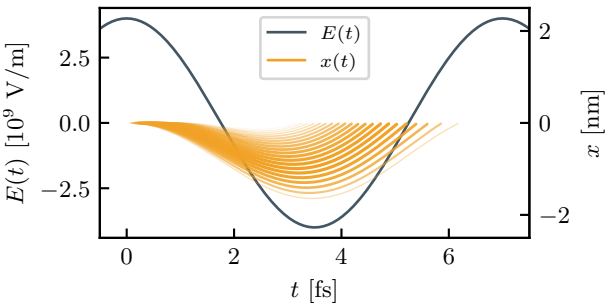

Figure 2.4: Classical electron trajectories returning to the parent atom for a given electric field. The strength of the lines indicate the velocity at $x = 0$.

Finally, the efficiency of the recombination process strongly depends on the driving wavelength and scales $\propto \lambda^{-5}$ to $\propto \lambda^{-7}$ [67–70, 98]. These experimentally obtained values represent a substantial challenge for the generation of high cut-off energy harmonics at high flux and are even more drastic than initially estimated ($\propto \lambda^{-4}$ [66]).

2.2.2 Statistical photoionization model

To overcome the strong restriction to few atomic species, a heuristic photoionization model, the statistical photoionization (SPI) model, has been introduced by Uiterwaal et al. in Ref. [99]. Uiterwaal et al. have demonstrated that their model adequately models the experimental data for ionization of various atoms, ions and di- and multi-atomic molecules over a frequency range from the IR to the UV and laser pulse durations from ns to few fs. The following part summarizes the main aspects of Ref. [99].

The SPI model relies on the assumption of one photon of energy $m\mathcal{E}_{\mathrm{ph}}$ being equivalent to m photons of energy $\mathcal{E}_{\mathrm{ph}}$ arriving within a characteristic time, a so-called timelet $\Delta t_m = \frac{T}{m}$ [99]. Consequently, the absorption of m photons of energy $\mathcal{E}_{\mathrm{ph}}$ can be described by the single photon absorption cross-section σ_m of a photon of energy $m\mathcal{E}_{\mathrm{ph}}$. As a result, the ionization of any species is described solely by the single-photon absorption cross-section, which is available for a large number of atomic and molecular species. For ionization to occur, a minimum number of photons $m_{\mathrm{min}} = \lceil \frac{I_{\mathrm{P}}}{\mathcal{E}_{\mathrm{ph}}} \rceil$ defined by the ionization potential I_{P} needs to be absorbed.

Following Ref. [99], the probability of the absorption of at least m photons is given by the Poisson distribution for $m \geq m_{\mathrm{min}}$,

$$\mathcal{P}_m(t) = \sum_{s=m}^{\infty} \frac{M_m(t)^s}{s!} \exp\left(-M_m(t)\right) = 1 - Q(m, M_m(t), \tag{2.24}$$

where $Q(m, M_m(t))$ is the regularized gamma function and $M_m(t)$ is the mean number of absorbed photons to level m within Δt_m,

$$M_m(t) = \frac{\sigma_m}{\mathcal{E}_{\mathrm{ph}}} \int_{t-\Delta t_m/2}^{t+\Delta t_m/2} I(t')\,\mathrm{d}t'. \tag{2.25}$$

Taking all levels $m \geq m_{\mathrm{min}}$ into account, the total ionization probability reads [99]

$$\mathcal{P}(t) = 1 - \prod_m \left(1 - \mathcal{P}_m(t)\right) = 1 - \prod_m Q(m, M_m(t)). \tag{2.26}$$

Taking all timelets into account, a universal index k can be defined to order them in time. The probability of an atom being ionized after the k-th timelet, Y_k^{ion}, can then be estimated by solving the following equations (Eq. (7) from Ref. [99]):

$$Y_k^{\mathrm{ion}} = Y_{k-1}^{\mathrm{ion}} + \left(1 - Q(m_k, M_k)\right) Y_{k-1}^{\mathrm{neut}} \tag{2.27}$$

$$Y_k^{\mathrm{neut}} = Y_{k-1}^{\mathrm{neut}} Q(m_k, M_k) \tag{2.28}$$

The derivative of the quantity Y_k^{ion} with respect to time, $\mathrm{d}Y_k^{\mathrm{ion}}/\,\mathrm{d}t$ is the corresponding ionization rate, the time dependence stems from the index k, which transfers to a point in time. Predictions of this ionization model have successfully been confirmed in the literature [99–102]. For a low ionization potential and high photon energy, considering the lowest timelet m_{min} only can be sufficient. In contrast, for low photon energies, as is the case with CO_2 lasers, more timelets with $m \geq m_{\mathrm{min}}$ need to be considered [99].

2.3 Signal formation of laser induced currents

In Sec. 2.2, I introduced various models for strong-field ionization. In all cases, a short laser pulse generates an ensemble of neutral and charged particles. The latter typically gain energy and momentum from the field, leading to enhanced charge carrier dynamics. The charge carriers might be displaced from their origin, forming a dipole, or can directly travel towards a detector in form of a real electric current. Such a detector can be a micro-channel plate, a semiconductor based detector, a metallic electrode, or a pair of them. In this thesis, the focus will be a pair of metal electrodes which allows a simple experimental setup and external electronic circuitry while offering manifold possibilities for petahertz scale photoconductive sampling of laser fields, for the detection of the carrier-envelope-phase, ion yield, or others. A sketch of a typical setup is shown in Fig. 2.5.

The signal formation of laser-generated currents between such metal plates has been investigated in detail in the PhD thesis of J. Schötz [103] and Ref. [104]. I will present

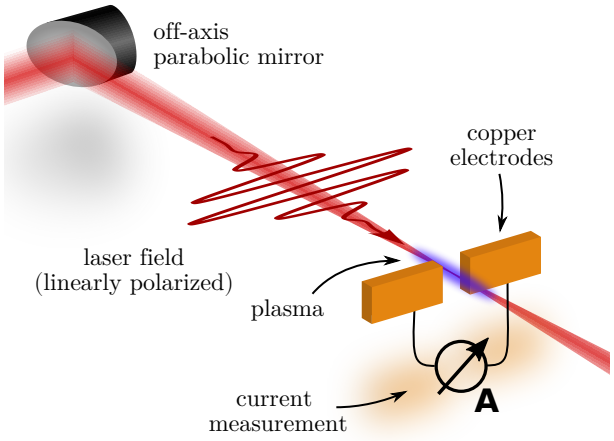

Figure 2.5: Sketch of a typical electric current sampling experiment: The laser beam is focused between a pair of electrodes, ionizes the gas in between them and generates a charge displacement or movement that can be sensed and measured.

a short introduction to the Shockley-Ramo model [104–108] that we introduced to the context of ultrafast light-matter interaction in Ref. [104]. This model will serve as a basis for a more profound understanding of the experimental results shown in Chapters 3 and 4.

The dipole generated by the laser-induced charge separation can induce an image dipole on a sensing electrode and thus generate a detectable signal, in addition to the direct current contribution. Since both contributions transition smoothly into each other, the Shockley-Ramo model has been introduced [104–108] to overcome that separation. For any given charge carrier configuration, defined by the position $\boldsymbol{r}$ and velocity $\boldsymbol{v}$ of the carrier of charge q, the induced charge Q on an electrode and current I that flows can be calculated by the following expression [104]:

$$Q = -q\phi_0(\boldsymbol{r}), \tag{2.29}$$

$$I = q\boldsymbol{v}\boldsymbol{E}_0(\boldsymbol{r}). \tag{2.30}$$

Here, ϕ_0 and $\boldsymbol{E}_0$ are the weighting potential and field, respectively. The latter quantities are defined solely by the geometry of the electrodes and can be calculated by setting the potential of the electrode under consideration to 1 V, all others to 0 [104–106]. This model assumes that the image dipole is formed instantaneously without delay, which is a good approximation for charge carrier dynamics much slower than a time constant of around 3 ps, corresponding to the typical gap size of 1 mm divided by the speed of light. Consequently, the model is appropriate for modeling the signal formation due to charge propagation after the laser, which is on a nanosecond timescale [104]. The initial signal modeling, however, requires different treatment. In particular, for femtosecond processes, e.g. as in Section 2.4, the signal is expected to build up over time - due to charge carrier propagation and the accompanying charge separation as well as due to the finite signal speed. Thus, their modeling can be treated independently and defines starting conditions on subsequent propagation.

The advantage of that model is the decoupling of the geometry of the detection electrodes from the charge carrier migration, meaning that once the weighting potential is calculated, the currents and charges on all electrodes are determined. Especially, the expensive calculation of image charges for each charge carrier configuration is circumvented. The weighting potential ϕ_0 has a simple analytic form for the case of infinite plates (index $1, 2$) at a distance d of [105]

$$\phi_{0,1}(x) = 1 - \frac{x}{d}, \tag{2.31}$$

$$\phi_{0,2}(x) = \frac{x}{d}, \tag{2.32}$$

assuming that electrode 1 is at $x = 0$, as can be seen in Fig. 2.6b). The corresponding weighting field $\boldsymbol{E} = -\nabla\phi_0$ is a constant in this simple case, but more complicated geometries can be considered, see Ref. [104, Methods]. As an example for a more realistic scenario with finite plates, the problem is treated numerically in Fig. 2.6a). There, the static electric potential for the electrode arrangement used in the experiments is solved using the scuff-static implementation of scuff-em [109]. The electrode geometry consists of two plates of dimensions $4 \times 2 \times 0.5\,\mathrm{mm}$, separated by 0.35 mm from each other. The 3D model is meshed with gmsh [110]. Figure 2.6a) shows a cross-section of that arrangement. Importantly, when comparing the potential on a line between the electrodes to the analytic solution, Fig. 2.6b), the deviation from the infinite pate case is negligible.

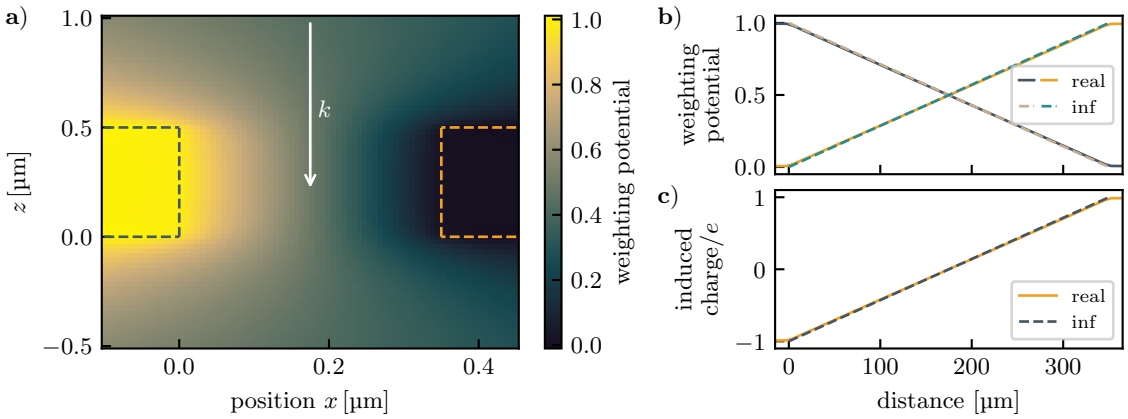

Figure 2.6: a) Weighting potential of finite electrodes at a distance $d = 350\,\mu\mathrm{m}$. The arrow indicates the direction the laser pulse travels through the setup (k vector). **b)** Deviation of the weighting potential of finite electrodes on axis from the infinite plate case. **c)** Induced charge in a differential measurement for infinite plates and finite ones, exhibiting a zero-crossing for a signal generated directly in the center.

As opposed to Ref. [104], where each electrode is measured separately against ground, one electrode is measured versus the other in Chapter 3. In such a differential kind of approach, the induced charge reads

$$Q_{\mathrm{total}} = Q_2 - Q_1 = -q\left(\phi_{0,1} - \phi_{0,2}\right) = -q\left(1 - \frac{2x}{d}\right). \tag{2.33}$$

In this case, the corresponding current contribution is a constant with respect to position. The total induced charge (Eq. (2.33)) is plotted in Fig. 2.6c) and exhibits a zero crossing for signals generated in the center of the electrode pair. Importantly, Eq. (2.33) implies that for any given charge ensemble, the position where it is generated defines the amplitude of the signal and its change with positions is

$$\frac{\partial Q_{\mathrm{total}}}{\partial x} = \frac{2q}{d}. \tag{2.34}$$

Equation (2.34) suggests that a large amount of laser beam pointing, i.e. a large dx, causes a smaller signal change if the gap size d is large. Comparison to the case of finite electrodes confirms that this equation remains valid in real-world applications.

2.4 Ionization effects in laser induced current sampling

In Section 2.3, I summarized a model explaining the macroscopic formation of currents generated by a laser pulse. The microscopic aspects have hitherto been assumed to have passed before that, e.g. as an event of laser driven ionization of the target. In this part, I will focus on an ionization-induced effect that occurs when the ionization process is

driven into saturation. In brief, for an unsaturated case, the electron emission rate is expected to follow the ionization rate as presented in Section 2.2. Importantly, the peaks of electron emission coincide with the peaks of the electric field. Now, if the ionization is driven into saturation, that is, when the amount of neutral atoms is significantly reduced before the laser pulse has passed through the target, the effective peak of electron emission shifts away from the peak of the field. Consequently, the vector potential is different, and thus the final electron momentum which influences the signal in electric current sampling experiments. This boost is particularly important in CEP dependent measurements, since enhances the signal contrast, i.e., the magnitude of the CEP dependent part of the signal. I will introduce the two-dimensional model that we published as part of Ref. [71] which explains the background behind this effect. Its consequences are observed experimentally in Sec. 3.3.2. In the calculations, I will vary the intensity to identify the scaling behavior for comparison to the experimental data.

2.4.1 Signal formation in saturation of ionization

To identify the role of saturation of ionization in ultrafast current generation experiments, the ultrafast interaction of a laser pulse with a gas target is modeled by the following steps:

1. Laser-driven strong-field ionization that frees electrons according to an ionization rate (for individual atoms/molecules), while obeying a rate equation to account for the depletion of neutral atoms/molecules
2. Classical propagation of the free electron in the electric field after the ionization event (comparable to Ref. [60])
3. Signal formation of the current, which is proportional to the acquired drift momentum of the electrons, i.e., the vector potential

Step 1 Ionization To model the interaction of a few-cycle laser pulse with a gas and to incorporate potential saturation effects, the rate equations

$$N(t + \mathrm{d}t) = N(t) - \mathrm{d}N, \tag{2.35}$$
$$= N(t) - w(t + \mathrm{d}t)\,\mathrm{d}t \cdot N(t), \tag{2.36}$$
$$Z(t + \mathrm{d}t) = Z(t) + \mathrm{d}N \tag{2.37}$$

are used. The total number of neutral atoms/molecules is denoted as $N(t)$, with an initial value of $N(t_0) = N_0$, whereas the number of ions is $Z(t)$ with $Z(t_0) = 0$. Only single ionization is considered. The ionization rate $w(t)$ is calculated by one of the models above (Sec. 2.2). Specifically, I employ the SPI model due to its capabilities in describing complex molecules such as ethanol, which is used in the experiments (see Chapter 3). The required data for the photon absorption cross-section of ethanol can be found in Ref. [111], the ionization potential is 10.47 eV [112]. The resulting electron emission rate $\mathrm{d}Z/\,\mathrm{d}t$ is shown Fig. 2.7b) for the electric field shown in part a) therein, together with the unsaturated ionization rate $w(t)$.

The comparison of the unsaturated ionization rate $w(t)$ with the actual electron emission rate reveals that the peak of maximum electron emission has jumped towards earlier half-cycles. This jump is a direct consequence of the depletion of neutral atoms, which limits the maximum emission at the peak of the pulse since a significant portion of neutral atoms has already been ionized by then. Additionally, each individual emission burst shifts away from the maximum of the field oscillation to an earlier instant in time within the same optical half-cycle. When considering the vector potential, this shift is of considerable importance since the maximum of the electron emission does not occur at the

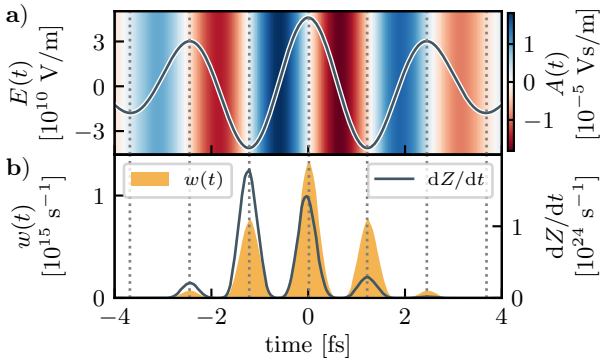

Figure 2.7: a) Electric field (solid line) and vector potential (colored area) at a peak field strength of 4.6×10^{10} V/m. **b)** Unsaturated ionization rate (filled area) and electron emission rate (solid line) in the saturated case.

zero-crossing of the vector potential anymore. Instead, most electrons are emitted at times with non-zero vector potential A, see Fig. 2.7a). Consequently, the electrons are expected to gain more momentum by the field due to the favorable shift of birth time.

Step 2 Propagation The information of the electric field imprinted on the momentum p of a single free electron after ionization can be estimated by the vector potential A of the electric field E [60]. With

$$A(t) = -\int_{-\infty}^{t} E(\tilde{t})\,\mathrm{d}\tilde{t}, \tag{2.38}$$

the final velocity v_{final} at time t_{final} of an electron that was set free at time t_1 can be written as

$$v_{\mathrm{final}} = -\frac{e}{m_{\mathrm{e}}}\int_{t_1}^{t_{\mathrm{final}}} E(t)\,\mathrm{d}t \tag{2.39}$$

$$= \frac{e}{m_{\mathrm{e}}}\left[A(t_{\mathrm{final}}) - A(t_1)\right] \tag{2.40}$$

$$= -\frac{e}{m_{\mathrm{e}}}A(t_1), \tag{2.41}$$

since $A(t_{\mathrm{final}}) \approx 0$ for $t_{\mathrm{final}} \gg \tau$ and pulses longer than sub-cycle optical transients. The expression above implies that the single particle contribution to the total current signal is proportional to the drift momentum, i.e., the vector potential. This agrees with the Shockley-Ramo model introduced in Sec. 2.3, where the detected signal is shown to be proportional to both the velocity of the particle and its displacement to the parent ion. The latter is the drift velocity multiplied with time, therefore again proportional to the vector potential. This is why the vector potential serves as a measure for the expected signal strength in this section, reminiscent of the Shockley-Ramo model.

Step 3 Signal formation If in total N free electrons contribute to the signal, all individual final velocities $v_{\mathrm{final},i}$ for each particle i born at $t_{1,i} = t_i$ with $i \in [1; N]$ must be considered. The vectorial sum $\bar{v} = \sum v_{\mathrm{final},i}$ estimates the net dipole (and direct current) that can form for a certain input laser field. This assumption is founded in the Shockley-Ramo model, in particular in Eqs. (2.29) and (2.30), where velocity and position of a charged particle are related to the detected charges and currents. Generally, $\bar{v}$ is a function of the electric field of the laser and therefore exhibits a CEP dependence. In particular, $\bar{v}$ changes sign for a CEP change of π. To investigate the influence of saturation of ionization on the CEP dependence of the signal, the value of $\bar{v}$ is determined for different CEPs of the laser, see Fig. 2.8a). A sinusoidal dependence of $\bar{v}$ with CEP is found and the maximum of $\bar{v}$ shifts versus CEP as the intensity changes. This shift can be interpreted

as phase shift $\Delta\phi$ between $\bar{v}$ and φ_{CEP} and is a consequence of the shift of the electron injection time, which depends on the intensity. Both the amplitude and the phase shift influence the total signal scaling.

Firstly, for the investigation of the amplitude scaling with intensity, the magnitude of the expected CEP-dependent signal $\hat{S}$ is defined by

$$\hat{S} = \frac{1}{N} \cdot \left[\max_{\varphi_{\mathrm{CEP}} \in [0,2\pi]} (\bar{v}(\varphi_{\mathrm{CEP}})) - \min_{\varphi_{\mathrm{CEP}} \in [0,2\pi]} (\bar{v}(\varphi_{\mathrm{CEP}})) \right], \tag{2.42}$$

where the prefactor $\frac{1}{N}$ normalizes per generated electron. This quantity can be interpreted as the net average drift momentum per emitted charge carrier and therefore as a measure for the CEP sensitivity of the signal. Importantly, in a non-saturated regime, the average drift momentum $\hat{S}$ is expected to scale linearly with the electric field strength. To identify

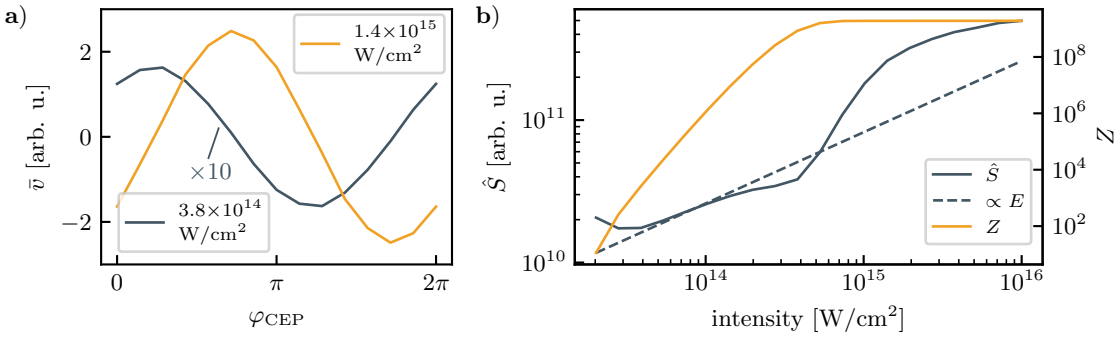

Figure 2.8: a) The net drift direction of the electrons favors a CEP dependent asymmetry. **b)** The scaling of the expected signal magnitude with intensity exhibits a boost at the saturation point. Here, focal volume effects are not included.

the role of saturation of ionization, $\hat{S}$ is calculated for exemplary 3×10^9 particles in a finite volume of constant intensity. The number of particles originates from a particle density of $\rho \approx 1 \times 10^{23}\,\mathrm{m}^{-3}$ and the volume of a typical focus. As can be extracted from the results in Fig. 2.8b), $\hat{S}$ experiences a boost of nearly one order of magnitude at an intensity of $5 \times 10^{14}\,\mathrm{W/cm}^2$. At this intensity, saturation sets in as evident from the kink in the total number of free electrons Z, which converges to the total number of particles N_0. For higher intensities, the scaling of $\hat{S}$ with intensity becomes flatter than the $\propto E$ scaling which indicates that the jump of electron emission to earlier optical half-cycles is dominant at high intensities. There, it overcomes the signal boost caused by the temporal shift of the injecting within the half-cycle.

Secondly, the intensity-dependent phase shift between the laser pulse CEP and $\bar{v}$ needs to be taken into account. Before considering the actual spatial intensity profile, the phase shift is investigated as a function of intensity. This shift can be extracted from the calculations above by fitting a sinusoidal function to $\bar{v}$ and is shown in Fig. 2.9. Clearly, the phase shift sets in at the saturation point, that is, where the number of free electrons Z saturates. For a given intensity profile (e.g. as shown in inset i)), this shift transfers to a spatial phase pattern, see insets ii) - iv). These patterns effectively indicate that charge carriers from different shells around the focus gain a different net momentum and thus propagate in different directions on average.

Therefore, the spatial intensity profile in the interaction region must be considered. To this end, a disk of thickness Δz is defined as the volume where signal is generated, assuming cylindrical symmetry. Phase effects along the propagation direction z are neglected which holds for small Δz. Assuming a Gaussian pulse in space with radius w_0, the problem reduces to the radial dimension. The number of particles $\mathcal{N}$ in a shell of thickness dr is

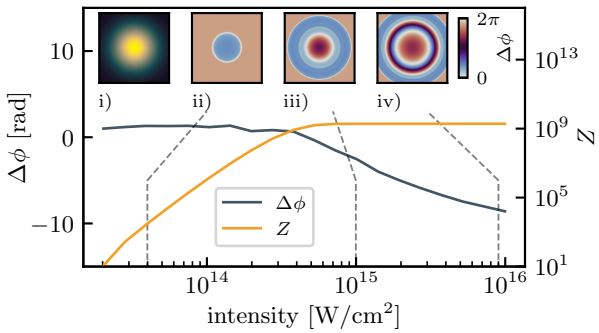

Figure 2.9: Phase shift between CEP and net charge carrier momentum as a function of intensity. The insets show a Gaussian beam profile i) and the corresponding spatial phase at different intensities ii)-iv).

given by

$$\mathcal{N} = \rho \cdot V = \rho \cdot d \cdot \pi \left((r + \mathrm{d}r)^2 - r^2\right) \tag{2.43}$$

$$= \rho d \pi (2r\,\mathrm{d}r + \mathrm{d}r^2), \tag{2.44}$$

and scales linearly with radius. The focal volume effect can be accounted for by either solving the rate equation (2.36) for different $N_0 = \mathcal{N}$ as described by Eq. (2.44) and different intensities, or by solving the rate equation for a continuous N just for different intensities and scaling of the results for the different number of particles $\mathcal{N}$ in a shell volume. The latter approach is chosen since it is computationally less expensive and thus, $\hat{S}$ is calculated for a $w_0 = 20\,\mu\mathrm{m}$ Gaussian beam after determination and summation of $\bar{v}$ for all individual shells. The results are illustrated in Fig. 2.10. A signal enhancement at the saturation point is visible; however, it is less pronounced than in the case of constant intensity which confirms the detrimental influence of the spatially varying phase. Thus, the signal gain by the shift of the electron emission time is counteracted by the spatially varying phase, which especially dominates at high intensities. The interplay between boost and phase shifts results in an intensity region where the net signal enhancement per particle is large, and it appears at the point where saturation sets in. In this example, which models a parameter set that is investigated experimentally in Chapter 3, the region of signal enhancement occurs at intensities in the range of $(4 - 9) \times 10^{14}\,\mathrm{W/cm^2}$.

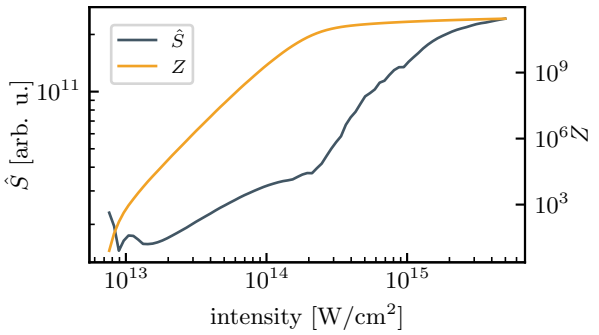

Figure 2.10: Scaling of $\hat{S}$ with intensity in a spatially integrated model.

Dispersion dependence of the signal scaling So far, a temporally compressed laser pulse was assumed. However, the model above can be applied to investigate the dispersion scaling of the expected signal. In particular, if a pulse is chirped, i.e., stretched in time, the peak intensity (assuming similar pulse energy) is reduced and the number of optical cycles is increased. As a consequence, both the ion yield is expected to drop, but also the asymmetry the field induces is smaller. To uncover the limiting aspect, a Gaussian pulse with 4.5 fs FWHM pulse duration and an intensity of $5 \times 10^{14}\,\mathrm{W/cm^2}$ is chirped by applying the spectral phase of fused silica corresponding to an insertion x. The latter data is retrieved from Ref. [79]. The calculation results shown in Fig 2.11 indicate a clear peak in

signal strength for best compressed pulses. The scaling of signal is not perfectly symmetric around the dispersion zero-point, but exhibits a steeper edge for negative insertions. The latter do not correspond to a negative material but rather to a lack of material needed for compression, as is the case when using dispersive multilayer mirrors that introduce a spectral phase of opposite sign than the material. The higher steepness of the curve can be attributed to a higher-order spectral phase term, which is inherently included by modeling the exact material properties. Note that here the total signal S is shown and not the per-particle signal $\hat{S}$.

Noteworthy, the signal S quickly reaches zero for material insertions $|x| > 0.2\,\mathrm{mm}$. There, the total electron yield Z is still of the order of 10^8 particles. This discrepancy indicates that the signal loss is not caused by a decreasing number of free electrons but rather a consequence of the increasing pulse duration and the accompanying decreasing asymmetry the field can generate.

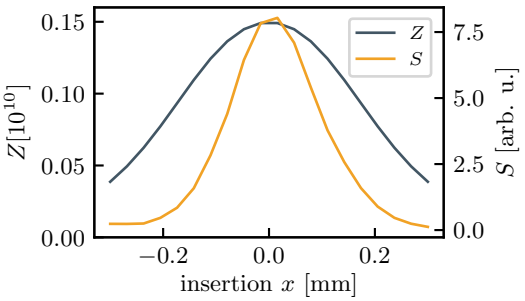

Figure 2.11: The dispersion scan of the asymmetry of the currents induced by the laser suggests a strong peak of the signal for well compressed pulses. Notably, the signal scaling is not perfectly symmetric but exhibits a steeper behavior for negative insertion values.

2.4.2 Discussion

In summary, solving rate equations for ionization around the saturation point has shown that the instant in time when electrons are emitted shifts from the peak of the field to an earlier instant within the optical half-cycle. In addition, the optical half-cycle where electron emission maximizes can jump to the ones earlier than the strongest one. As a consequence of the shift within the half-cycle, the peak of electron emission preferably happens at times when the vector potential is non-zero, and therefore the signal increased due to its proportionality to the vector potential. Spatial integration has shown that the intensity dependence of this effect counteracts the scaling and results in a confined intensity region where the effect is present.

The presented model is two-dimensional in space, i.e., it does not account for propagation of the laser through the target. Besides linear effects, such as the Gouy phase shift, reshaping of the laser could take place. Spatiotemporal reshaping of laser beams passing through a plasma in the saturation regime has recently been investigated in the literature by Ansari et al. [113]. They showed that Ti:Sa lasers with intensities in the saturation regime passing through Argon undergo various effects, ranging from spectral broadening, compression to reshaping of the beam profile. However, they found that these processes start from pressures above 100 mbar towards 1 bar, thus a much higher particle density is present there compared to the ones investigated above. The particle density above of $\rho = 1 \times 10^{23}\,\mathrm{m}^{-3}$ corresponds to a pressure of around 4 mbar and is thus lower. Therefore, such effects are expected to have less influence. If they influenced the measurement, the CEP would change along the propagation and therefore lead to a cancellation of the signal, which is not observed experimentally. However, in the experiment, electrodes with a sufficiently small extension along the propagation direction are required to prevent signal cancellation due to spatial phase effects. In Sec. 3, data on the spatial dependence of the detected currents is presented, verifying that the pulse reshaping occurs on a length scale longer than the electrode expansion.

Additionally, only the average velocity of the free charge carriers was considered, while the expansion of the volume they have been generated in was neglected. According to the Shockley-Ramo model introduced in Sec. 2.3, a linear dependence on the position between the electrodes is expected. Thus, this assumption is only valid if the transverse expansion of volume the charge carriers are generated in is small compared to the electrode distance. In the case under consideration, the sensing electrodes (distance $D \approx 350\,\mu m$) are far away from the signal generating volume (expansion $d < 25\,\mu m$), such that this assumption is valid.

A thorough discussion of how this model is related to our previous work (Schötz et al. [104]) and how multiply charged ions influence the signal is presented in Chapter 3 since experimental data is required.

2.5 Sampling of optical fields

The measurement of the electric field of visible (VIS) to near infrared (NIR) light had been an open question of science until the advent of attosecond science, which for the first time measured the light oscillation [64]. Along with pioneering attosecond streaking [63, 64, 114], numerous other techniques have been developed, among them the petahertz optical oscilloscope [115], linear [116] and non-linear photoconductive sampling [33, 117, 118], femtosecond streaking [119], electro-optic sampling [120], generalized heterodyne optical-sampling techniques (GHOST) [32], the third-order reconstruction of electric fields via cross(X)-correlation (TREX) [121] or the **T**unneling **I**onization with a **P**erturbation for the **T**ime-domain **O**bservation of an **E**lectric field (TIPTOE) technique [26, 28–31, 34, 122–125]. Recently, another perturbation technique using third-harmonic generation in air and spectral detection of the signal has been demonstrated [126]. While all of these methods are accompanied by their advantages and disadvantages, novel approaches exploit the detection of laser generated currents for the sampling of optical fields [26, 28–31, 33, 117–119, 123], considerably improving the measurement speed and simplifying the experimental setup.

For the characterization of the light waveforms in Chapter 4, TIPTOE is the method of choice due to its widely confirmed reliability, simplicity of the setup and large detection bandwidth, provided short pulses [26, 28–31, 34, 122–125]. Below, I will introduce the main principle of TIPTOE following seminal work by Park et al. [26]. I will also discuss the spectral response of TIPTOE, similar to Ref. [28], where the response for TIPTOE on a surface was discussed. Notably, the spectral response of TIPTOE has been discussed theoretically in the literature before [26, 28, 31, 125], but to the best of my knowledge, no systematic investigation of the spectral response as a function of laser pulse CEP has been performed experimentally without second harmonic generation [26]. This might be connected to the appearance of these effects at even-order harmonics of the fundamental frequency only, see below, which otherwise requires multi-octave supercontinua. Notably, TIPTOE was used to characterize single-cycle pulses generated from cascaded single-pass gas cells, but despite the large bandwidth, no CEP response effects of TIPTOE were discussed in Ref. [127].

A typical TIPTOE measurement consists of two interfering laser pulses that generate a charge Q in a gas, which is detected by biased electrodes in a charge or current measurement, c.f. Ref. [26]. The setup is comparable to the one treated in Sec. 2.3, except that an additional bias voltage drives the charge carriers towards the plates. One of the beams, the pump beam E_{Pump}, ionizes the gas according to one of the presented models. Since the photon energy of the laser must be lower than the ionization potential of the gas, the ionization process is nonlinear and therefore field-dependent. The corresponding electron emission happens only during the peaks of the (one or several) strongest half-cycle(s) of the pump beam, forming a sub-cycle temporal gate, see Fig. 2.12a). This generated charge

is modulated by the second beam, E_{Signal}, which interferes with the pump beam. Since E_{Signal} is weak, it does not drive its own ionization process but can only modulate the ionization process of the pump due to the nonlinearity. For sufficiently small E_{Signal}, this modulation is linear and proportional to the field of the signal beam during the gate [26].

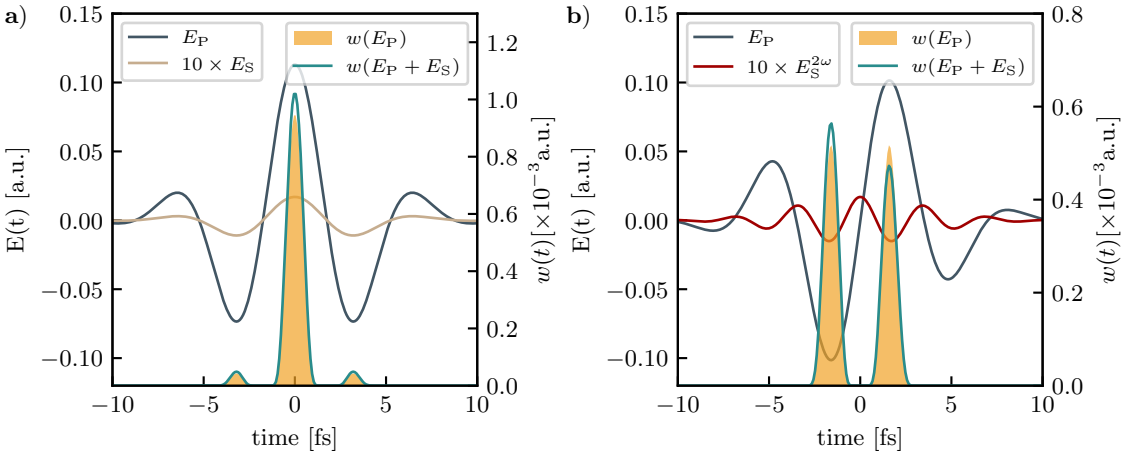

Figure 2.12: *The principle of* TIPTOE - **a)** The ionization rate of the pump beam E_P is perturbed by the signal beam E_S during the temporal gate formed by the ionization burst. **b)** For a different CEP of the pump, the modulation of a 2ω field cancels out. Atomic units are used in this figure for E and w.

The total charge can be expressed as a function of delay τ between the beams [26]

$$Q(\tau) \propto \int w\left(E_{\text{Pump}}(t) + E_{\text{Signal}}(t+\tau)\right) \mathrm{d}t. \tag{2.45}$$

The sign of the delay is chosen such that for positive τ, E_{Signal} arrives at the target before E_{Pump} and therefore, the tailing part is being sampled [128] - in accordance with the convention on the direction of the time axis introduced in Sec. 2.1. Similar to Refs. [26,28], Taylor-expanding the expression for Q around the pump yields

$$Q(\tau) \propto \int w(E_{\text{Pump}}(t))\,\mathrm{d}t + \int \left.\frac{\partial w(E)}{\partial E}\right|_{E_{\text{Pump}}(t)} \cdot E_{\text{Signal}}(t+\tau)\,\mathrm{d}t = Q_0 + \Delta Q(\tau). \tag{2.46}$$

If E_{Pump} is sufficiently short, the term $\frac{\partial w(E)}{\partial E}$ can be approximated as a δ-function [26], which directly demonstrates the proportionality of $\Delta Q(\tau)$ to $E_{\text{Signal}}(\tau)$ [128]. In more realistic scenarios, the actual number, width, and amplitude of the occurring ionization bursts influence the detected charge modulation and thus its proportionality to the perturbing field must be investigated. In particular, the modulation can cancel out for a signal field at twice the fundamental frequency of the pump, e.g., if the pump CEP is $\frac{\pi}{2}$, see Fig. 2.12b). Therefore, the spectral response function of TIPTOE is defined similarly to Ref. [28]. There, the Fourier transform of the charge modulation

$$\mathcal{FT}\left[\Delta Q(\tau)\right] = \Delta Q(f) \propto \mathcal{FT}^*\left[\left.\frac{\partial w(E)}{\partial E}\right|_{E_{\text{Pump}}(t)}\right] \cdot \mathcal{FT}\left[E_{\text{Signal}}(t)\right] = H(f) \cdot E_{\text{Signal}}(f) \tag{2.47}$$

is taken as the product of the spectral response $H(f)$ and the expected complex spectrum $E_{\text{Signal}}(f)$, see Appendix A.3 for a derivation. Note that, in comparison to my previous publication (Ref. [31]), where the ratio of charge to the expected field, estimated with the full ionization rate, was used, this expression is equivalent. The reason lies in the definition of the spectral response, which is only well-defined if the detected signal is a linear function of the input field; therefore, the first-order Taylor approach is equivalent to using the full expression with a very weak perturbation only.

The calculated response function $H(f)$ for a 6 fs Gaussian pulse as pump centered at 1.8 µm central wavelength at an intensity of $4.5 \times 10^{14}\,\mathrm{W/cm^2}$ is shown in Fig. 2.13. The ionization process is modeled according to Ref. [89], introduced in Sec. 2.2.1. The spectral response amplitude $|H(f)|$ is maximum at the central frequency f_0 and drops to both the low and high frequency side. For a CEP of 0 or π, the decrease is less pronounced than for a CEP of $\pm\frac{\pi}{2}$, where the modulation actually reaches zero since multiple ionization bursts occur (see Fig. 2.12b)). For maximum sampling bandwidth, it is thus necessary to calibrate the absolute CEP of the pump. In the experiment, Sec. 4, this characteristic modulation of the $2f$ spectral components is exploited to calibrate the CEP of the pump beam.

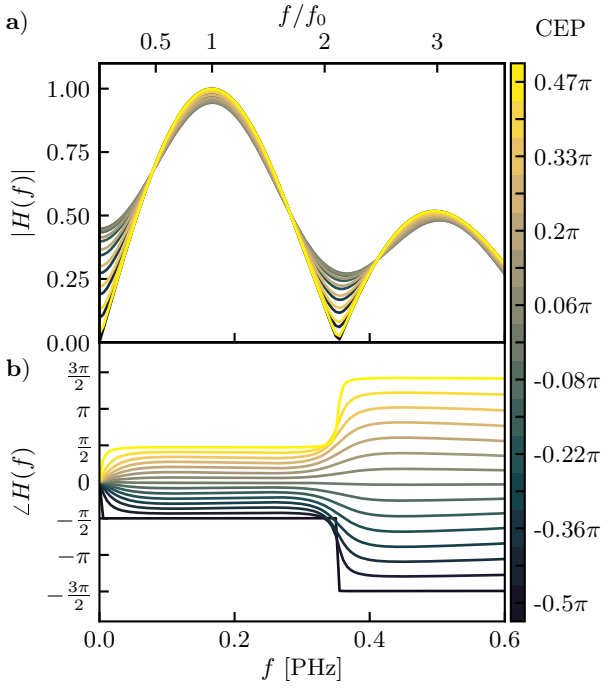

Figure 2.13: TIPTOE *response function* **a)** The spectral amplitude of the response function $|H(f)|$ exhibits minima at twice the fundamental frequency, depending on the pump pulse CEP. **b)** The phase of the response function is proportional to the CEP around the fundamental frequency, but three times the CEP around the $3f$ region. The colorbar applies to both panels. For $\varphi_{\mathrm{CEP}} = 0$, the response phase is flat and the minima are least pronounced.

The response phase, as plotted in Fig 2.13b), is only flat for a CEP of the pump of 0. For CEPs other than that, the response phase is proportional to the CEP in the spectral range around the central frequency f_0, but changes to $3\varphi_{\mathrm{CEP}}$ at around the $3f_0$ region, with a changing point at $2f_0$. This behavior differs from the one investigated in Refs. [28, 31] since there, surface ionization caused different constraints on the symmetry resulting in a response function exhibiting minima at different multiples of the fundamental frequency. Additionally, due to the inversion symmetry of the gaseous target under consideration here, a π-flip in CEP results in the same spectral response amplitude. Note that due to the definition of the CEP in Eq. (2.6), and the sign conventions of the Fourier transform (see comment in Appendix A.3), the phase of $H(f)$ leads to a cancellation of the detected CEP if it is shifted synchronously for pump and signal beam. Consequently, the detected waveforms do not exhibit a CEP change. On the other hand, if the CEP of either pump or of signal is fixed whilst the other one is being scanned, the change in CEP can indeed be detected, see the supplementary information of my article on field sampling with nanotips, demonstrating this effect (Ref. [31]). Methods for CEP sampling will be presented and discussed in Chapter 3.

2.6 Nonlinear propagation of lasers in gas-filled hollow waveguides

In the next section, I would like to present mechanisms for pulse compression and spectral broadening. Since lasers and optical parametric amplifiers (OPAs) have limited gain bandwidth [1], broadband laser sources typically employ additional spectral broadening and compression schemes. Mechanisms are manifold and involve nonlinear optical phenomena which can be driven in solids, liquids, gases and even in plasmas [129]. The choice of the suitable mechanism goes hand in hand with the desired spectral range and bandwidth. I will comment on design considerations in Chapter 4 and explain why the usage of HCFs is superior to all other methods for the high power spectral broadening scheme I am going to present there. Therefore, I will now introduce basic properties of linear and nonlinear propagation of light through hollow waveguides, comment on the main nonlinear effects, and discuss solitonic dynamics in such fibers.

2.6.1 Propagation in waveguides

The propagation of laser waves through waveguides and its application in nonlinear optics has been studied thoroughly in the literature [35, 36, 130, 131]. I summarize some aspects of propagating waves through waveguides important for the scope of this work. Therefore, I present the key elements from the seminal work by Marcatili and Schmeltzer [132] in the following. In waveguides, three different types of modes exist, firstly, transverse circular electric modes (TE modes) that have field components in E_ϕ, H_r and H_z direction. Secondly, transverse circular magnetic modes with components in H_ϕ, E_r and E_z (TM modes). Thirdly, hybrid modes with all E and H components present (EH modes) [132]. Within this thesis, the focus lies on linear polarized laser light coupled into a fiber, therefore a hybrid mode is necessary to describe the polarization state. The modes inside the waveguide in that case, the EH_{nm} modes, are given by ($n \neq 0$) [132]

$$E_{\phi nm} = \left\{ J_{n-1}(k_i r) + \frac{i u_{nm}^2}{2nka} \sqrt{\nu^2 - 1} J_n'(k_i r) \right\} \cos\left[n(\phi + \theta_0)\right] \exp\left[i(\gamma z - \omega t)\right] \tag{2.48a}$$

$$E_{rnm} = \left\{ J_{n-1}(k_i r) + \frac{i u_{nm}}{2kr} \sqrt{\nu^2 - 1} J_n(k_i r) \right\} \sin\left[n(\phi + \theta_0)\right] \exp\left[i(\gamma z - \omega t)\right] \tag{2.48b}$$

$$E_{znm} = -i \frac{u_{mn}}{ka} J_n(k_i r) \sin\left[n(\phi + \theta_0)\right] \exp\left[i(\gamma z - \omega t)\right]. \tag{2.48c}$$

Note that the sign convention used here follows Ref. [132]. The J_i are Bessel functions of first kind, u_{nm} the zeros of the $n-1$ Bessel function, ν is the complex refractive index of the cladding and has been renamed not to be confused with the indices n, m describing the mode order. The constant γ is the so-called propagation constant, see below, whereas θ_0 is used to account for waveguide curvature since it describes the angle between the electric field polarization and the plane of curvature [132, p. 1806]. An illustration of the first hybrid mode, EH_{11}, is shown in Fig. 2.14a)-c).

The coupling efficiency of the incident laser beam to the fiber ground mode is important for achieving highest transmission. To estimate the coupling efficiency η of a Gaussian beam in space, as represented by Eq. (2.9), to a waveguide with the mode defined in Eqs. (2.48), the coupling model from Ref. [133] is considered. With

$$\eta = \frac{\left| \iint \hat{E}_{\mathrm{in}}^y \hat{E}_{11}^y \, \mathrm{d}x \, \mathrm{d}y \right|^2}{\iint |\hat{E}_{\mathrm{in}}^y|^2 \, \mathrm{d}x \, \mathrm{d}y \iint |\hat{E}_{11}^y|^2 \, \mathrm{d}x \, \mathrm{d}y}, \tag{2.49}$$

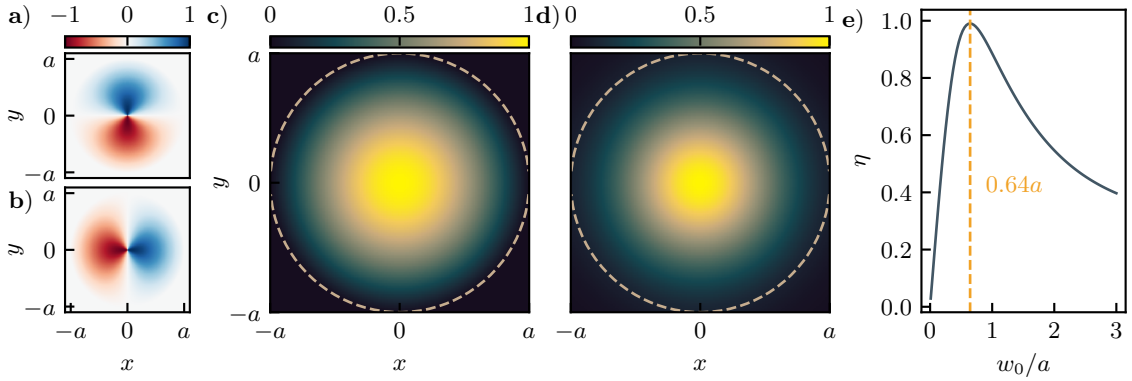

Figure 2.14: a,b) Radial and azimuthal field components E_r and E_ϕ in a fiber of radius a, respectively. Their superposition **c)** forms a linearly polarized field in y direction, E_y. **d)** Gaussian beam profile with waist $w_0 = 0.64a$, the value of optimum coupling efficiency, as shown in **e)**.

the overlap between the y components (the polarization direction) of the fiber mode and the incident mode is determined which estimates the coupling efficiency. The hat symbol denotes that the quantities are normalized to an energy content of unity. The values for η are shown in Fig. 2.14e) as a function of the mode size ratio. Clearly, an optimum with 99% overlap is found for a beam waist of the incident beam of $w_0 = 0.64a$.

The propagation constant γ is derived in Ref. [132] to be

$$\gamma \approx k\left[1 - \frac{1}{2}\left(\frac{u_{nm}\lambda}{2\pi a}\right)^2\left(1 - \frac{i\nu_n\lambda}{\pi a}\right)\right], \tag{2.50}$$

where the real and imaginary parts of γ are the phase constant and attenuation constant, respectively, given by

$$\beta_{nm} = \frac{2\pi}{\lambda}\left\{1 - \frac{1}{2}\left[\frac{u_{nm}\lambda}{2\pi a}\right]^2\left[1 + \Im\left(\frac{\nu_n\lambda}{\pi a}\right)\right]\right\} \quad \text{and} \tag{2.51}$$

$$\alpha_{nm} = \left(\frac{u_{nm}}{2\pi}\right)^2\frac{\lambda^2}{a^3}\Re(\nu_n), \tag{2.52}$$

which for straight dielectric waveguides, where the refractive index ν is real, simplifies to

$$\beta_{nm} = \frac{2\pi}{\lambda}\left[1 - \frac{1}{2}\left(\frac{u_{nm}\lambda}{2\pi a}\right)^2\right] \tag{2.53}$$

$$\alpha_{nm} = \left(\frac{u_{nm}}{2\pi}\right)^2\frac{\lambda^2}{a^3}\frac{\nu^2+1}{2\sqrt{\nu^2-1}}, \tag{2.54}$$

where $\nu_n = \frac{\nu^2+1}{2\sqrt{\nu^2-1}}$ for hybrid modes [132]. Note that these results also apply to metallic waveguides far away from cutoff [132]. From these results a general scaling law for losses in a waveguide can be extracted, namely that losses scale with $\alpha \propto \frac{\lambda^2}{a^3}$. In particular, this scaling law hinders the combination of long-wavelength lasers with small diameter waveguides since the transmission decreases drastically. Nevertheless, small waveguides are appealing for their dispersion, which is encoded in the parameter β.

Before starting the discussion about waveguide dispersion, I briefly review the results from Marcatili and Schmeltzer on curved waveguides and their losses, c.f. Ref. [132]. For a toroidal waveguide with radius of curvature R, the attenuation constant is

$$\alpha_{nm}(R) = \alpha_{nm}(\infty) + \frac{a^3}{\lambda^2 R^2}\Re V_{nm}(\nu), \tag{2.55}$$

where $\Re V_{nm}(\nu)$ are positive values depending on the mode order, refractive index, and the polarization angle with respect to the plane of curvature θ_0. The exact dependence is given in Eq. (45) in Ref. [132] and in Appendix A.4. Importantly, the dependence on the radius of curvature R suggests that straightness of the waveguide is essential for high transmission. This scaling law is the main motivation for the employment of stretched fibers [52], which will be elaborated in more detail in Chap. 4.

The propagation parameter β in Eq. (2.53) accounts for the properties of the empty waveguide. It has to be extended by terms describing the propagation through a gas with refractive index $\nu_{\text{gas}} = \sqrt{1+\rho\chi}$, where χ is the susceptibility and ρ the pressure relative to the conditions at which the susceptibility has been measured, and then reads in first-order Taylor approximation [51, supplementary information]

$$\beta \approx \frac{\omega}{c}\left(1 + \frac{\rho\chi}{2} - \frac{u_{nm}^2 c^2}{2a^2\omega^2}\right). \tag{2.56}$$

Since β describes a phase term comparable to what I introduced in Sec. 2.1, the group velocity dispersion can be extracted by the second derivative (c.f. Ref. [51])

$$\beta_2 = \frac{\lambda^3}{4\pi c^2}\left(\rho\frac{\partial^2\chi}{\partial\lambda^2} - \frac{u_{nm}^2}{2\pi^2 a^2}\right). \tag{2.57}$$

This relation summarizes the key element of propagation through a waveguide: The dispersion introduced by the medium, entering in the first term with positive sign in Eq. (2.57), is counteracted by the waveguide dispersion, second term with negative sign. In sum, both contributions can balance - in particular for small fibers where the waveguide dispersion becomes larger. Additionally, the fiber dispersion (negative sign) can be sufficiently small to compensate for dispersion introduced by nonlinear effects (positive sign), as described in the next section, such that nonlinear spectral gain and dispersion compensation happens simultaneously - and self-compression occurs. In the following sections, I will introduce the main non-linear effects causing a gain of spectral bandwidth, self-phase modulation (SPM) and self-steepening.

2.6.2 Nonlinear effects

If the light intensity is high enough, nonlinear effects alter the propagation, which can lead to the generation of new frequency components. In this subsection, self-phase modulation as the diving effect for spectral gain will be introduced, along with self-steepening. Both effects can be predominant in hollow-core fibers and lead to a gain in spectral bandwidth.

Self-phase modulation

One of the main effects generating new frequency components in fibers is SPM. It occurs when the refractive index of a material becomes intensity dependent, i.e., for strong laser fields, and has the form [134, 135]

$$n(t) = n + n_2 I(t), \tag{2.58}$$

with the non-linear refractive index n_2. The field after propagation over length L reads

$$E(t,L) = E_0 f(t)\exp\left(i\omega_0 t - i\frac{n\omega_0 L}{c} - i\frac{n_2 I(t)\omega_0 L}{c}\right), \tag{2.59}$$

which transfers to an instantaneous frequency defined by the derivative of the exponent with respect to time

$$\omega(t) = \omega_0 - \frac{n_2\omega_0 L}{c}\frac{\partial I(t)}{\partial t} = \omega_0 + \Delta\omega. \tag{2.60}$$

Apparently, the temporal pulse shape induces a frequency change by n_2, as illustrated in Fig. 2.15a). The pulse after SPM is red-shifted in the leading part and blue-shifted in the trailing edge, which corresponds to the generation of new frequency components, see Fig. 2.15b). However, it is accompanied by positive chirp, as evident from the curved spectral phase. Again, note the sign convention where positive chirp appears as concave phase function, as approximated by the dotted fit in the aforementioned figure. The exact shape of the spectral gain depends on the temporal shape of the intensity profile, but generally, positive chirp accumulates for most materials with $n_2 > 0$. This chirp must be compensated, either with post-compression schemes or by self-compressing schemes via the waveguide dispersion.

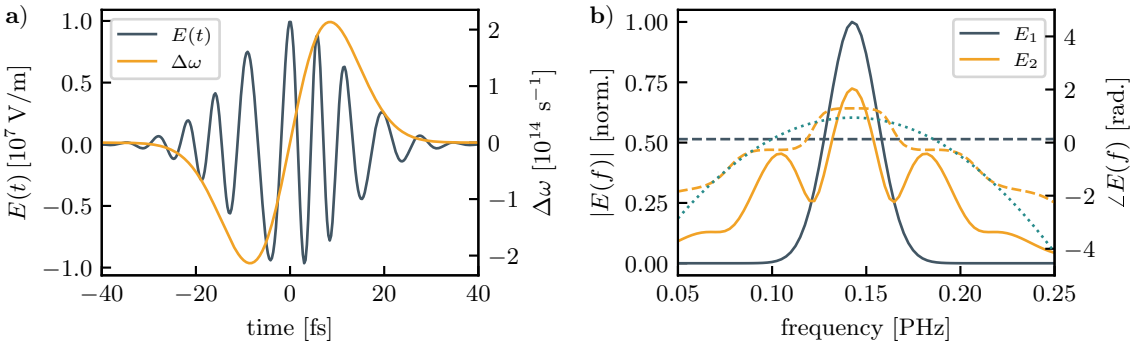

Figure 2.15: a) Electric field and instantaneous frequency change after propagation of 10 cm through a medium with $n_2 = 10^{-19}\,\frac{\mathrm{cm}^2}{\mathrm{W}}$ at an intensity of $1 \times 10^{14}\,\frac{\mathrm{W}}{\mathrm{cm}^2}$. **b)** Spectrum of the incident beam (E_1) and after SPM (E_2) with spectral phase (dashed) and polynomial fit (dotted).

Self-steepening

Another effect leading to spectral gain is self-steepening, or optical shock-wave formation. The interested reader is referred to Ref. [134], where a detailed derivation is provided. Summarizing the results, when self-steepening occurs, the group refractive index becomes intensity dependent, similar to SPM, where the phase index becomes intensity dependent. For most gases, $n_2^{(\mathrm{g})}$ is positive and therefore, the high intense part of the laser pulse, i.e. its maximum is delayed more than the edges. This effect transfers to a sharp trailing edge of the pulse, which appears as a blue shift in the spectrum [129, Chapter 2.12.3 therein].

2.6.3 Soliton dynamics and numerical simulations

Knowing the main effects generating additional spectral components, I will now discuss how the different aspects interplay. First, I consider characteristic length scales associated with the various properties of the waveguide and the nonlinear interaction. The attenuation coefficient α transfers to the so-called loss length

$$L_{\mathrm{loss}} = \frac{1}{\alpha}, \tag{2.61}$$

which is the $\frac{1}{e^2}$ attenuation length of the intensity [51, 132]. In addition, the length of propagation over which dispersive effects become important, the dispersion length, is defined as [51, 130, 134]

$$L_{\mathrm{disp}} = \frac{\tau_{\mathrm{fwhm}}^2}{1.763^2 \cdot |\beta_2|^2}. \tag{2.62}$$

Similarly, the characteristic length where nonlinear effects become effective for the pulse propagation can be defined as the nonlinear length [130]

$$L_{\mathrm{nl}} = \frac{1}{\xi P_0}. \tag{2.63}$$

Here, P_0 is the peak power and $\xi = \frac{2\pi n_2}{\lambda A_{\mathrm{eff}}}$ is the nonlinear coefficient, A_{eff} is the effective mode area [51]. The ratio between those two length scales

$$N = \sqrt{\frac{L_{\mathrm{disp}}}{L_{\mathrm{nl}}}} \tag{2.64}$$

identifies different regimes of propagation through fibers [130]. This quantity is the soliton order [51]. The soliton order can be used to describe the propagation dynamics qualitatively [129, 130]. If $N \ll 1$, propagation is dispersion dominated, whereas for $N \gg 1$ a nonlinearity dominated regime is present [130]. In the case where N is of the order of unity [130] (or $N < 15$ [51, 136]), both dispersion and nonlinearity act together and the propagation can be different - from the formation of optical solitons to self-compressing spectral broadening ($\beta_2 < 0$) [130]. The first-order soliton ($N = 1$) is the fundamental soliton and its shape does not change during propagation [130]. It thus describes a laser pulse propagating in balanced situation where dispersion and nonlinearity compensate each other. Corresponding simulations evidencing similar behavior are shown in Fig. 2.16 and discussed below. For a soliton order larger than unity, pulse compression can be followed by pulse stretching, referred to a solitonic breathing [137]. It has been predicted that in extreme cases, such solitonic breathers can generate light transients down to fractions of the optical period [137]. Nevertheless, such short light field transients are found in the literature as a consequence of resonant dispersive wave emission, a phenomenon that occurs when the group velocity dispersion vanishes, $\beta_2(\lambda_{\mathrm{zd}}) = 0$ [51]. The vanishing point, the zero-dispersion wavelength λ_{zd} can be tuned with gas pressure and may be much shorter than the driving wavelength, thus corresponding to UV emission [51] and a possible significant pulse compression [41, 42, 51, 138, 139]. The characteristic length scale on which the soliton forms, the fission length L_{fiss}, is given by [51]

$$L_{\mathrm{fiss}} = \frac{L_{\mathrm{disp}}}{N} = \sqrt{L_{\mathrm{disp}} L_{\mathrm{nl}}}. \tag{2.65}$$

Note that some expressions in literature differ by a factor $\sqrt{2}$ [140]. For detailed studies of the scaling laws for solitons in HCFs, the reader is referred to Refs. [42, 141].

The numerical simulations shown in Fig. 2.16 indicate that for a soliton order of $N = 1$, the temporal shape of the pulse remains invariant, whereas for higher N, an oscillatory broadening and narrowing in spectrum, corresponding to a compression and temporal stretching in pulse duration appears. The data is produced with the Luna.jl simulation package [142] assuming a laser pulse with 1 mJ energy at 2.1 µm wavelength in an $a = 143\,\mu\mathrm{m}$ fiber. The pulse duration is varied to cover different soliton orders as the corresponding peak power of the Fourier transform limited Gaussian pulse changes. For an increased visibility of the solitonic manner of the propagation, third-harmonic generation, plasma effects and losses are disabled. However, the gas dispersion is considered and as a consequence, higher-order dispersion is present which causes slight deviations of the symmetric temporal spread and compression as presented in textbooks [130]. For $N \approx 2$, the pulse compresses and spreads during propagation, whereas for $N \approx 3$ or $N \approx 4$, the temporal compression is followed by a spread that generates up to $N - 2$ minima in the center of the pulse envelope. Such behavior is referred to as solitonic breathing and is characterized by its capabilities in generating even sub-cycle transients [137]. Noteworthy, the comparison of the different propagation dynamics in Fig. 2.16 shows that long

pulses can undergo self-compression, that is the spectral spread with simultaneous temporal compression. The fiber length has to be adapted to stop the oscillatory manner at the point of best temporal compression. As an example, the 40 fs pulse in panels e) and f) reaches a higher peak power after 3 m of propagation than the 12 fs pulse in panels g) and h). These propagation dynamics suggest that soliton propagation is an excellent tool for pulse compression without any external dispersive elements for pulse shaping. Finally, the losses in real waveguides will limit the extension of such small HCFs to not more than several meters, which must be considered in the experiment design, see Chapter 4.

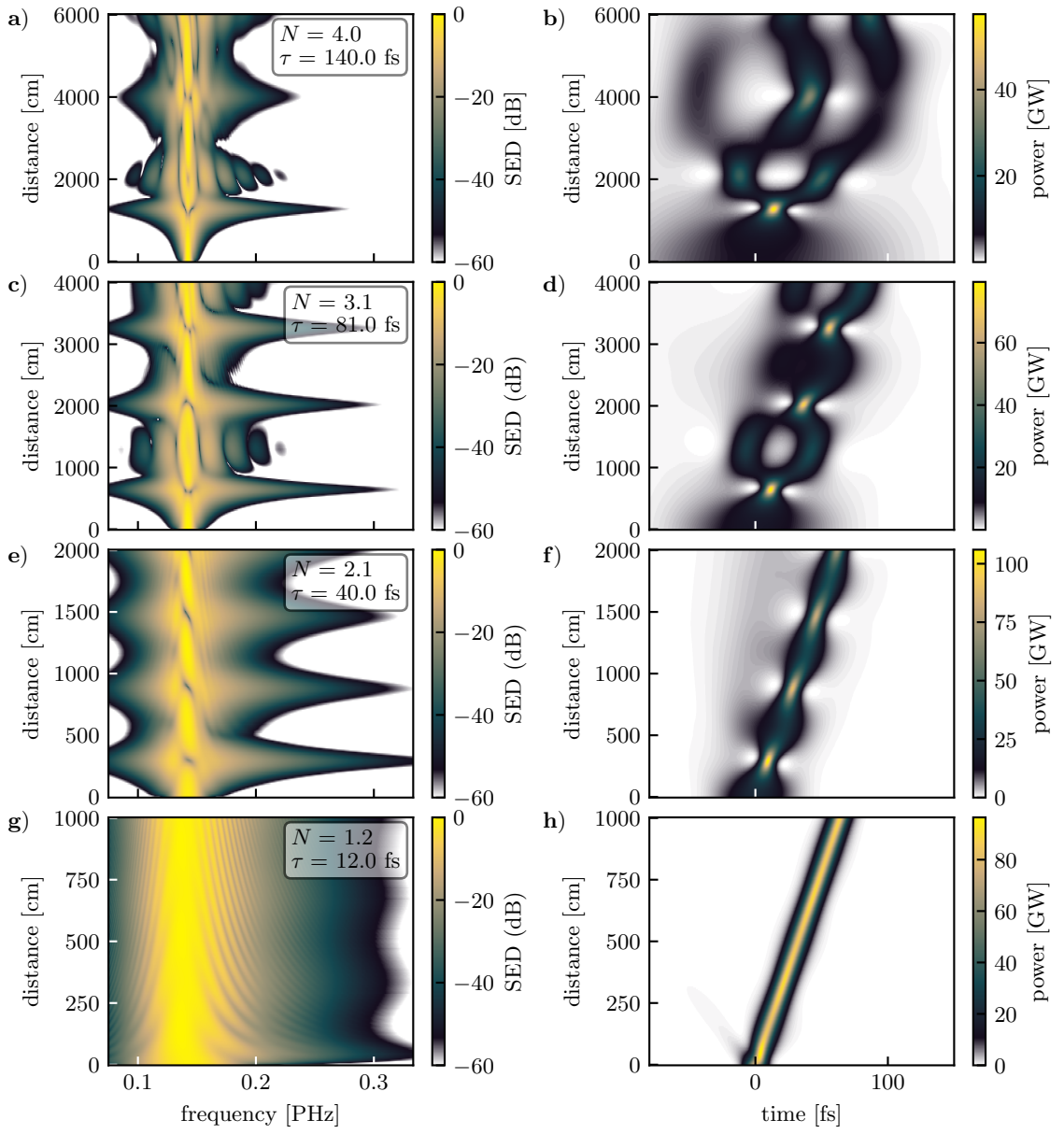

Figure 2.16: Propagation of optical solitons. Simulation data generated with Luna.jl [142] for a pulse with 1 mJ energy propagating through a 143 µm core radius hollow fiber filled with 0.7 bar of Neon. The central wavelength of the pulse is 2.1 µm and spectral bandwidth and peak power are defined via the different pulse durations. **a),b)** Frequency and time domain propagation dynamics for a $\tau_{\mathrm{fwhm}} = 140$ fs pulse, **c),d)** for $\tau_{\mathrm{fwhm}} = 81$ fs, **e),f)** for $\tau_{\mathrm{fwhm}} = 40$ fs and **g),h)** for $\tau_{\mathrm{fwhm}} = 12$ fs.

2.7 Interference of laser beams in Mach-Zehnder type interferometers

The interferometers used in this thesis will be of the Mach-Zehnder type. After recombination of the interferometer arms, two laser beams can co-propagate but also favor a small angle between them in the case of an imperfect alignment. This small angle is an advantage for the detection of the path length difference, as the appearing interference pattern can be captured with a camera and its Fourier transform delivers a phase value proportional to the optical path length difference, as I will briefly show here. Two plane waves propagating under an angle φ are described by

$$\boldsymbol{E}_1(\boldsymbol{r},t) = \boldsymbol{E}_1 \exp(i\boldsymbol{k}_1\boldsymbol{r} - i\omega_0 t) \tag{2.66a}$$
$$\boldsymbol{E}_2(\boldsymbol{r},t) = \boldsymbol{E}_2 \exp(i\boldsymbol{k}_2\boldsymbol{r} - i\omega_0(t-\tau)), \tag{2.66b}$$

with their k-vectors $\boldsymbol{k}_{1,2}$, the frequency ω_0 and a time delay between the waves τ. For the k-vectors, the following relation holds according to Fig. 2.17:

$$\boldsymbol{k}_1 = k\begin{pmatrix}0\\ \sin(\varphi)\\ \cos(\varphi)\end{pmatrix} \quad \text{and} \quad \boldsymbol{k}_2 = k\begin{pmatrix}0\\ -\sin(\varphi)\\ \cos(\varphi)\end{pmatrix} \tag{2.67}$$

and for the polarization vectors

$$\boldsymbol{E}_1 = E_1\begin{pmatrix}0\\ \cos(\varphi)\\ \sin(\varphi)\end{pmatrix} \quad \text{and} \quad \boldsymbol{E}_2 = E_2\begin{pmatrix}0\\ \cos(\varphi)\\ -\sin(\varphi)\end{pmatrix}. \tag{2.68}$$

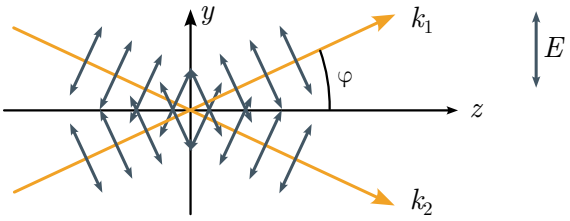

Figure 2.17: Interference of in a Mach-Zehnder interferometer with k-vectors crossing under an angle φ.

The resulting interference pattern on a screen parallel to the y-axis $I(\boldsymbol{r},\tau) = \|\boldsymbol{E}_1 + \boldsymbol{E}_2\|^2$ reads

$$\begin{aligned} I(\boldsymbol{r},\tau) &= E_1^2 + E_2^2 + \boldsymbol{E}_1\boldsymbol{E}_2 \exp\left[i\boldsymbol{k}_1\boldsymbol{r} - i\boldsymbol{k}_2\boldsymbol{r} - i\omega_0\tau\right] \\ &\quad + \boldsymbol{E}_1\boldsymbol{E}_2 \exp\left[-i\boldsymbol{k}_1\boldsymbol{r} + i\boldsymbol{k}_2\boldsymbol{r} + i\omega_0\tau\right] \end{aligned} \tag{2.69a}$$
$$= E_1^2 + E_2^2 + 2E_1E_2(\cos^2(\varphi) - \sin^2(\varphi)) \cos\left(2k\sin(\varphi)y - \omega_0\tau\right). \tag{2.69b}$$

The angle between the beams defines the periodicity of the fringe pattern in space due to the $2k\sin(\varphi)y$ term in the cosine. More importantly, this pattern is shifted if one beam is delayed with respect to the other, since the $\omega_0\tau$ term is effectively a phase term that maps the delay to the phase of the interference pattern. For a fixed angle φ, the spatial Fourier transform of the interference pattern reads:

$$\begin{aligned} \mathcal{FT}\left[I(y)\right] &= \mathcal{FT}\left[E_1^2\right] + \mathcal{FT}\left[E_2^2\right] \\ &\quad + \frac{2}{\sqrt{2\pi}} E_1E_2(\cos^2(\varphi) - \sin^2(\varphi)) \int_{\mathbb{R}} \cos\left(2k\sin(\varphi)y - \omega_0\tau\right) \exp(ik_y y)\,\mathrm{d}y \end{aligned} \tag{2.70a}$$
$$\begin{aligned} &= \mathcal{FT}\left[E_1^2\right] + \mathcal{FT}\left[E_2^2\right] + 2\sqrt{2\pi}E_1E_2(\cos^2(\varphi) - \sin^2(\varphi)) \\ &\quad \cdot \left[\exp(-i\omega_0\tau)\delta(k_y - 2k\sin(\varphi)) + \exp(+i\omega_0\tau)\delta(k_y + 2k\sin(\varphi))\right]. \end{aligned} \tag{2.70b}$$

Consequently, the temporal delay appears as a phase term $\exp(-i\omega_0\tau)$ at the spatial frequency of the modulation in the interference pattern, $k_y = 2k\sin(\varphi)$. This appearance enables the detection of the delay directly via Fourier transform of the captured image of the interference pattern and extraction of the phase value at k_y. Noteworthy, intensity drifts of the laser appear in the Fourier transform as amplitude changes, but they leave the phase value invariant. Therefore, the phase extraction via Fourier transform is inherently robust against intensity fluctuations as compared to a fringe measurement with a single photodiode. The latter case can only track the phase in a $[0;\pi]$ interval, whereas the Fourier transform approach can resolve $[0;2\pi]$. I will present a detailed description of the experimental implementation, dynamic performance, and a comparison to other stabilization schemes in Chapter 5.

Chapter 3

Single-shot detection of the carrier-envelope phase

In this chapter, I will present the results on single-shot carrier-envelope phase (CEP) detection with laser-induced currents in gases. After an introduction motivating the importance of CEP detection and presenting an overview of related work, I will focus on the details of the experimental setup. Subsequently, I will present data characterizing not only the CEP proportionality of the captured signal but also the performance of the detection scheme as a function of various parameters, such as gas pressure, intensity, or pulse duration. In particular, the achievement of long-term stability is highlighted. I will conclude with a proof-of-principle demonstration of the very same method at a SWIR laser source, which demonstrates its universal applicability.

The results presented in this chapter build upon a technique proposed by B. Bergues [143], and developed in the context for circularly polarized pulses by M. Kubullek et al. [144]. In these works, the phase-dependence of strong-field photoionization [145] is exploited. Investigations on the general signal formation both experimentally and with extensive simulations have been done by J. Schötz et al. [104], where I also contributed. The work presented here mainly extends the findings from Ref. [104] to single-shot detection of the CEP, as demonstrated in Ref. [144], but with linearly polarized pulses, and for the first time demonstrates long-term stability of CEP detection with such a device. In addition, the detection setup is operated in a regime where saturation of the ionization process is expected, which explains the experimentally observed signal scaling. I also demonstrate the capabilities of the technique in the infrared (IR) wavelength region.

The data shown have been produced by me under the supervision of Boris Bergues and with much input from Hartmut Schröder, especially on the theoretical aspects which I presented in Sec. 2.4. The data taken with the SWIR laser source have been taken with the help of Maximilian F. Kuthe under the supervision of Thomas Nubbemeyer. Tobias Kleinhenz helped with the technical drawings of the gas cell, and Harald Haas provided solutions for the electronic circuitry. We published the essence of the following in Ref. [71].

3.1 Introduction

The carrier-envelope phase is one of the most important parameters in describing ultrashort laser pulses, especially in attosecond science [4, 5, 7, 146]. Since the shape of short compressed laser pulses with a given envelope can entirely be described by the CEP in good approximation, its precise measurement is essential for investigating ultrafast light-matter interaction.

The detection of the CEP by measuring spectral interference between fundamental and harmonic frequencies [147, 148] is possible due to the CEP dependence of the appearing

fringes. Such measurements have even been demonstrated in a single shot way [149] and were initially suffering from slow detectors and the requirement of a Fourier transform of the data [150]. Novel approaches eliminate that necessity by the implementation of an analog detector [151], an optical Fourier transform [152] or heterodyne detection [153]. Besides that, single-shot dispersive $f-2f$ interferometry [154] and an extension towards long wavelength, terahertz frequencies [155] have been demonstrated. Spectral interference has also been employed for stabilization of the CEP slippage of laser oscillators, where the beating of a $f-0$ interferometer is used to measure the comb offset, see Sec. 3.2.1 for details.

Since the discovery of the plateau in the electron energy spectra in ATI [156] and its CEP dependence [157], CEP detection by electron spectroscopy is feasible [158], also in single-shot configuration [146, 159, 160]. Single-shot CEP detection with the stereo-ATI phasemeter has continuously been pushed towards long acquisition times [161], SWIR sources [162], or high repetition rates [163]. The performance of the stereo-ATI phasemeter is comparable to the one of single-shot spectral interference phasemeters [150], and the properties of the atomic dynamics have been investigated regarding phase and intensity [164].

These two kinds of CEP detection have been superseded by recent developments in petahertz electronics, that is, the generation, manipulation and control of light wave triggered electric currents at optical frequencies [6,17,18,22], which have led to more compact CEP detectors requiring much lower pulse energy. In particular, the requirement of ultrahigh vacuum (UHV) for the stereo-ATI phasemeter makes the technique comparatively expensive and bulky. The spectral interference phasemeter, on the other hand, requires nonlinear crystals cut to fit to a particular wavelength region, and the detectors are either wavelength dependent, since they are semiconductor based [149] or even require additional expensive polarization optics [152, 153]. Electric currents, however, may favor a CEP dependence, which has been observed in the gas [71, 104, 144, 165], at metal surfaces [166], nanometric tips [20], or in solids [14,15], but also in micro- and nanostructures [22, 24, 25, 167–171]. The latter can be combined to larger arrays of nano sensors, often referred to as petahertz electronic networks [22, 24]. Such measurements allow the detection of the CEP at high repetition rate with low pulse energy due to the local field enhancement of the structures [18]. These developments profited from the investigation of fundamental physics at nanometric structures [172–176].

Literature focuses mainly on currents for CEP detection generated in samples other than gases, except few works by our group [71, 104, 144] and some others [165]. The drawback of currents generated in gases is the higher intensity required as compared to nanostructures that favor local field enhancement [22, 24, 25, 168–171], or solids that have lower ionization potential [14, 15, 18]. However, CEP detection with currents generated in gases has some important advantages, including the inherently high damage threshold, a wide wavelength independence due to the missing non-linear crystals, near-field effects, or interband transitions, and the simplicity of the optical setup, which basically consists of two pairs of electrodes. These considerations form the basis for the investigations presented in this chapter.

3.2 Experimental methods and detection scheme

In this section, I will present the laser system, the experimental setup and the detection scheme used for the single-shot CEP meter, hereafter referred to as phasemeter. Starting with the laser system, the general optical setup and the electronic circuitry, I present the basic characteristics of the detection scheme, how the currents depend on the spatial

arrangement of laser beam and sensing electrodes, and confirm the validity of the Shockley-Ramo model as presented in Sec. 2.3.

3.2.1 Laser system

The Ti:Sa laser system used in the scope of this thesis is a typical chirped-pulse amplifier chain consisting of a broadband oscillator, a CEP control module, and a subsequent multipass amplifier, see Fig. 3.1.

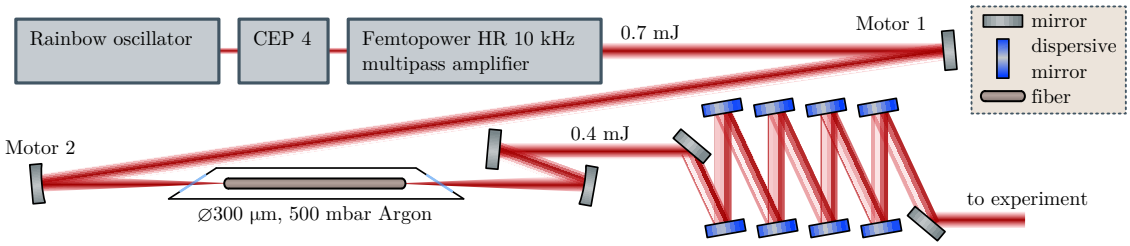

Figure 3.1: Titanium:Sapphire laser system. The pulses originating in a broadband oscillator are CEP stabilized in the CEP 4 module, then amplified in a multipass amplifier and subsequently spectrally broadened in a HCF. Post-compression is done with dispersive mirrors (PC 70, UltraFast Innovations).

The laser system is described in more detail in Ref. [177] and here, I summarize the key features of the system. Among them, a conventional Ti:Sa oscillator (Femtolasers Rainbow) with a repetition rate of $f_{\mathrm{rep}} = 75\,\mathrm{MHz}$ followed by a CEP stabilization (CEP 4) module which implements a feed-forward stabilization scheme [178, 179]. It consists of an $f-0$ interferometer that measures the carrier-envelope offset frequency $f_{\mathrm{CEO}} = f_{\mathrm{rep}}\varphi_{\mathrm{slip}}/2\pi$ [178–180], a quantity depending on the per-roundtrip phase slippage φ_{slip} [178]. The latter describes the CEP change from one emitted pulse to the next one. It depends on the intra-cavity dispersion, the pump power sent to the oscillator, or the crystal temperature [179]. In particular, f_{CEO} can be controlled in a wide range from 0 to f_{rep} by adjusting one or several of these parameters [177]. When the emitted pulse train from the oscillator is interpreted as a frequency comb, the spacing between the comb lines is related to f_{rep}, whereas the offset from 0 is described by f_{CEO} [180]. Consequently, the frequency of the n-th comb line can be expressed as $f_n = f_{\mathrm{CEO}} + nf_{\mathrm{rep}}$ [177].

A subsequent acousto-optic frequency shifter shifts the entire frequency comb by f_{AO}, such that the resulting frequency comb has frequencies $f_{\mathrm{out},n} = nf_{\mathrm{rep}} + f_{\mathrm{CEO}} - f_{\mathrm{AO}}$ [177]. If f_{AO} is chosen to be $f_{\mathrm{AO}} = f_{\mathrm{rep}} + f_{\mathrm{CEO}}$, the resulting frequency comb is $f_{\mathrm{out},n} = (n-1)f_{\mathrm{rep}}$ and thus independent of the phase slippage per roundtrip which means that the CEP is the same for all pulses [177]. Therefore, f_{AO} is derived from mixing f_{rep} with f_{CEO}, where f_{CEO} is kept in the range of 10 MHz to keep f_{AO} within the working range of the frequency shifter. In addition, the CEP 4 module offers CEP control by an analog voltage input that drives a Sigatek SF28A7 RF phase shifter placed in the f_{rep} signal path.

As counterpart to the stabilization of the CEP, f_{AO} can be derived from mixing with a fixed radio frequency generator via $f_{\mathrm{AO}} = f_{\mathrm{rep}} + f_{\mathrm{RF}}$, where $f_{\mathrm{RF}} \neq f_{\mathrm{CEO}}$. In this configuration, the mismatch between the round trip slippage frequency and f_{RF} results in a varying CEP from shot to shot which enables measurements with quasi-random CEP. This approach is chosen in some measurements in Chapter 3 and has the advantage over sweeping a stabilized CEP in a $[0; 2\pi]$ interval as it favors a basically uniform distribution. For sweeping, the exact interval has to be adjusted carefully to cover the $[0; 2\pi]$ interval precisely.

Following the CEP stabilization module, a commercial 9-pass multipass amplifier (Femtolasers Femtopower HR 10 kHz) delivers 0.7 mJ pulse energy at 10 kHz repetition rate. Its compressed output is sent into a HCF filled with 500 mbar of Argon for spectral broaden-

ing. Subsequent post-compression with dispersive mirrors (UltraFast Innovations PC 70) and an ammonium dihydrogen phosphate crystal for third-order dispersion compensation [181] delivers 4.5 fs FWHM pulses. The temporal characterization is done with the dispersion scan technique [182] and presented in Fig. 3.2, where an evolutionary algorithm has been employed for spectral phase retrieval [183].

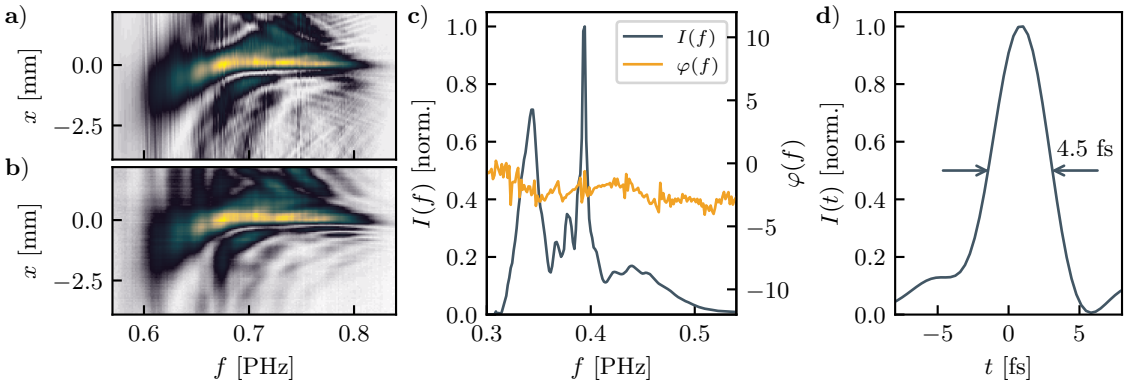

Figure 3.2: **a)** Measured dispersion scan data and **b)** retrieval. **c)** spectral intensity and phase **d)** intensity as a function of time with a FWHM pulse duration of 4.5 fs.

3.2.2 Optical setup

For the detection of the laser induced currents in the gas phase, a setup consisting of metal electrodes in a capacitor-like arrangement is employed, see Fig. 3.3. A pair of such electrodes forms one detector and is kept in an enclosed environment, such as a gas cell that enables control of gas pressure and species. The gas in the gap between the two plates is ionized by the laser pulse according to one of the models introduced in Section 2.2. The resulting free carriers experience a laser-induced net displacement and might even travel to the electrode, depending on the gas pressure and mean free path, see Sections 2.3, 2.4 and Ref. [104].

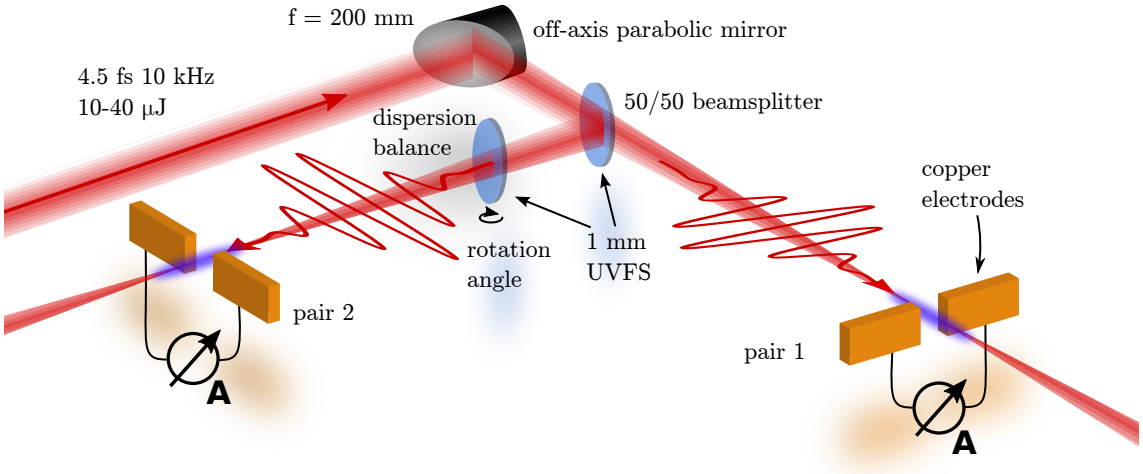

Figure 3.3: Setup for the single-shot CEP meter. Two foci of a few-cycle laser beam (VIS-NIR in this case) are generated with an off-axis parabolic mirror (OAP) and an UVFS beamsplitter. The laser induced charge separation in the ionized gas between each electrode pair is detected via a current measurement. A dispersion balancing plate adjusts the relative phase between the two arms. Figure adapted from Ref. [71], licensed under CC BY `https://creativecommons.org/licenses/by/4.0/`

The p-polarized laser beam is focused with an OAP (focal length $f = 200\,\mathrm{mm}$) between two electrode pairs by means of a 50/50 beamsplitter, see Fig. 3.3. The material dispersion of the latter is compensated with an equally thick dispersion balancing plate made of the same substrate, where the tilt angle allows for fine tuning of the relative phase between the two arms. Substrates of UVFS are used except for the data taken with the SWIR laser source, where CaF_2 is requried for its lower dispersion. Near each focus (focal size 25 µm FWHM), a pair of copper electrodes is placed with a gap size of 350 µm unless specified differently. The electrodes are kept in gas cells with optical windows (not shown) to adjust pressure and target gas type. The extension of the plates is 0.5 mm along the laser beam propagation direction, which is smaller than the Rayleigh length of approximately 0.7 mm in the setup used here. By choosing this set of parameters, the averaging effects due to the Gouy phase shift along the focus are minimized since the effective measuring volume is limited. This limitation is not sharply defined by the extension of the electrodes, but rather by the weighting fields for the electrode geometry, see Sec. 2.3, which nonetheless drop quickly along the propagation direction. The copper plates are electronically connected to a coaxial cable and subsequently amplified outside the cell. The gas cells are filled with evaporated ethanol at a pressure in the range of $1-15\,\mathrm{mbar}$ to exploit the small ionization potential of 10.45 eV [112].

3.2.3 Electronic circuit and signals

The laser induced current sensed by the electrodes is fed into a transimpedance amplifier (TIA) (Femto DLPCA-200), see Fig. 3.4. The TIA allows for variable gain, typically set to $10^8\,\mathrm{V/A}$. There, the $-3\,\mathrm{dB}$ bandwidth is 7 kHz or 200 kHz in low noise or high speed mode according to Ref. [184], respectively. Best signal-to-noise performance is found in low-noise mode while maintaining sufficient bandwidth to support the laser repetition rate. After amplification, the signal is sent to an integrate-and-hold circuit I have built using the Burr-Brown `IVC102` gated integrator. The timing electronics controlling the integrate and reset time windows have been developed based on a circuit provided by Harald Haas, but with a digital interface. A more extended circuit diagram and a brief technical explanation of the detection electronics can be found in Appendix B.

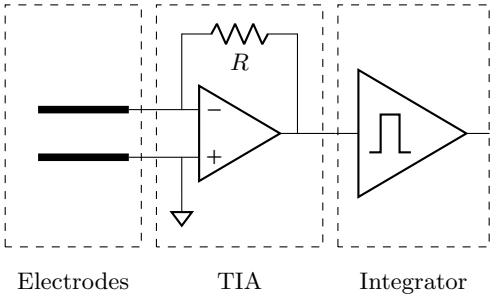

Figure 3.4: Schematic overview of the detection electronics that consist of a TIA in which the electrode signal is amplified for subsequent boxcar integration. The gain of the TIA is variable and in the range of $R = 10^6\,\Omega$ to $10^9\,\Omega$ here.

As discussed in Sec. 2.3, the amplitude of the laser-generated current mostly depends on the position of the driving laser between the electrodes. This property is experimentally confirmed in Fig. 3.5a) for a focus position in the middle of the two electrodes, and on the left and right side, respectively. The amplitude change is clearly visible and systematically investigated below in Sec. 3.2.4. In addition, the CEP can introduce an additional signal amplitude change, as illustrated in Fig. 3.5b) and c). There, the focus is in the center of the two electrode pairs and the respective signals are detected. A 90° phase shift between the two electrode pairs is introduced and data for different values of the relative CEP φ_{rCEP} are measured. Apparently, the signal amplitude varies with CEP if the laser pulses are sufficiently short. The peaks shown there are normalized by their CEP averaged value of $V_0 = -41\,\mathrm{mV}$ and $V_0 = -50\,\mathrm{mV}$ for the first and second electrode pair, respectively.

The CEP dependent amplitude in this case is roughly 20 % of the peak. The subsequent boxcar integration is primarily used to eliminate high-frequency noise and to extract a single measurement value out of the time-dependent curves coming from the amplifier. There is reason to believe that boxcar integration is superior to peak detection since fast fluctuations that are inherently part of the signal (see Fig. 3.5b),c)) are smoothed.

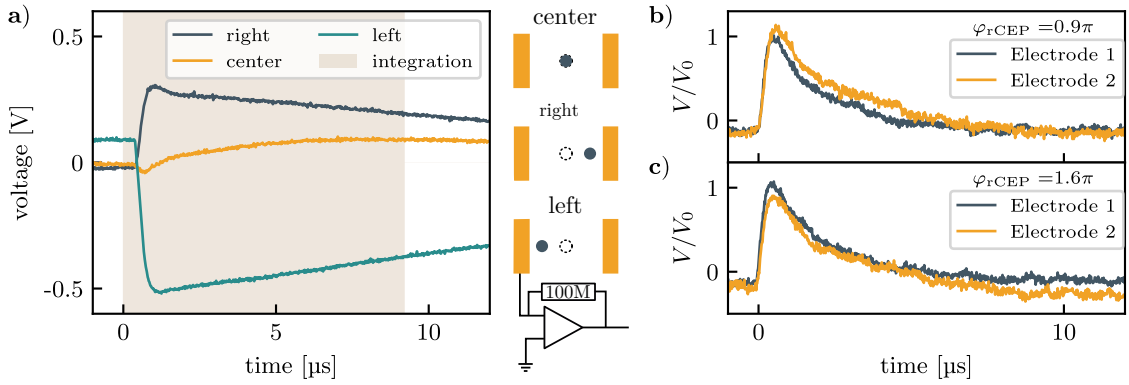

Figure 3.5: a) Raw signals after TIA for three different electrode positions with respect to the focus. The shaded area indicates the integration time window. The sketch next to the plot indicates the position of the focus relative to the electrodes and amplifier inputs. **b)** For a focus in the center, the CEP dependence of the signal is around 20% of the amplitude. Here, we normalized per CEP averaged amplitude V_0 **c)** Same as b) but the relative CEP φ_{rCEP} is shifted.

3.2.4 Determination of the Shockley-Ramo weighting potential

For systematic investigation of the transverse scaling of the weighting potential, data of a single electrode pair in the focus of a $f = 250\,\mathrm{mm}$ spherical mirror is captured. A motorized stage allows for precise transverse (x) position tuning. Its position is scanned while detecting the current after the TIA, as shown in Fig. 3.6 where numerical integration of the raw curves measures the signal strength at different positions. Between the electrodes, a clear linear scaling of the signal amplitude appears, in accordance with Sec. 2.3. Here, the CEP is stabilized to remove any signal amplitude variations due to CEP drifts. A fit to the data yields a change of signal with position of $1.5\,\mathrm{mV/\mu m}$ in the linear regime, which is a measure for the pointing sensitivity of the device. This value depends on the gap size, the laser intensity and the target gas type and pressure and is thus subject to change. Nevertheless, given a certain pointing amplitude Δx, a signal change according to that value is expected and for a stable measurement, it is necessary that the CEP dependent signal amplitude exceeds the signal drifts caused by laser beam pointing.

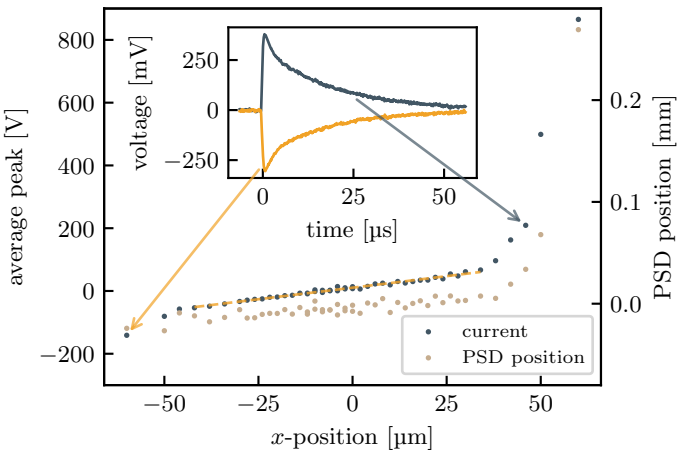

Figure 3.6: Transverse scan of the electrode position for fixed laser and CEP. Between the electrodes, the current signal scales linearly with position (see dashed line). The position on a position sensitive detector (PSD) for the fixed laser is correlated.

For a current generated too close to the electrode, the signal strength deviates from the linear scaling as ionization of the electrode material significantly increases the signal strength. Thus, a full scan of the Shockley-Ramo weighting potential between the electrodes is hindered by the finite size of the focus, which yields a convoluted signal. Deconvolution is complex since the free parameters include the focal size, the gap size, and the nonlinearity of the signal generation in the gas and on the electrode. The latter has to include the particle densities since the total amount of generated charges is required. Additionally, the scan cannot be performed on the electrodes since laser-induced damage occurs at direct illumination. These reasons hinder the final retrieval of the weighting potential, but the linear scaling can be confirmed. In particular, the linear scaling would enable the correction of pointing fluctuations, which would improve signal stability for CEP dependent measurements. In a demonstration experiment, the focus between the electrodes is imaged onto a PSD while scanning the electrode position. The detected position is correlated with the electrode position, which hinders the position tracking since the laser in this experiment is fixed, and thus a constant signal is expected. Nevertheless, the measurements confirm the validity of the Shockely-Ramo model as introduced in Sec. 2.3.

3.3 Measurement of the carrier-envelope-phase

Following the discussion of the experimental setup and measurement techniques as well as of the typical signal shapes, I will now present the data for single-shot CEP detection. For all data that follows, the experimental setup used the same parameters of the setup, among them the amplification factor of $10^8\,\mathrm{V/A}$, the gap size of $350\,\mu\mathrm{m}$, the focal length of $f = 200\,\mathrm{mm}$, or the boxcar settings as introduced in Sec. 3.2.2 and 3.2.3. I will first discuss measurements that confirm the proportionality of the detected data to the CEP and that demonstrate long-term stability of every-single-shot detection. Building on this basis, I will elaborate on the intensity scaling of the signal in connection to the model introduced in Sec. 2.4, where the best working conditions are found in a regime in which saturation of ionization is expected to be predominant. Subsequently, data analyzing the Gouy phase will be presented, followed by a proof-of-principle demonstration of single-shot CEP detection at a SWIR laser system that confirms the applicability of the method to long wavelength lasers without any changes to the detector.

3.3.1 Single-shot CEP detection and quantification

Above, I presented that electric currents generated by few-cycle laser pulses exhibit a phase CEP dependence. As shown in Sec. 2.4, the signal generated is a sinusoidal function of the CEP. While this single electrode signal is sufficient for the determination of a relative CEP in a scanning mode where the sinusoidal curve can be extracted, single-shot detection requires a bijection of each single data point to a CEP value. Such a bijection is obviously impossible for sinusoidal functions in a $[0; 2\pi]$ interval. However, when detecting two such signals generated from the same laser pulse, one of them shifted in phase versus the other, a unique phase value can be assigned to each pair of synchronously acquired data. In particular, each data pair can be represented as a point in a parametric asymmetry plot (PAP) where the first and second value are used as abscissa and ordinate in a Cartesian coordinate system, respectively. When having data for various CEP values in $[0; 2\pi]$, a ring forms whose center can be shifted to the origin by subtracting a constant signal, similarly to the procedure described in Refs. [144, 161]. Afterwards, the polar angle of each data point can be interpreted as a phase value, given that the phase shift between the two signals is 90°. The latter can be confirmed by the circular shape of the plot, which

would not be the case for phase shifts other than that. Figure 3.7 shows an example of a PAP.

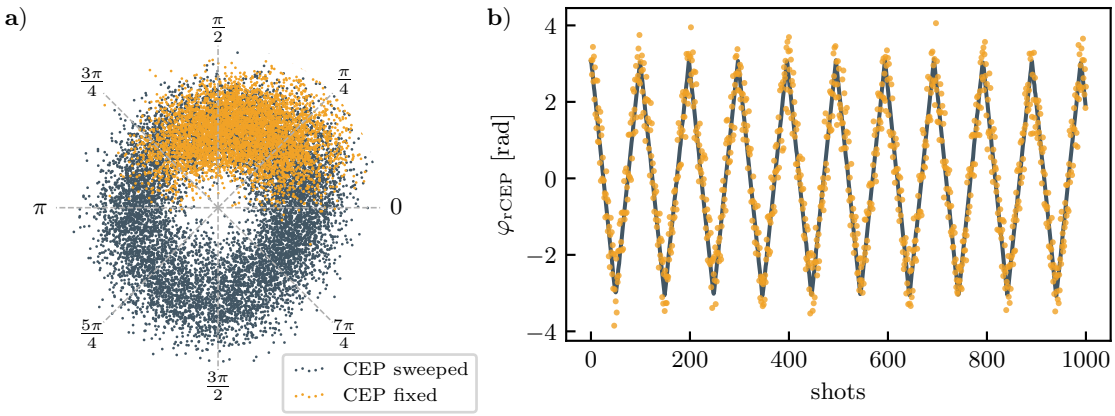

Figure 3.7: a) Parametric asymmetry plot for modulated CEP and fixed CEP. **b)** Retrieved relative CEP in comparison to the nominal CEP (solid line) as retrieved from the applied voltage.

There, the CEP of the Ti:Sa laser system is swept by applying a voltage to the CEP 4 module and the signal is detected as described above. The incident pulse energy is 20 µJ. For each data point, the phase value is extracted and compared to the expected nominal value, which is derived from the applied voltage, see Fig. 3.7b). A direct correlation of the extracted phase φ_{rCEP} with the nominal values is found, despite small fluctuations around the set point. These fluctuations arise from two distinct sources: Firstly, the measurement precision of the device and secondly, the shot-to-shot CEP stability of the laser. The device precision depends again on laser parameters such as pulse duration or intensity, but it can be estimated for a given set of them. Assuming that the device measurement error is random, i.e., it does not favor any direction, the radial direction can be picked for its quantification, in particular the radial width in relation to its standard deviation, σ_r/r, see Ref. [159]. By doing so, CEP fluctuations of the laser that occur in angular direction are not considered. The origin of that estimation is explained in detail in Ref. [152]. There, the signal is interpreted as a vectorial sum of an errorless real signal vector and a random error vector whose direction is arbitrarily distributed and whose length obeys Gaussian statistics. Since the direction is isotropic, the noise can be quantified in radial direction. The device precision is $\Delta\varphi_{\mathrm{device}} = \sigma_r/r = 226\,\mathrm{mrad}$ for the data presented in Fig. 3.7a). The deviation of the retrieved values of φ_{rCEP} from the nominal phase in Fig. 3.7b) is 574 mrad, much higher than the device precision. This deviation is connected to the single-shot CEP stability of the laser, which can be quantified by the angular spread of the data for a fixed CEP. The value of the latter is 587 mrad, see scattered dots in Fig. 3.7a). However, this value now includes both the device and laser variations, indicating that the laser single-shot CEP stability is below that value. To be precise, the device error and the single-shot CEP fluctuations are independent noise sources, such that the total noise can be written as $\Delta\varphi_{\mathrm{total}} = \sqrt{\Delta\varphi^2_{\mathrm{laser}} + \Delta\varphi^2_{\mathrm{device}}}$. Using this expression, a laser single-shot CEP noise of 530 to 544 mrad can be extracted.

In the phase extraction procedure, a re-binning process is carried out [159] ensuring that nonlinearities of the device are corrected. This correction is achieved by detecting a full $[0; 2\pi]$ interval of the CEP and extraction of the polar angle attributed to each data point. The resulting values are then mapped to a uniform distribution as it is expected for a perfectly linear detection device. Typically, the mapping is found in a calibration measurement, where the CEP is scanned or randomly distributed in a $[0; 2\pi]$ interval prior to the actual measurement. Once the calibration is done, any phase value can be detected and converted to a relative CEP value via this function.

In the case of a randomly distributed CEP, this calibration can be performed on-the-fly [161], meaning that a subset of the data can be used for calibration in a continuously running measurement. Additionally, potential calibration errors originating from an imperfect coverage of a full $[0; 2\pi]$ interval are inherently prevented. This is the motivation for the demonstration of long-term stability of the device using the random CEP mode of the laser by feeding a 10 MHz RF signal to the CEP 4 module, as described in Sec. 3.2.1. The results of a scan measuring each laser shot over a period of more than 5 hours are shown in Fig. 3.8 for 30 µJ incident pulse energy. There, the data are binned into 400×400 bins after the re-centering procedure [144, 161]. In total, 1.8×10^8 consecutive laser shots are detected, with a device resolution $\Delta\varphi_{\text{device}} = 194\,\text{mrad}$. This value is even better than presented above, since the intensity is different. A more rigorous investigation of the intensity scaling follows below in Sec. 3.3.2.

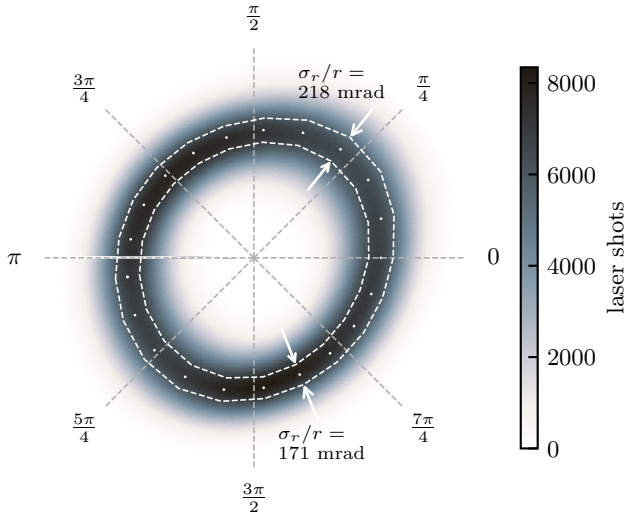

Figure 3.8: Parametric plot for a 5 hours measurement detecting 1.8×10^8 consecutive shots. The data is binned into 400×400 bins.

The long-term stability of the signal is achieved due to an interplay of various parameters. Among them the pressure, the gap size, and the general optical setup. The influence of the pressure is discussed below in Sec 3.3.2. The choice of gap size is a trade-off between signal strength and signal stability. For a larger gap size, the signal strength decreases as observed in Ref. [104]. The reduction of signal can be explained by a decreasing number of field lines entering electrodes at larger distance from the generating dipole. This effect can partially be compensated for by increasing the electrode size in the out-of-plane direction to 2 mm despite the focus being just several tens of microns in size. Towards the propagation direction, however, further expansion is hindered by the focal phase, see Sec. 3.3.3. On the other hand, a large electrode distance minimizes the pointing sensitivity of the signal. As shown in Sec. 2.3, a basically linear connection between the position of signal generation and detected current is found. For pointing fluctuations of amplitude Δx, this connection immediately transfers to a signal change $\Delta S \propto \frac{\partial Q}{\partial x}\Delta x = \frac{2q}{d}\Delta x$, where d is the gap size. Thus, larger gap size reduces the pointing sensitivity. Best conditions are met with a gap size of $d = 350\,\mu\text{m}$ for the presented data. The optical setup employs linearly polarized pulses and electrodes oriented along the polarization axis. Compared to the optical arrangement presented in Ref. [144], the approach presented here comes at the cost of requiring a second electrode pair but eliminates the need of spatially resolved current sensing. Hence, pointing fluctuations are only detected if they happen in the electrode axis but not perpendicular to it.

3.3.2 Pressure and dispersion dependence

Having confirmed the validity of the CEP dependent currents, it is crucial to elaborate the role of the laser intensity and the gas pressure in the experiment. For this purpose, the phase dependent data are acquired for different intensities of the laser at different pressures of the evaporated ethanol. An intensity range from 8×10^{13} to $9 \times 10^{14}\,\mathrm{W/cm^2}$ is found to cover the range for best signal with pressures ranging from 3 to 10 mbar, see Fig. 3.9a). The device resolution is best (i.e. σ_r/r smallest) for pressures in the range of $3-6$ mbar for an intensity of $4 \times 10^{14}\,\mathrm{W/cm^2}$. For pressures above this range, the device resolution is worse. The PAP collapses to a central spot which hinders the retrieval of the device resolution for pulse energies above 20 µJ. The intensity of the minimum in σ_r/r, as shown in Fig. 3.9a), parallels the region of signal boost by saturation of ionization, as introduced in Sec. 2.4.

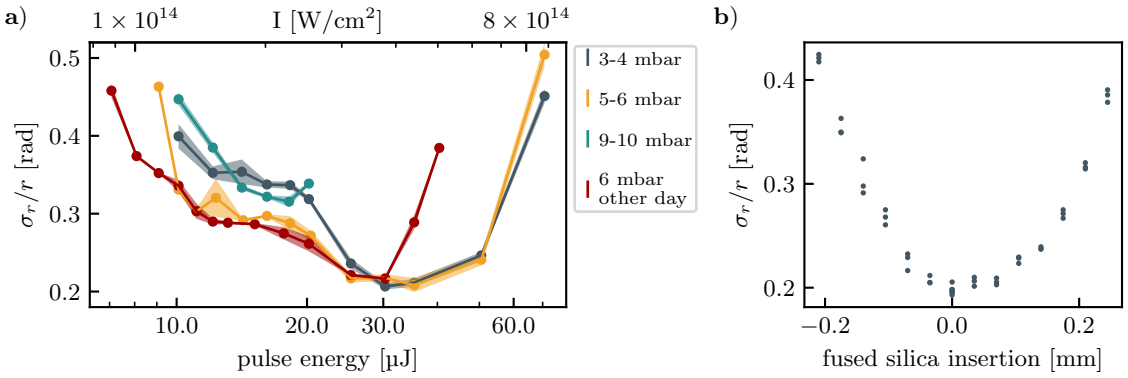

Figure 3.9: a) The intensity dependent device resolution σ_r/r for different pressures maximizes at an intensity of around $4 \times 10^{14}\,\mathrm{W/cm^2}$. The pulse energy denotes the incident energy for both foci. **b)** A scan of the fused silica insertion yields best device performance for best compressed pulses.

A scan of the pulse duration via the dispersion, Fig. 3.9b), shows a clear minimum when pulses are shortest. Here, negative material insertion means removal of material needed for best compression, as the usage of dispersive mirrors enables pre-compensation of material dispersion. The slope for negative material insertion is steeper than for positive material insertion, similar to what the simulation in Sec. 2.4 suggests. Additionally, the PAP collapsed for material insertions larger than 0.2 mm, which aligns well with the predicted asymmetry drop predicted by in Sec. 2.4.

3.3.3 Measurement of the Gouy phase

Due to the well-known Gouy phase shift, the CEP of the laser is a function of space. The phasemeter setup allows for probing the phase spatially resolved, since the expansion of the electrodes is smaller than the typical length scale of the focus. Instead of measuring the CEP dependent signal of one electrode pair at different positions along the focus, it is superior to measure the signal of two electrode pairs for random CEP. By doing so, no reference CEP measurement is necessary; instead, the phase difference between the two electrode pairs can directly be related to the spatial CEP variation. Therefore, interferometric drifts between probing and reference measurement are minimized. For the measurement, the position of one electrode pair is fixed while the position of the other one is scanned along the focus. Since the phase difference between the electrode pairs directly influences the ellipticity of the parametric plot, it can be used to extract the phase difference, see Fig.3.10.

Starting from the zero position, where the parametric plot is circular (and therefore, the phasedifference is $\pi/2$), the electrode position is scanned towards the incoming beam

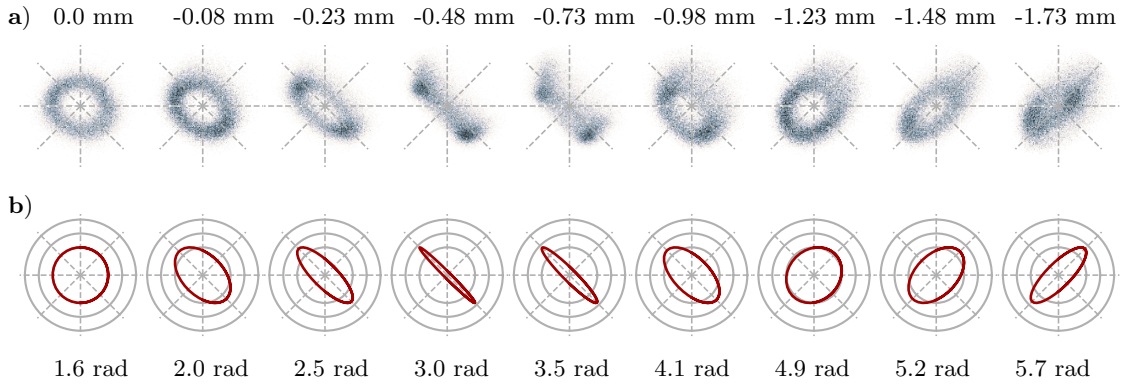

Figure 3.10: a) Parametric asymmetry plot for different electrode positions along the laser propagation axis. **b)** Calculated ellipticity for given phase difference.

leaving the vicinity of the focus. The phase shift is around 4.1 rad - more than the expected Gouy phase shift of $\pi/2$ for one half of the focus. Here, the intensity change along the focus modifies the ionization dynamics, especially regarding the saturation effects introduced in Sec. 2.4. This dependence can be extracted from the simulation data in Sec. 2.4 and amounts to -4.9×10^{-15} rad cm^2/W for intensities around 4×10^{14} W/cm^2. Extrapolation of that value to the expected intensity profile along the propagation direction yields an additional phase change of 2 rad along the scanned distance. In sum, the Gouy phase and the intensity dependent phase shift accumulate to around 3.6 rad, which is close to the observed value. The final discrepancy can be caused by various effects that have not been included in the models here, such as the wavefront curvature for a Gaussian beam outside of focus or reshaping of the latter during its propagation through the plasma. Importantly, the measured phase change happens on a length scale larger than the electrodes. So, a reshaping of the beam within the electrode distance is not expected and thus the 2D model presented in Sec. 2.4 is expected to be adequate.

3.3.4 Proof-of-principle at a 2 µm laser source

To demonstrate the capabilities of laser-induced currents in gases for CEP detection of SWIR pulses, the output of the frequency broadened **H**igh-power **O**PCPA system for high **R**epetition rate **U**ltrafast **S**pectroscopy (HORUS), as described in detail in Chapter 4, is measured. In similar fashion as before, the proportionality of the detected single-shot data to the CEP of the laser is confirmed. Therefore, the applied voltage to the piezo delay stage in the difference frequency generation (DFG) part of the seed generation, see Sec. 4.3.1, is modulated. In contradiction to the Ti:Sa laser system, there is a small hysteresis due to the piezo, which translates to a slight non-uniformity in the CEP distribution. To reduce this effect, the CEP is swept in a 4π interval. The results can be seen in Fig. 3.11, where a parametric plot of the data yields a resolution of $\sigma_r/r = 154$ mrad. After re-centering [144, 161] and re-binning [159], a comparison of the measured CEP to the nominal CEP derived from the applied voltage can be done. Generally, the measured data decently follows the nominal phase, but small deviations that can be connected to the piezo hysteresis occur.

Having confirmed the validity of the data, long-term stability at the 2 µm laser source can be demonstrated. The results of a 1.5 h measurement capturing around 5.5×10^7 laser pulses are shown in Fig. 3.12 as a parametric plot. Overall, a resolution of 210 mrad is achieved. A small inhomogeneity in the angular distribution of the CEP appears, which, however, cannot be attributed to the piezo hysteresis for the following reasons: Firstly, the piezo hysteresis is a repeated process and therefore reproduces the same inhomogeneous

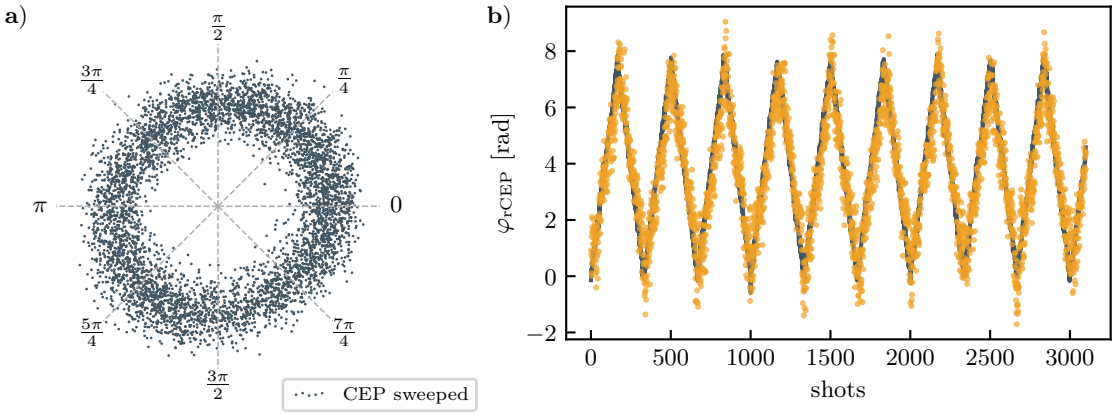

Figure 3.11: a) Parametric asymmetry plot for sweeped CEP, with a standard deviation amounting to 154 mrad. **b)** Retrieved relative CEP in comparison to the nominal CEP (solid line) as retrieved from the applied voltage.

phase distribution. Secondly, the acquisition time is extended such that the CEP between the piezo-shifter and the measurement will drift as it is free-running. Therefore, the inhomogeneities caused by the piezo hysteresis are expected to cancel out for long acquisition times. The inhomogeneity appears as a reduction of the detected laser pulses for certain angles, in particular, a 25.3% decrease from the average is found for $\varphi_{\mathrm{rCEP}} \approx 0.7$ rad. Note that in Fig. 3.12, the suppression seems larger due to the additional radial spread of the data at that phase value. This systematic measurement artifact can be corrected easily by a rebinning procedure [159].

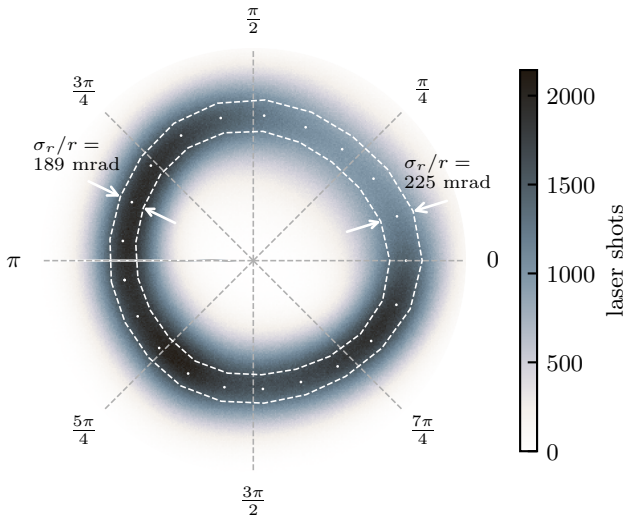

Figure 3.12: Parametric asymmetry plot at the exit of the frequency broadened 2 µm laser system. The data is binned into 400×400 bins. The overall resolution $\sigma_r/r = 209$ mrad.

The pulse duration is expected to be slightly longer than what will be presented in Chap. 4, since the dispersion of a total amount of 3 mm of CaF_2 from the required optical windows and 2 m of air contribute. As described in Chap. 4, the laser pulse shape could not be characterized at the position of the phasemeter. However, numerical propagation of the beam with the propagation module of Luna.jl [142] to estimate the pulse duration in the phasemeter yields a duration of around 8 to 9 fs, corresponding to around 1.3 to 1.5 optical cycles, assuming a central wavelength of 1.8 µm. This difference in pulse duration (in optical cycles) as compared to the Ti:Sa laser system with 1.8 optical cycles explains the better device performance of 154 mrad versus 194 mrad, respectively.

3.4 Discussion and conclusion

In this chapter, I demonstrated the capabilities of laser-induced currents for the detection of the CEP in a single-shot measurement. In particular, the method appears to be long-term stable while maintaining high precision. Not only have I confirmed that the detection of such currents constitutes a simple but robust way of single-shot phase detection, I also investigated the influence of the different parameters such as laser intensity, gas pressure, dispersion or focal phase. The set of parameters where best operation conditions are met aligns with the theoretical investigation of the saturation phase effects in Sec. 2.4. The intensity scan (Fig. 3.9) identifies an intensity of around $4 \times 10^{14}\,\frac{\mathrm{W}}{\mathrm{cm}^2}$ as ideal for the given laser parameters, similar to the intensity at which the onset of saturation is expected theoretically. In addition, the very same detection setup can be used to probe the CEP of SWIR laser pulses without any changes to the geometry of the detection electrodes.

I would like to discuss these results in the context of Ref. [104], where the macroscopic signal formation in a similar context has been examined and scaling laws have been identified. In brief, Schötz et al. [104] discovered that the CEP dependence of laser-induced currents between a pair of passive electrodes exhibits a maximum at low pressures in the range of 1 to 100 mbar. The pressure at which the signal is maximized depends on the gas type and on the laser intensity. Its origin is the interplay of decreasing particle density towards low pressures, which reduces the signal, and the increasing charge interaction and scattering towards higher pressures, which lead to a reduction of signal as well. In particular, electron-neutral scattering and electron-ion interaction become increasingly dominant a higher pressure, such that the large amount of scattering and the high ionic background introduce a higher randomness to the signal or undo the electron displacement, reducing the CEP dependence. These findings parallel the pressure dependence observed experimentally: For pressures lower and higher than those investigated in Fig. 3.9, the PAP collapsed, with an optimum in the range of 3 to 10 mbar, which indicates a too low CEP signal for pressures other than those, similar to Ref. [104]. In principle, one can assume that effects connected to the particle density are similar here and in Ref. [104], since the pressures are in the same regime. However, effects connected to the plasma density, in particular, the amount of electron interaction with the ionic background, are expected to be higher in this context and electron-ion scattering (neglected in Ref. [104]) is more present. Since these effects cause the drop of signal towards higher pressure (c.f. Ref. [104, Fig. 7b)]), the drop is expected to be more prominent in this case. Apparently, a stronger pressure dependence of the signal is observed, in particular since a change of 10 mbar covers the entire range where CEP detection is possible (see Fig. 3.9), as opposed to Ref. [104], where the range covers at least several tens of millibars. Note that dissociative effects of ethanol are expected to occur [185], and various molecular fragments of different types are expected to be present [186]. However, due to the much higher mass of the ions, it can be assumed that they can be seen as a static background. A similar approximation has been done in Ref. [104] and the experimental data there confirms the validity in such experiments.

The signal scaling with intensity has been investigated in Ref. [104] as well, and a kink in the scaling law has been found: The signal increases with intensity, but the steepness of the curve decreases slightly above $1 \times 10^{14}\,\frac{\mathrm{W}}{\mathrm{cm}^2}$. This saturation of the signal arises from the collective effects of the charge carrier dynamics. Here, the intensity is higher and the ionization potential is lower; therefore, the kink observed in Ref. [104] would occur at even lower intensities. Consequently, the signal boost originating in the saturation process counteracts the expected suppressed signal increase with intensity, as described in [104]. Note that the effects described in Sec. 2.4 happen on a timescale of a few femtoseconds, directly during the generation of the free charges. The effects discussed by Schötz et al. [104] are propagation effects that happen on a time scale up to 1 ns after the generation

of free electrons. Therefore, both effects are not mutually exclusive; but rather, the effects introduced in the frame of this thesis imprint more CEP information on the starting conditions of the dynamics discussed in Ref. [104].

The model introduced in Sec. 2.4 predicts an increasing signal even above $8\times10^{14}\,\mathrm{W/cm^2}$ that could not be observed experimentally. There, the PAP collapsed and single-shot CEP information could not be retrieved anymore. This behavior might go back to the occurrence of multiply ionized target molecules and the additional free charge carriers, which again obey a comparable scaling, as presented in Sec. 2.4, but shifted in intensity. Therefore, a phase difference between the electrons from singly and doubly charged ions is expected, reducing the phase sensitivity due to averaging effects. Calculations using coupled rate equations by Haniel et al. [102] have shown that doubly charged ions start appearing in significant amounts when the singly charged ion yield is above 80 %, which is around $1\times10^{15}\,\mathrm{W/cm^2}$ in this framework according to the model in Sec. 2.4. This intensity region aligns with the experimentally intensity at which the PAP collapsed.

I want to note that the Keldysh parameter [84] is below unity for all experimentally investigated intensities, therefore the dip in device resolution in Fig. 3.9 cannot be connected to a transition from multiphoton-like ionization to tunneling ionization.

The presented scheme for CEP detection is competitive to the established stereo-ATI phasemeter regarding the necessary pulse energy of down to 10 µJ in the VIS-NIR range for the device presented here compared to 40 µJ [159] and 30 µJ [146, 160, 163] for the stereo-ATI phasemeter. In the SWIR range, around 100 µJ are required as compared to 300 µJ in the SWIR range [162] for the stereo ATI phasemeter. In the circular polarization phasemeter in ambient air, a pulse energy of 100 µJ was required [144], which is reduced by a factor of 3 to 10 despite the two electrode approach presented here. The spectral interference phasemeter, on the other hand, requires pulse energies of few microjoules [151], 0.5 µJ [152], 5 µJ [154], which is therefore much lower than the method presented here. The nonlinearity of the process is mainly responsible for this difference, since $f-2f$ interferometry is a 2-photon process, whereas the fundamental process for the data presented above requires strong-field ionization (see Sec. 2.2); therefore it has a much higher nonlinearity for the generation of the charges.

The achieved phase resolution of down to 154 mrad nearly reaches the values of the stereo ATI phasemeter with a performance of 120 mrad [162], 113 mrad [160], 10 mrad [159], 82 mrad [163]. The spectral interference phasemeter, on the other hand, outperforms the performance of both the gas current phasemeter and the stereo ATI phasemeter since values of 0.5 mrad [153], 4 mrad [152], and 19 mrad [154] have been reported. Kubullek et al. achieved 107 mrad [144], whereas other groups using gas currents for phase measurements did not specify their resolution [165]. Petahertz electronic networks are capable of delivering single-shot CEP information with nano-Joule pulse energies at high repetition rates in the IR [18, 22, 24]; therefore, single-shot CEP tagging appears straightforward and will probably be demonstrated soon.

The presented approach is capable of measuring the single-shot CEP of both a VIS-NIR and of a SWIR laser source without any changes to the detector, except for the substrate of the beam splitter. This versatility makes the presented method superior to others regarding the flexibility. In particular, the $f-2f$ method and its derivatives require crystals that need to support the nonlinear process at the specific wavelength, among other wavelength dependent components and semi-conductor based detectors [151–153]. The stereo ATI phasemeter, on the other hand, does not require specialized components, but the necessary rescattering process that generates the signal favors an unfortunate wavelength dependence of λ^{-4} [66]. Thus, its applicability to long wavelengths is challenging, as opposed to my method, whose implementation is straightforward. Petahertz electronic networks, in contrast, exploit the local field enhancement of nanostructures, which in-

creases when going to longer wavelengths, but decreases towards shorter ones. Therefore, there is a potential wavelength scaling that requires smaller structures for shorter wavelengths. It is thus not surprising that most of the work has been demonstrated in the SWIR range [24, 167, 169–171], but some articles report similar effects in the NIR, though not in single-shot mode [25].

In conclusion, the presented CEP detection method constitutes a simple and robust characterization device. It may serve as a direct replacement for the stereo-ATI phasemeter and appeals with a significantly reduced experimental effort. The spectral interference phasemeters offer higher resolution but need to be designed for specific wavelength ranges and are therefore not quite versatile. The unique selling point of the method presented here is the large wavelength independence, where other methods can hardly compete. Possible extensions to the mid or far-IR seem feasible when providing a strong enough laser source.

Chapter 4

Frequency broadening of ultrashort laser pulses

In this chapter, I present details on nonlinear spectral broadening of a SWIR laser source. Starting with an introduction covering the general design constraints arising from the high peak power, average power, and large bandwidth, as well as covering the waveguide properties, I then present data on the achieved performance of the experimental implementation. Among them, general characterization such as CEP and power stability, beamprofile, or the temporal pulse shape. The latter is characterized by the TIPTOE technique where I observe the characteristic modulations of the spectral amplitude and exploit them for an intrinsic and absolute CEP characterization. Finally, I conclude with a discussion of the spectral response amplitude of the method, which can be extracted from experimental data and a theoretical model of the interferometer.

The content of this chapter is published in Ref. [128]. The work presented here was performed at the HORUS laser system at MPQ with the help of Maximilian F. Kuthe and Thomas Nubbemeyer as well as with the support of Hartmut Schröder. Mechanical parts for the fiber assembly were designed with the help of Tobias Kleinhenz; Andreas Küchler designed parts of the delay line in the interferometer; Harald Haas helped with fixing electronic and mechanical noise issues and grounding problems.

4.1 Introduction

The indispensable need of powerful, highly stable laser sources with ultrashort pulses in industry and science has pushed the development of such sources in recent years [1, 2, 187, 188]. Ultrafast strong-field science demands additional CEP stability and SWIR wavelengths to enhance the precision of sub-cycle control of electron dynamics and the cutoff in HHG, respectively [1, 5]. For HHG, the scaling of the cut-off energy $\propto I_\mathrm{P} + 3.17U_\mathrm{P}$ [60] with the ionization potential I_P and the ponderomotive potential U_P, see Appendix A.2, thus growing with λ^2, highlights the importance of long-wavelength drivers in reaching the X-ray range. Such systems would then be competing with free electron lasers at large-scale facilities while being table-top sources. However, the flux is low due to the scaling of the recombination probability of $\propto \lambda^{-4}$ [66] or even $\propto \lambda^{-6.5}$ [69], which reduces the efficiency for HHG drastically. The small conversion efficiency can thus only be compensated by upscaling the interaction volume, which on the other hand requires more powerful laser sources that allow loose focusing. In addition, short pulses are necessary for the generation of isolated attosecond pulses with amplitude gating [7].

The investigation of relativistic optics requires high peak intensities, both achievable by boosting either pulse energy or decreasing the pulse duration, in order to reach a normalized vector potential $a_0 = \frac{eE}{mc\omega_0}$ larger than unity [1]. Here, e is the elementary

charge, E the peak field strength, m the electron mass and ω_0 the central angular frequency. For a 2.1 µm laser, this regime is reached at a field strength of 1.5×10^{12} V/m, or an intensity of 3.1×10^{17} W/cm^2, which is achievable with the system I present below.

In Section 2.1 (Eq. (2.1)), I showed that short pulses in time necessitate a superposition of many frequency components, i.e. a broad spectral bandwidth of the pulse. Moreover, all of these components need to be temporally overlapping, equivalent to a flat spectral phase $\varphi(\omega)$, or vanishing GDD, TOD and higher orders of dispersion. While the generation of spectral bandwidth is generally possible via non-linear optical processes (see Sec. 2.6) in gases, solids or even liquids, see Ref. [129], its temporal compression is typically challenging. The workhorses of spectral broadening of high-power systems are hollow-core fibers [36, 37] and multi-pass cells [38]. Multi-pass cells appear to be the solution for broadening and compression of picosecond and 100-fs scale pulses towards few tens of femtoseconds, even at kilowatt power levels [38] or in the SWIR range [189]. Here, the focus will be on fiber-based approaches since they have proven their capability in generating multi-octave supercontinuua [36, 37, 129].

In early times, the generation of additional spectral components in fibers was decoupled from their temporal compression, which is nowadays referred to as post-compression [35–37, 129]. Typically, dispersive multilayer mirrors were used [39, 40] in combination with (wedged) materials or special crystals for higher order dispersion compensation [181]. The advantage of post-compression schemes is the intrinsic decoupling of the generation and temporal shaping of the spectral components which allows to optimize the spectral bandwidth independently. However, limitations arise when the spectral bandwidth reaches the technical limitations of the dispersive mirrors demanding for light-field synthesis [53, 190–193], where different spectral regions are compressed separately and then coherently overlapped. Another limitation of such approaches are transient nonlinearities in dispersive mirrors at high intensities [194], which prevent their usage in high-power systems or require sufficiently large beam diameters that might degrade the stability due to the increasing size of the system. These limitations also transfer to multi-pass cells which are basically limited by the available mirrors.

Novel approaches in fiber-based spectral broadening circumvent those issues by tweaking the propagation dynamics in a fiber such that all dispersion is compensated and self-compression is achieved [138,195]. Furthermore, soliton propagation [196] or the emission of resonant dispersive waves in the UV [41,42,51] and mid infrared (MIR) range [197] have been demonstrated. Such effects have also been observed in hollow-core photonic crystal fibers [37, 41, 198–200], which favor high nonlinearity but have a more limited power scalability than single-core hollow fibers. Nevertheless, gigawatt range systems have been successfully implemented [50,201,202]. Recently, field-resolved studies of resonant dispersive waves in the UV have been presented [139, 203].

For self-compression, the group velocity dispersion introduced by the gas and SPM should balance with the waveguide dispersion [51, 195], which, according to Eq. (2.57), have opposite signs (c.f. Ref. [51]):

$$\beta_2 = \frac{\lambda^3}{4\pi c^2}\left(\rho\frac{\partial^2\chi}{\partial\lambda^2} - \frac{u_{nm}^2}{2\pi^2 r^2}\right). \tag{4.1}$$

The first term accounts for the gas, whereas the second one is the waveguide dispersion, which scales with r^{-2}, where r is the fiber radius. For self-compression, $\beta_2 \overset{!}{<} 0$ to compensate for the positive contribution from SPM [204]. Consequently, small fibers tend to support self-compression more, but limitations arise when focusing highly powerful beams to small areas as the gas will be ionized and self-focusing might occur. Additionally, waveguide losses ($\propto \frac{\lambda^2}{r^3}$) increase drastically for small fibers, see Eqs. (2.54) and (2.55).

In the following, I will present several design considerations for a spectral broadening system that allow to maximize the bandwidth while maintaining the beam quality, throughput and temporal pulse integrity. I will also focus on constraints by the high peak power the system is designed for and also consider the general design of the fiber parameters to achieve significant spectral bandwidth. In addition, I will briefly discuss parameter constraints by the waveguide dispersion and finally conclude with an optimum supporting self-compression for the HORUS SWIR laser system.

4.2 Design criteria of a spectral broadening system

As discussed in Chapter 2, the main effect responsible for the gain in spectral bandwidth is self-phase-modulation, a χ_3-process. Its strength depends on the non-linear refractive index n_2 and on the intensity I_0 of the laser. Therefore, having high-intensity in a medium with high n_2 is crucial for achieving a large gain in bandwidth.

The high intensity required to drive the process competes with plasma formation and with self-focusing, both effects degrading the broadening performance [205]. Following the description of Refs. [205, 206], a limit on the plasma formation can be defined by requiring that the induced refractive index change by the plasma, $\Delta n_\mathrm{P} = \frac{\omega_\mathrm{P}^2}{2\omega_0^2}$, is much smaller than the refractive index change by the Kerr-effect $\Delta n = n_2 I$. Here, ω_0 denotes the central frequency of the laser spectrum, ω_P is the plasma frequency. The latter depends on the free-electron density in the gas ρ_e, the electron mass m_e and charge e via $\omega_\mathrm{P} = \sqrt{\rho_\mathrm{e} e^2/(m_\mathrm{e}\epsilon_0)}$ [205]. The free-electron density can be calculated by one of the methods described in Sec. 2.2. Assuming a condition of $\Delta n_\mathrm{P} \leq 10^{-3}\Delta n$ and an ADK ionization rate, a minimum fiber core-radius of

$$r_\mathrm{min} = A \left(\frac{\tau_\mathrm{fwhm}}{1.665}\right)^{-\alpha} \mathcal{E}^\beta, \tag{4.2}$$

can be estimated [205], where A is a gas-type dependent constant, α and β are coefficients between 0.44 and 0.52 and favor a wavelength dependence [207]. For the most common Ti:Sa laser systems, $\alpha = 0.45$ and $\beta = 0.51$ [205], or $\beta = 0.50$ [207], respectively. For 2.1 µm central wavelength, on the other hand, values of $\alpha = 0.457$ and $\beta = 0.516$ can be extrapolated from Fig. 2 in Ref. [207]. According to Ref. [205], the constant A for Helium is $A_\mathrm{He} \approx 2.62 \times 10^{-9}\,\mathrm{ms}^\alpha\mathrm{J}^\beta$, for Neon $A_\mathrm{Ne} = 1.14 A_\mathrm{He}$ and for Argon $A_\mathrm{Ar} = 1.79 A_\mathrm{He}$. For the parameters of interest here, 23 fs at 2.1 µm central wavelength, the values for the minimum fiber radius are presented in Table 4.1, suggesting a minimum radius of 0.57, 0.36 and 0.32 mm for Argon, Neon and Helium at a pulse energy of 3.75 mJ, respectively. The latter value is the energy available from our system after all diagnostics, compression and beam steering optics.

r_min [mm]	1 mJ	2 mJ	3 mJ	3.75 mJ	4 mJ	5 mJ
Ar	0.27	0.41	0.50	0.57	0.59	0.66
Ne	0.18	0.26	0.32	0.36	0.37	0.42
He	0.16	0.23	0.28	0.32	0.33	0.37

Table 4.1: Minimum fiber radii due to plasma formation for different pulse energies and gases according to Eq. (4.2).

Knowing those limits, the maximum gas pressure to prevent self-focusing can be estimated by considering the critical power $P_\mathrm{cr} = \frac{\lambda_0^2}{2\kappa_2}$ of the medium [205, 208]. Here, λ_0 is the central wavelength, p the pressure and κ_2 is related to the nonlinear refractive index by $\kappa_2 = n_2 \frac{p}{p_0}$, p_0 is the reference pressure at which n_2 was measured, typically 1 bar. Literature recommends limiting the maximum peak power of the laser to less than 30 % of the critical power, $P_0/P_\mathrm{cr} \leq 0.3$ [205], which is equivalent to limiting the gas pressure

to

$$p_{\max} = 0.15 \frac{\lambda_0^2 p_0}{n_2 P_0}. \tag{4.3}$$

Since the literature values for n_2 vary significantly, see Table 4.2, the influence of the variation on the maximum pressure of

$$\Delta p_{\max} = \frac{\partial p_{\max}}{\partial n_2} \Delta n_2 = -\frac{0.15 \lambda_0^2 p_0}{n_2^2 P_0} \Delta n_2 \tag{4.4}$$

has to be considered. Resulting values are presented in Table 4.3, where the expressions for the peak power introduced in Eq. (2.8) for a Gaussian pulse of 23 fs at 2.1 µm central wavelength were used. The corresponding pressure limit, as calculated in Table 4.3, is rather low in the case of Argon (0.43 bar) at the design pulse energy of 3.75 mJ, but higher for Neon (4.21 bar) and Helium (10.4 bar) due to their lower n_2. However, a lower n_2 also results in reduced SPM and, therefore, a lower gain in spectral bandwidth which is to be compensated by pressure or fiber length. With these limitations in mind, the expected gain in spectral bandwidth can be estimated, including a discussion of the waveguide dispersion for achieving simultaneous pulse compression.

n_2 [m^2/W]	value	from Refs.
Ar	$(1.0 \pm 0.2) \times 10^{-23}$	[207, 209–211]
Ne	$(1.0 \pm 0.2) \times 10^{-24}$	[209, 211]
He	$(4.2 \pm 1) \times 10^{-25}$	[209, 211]

Table 4.2: Average n_2 values from the literature. Note, another reference [212] suggests values different by more than one order of magnitude.

$p_{\max}$ [bar]	1 mJ	2 mJ	3 mJ	3.75 mJ	4 mJ	5 mJ
Ar	1.61 ± 0.29	0.80 ± 0.14	0.54 ± 0.10	0.43 ± 0.07	0.40 ± 0.07	0.32 ± 0.6
Ne	15.79 ± 3.82	7.90 ± 1.91	5.26 ± 1.28	4.21 ± 1.02	3.95 ± 0.96	3.16 ± 0.77
He	39.00 ± 9.97	19.50 ± 4.99	13.00 ± 3.33	10.40 ± 2.66	9.75 ± 2.50	7.80 ± 2.00

Table 4.3: Maximum gas pressure in a hollow waveguide for different pulse energies according to Eq. (4.3).

Broadening factor Knowing the constraints of plasma formation and self-focusing on the fiber dimensions, I can now consider the expected gain in spectral bandwidth and the output pulse shape. In the previous section, the gas type, pressure and fiber radius were constrained. Now, the parameters left to determine are the fiber length and the actual pressure needed to generate sufficient spectral bandwidth. Finally, the waveguide dispersion must be considered which is necessary for self-compression of the pulses during spectral broadening.

To this end, it is illustrative to use an analytical estimation of the expected broadening factor G due to SPM for a fiber of length L according to Ref. [205, Eq. (7)] that is defined as

$$G = \frac{\Delta\omega}{\Delta\omega_0} = \sqrt{1 + \frac{4}{3\sqrt{3}} \varphi_m^2} \tag{4.5}$$

with the maximum phase shift $\varphi_{\mathrm{m}} = \xi P_0 L_{\mathrm{eff}}$. The peak power P_0 enters the equation together with the effective length $L_{\mathrm{eff}} = \frac{1-\exp(-\alpha L)}{\alpha}$, the nonlinear parameter $\xi = \frac{\kappa_2 \omega_0}{c A_{\mathrm{eff}}}$, the attenuation constant α, and the effective mode area $A_{\mathrm{eff}} \approx 0.48\pi r^2$, adapted from [205]. The attenuation constant is given by Eq. (2.54) or Eq. (2.55). Due to the variations of n_2, see Table 4.2 and Ref. [212], the broadening factor varies significantly. Thus, instead of calculating the error prone broadening factor for different configurations, I consider

general scaling laws of Eq. (4.5). To this end, let the peak power P_0 be the same in all cases. Then, if the expected broadening factor is large, it scales directly proportional to ξ and thus to the nonlinear refractive index at the experimental pressure κ_2. Consequently, a similar spectral gain is expected for different gases but similar κ_2, neglecting the gas type dependence of L_{eff}. As an example, the n_2 of Neon is roughly one order of magnitude smaller than the one of Argon, thus requiring one order of magnitude more pressure. Since the minimum fiber radius for Neon can be chosen smaller by a factor of 0.67 compared to Argon, see Table 4.1, the effective mode area can be smaller by a factor of 0.45. Therefore, the required pressure would be less than 5 times as much when transferring from Argon to Neon. However, the scaling of the effective length for different gas types and fiber radii has been ignored so far, which partially counteracts that scaling law. The gas type dependence enters via the linear refractive index to α (Eq. (2.54)), therefore its dependence is rather weak compared to the dependence on the radius $\alpha \propto \frac{1}{r^3}$. As a result, a more than 3 times higher attenuation constant is expected for Neon compared to Argon that reduces the expected spectral gain, however, only for long fibers.

In conclusion, the spectral gain for gases with lower n_2 can be enhanced to match that of gases with higher n_2 by increasing the pressure. However, a further reduction in fiber diameter leads to increased attenuation, which can hinders this scaling law, particularly in long fibers. It is important to note that this analysis does not account for self-steepening and dispersive effects [205]. While self-steepening can increase the spectral bandwidth towards the shorter wavelengths (as discussed briefly in Sec. 2.6), dispersive effects are expected to impact the dynamics significantly. Specifically, smaller fibers that favor higher waveguide dispersion can compress the pulses during propagation, resulting in increased peak intensity and therefore in higher nonlinear effects and more gain of spectral bandwidth. These dispersive effects are expected to partially compensate the comparatively poor performance of Neon compared to Argon, allowing for a reduction in pressure in the first case. Therefore, a discussion of solitonic propagation behavior including dispersive effects follows. An experimental comparison of selected gases and fiber geometries will be presented in Sec. 4.4.

Soliton self-compression Before introducing the experimental setup and results, I will discuss the nonlinear propagation in the context of optical solitons. To this end, the characteristic length scales introduced in Sec. 2.6 will be used due to their intrinsic coverage of linear, nonlinear and dispersive effects. For the parameters the experiments were conducted with, the loss length is $L_{\text{loss}} \approx 23 - 32\,\text{m}$ (Eq. (2.61)), assuming a central wavelength in the range of 1.8 µm to 2.1 µm and a FS fiber with the refractive index from [79]. The used fiber length of 2.4 m, see below, is an order of magnitude shorter; and therefore, losses by the waveguide attenuation play a minor role.

In addition, the dispersion length is $L_{\text{disp}} \approx 7.5\,\text{m}$ (Eq. (2.62)) with $|\beta_2| \approx 1.9 \times 10^{-29}\,\frac{\text{s}^2}{\text{m}}$ from Eq. 2.57 and the refractive index data from Ref. [213] for a pulse with 21 fs FWHM pulse duration. This value transfers to a nonlinear length of roughly $L_{\text{nl}} = 0.5\,\text{m}$ to $0.77\,\text{m}$ (Eq. (2.63)), considering an n_2 value for Neon from Table 4.2 at 700 mbar, which is the pressure used in the final experiments. Consequently, the soliton order is $N \approx 3.1$ to $3.8 \approx 4$ (Eq. (2.64)) and the fission length is $L_{\text{fiss}} \approx 2.0$ to $2.4\,\text{m}$ (Eq. (2.65)), which aligns with the fiber length in the experiment. The large range of the values given originates in the variations of n_2. As the soliton fission is of the order of the fiber length, but the dispersion length is much larger, a self-compressing scheme is present.

The detailed investigation of nonlinear propagation through gas filled waveguides requires numerical treatment. With with Luna.jl [142] by John C. Travers and Christian Brahms, the presented system can be modeled including third-harmonic generation, plasma effects, and waveguide losses. Details on the simulation can also be found in

Ref. [204]. Simulations for a Gaussian laser pulse with $\tau_{\mathrm{fwhm}} = 21\,\mathrm{fs}$, a central wavelength $\lambda_0 = 2.1\mu\mathrm{m}$, and a pulse energy of 3.3 mJ entering a fiber of 2.4 m in length, filled with 0.7 bar of Neon, are shown in Fig. 4.1. To elucidate the role of plasma effects in the fiber, the simulations were performed considering the formation of a plasma obeying an ADK ionization rate (panels a) and b)) and without plasma effects (c) and d)). Their comparison reveals a minor influence of plasma formation for the parameters given, even though the maximum peak power is slightly higher for the case without plasma. These findings agree well with the constraints on the fiber parameters presented above. The pulse duration at the exit of the fiber is 3.7 and 3.6 fs, respectively. As evident from the time domain plots (part b) and d)), the pulse duration decreases during the propagation, whereas the spectral bandwidth increases significantly, manifesting a self-compressing broadening scheme.

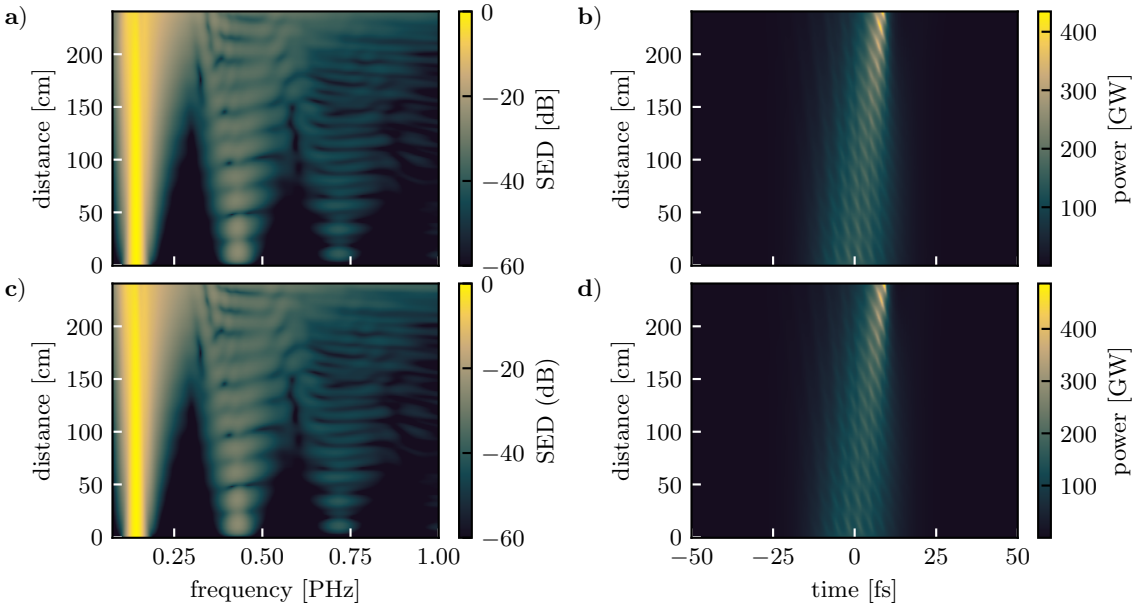

Figure 4.1: Simulated nonlinear propagation with Luna.jl [142] with plasma effects (a) and b)) and without (c) and d)).

Spectrally, see Fig. 4.1a), harmonic frequencies at $3f$ and $5f$ are generated. Especially the $3f$ components interfere with the fundamental as soon as the spectral bandwidth of both is large enough to overlap, which according to the simulations is possible from 1.5 m fiber length on. This interference is experimentally observed, as will be discussed later in this chapter. The parameters are designed such that the formation of dispersive waves in the UV [51] or mid-IR [197] does not yet start, even though even shorter pulse durations could be achieved [138]. Extending the bandwidth even further would require the optical windows in the setup to be removed (see Section 4.3), which directly calls for a differentially pumped scheme.

4.3 Optical and mechanical setup

Prior to the experimental results, the laser front-end is presented, followed by a discussion of the mechanical properties of the fiber mount. Subsequently, the general optical setup of the fiber broadening system and the details of the detection interferometer for the field sampling measurements are presented.

4.3.1 Laser front-end

The **H**igh-power **O**PCPA system for high **R**epetition rate **U**ltrafast **S**pectroscopy (HORUS) is an in-house developed few-cycle SWIR laser system that has principally been developed by T. Nubbemeyer and M. F. Kuthe. Details on the laser system can be found in Refs. [214, 215], whereas in the following, a short summary focusing on the main aspects will be presented.

A kilowatt-class Ytterbium doped Yttrium Aluminium garnet (Yb:YAG) thin-disk laser chain similar to Ref. [216] serves as pump source for a subsequent self-seeded optical parametric chirped-pulse amplifier (OPCPA), see Fig. 4.2 for an overview. For generation of CEP-stable SWIR seed radiation, a frequency doubled portion of the laser (second harmonic generation (SHG)) is used for white light generation in Yttrium Aluminium garnet (YAG) spanning a range from 650 nm to 750 nm. DFG between the white light and SHG yields the SWIR seed in the range of $1.7 - 2.5\,\mu m$. This seed is CEP-stable by the properties of the DFG. However, the setup is non-collinear, such that the interferometric difference between white light and SHG results in a net CEP that can be controlled by changing the delay of the SHG.

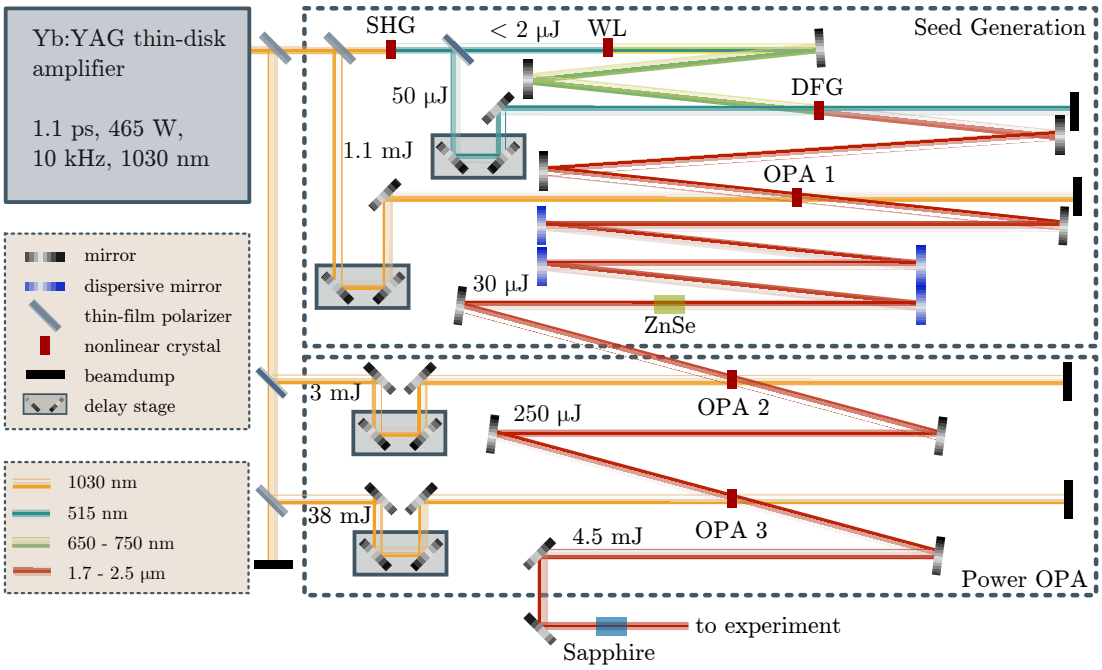

Figure 4.2: Outline of the HORUS - SHG: second harmonic generation, WL: white light generation, DFG: difference frequency generation, OPA: optical parametric amplification, ZnSe: Zinc Selenide. Focusing elements and telescopes are omitted for a better overview.

Subsequently, the SWIR seed is amplified in a first optical parametric amplifier (OPA). After a dispersion control setup that stretches the pulse with Zinc Selenide (ZnSe) and two types of dispersive mirrors that compensate for third-order dispersion and for the material dispersion of sapphire, the seed is amplified in two consecutive OPAs. Finally, Sapphire is used to post-compress the pulses by its material dispersion down to 23 fs FWHM as confirmed via SHG-frequency-resolved optical gating (FROG) [217, 218], see Fig. 4.3.

The CEP of the system is controlled with a piezo mirror in the SHG beam path. The voltage applied to the piezo can then be used to correct for any drifts of the CEP. The achievable stability depends on the stability of the generated white light and can reach values below 100 mrad after the third OPA stage [214].

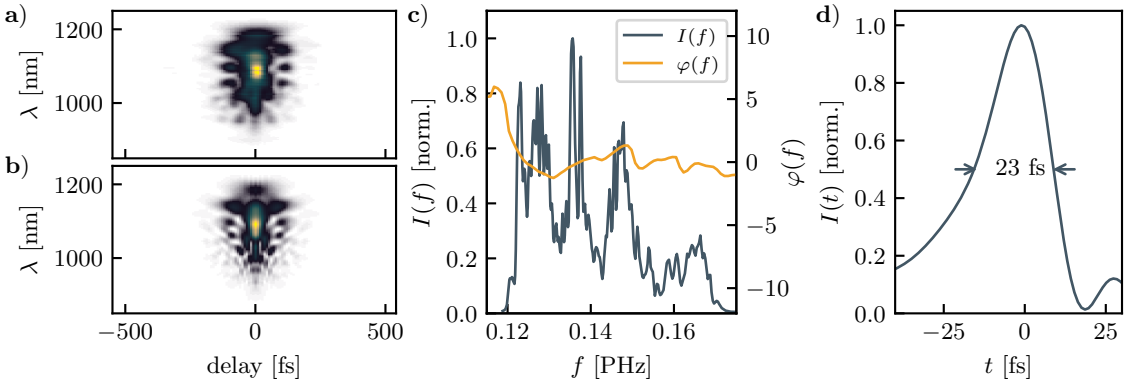

Figure 4.3: **a)** Measured and retrieved FROG trace (**b)**). **c)** Spectral intensity and phase **c)** Temporal pulse shape.

4.3.2 Mechanical design of the fiber mount

Despite the large number of publications or patents [219–223] on stretched HCFs and even their commercial availability in some parameter ranges[1], few details on the exact mechanical design of such fiber holders are known. It seems common to pre-stretch the fiber and then permanently fix it to a supporting mount, as evident from the technical details disclosed in corresponding patents [219, 223], or to stretch it by means of threaded mounts that allow to apply axial force on the waveguide [224]. Within the approach chosen here, one of the fiber holders (either entrance or exit) is mounted to a linear stage which is pulled by a spring. This way, the fiber tension can be adjusted carefully and more importantly, thermal expansion of the fiber is compensated. The typical expansion distance in the experiment is below 0.5 mm, such that the movable part can be place at the entrance as well, since the typical focal length is longer.

One of the individual mounts developed with aid of Tobias Kleinhenz is outlined in Fig. 4.4. The key elements of the design are the integrated ceramic ferrule to protect the fiber entrance, which is a feature employed by others as well [224]. More importantly, a retainer ring with a spherical surface on the inside holds a spherical nut with the actual fiber mount. The nut is pressed against a rubber gasket and custom-made KF flange for vacuum sealing. Micrometer screws at the flange allow to adjust the tilt of the fiber tip that can move due to the flexibility of the rubber gasket. The spherical surface of the nut and the retainer are designed such that its center sits at the fiber entrance and any tilt movement happens around that point. Due to this special design the tilt can be adjusted without compromising the in-coupling efficiency by a transverse displacement of the tip.

This design of the fiber mount allows to stretch a HCF while each side is attached to a vacuum chamber and pumped individually. The tension of the fiber must be adapted to the required straightness for the compensation of losses due to the bending radius, see Sec. 2.6.1. The influence of the fiber curvature is the term that can be minimized by increasing the fiber tension since the radius and tension are related by

$$R = F/\hat{m}, \tag{4.6}$$

with the pulling force F and the weight per unit length $\hat{m}$ [37]. Here, the available fibers have a mass per unit length of $m_1 = 0.345\,\mathrm{g/m}$ [225] and $m_2 = 0.322\,\mathrm{g/m}$ [226], and therefore, a pulling force of a few Newton results in the desired straightness of several thousands of meters in radius of curvature. In the experiment, the pulling force is approximately 20 N according to the datasheet of the spring [227] and the expansion of 25 mm. This value transfers to a radius of curvature of $\approx 6\,\mathrm{km}$.

[1]Suppliers are, for example, Few-Cycle Inc., UltraFast Innovations GmbH or IF Nano Göttingen

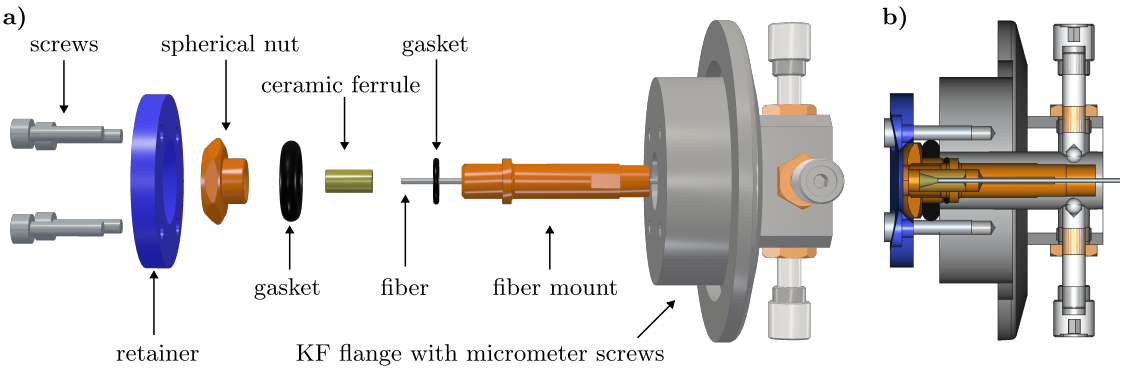

Figure 4.4: a) Exploded view of the fiber holder. The retainer and the spherical nut are designed such that the center of the sphere is at the fiber entrance. The laser enters from the left. **b)** Sectional view of the assembled mount.

4.3.3 Fiber broadening system

The fiber broadening setup consists of a position and angle sensitive beam stabilization with hybrid motor and piezo driven actors (Aligna, TEM Messtechnik GmbH), see sketch in Fig. 4.5. The stabilization system features the definition of independent set points for angle and position, which are used for alignment of the laser beam with respect to the stretched fiber. The second motorized mirror is curved with a radius of curvature of −2500 mm. It is placed on a linear stage along the fiber axis allowing the focus position to be shifted for maximum coupling efficiency. The desired focal size is derived from Fig. 2.14, but the final combination of beam size, beam quality and focal length resulted in an estimated coupling efficiency of 86 %. The latter number originates in a numerical evaluation of the overlap integral (Eq. (2.49)) with the experimentally determined beam profile taken with a microbolometer camera. Since the beam profile could only be measured in air and at low power, deviations from that value are expected due to a focal shift along the propagation direction and spatio-temporal reshaping, as investigated in Ref. [228]. While the first effect can partially be compensated by moving the focusing mirror, the influence of the latter is reduced by increasing the distance of the entrance window to the fiber as much as possible within the geometrical constraints of the setup.

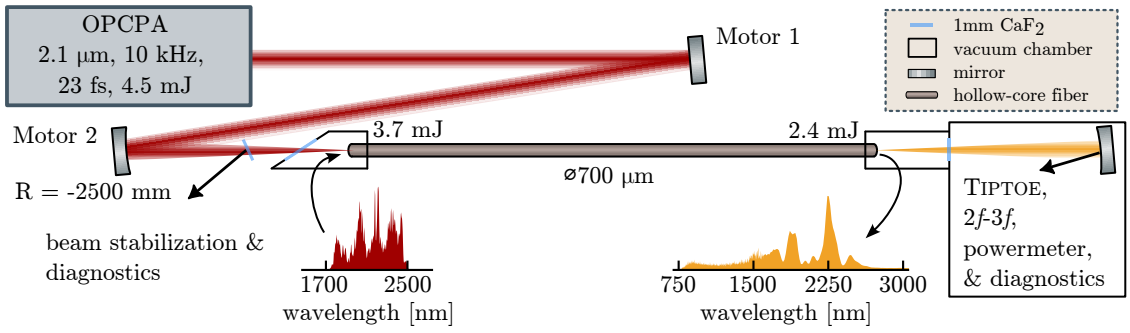

Figure 4.5: The output of the OPCPA system is compressed in the bulk (not shown) and focused into a HCF. Active stabilization with motorized mirrors additionally allows alignment of the setup. After re-collimation, the beam is guided in vacuum to the characterization setups. The ordinate for the spectra shown is linear.

The fiber is mounted as described above, and both the input and exit parts can be evacuated and filled with gas. Additionally, the fiber length can be varied in a large range, but best performance is found for a 2.4 m fiber with 700 µm core diameter filled with 0.7 bar of Neon. The spectra shown in Fig. 4.5 are taken with this configuration. Other gases and

fiber dimensions are investigated as well, see Sec 4.4.1, but this parameter set provides the best compromise for achieving shortest output pulses.

4.3.4 Field-sampling setup

For characterization of the temporal pulse shape of the spectrally broadened fiber output, the TIPTOE technique is used. Alternative and frequently used characterization schemes, such as dispersion scan [182] and FROG [217, 218], both suffer from phase matching limitations in the nonlinear crystal, which has to support broadband SHG over two octaves. As an example, β-barium borate (BBO) has a phase matching bandwidth[2] of 2535 GHzcm, as determined with Ref. [229], corresponding to 253.5 THz for a 10 µm thin crystal, which is barely enough to cover the spectral range of 300 THz. For such a broad bandwidth, an even broader phase matching bandwidth is required to prevent the suppression of spectral components at the edge of the spectrum. In addition, the absorption of the crystal hinders the measurement of wavelengths above 2.5 µm [230]. Therefore, field measurements have to be preferred over those methods for the sampling of multi octave spanning laser pulses. However, it is possible to phase-match the central part of the spectrum and to obtain information about the pulse compression in that part from d-scan or FROG, similar to what is used for initial characterization of the fiber output below.

For multi-octave spanning spectra, additional restrictions arise, primarily for the d-scan [182], which is hindered by parasitic spectral interference of the generated $2f$ components with the fundamental and third harmonic of the laser pulse, which spectrally overlap. Despite the use of broadband polarizers, this interference could not be fully prevented. Only approaches with spatially separated beams, like in a transient-grating dispersion scan [135], allow to overcome that limitation. Despite that, a dispersion scan requires that the GDD can be scanned over the maximum (otherwise the retrieval algorithm might not work reliably anymore). Since the broadening scheme is self-compressing, there is no large dispersion scanning range. Instead, dispersion can only be introduced to stretch the pulse which hinders the measurement of peak of the signal. These constraints in the dispersion transfer to the requirement of a dispersion-free interferometer for the field-sampling experiments.

Generally, three different types of dispersion-free interferometers could be chosen: Firstly, an annular mirror with an inner mirror shifted relative to the outer ring, introducing a delay between the respective reflected portions of the laser beam. Secondly, the usage of D-shaped edge mirrors allows to split the beam in two halves and to form a Mach-Zehnder interferometer. Recombination is done with another D-shaped mirror. Thirdly, holey mirrors that reflect the outer ring and transmit the inner part of the laser beam. Two such mirrors can be used to form a Mach-Zehnder interferometer, as shown in Fig. 4.6. For the following reasons, only the third option is appropriate for this purpose: The first interferometer type is collinear, such that no optical chopper can be placed in one of the beam parts, which hinders lock-in detection for current sampling. Nonetheless, differential measurements as in Ref. [26] would be possible. The second type of interferometer would in principle allow an optical chopper, but when focusing two parallel semi-beams with an offset, they will propagate through the focus under an angle with respect to each other. This angle between the phase fronts transfers to different ion yield modulations in a TIPTOE measurement, depending on the transverse direction of the focus. In sum, a cancellation of signal is expected if the phase difference in space exceeds π. This is equivalent to the observation of interference fringes in the focus of two beams with a parallel offset, see Sec. 2.7. For successful TIPTOE measurements, such situation

[2] In SNLO [229], this bandwidth is defined where the product of length and k vector mismatch, $L\Delta k$, varies between $-\pi$ and π.

must be prevented. Therefore, only the third option remains since it allows for an optical chopper and for TIPTOE measurements due to the concentric setup.

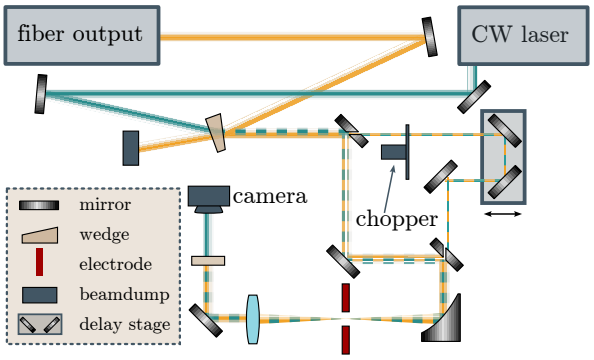

Figure 4.6: Interferometer for the TIPTOE measurements. The beam is split and recombined with perforated mirrors. A co-propagating continuous wave (CW) laser tracks the optical path length via its interference pattern on a camera. The beam being sampled is chopped. Both beams are focused with an $f = 100\,\mathrm{mm}$ OAP.

For adjustment of the output power to the required level in the field-sampling setup, a combination of different filter methods is used, e.g., a reflection at an uncoated IR-FS wedge, or dispersion free diffractive attenuators (custom component from Lasnix and TEM grids). In combination with the geometry of the holey mirror, an intensity ratio of $I_{\mathrm{Signal}}/I_{\mathrm{Pump}} \approx 3 \times 10^{-4}$ is achieved ensuring that the perturbing field strength is low enough to form a linear perturbation, 1.7 % in this case. The beams are focused with an $f = 100\,\mathrm{mm}$ OAP between two copper electrodes with an extension along the propagation direction of 0.3 mm only. This size constraint enables the detection of CEP effects in TIPTOE since focal averaging effects due to the Gouy phase shift are prevented. The perforated mirrors in the interferometer also alter the focal shape of pump and signal beam after the TIPTOE interferometer. Since the signal beam is smaller, its focal size is larger compared to the pump focus, see Fig. 4.7. This is an advantage for the measurement since it ensures a spatially smooth perturbation of the ionization and reduces the intensity such that a first-order perturbation is valid. The pump beam is larger and therefore its focus is smaller than the one of the signal beam. This property ensures that no potential diffraction rings of the signal beam caused by apertures of the holey mirrors are being sampled. In addition, diffraction rings of the pump beam that could influence the measurement are suppressed by the nonlinearity of the ionization process.

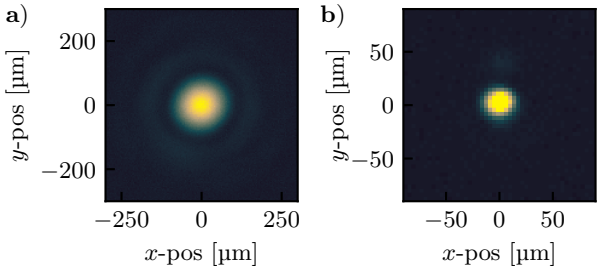

Figure 4.7: Beamprofile in the focus of the TIPTOE measurement taken with a silicon camera and a 1 µm longpass filter. **a)** Signal beam **b)** Pump beam.

The optical path length is tracked and actively controlled with a co-propagating frequency stabilized Helium-Neon laser. Its interference pattern is detected downstream with a camera and evaluated in real time, with a cycle time of 16.5 ms, similarly to what is explained in Chapter 5. Feedback is applied to the piezo-driven delay stage in the transmitted arm of the interferometer. The achieved in-loop stability is 2.99 nm over a time of more than 80 min, see Fig. 4.8.

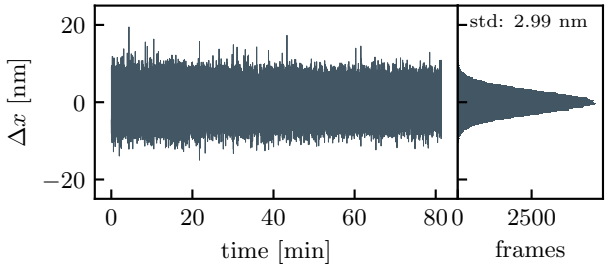

Figure 4.8: The interferometric stability of the field sampling interferometer reaches 29.7 mrad at 632.8 nm wavelength, corresponding to 2.99 nm (rms) over a time of 81 min.

4.4 Investigation on the achievable performance

To achieve best performance, it is essential to investigate both the spectral bandwidth depending on the fiber geometry, gas type and pressure, but also the compressibility of the pulses. I will first present data on the spectral bandwidth depending on gas type, pressure and some selected fiber geometries and conclude with a parameter set to be investigated afterwards.

4.4.1 Dependence of the spectral conversion on gas density and type

In order to find the most promising candidate for a fiber broadening setup, a comparison of the performance of different gases regarding the gain in spectral bandwidth is necessary. To this end, the noble gases Argon, Helium and Neon are tested. According to the limits from Table 4.1, the minimum diameter for Argon is roughly 1 mm, whereas for Neon and Helium, smaller diameters can be used. For Argon, a 1 m solid fiber is used, whereas for Neon and Helium, a stretched fiber is used. Since the fiber tips must be adapted to the fiber diameter, two different sizes are available: 530 µm [226] and 700 µm [225] core diameter. Due to the limitations from Table 4.1, the smaller diameter could only be used with Helium. However, in the experiment the losses with the small fiber are larger and therefore, the 700 µm diameter one is installed for both Ne and He. The smaller nonlinearity of He is compensated for by the pressure, which is in accordance with Table 4.3. The stretched fibers have a length of 2.4 to 2.5 m, as suggested by numerical simulations.

A comparison of the different gas types in different fibers is presented in Fig. 4.9. These spectra are taken with a broadband and fast scanning spectrometer (Mozza, Fastlite), which, however, has limited capabilities in resolving spectral data in the range of $1 - 1.5$ µm and deviated from the data taken by other devices. Therefore, only the long wavelength side of the spectra is considered for further conclusions. The dynamic range of the device appears small, but as opposed to the multi-device approach presented later in this thesis, the straightforward implementation without complicated calibration is a major experimental advantage. As shown in Fig. 4.9, all configurations yield a broad output spectrum, but the case of Argon yields largest bandwidth. The bandwidths can be compared by considering the drop in amplitude towards the long wavelengths, where the arrows in Fig. 4.9 indicate a 2 % of maximum threshold. Please note that a better method would be to calculate the supported pulse duration by a Fourier transform limit. Here, due to the strong performance issues of the device at the short wavelength side, this method is yielding misleading results - in particular regarding the noise amplitude in the He case.

The investigated pressures are chosen to prevent any distortions of the mode shape or any reduction of the transmitted power. For Argon, the pressure aligns well with the expected maximum pressure from Table 4.3, whereas deviations occur in the case of Neon and Helium. In particular, the transmitted power started to decrease for higher pressures than the ones shown, whereas the spectral bandwidth did not increase any further. This finding is in contradiction to simulations with Luna.jl [142], which suggest

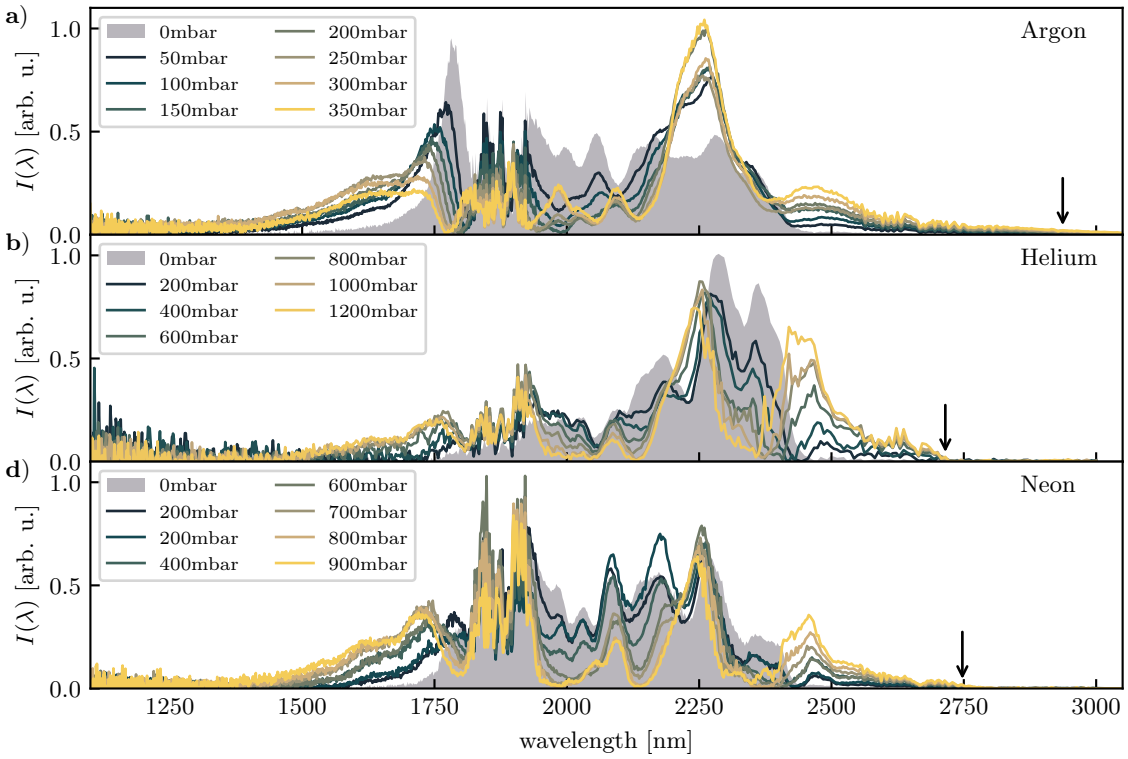

Figure 4.9: Pressure scan for different gases - **a)** Argon with fiber diameter 1 mm and 1 m length **b)** Helium in a 2.5 m fiber with 700 µm diameter **c)** Neon in a 2.5 m fiber with 700 µm diameter. The arrows indicate the wavelength at which the spectrum dropped to 2 % of the maximum.

an increase in bandwidth for higher pressures. Presumably, the observations are founded in effects that are neither included in the simulations nor in the design criteria presented above, such as impurities of the gas species that increase the plasma fraction, or pulse reshaping before the fiber entrance due to the high gas density [228]. In the case of Neon, a strong performance degradation appeared if a small amount of a different gas is present in the fiber. Interestingly, the pressure did not change by an amount detectable with our gauge (Swagelok), but the color of the plasma at the entrance changed from the typical orange/red to include a blue hue. This stronger plasma formation portends the presence of a gas with lower I_P, such as Nitrogen or Oxygen. For the pressures presented in Fig. 4.9, however, decent agreement with simulations of the fiber parameters is found.

Since the configuration with Argon results in most spectral bandwidth, which is essential for short pulses, its implementation and characterization seems obvious. Temporal characterization of the output pulses with FROG, however, has revealed that the pulses downstream the fiber are not fully compressed, but rather showed a pulse duration of ≈ 11 fs, despite the Fourier limit in the retrieval being on a one-digit femtosecond scale, see Fig. 4.10. For the case of Neon, FROG measurements showed better compression, yielding a pulse duration of 7 to 8 fs. The retrieval turns out to be error-prone as the data in any case is noisy. In addition, the direction of the time axis cannot be determined. In case of Argon, the visible spectrometer is not used which explains the missing spectral components below 800 nm. However, the data towards the long wavelength side also shows less signal compared to the Neon case, evidencing poor pulse compression since the spectral coverage of the output is provided (Fig. 4.9).

These insights are a manifestation of the low waveguide dispersion not being sufficient to provide a self-compressed broadening scheme with Argon. Thus, either smaller fibers (waveguide dispersion $\propto r^{-2}$) or longer fibers (dispersion $\propto$ length) are desirable. Smaller fibers are possible with Neon, which will be investigated in the rest of this chapter.

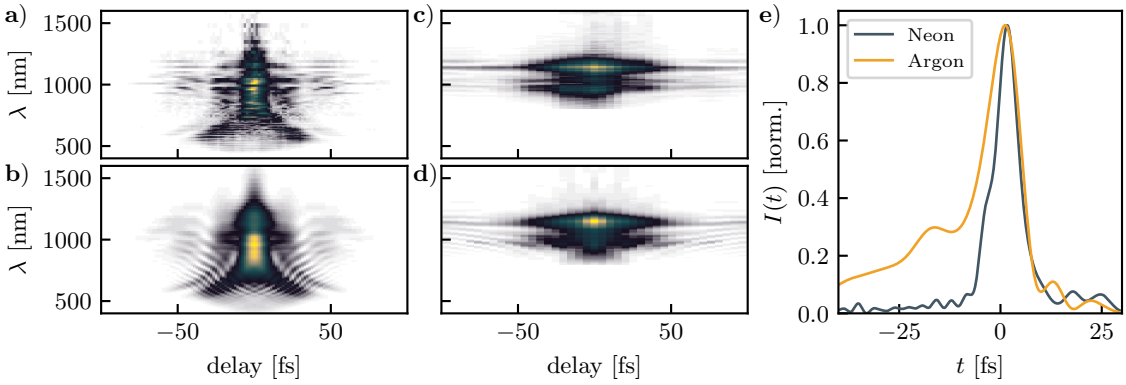

Figure 4.10: a) Measured and retrieved (**b)**) FROG traces for the case of Neon, respectively. **c,d)** for Argon **e)** Temporal pulse shapes corresponding to the retrieval.

The results presented in the following demonstrate that a fiber diameter of 700 µm at a length of 2.4 m indeed constitutes a self-compressing scheme, as expected from the design considerations above.

As a final remark of this paragraph, I would like to highlight the scaling laws of fiber dynamics, as discussed in detail in Ref. [51]. The fiber dynamics are invariant under scaling by a factor of ζ (except losses), if one scales the radius by a factor of $\sqrt{\zeta}$, gas pressure by $\frac{1}{\zeta}$ and the length and peak power by ζ. These scaling laws suggest a straightforward implementation of a self-compressing scheme from the literature at the parameters provided by the laser used here. As an example, in Ref. [138], a 1.8 µm system is compressed in an Argon-filled HCF to 2 fs. Scaling the 289 µJ system from there with a 2.5 m fiber to the parameters here requires $\zeta = 13$, thus a fiber length of 32.5 m. Such fiber lengths are hard to implement, in particular regarding the mechanical stability, the straightness, and the required laboratory space. Therefore, the approach of finding a set of parameters that employs smaller core diameter fibers at shorter length is more promising, which is why Argon cannot be used.

4.4.2 Power stability and beam shape

Strong field experiments investigating small signals can profit from high-power lasers that allow to increase the interaction volume for more signal generation. Thus, having a high field, high average power source is essential and the presented broadening scheme fulfills those requirements, as evident from the data presented in Fig. 4.11. The achieved average power at the fiber exit is 23.5 W and only fluctuates by 226 mW (standard deviation), which is below 1 %. The input pulse energy is 3.75 mJ, which corresponds to a transmission of 63 %. This value is lower than the 90 % that are theoretically expected from simulations with Luna.jl [142]. With the incoupling efficiency of above (86 %), a transmission of 77 % is expected. The residual difference must therefore be connected to non-linear effects in the entrance window, the gas in front of the fiber [228], or plasma effects. Losses by a curved waveguide can be excluded since the corresponding attenuation factor is $\alpha_{\text{curvature}} \approx 8.1 \times 10^{-6}\,\text{m}^{-1}$, and therefore negligible for $L = 2.4$ m.

The beam profiles of the fiber output are shown in Fig 4.11b) in the focus of a $f = 40$ cm spherical mirror and for the collimated beam in part c) and d). In panel c), a 1 µm longpass filter is added, which demonstrates that the short wavelengths are more in the center of the beam when comparing the profile to the one without filter (d)). Since the holey mirror in interferometer splits off a small portion of the very center part of the beam, it is expected that the long wavelengths are underrepresented in the field-resolved data. This property will be discussed in Sec. 4.5.3 and Appendix A.3.

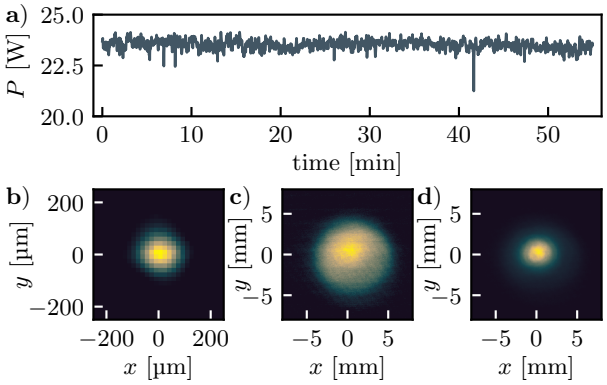

Figure 4.11: a) Power stability (23.5 W) of the fiber output with a standard deviation of 226 mW. **b)** Focus of an $f = 40$ cm spherical mirror on a microbolometer camera (Swiss THz Rigi) **c)** collimated beam on a Pyrocam IV with 1 µm longpass filter, **d)** and without.

4.4.3 Carrier-envelope phase stability

For single- and sub-cycle pulses, the CEP stability is the key parameter for guaranteeing waveform stability and controllability. Its characterization is thus important. Using $2f - 3f$ spectral interferometry, the relative drifts of the CEP over time are measured. For this purpose, the backside reflection of the wedge (c.f. Fig. 4.6) is sent to a BBO crystal for the generation of the second harmonic of the fiber output. A second wedge compensates for spatial chirp. After passing through a 45° polarizer, spectral interference with the third harmonic generated in the fiber occurs. It is split and detected by two silicon-based spectrometers, one of them capturing signal for a feedback loop, the other one for a reference measurement. The feedback loop controls the piezo stage in the DFG part of the laser system, see Fig. 4.2, with a feedback signal derived from a software proportional–integral–derivative (PID) control. The out-of-loop reference data for a measurement of more than 50 minutes are shown in Fig. 4.12. After detecting spectral interference fringes (panel a)), the corresponding relative CEP is extracted via a Fourier transform and the phase value at the point of the reciprocal frequency defined by the spectral fringe spacing. The standard deviation of the extracted phase amounts to 138.2 mrad and is averaged over several laser shots. A dataset is acquired every 64 ms in Fig. 4.12.

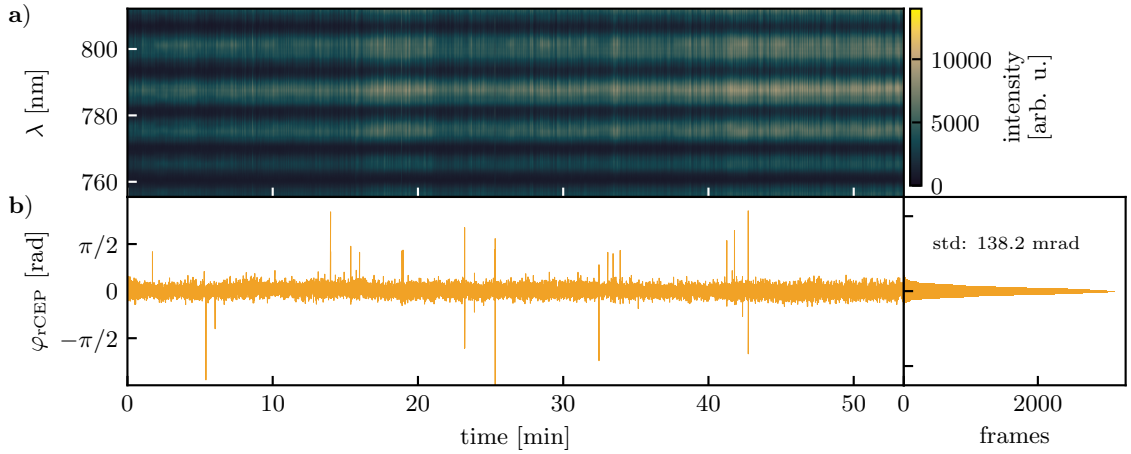

Figure 4.12: a) $2f - 3f$ interference fringes as measured with a spectrometer for more than 50 minutes **b)** Extracted relative CEP value over time with a standard deviation of 138.2 mrad.

To obtain non-averaged data, the integration time of one of the spectrometers (Avantes Avaspec ULS-4096CL-EVO-UA-10) is reduced to 90 µs, shorter than the laser repetition time, and the device is triggered by the laser. Thus, the detected spectral fringes are generated by a single laser shot only, see Fig. 4.13. However, due to a technical limitation not every single shot could be resolved, but there is a deadtime of the acquisition of 698 µs after each shot [231]. Therefore, at least 7 pulses are expected to be skipped between two

consecutive measurements. Nevertheless, a CEP stability of 381.1 mrad can be confirmed in this measurement, which proves CEP stability from a near shot-to-shot basis to a one hour time scale. These values are, to the best of my knowledge, the best values reported in the literature for a multi-millijoule single-cycle SWIR laser system at a high repetition rate.

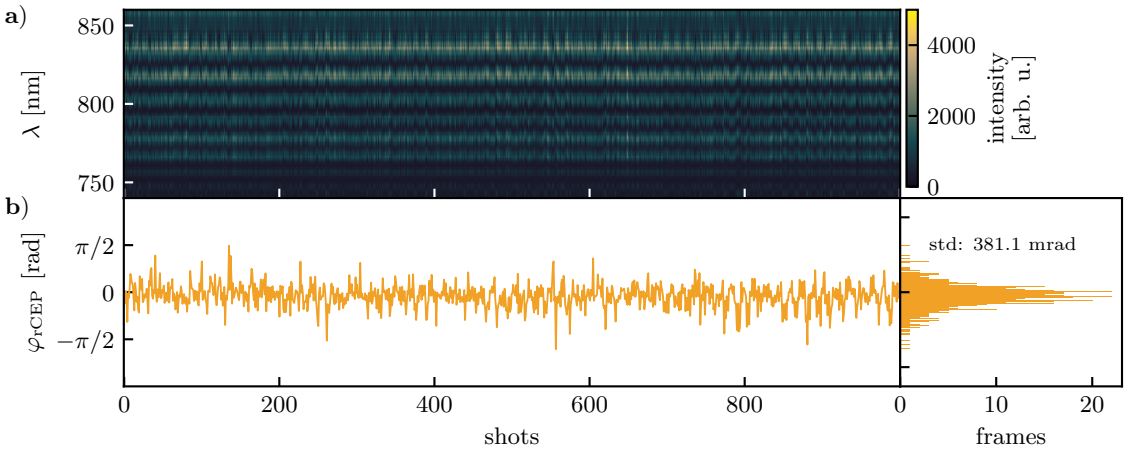

Figure 4.13: a) $2f-3f$ interference fringes for single laser shots taken with a triggered spectrometer for 1000 shots **b)** Extracted relative CEP value with a standard deviation of 381.1 mrad.

4.5 Field-resolved characterization of the output

Due to the limitations discussed above, measuring the electric field of the light oscillation is the correct approach for its characterization. In this section, the TIPTOE technique as introduced in Ref. [26] and in Sec. 2.5 serves as method for time-domain measurements. Starting with a presentation of the time-domain data and the corresponding spectral amplitude and phase, the pulse duration and spectral coverage are identified. Subsequently, its validity is confirmed by investigation of the origin of the spectral phase and by the characterization of the complex spectral response function.

4.5.1 Time-domain sampling of the electric field

The results of a time delay scan and simultaneous detection of the generated ion yield are shown in Fig. 4.14a). For the data there, a Tukey window in Fourier space is applied between 0.03 and 0.5 PHz to remove both low and high-frequency noise. The extracted pulse duration is 6.9 fs FWHM of the intensity envelope, which is slightly shorter than a single optical cycle of the driving wavelength. The measured pulse shape and the pulse energy transfers to a maximum peak power of the generated pulses of 0.26 TW. The extracted Fourier limit is 3.8 fs, comparable to value obtained from simulations in Sec. 4.2.

The two curves in Fig. 4.14a) show the measured electric field waveform for two different values of the CEP of the incident pulse, shifted by $\approx \pi/2$ versus each other. In the case of a relative CEP of $\varphi_{\mathrm{rCEP}} = 1.5$ rad, higher frequency oscillations are visible as compared to $\varphi_{\mathrm{rCEP}} = 3.1$ rad, see inset. As will be evident from the systematic scans presented below, this change of the waveform corresponds to the spectral response function of TIPTOE, which suppresses high-frequency components depending on the CEP of the driving pulse. Note that the CEP of the measured waveform does not change with the changing CEP of the incident pulses, since both pulses are shifted simultaneously. According to the spectral response function, see discussion in Sec. 2.5 and Appendix A.3, a simultaneous CEP shift

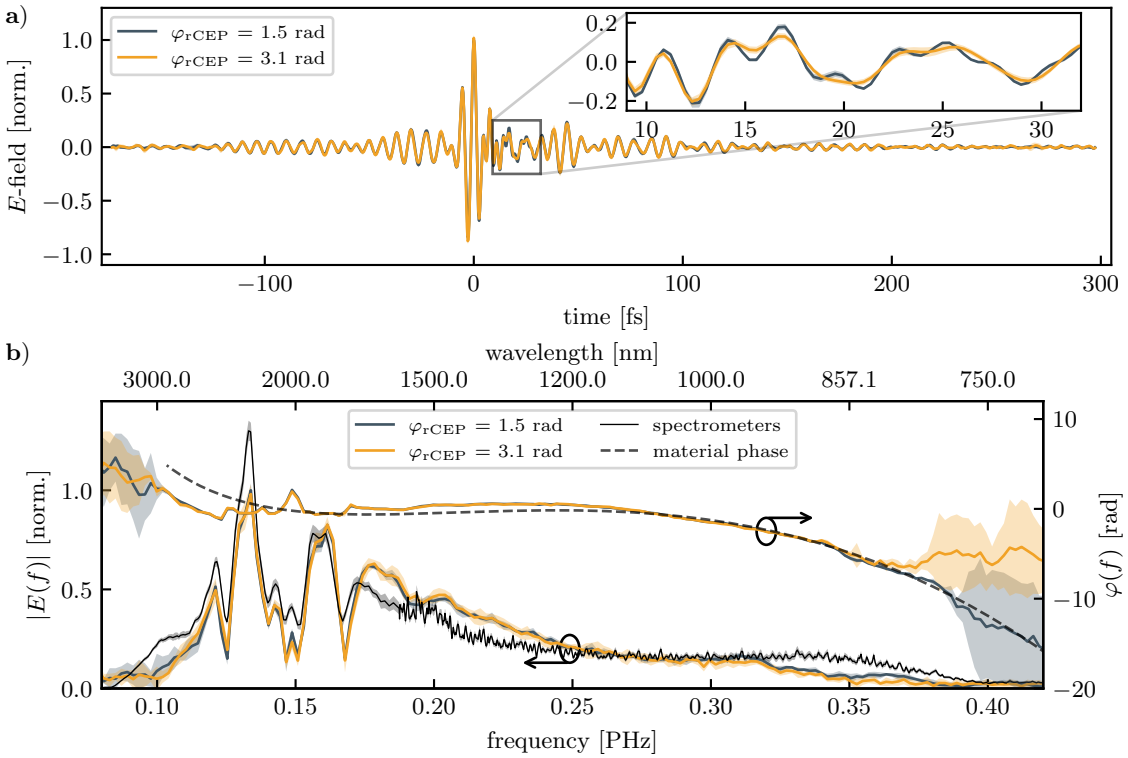

Figure 4.14: a) TIPTOE data for two different relative CEPs shifted by $\pi/2$ with respect to each other. **b)** Spectral amplitudes for both cases in comparison to spectrometer data. The corresponding spectral phase agrees well with the expected phase for the material combination (dashed line). The amplitudes are given for the frequency axis, the wavelength axis is only a guide to the eye.

cancels out. If only one of the two pulses in the interferometric measurement exhibited a change in phase, such a change would be visible - I confirmed this effect in the framework of TIPTOE measurements on nanometric needle tips, see Ref. [31, supplement]. Only the waveform for a CEP of the pump pulse of 0 represents the real electric field of the signal pulse. The case of $\varphi_{\mathrm{rCEP}} = 1.5\,\mathrm{rad}$ can be identified with a pump pulse CEP of 0, as will be shown below in the section on CEP scans.

Spectrally, a suppression of the amplitude appears in the region of 0.3 to 0.4 PHz depending on the CEP, see Fig. 4.14b). The spectral phase is similar in both cases, except that for the case of $\varphi_{\mathrm{rCEP}} = 1.5\,\mathrm{rad}$, the retrieved phase value has a lower error bar at 0.39 PHz than the other case, indicating a slightly larger bandwidth. Note that those measurements are performed in an alternating manner, where the CEP is flipped several times in series to eliminate the influence of drifts of the laser and of the detection setup. The detected spectral amplitudes agree well with the data taken with spectrometer, see black line in Fig. 4.14b). Residual differences are discussed below. For this measurement, data from three different types of spectrometers, an Ocean Optics HDX (Si detector), an Ocean Optics NIRQuest-512 (InGaAs detector) and a Spectral Products SM-301-EX (PbSe detector), are used simultaneously. The devices are fed by a splitting unit where the laser is coupled in with a ZrF_4 fiber, and amplitude calibration of the entire setup is performed using a calibration lamp (StellarNet). Details on the calibration procedure can be found in Appendix C.

The spectral phase is not perfectly flat, as one would expect for a self-compressing scheme. The origin of that dispersion is the material in the beam path, 1 mm of CaF_2, 0.3 mm of FS, and 0.7 m of Neon at the exit of the fiber. This combination results in the phase shown as a dashed line in Fig. 4.14b) and overlaps decently with the spectral phase from the field measurement. The material phase is derived from Sellmeier expressions

[77, 78] for the refractive index of CaF_2 [80], FS [79] and Neon [213], where constant and linear terms are subtracted to match the data. The good agreement of both curves verifies that the phase at the fiber exit is flat and the presented scheme is self-compressing. The slight mismatch of the phase for the low-frequency part might originate in the available refractive index data, which is extrapolated to the required bandwidth. The pressure in the TIPTOE chamber is 10 mbar. When measuring the output pulses in ambient air, in total 0.6 mm FS are required for compression. However, the signal to noise ratio in the TIPTOE measurements is worse and side pulses appear, which are most likely caused by higher-order dispersion of the gas and the material. The decreasing signal-to-noise ratio can be connected to the bias voltage (10 V), which is appropriate at lower pressures but may be too low at ambient ones, similar to Ref. [26].

4.5.2 Investigation of carrier-envelope-phase effects

Above, I introduced the effects of changes of the CEP on the detected spectral amplitude by showing the two opposing cases. A systematic investigation of the resolved spectral amplitude depending on the incident pulse CEP is shown as an asymmetry map in Fig. 4.15a). There, the asymmetry A defined by

$$A = \frac{|E(f)| - \langle |E(f)| \rangle}{\langle |E(f)| \rangle}, \tag{4.7}$$

is shown. It is a measure for the normalized difference of the spectral amplitude from its mean (i.e., CEP-averaged) value. The results show two distinct features at the high-frequency side: First, in the region of 0.3 to 0.37 PHz, the amplitude is modulated with CEP and a periodicity of π. Second, in the region of 0.37 to 0.4 PHz, a diagonally oriented fringe pattern is present. Comparison of the experimentally determined asymmetry map with simulated ones manifests the origin of both kinds of spectral modulations. The first kind originates in the TIPTOE response, which appears as an asymmetry map as shown in Fig. 4.15c). The second type of fringes, the diagonal ones, are $f - 3f$ interference fringes that originate in the fiber, where the third harmonic in the gas is generated. A simulation of the nonlinear propagation through the HCF with Luna.jl [142] confirms the spectral interference pattern. The asymmetry map shown in Fig. 4.15d) is calculated for different values of the CEP of the pulse before the fiber. The combination of both the TIPTOE response and the $f - 3f$ interference in the fiber reproduces the experimentally determined asymmetry map as shown in Fig. 4.15b). There, a CEP shift between the fiber and the TIPTOE measurement is introduced, which determined the relative shift of both features versus each other. Comparison of the simulations, which take the absolute CEP into account, with the experiment, which only determines a relative CEP value, now fixes the latter. The minima occurring at $\varphi_{\mathrm{CEP}} = 0, \pi$ and $\varphi_{\mathrm{CEP}} = 2\pi$ are present in the data at $\varphi_{\mathrm{rCEP}} \approx 1.5$ rad and $\varphi_{\mathrm{rCEP}} \approx 4.6$ rad, identifying a relative CEP of 1.5 rad with an absolute (pump) CEP of 0 rad or π. Consequently, this scan allows an absolute CEP calibration up to a factor of π, which, by the inversion symmetry of space, cannot be determined. Therefore, the waveform shown in Fig. 4.14a) for the case of $\varphi_{\mathrm{rCEP}} = 1.5$ rad corresponds to the real waveform, up to a pre-sign.

Note that a similar spectral modulation is expected at DC frequencies, see Fig. 2.13. However, the modulation is only pronounced clearly for frequencies below 0.1 PHz, which is outside the generated spectral bandwidth.

4.5.3 Spectral amplitude response of the field sampling procedure

In the previous section, I presented the electric field measurements and discussed properties of the CEP and spectral phase as well as the relative change of the spectral amplitudes

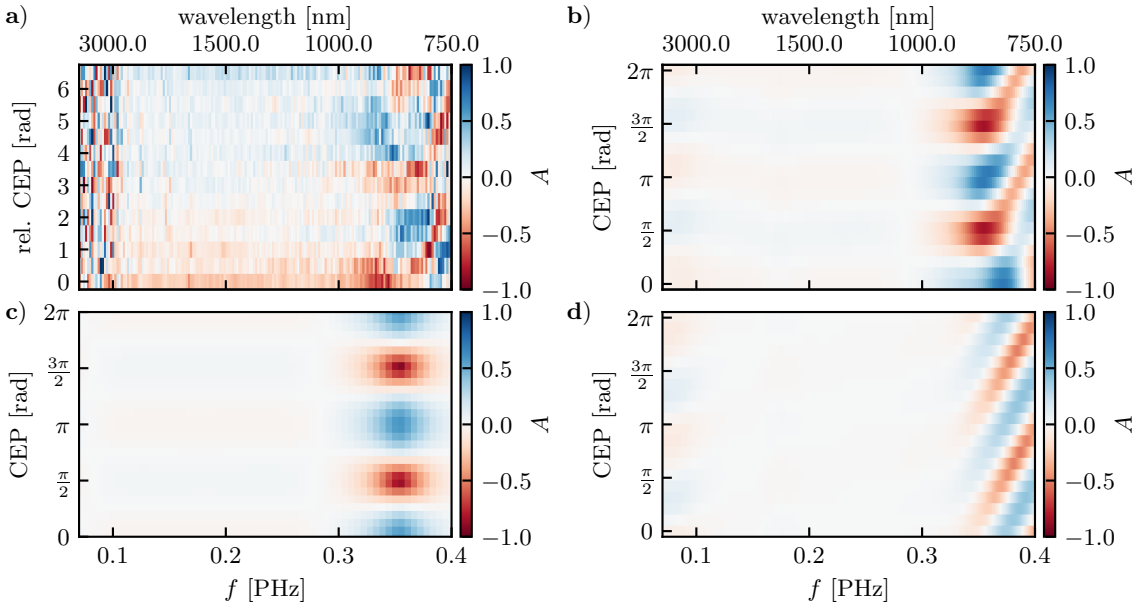

Figure 4.15: Spectral CEP dependent asymmetry map **a)** experimental data (relative CEP), **b)** simulated, **c)** TIPTOE only, **d)** fiber output only. The simulated data take the absolute CEP into account.

with CEP. Here, I would like to focus on the absolute value of the spectral amplitudes. For a perfect field measurement with a response of unity over the entire spectral bandwidth, the comparison of the spectral amplitudes extracted from the Fourier transform of the waveform, $|E_{\text{meas}}(f)|$, to those taken with a spectrometer, $|E_{\text{spectrometer}}(f)|$, should yield no difference. Comparison of the data in Fig. 4.14b) reveals that there are deviations between both curves. To determine their origin, an experimental spectral response can be defined as

$$|H_{\text{exp}}(f)| = \frac{|E_{\text{meas}}(f)|}{|E_{\text{spectrometer}}(f)|}. \tag{4.8}$$

The extracted experimental response should resemble the expected response function of TIPTOE. The direct comparison, see right panel in Fig. 4.16, indicates a blue shift of the measurement, since the experimental response function suppresses the low-frequency part more than expected. This spectral shift originates in the geometry of the interferometer: The perforated mirror selects the inner part of the collimated laser beam and therefore spectrally selects more short wavelengths, see Fig. 4.11c) and d) for a comparison of the beam profiles with a spectral filter. Similar effects have been observed and characterized in the literature [232], but since the spectrum covers a larger bandwidth than Ref. [232], the effect is even more prominent in this case. The spectral distribution in the collimated beam can be modeled by assuming that the beam exiting the fiber forms a homogeneous disk[3] of the size of the effective mode area, see Appendix A.3 for details. The wavelength-dependent far-field distribution can be transferred to a spectral response curve that the experimentally detected one can be corrected for, see right panel of Fig. 4.16. The corrected experimental response reproduces the expected TIPTOE response within the error bars and confirms the validity of the field-resolved measurements.

4.6 Discussion and conclusion

In the last sections, I demonstrated that a multi-millijoule SWIR laser system with a high repetition rate can be spectrally broadened and simultaneously compressed in a stretched

[3]Following discussions with Nick Karpowicz

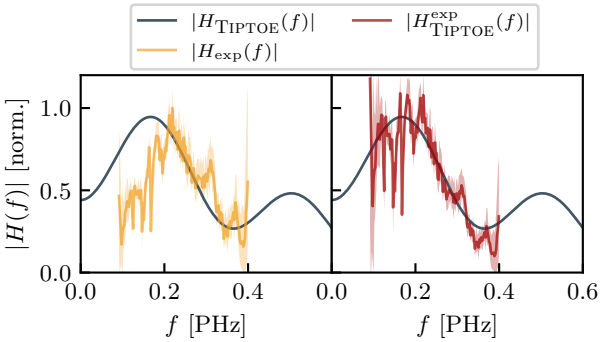

Figure 4.16: Experimentally determined response function. Left panel: spectral difference $|H_{\text{exp}}(f)|$ extracted from the data in comparison to the TIPTOE response. Right: Experimental response corrected for the effects due to the holey mirror.

HCF. The achieved peak power of 0.26 TW sets a new milestone among laser systems in the SWIR region with a comparable repetition rate, see Fig. 4.17 for an overview. There, SWIR laser systems with a repetition rate from 1 to 100 kHz are compared to the presented system. To estimate the peak power of the systems, I assumed that 90 % of the pulse energy is confined in the main pulse of sech^2 shape and used Eq. (2.8), unless specified explicitly. Since a high peak power can be achieved in two ways, by boosting the pulse energy or by decreasing the pulse duration, the comparison of pulse duration to peak power reveals the technical approach. In particular, the combination of both high pulse energy and short pulses is unique for the presented system; only Ref. [56] achieves even shorter pulses with a peak power above 200 GW. The system there is a light-field synthesizer operating at one tenth of the repetition rate. There are other systems in the literature with lower repetition rate but high pulse energy, e.g. Refs. [233,234], and Ref. [235] as an example for the MIR.

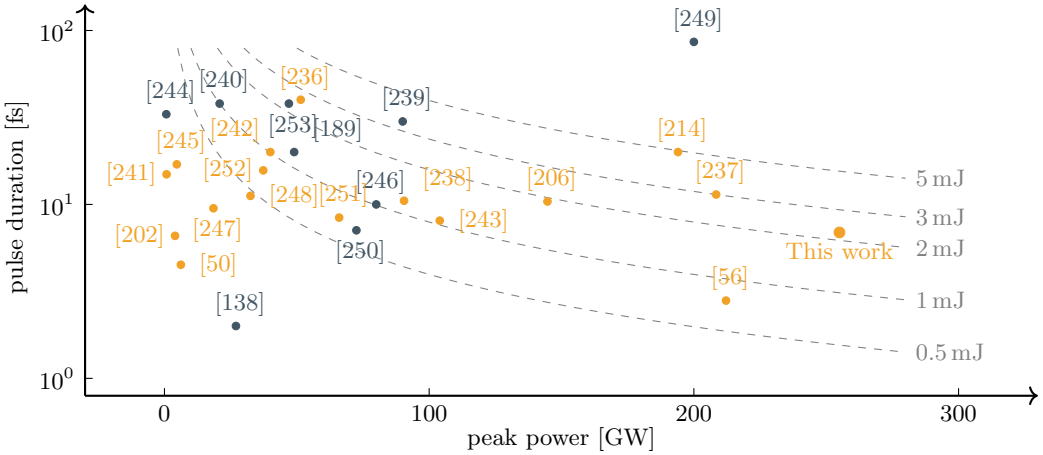

Figure 4.17: Overview of state-of-the-art laser systems in the SWIR region. Orange: CEP-stable systems, grey: not CEP-stable. The dashed lines indicate the pulse energy according to the given conversion law. For systems with a different peak power, however, they do not apply.

By self-compression in a fiber with carefully chosen parameters, the necessity of multi-octave spanning dispersive optics or light-field synthesis is avoided. Despite the freedom in waveform shaping such a synthesis system provides [5, Fig. 14 therein], the approach presented here is appealing due to its reduced complexity and competes in cases where the desired pulse form is close to the transform limited one. Here, single-cycle pulses of a duration of 6.9 fs are generated and compressed without any further dispersive mirrors required. Since a static pressure can be used, the presented scheme is suitable for outside vacuum applications, such as the single-shot CEP detection presented in Sec. 3.3. The system lacks polarization-dependent optics for the generation and compression of the supercontinuum, and therefore, the extension to arbitrarily polarized laser beams appears to

be straightforward. In particular, spectral broadening of radially or azimuthally polarized laser beams has been demonstrated [254], and the self-compressing method I presented would enable the generation of millijoule level single-cycle vector beams, if the parameters are adapted accordingly. Such beams open up new perspectives in the generation of strong magnetic impulses from ring-shaped electric currents induced by the laser [27,255]. However, their temporal compression has hitherto been hindered by the polarization sensitivity of dispersive mirrors. Even though there are concepts for dispersion independent chirped mirrors in certain wavelength regions [256], the bandwidth is still limited. Self-compression overcomes these limitations.

The demonstrated CEP stability is, to the best of my knowledge, the best value reported for a multi-millijoule single-cycle SWIR laser system; only sub-millijoule systems with better values have been reported, e.g. Refs. [56, 241, 257]. With a precision of 138 mrad, corresponding to a timing jitter of the waveform of 150 as, the laser system is an excellent driver for field resolved experiments. As first application profiting from that phase resolution, the TIPTOE response function is investigated. Owing to the multi-octave bandwidth of the generated supercontinuum, no second-harmonic generation (e.g., as discussed in Ref. [26,28]) for the observation of the $2f$ spectral components is required. Due to the modulations of the retrieved spectral amplitudes with the CEP of the driving pulses, an absolute phase calibration is possible. However, the sign of the wavefunction cannot be determined since the entire detection setup is symmetric for a change $E(t) \rightarrow -E(t)$.

The field-resolved data presented above not only characterize the output of the laser, but the remaining differences between the spectral amplitude and spectrometer data can entirely be explained by the spectral response amplitude and the geometry of the interferometer. In addition, this good agreement verifies the validity of the TIPTOE measurement, also regarding the underlying first-order approximation. If already second order corrections to the perturbation of the ion yield were required, enhanced spectral amplitudes at the sum and difference frequencies of the spectrum would be expected [26,31]. In such a case, the comparison of the spectral amplitudes with the spectrometer data would differ, therefore, the first-order approximation is valid.

The short nature of the laser pulses allows amplitude gating in HHG [4,5], and thanks to the high average power, the HHG process could be upscaled compared to related works using lower pulse energies in the SWIR range [56, 127, 193, 236, 239, 242, 248, 258]. I will study the technical challenges connected to the high average power in such experiments thoroughly and present solutions for some of them in Chapter 5.

Chapter 5

Characterization of an attosecond beamline

In this chapter, I will present a characterization of an attosecond beamline. The work here builds upon a first design of a beamline by Shubhadeep Biswas, Sambit Mitra, and Kilian Unterguggenberger. However, the general setup will be modified. In addition, several novel aspects are investigated, among them a UHV-compatible soft X-ray (SXR) spectrometer, which is an extension of an existing device developed in the group. The main focus of this chapter is the interferometric stabilization scheme of the beamline, which is subject of a pending patent by Blöchl et al. [259].

In the following, I will motivate the necessity of a high-power XUV-SXR beamline for attosecond science and comment on the difficulties arising from the demand for high energetic photons, the high average power, and the broadband spectrum in the XUV-SXR region. I finally present solutions for the power handling, interferometric stabilization of the delay line, and the XUV-SXR spectrometer. The latter has been designed with the aid of Andreas Küchler. The beamline is driven by the OPA output of the Horus system, as described in Sec. 4.3.1 and in Ref. [214].

5.1 Introduction

In the previous section, the demand for high-power phase-stable SWIR lasers for driving HHG was motivated. In brief, the scaling of the cut-off energy with λ^2 [60] allows for the generation of high-energetic radiation with sufficiently long-wavelength driving lasers. By doing so, a large bandwidth can be generated, demanding suitable detection, i.e., in form of broadband and precise spectrometers. Additionally, since the low conversion efficiency ($\propto \lambda^{-4}$ [66] to $\propto \lambda^{-6.5}$ [69]) is to be compensated with power and an increased interaction volume, problems arise. Especially the high peak and average power can cause issues regarding the damage threshold of the required components, e.g., the HHG gas target or filters. For the HHG gas target, the use of ceramic targets has emerged over the years and turned out to be among the best solutions in our lab.

Guiding the generated high-energy radiation to an experiment is challenging due to the low reflectivity of the available mirrors, which typically requires grazing incidence and a surface quality reaching the single nanometer level, see Fig. 5.1b). The usage of XUV multilayer mirrors is possible, but the reflectivity is limited especially for high energies [260].

In addition, filtering HHG from the driving laser requires more attention. Firstly, a high IR suppression of several orders of magnitude is desirable while ensuring a high XUV-SXR transmission. To this end, thin metal foils are used since they act as a high-pass filter. For high XUV-SXR transmission, however, the thickness of such foils typically has to be

below 500 nm. Therefore, such foils are very sensitive to both mechanical disturbances and high laser power. Especially the heat deposited on the foil can only dissipate through the material (no cooling gas in vacuum), which limits the power threshold even more. Moreover, some metals have lower heat conductivity than others (like Zr compared to Al, see Table 5.1c)) and thus, they cannot be simply interchanged when working close to the damage threshold.

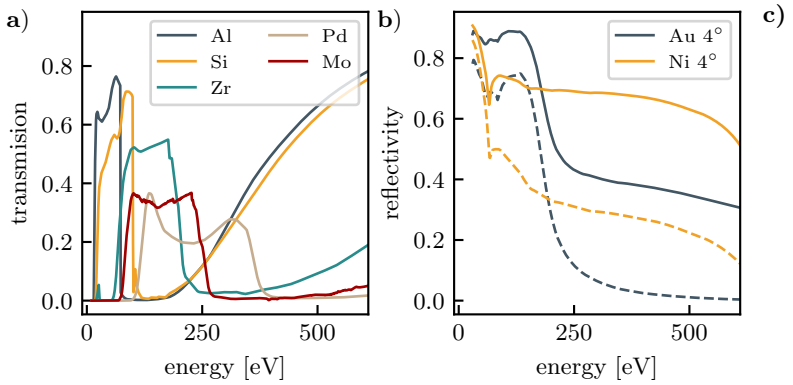

c)

species	κ [W/(cmK)]
Al	2.37 [261]
Mo	1.38 [261]
Si	1.48 [261]
Pd	0.718 [261]
Zr	0.227 [261]

Figure 5.1: a) XUV transmission through a 200 nm thick sample. Data retrieved from Ref. [262]. **b)** Reflectivity of solid mirrors for no roughness (solid) and 6 nm rms surface roughness at 4° grazing angle. Data retrieved from Ref. [262]. **c)** Thermal conductivity κ of selected elements at 300 K.

Secondly, these metal foils have very characteristic transmission curves, see Fig. 5.1a), which might be used to select certain spectral regions. However, they also represent a challenge in case there is no suitable material providing high transmission in the desired energy range. Thus, a broadband high-pass filter that transmits a large portion of the XUV-SXR is desirable.

Such high-pass filters exist for applications in the MIR to far-infrared region [263–265]. They are based on waveguide properties as discussed in Sec. 2.6. In detail, if the size of the waveguide reaches the wavelength, the attenuation increases according to Eq. (2.52), where the complex refractive index of the material is considered. Figure 5.2 shows an example for a Gold waveguide. In panel a), the transmission of a laser with 2.1 µm central wavelength through waveguides of different sizes is shown. A waveguide length of 10 µm is assumed. Clearly, if the waveguide is smaller than half of the wavelength, significant attenuation of the radiation is expected.

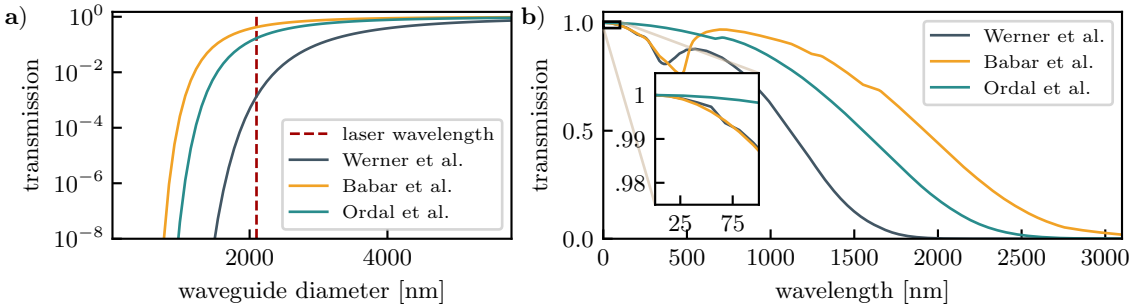

Figure 5.2: a) Transmission through a metal waveguide of different diameters for a central wavelength of 2.1 µm (dashed line). The refractive index data vary but generally reproduces the cutoff at around half of the wavelength. **b)** Transmission through a waveguide with radius 1 µm. The refractive index data are taken from Werner et al. [266], Babar et al. [267] and Ordal et al. [268].

On the other hand, the transmission through such a waveguide for very short wavelengths can still be high, as indicated in panel b) of Fig. 5.2. There, the transmission through a waveguide with a radius of 1 µm is shown. While the transmission in the in-

frared is significantly reduced, the XUV-SXR transmission, that is below 10 nm (see inset), is still close to unity and therefore much higher than that of metal foils (see Fig. 5.1).

As a consequence of beam sizes of the order of millimeters, such small waveguides have to be arranged in a regular pattern. On that ground, the XUV-SXR transmission is reduced according to the open area of the structure. However, the diffractive effects appearing due to the grating like arrangement need to be considered. At first, the diffraction of the IR increases its attenuation and also attenuates the IR beam if the waveguide size is larger than the wavelength. This is the working principle of the commercially available laser attenuators by Lasnix, as disclosed and investigated in Refs. [263, 264, 269]. The approach allows to design the desired IR attenuation carefully; however, it will be less than the values presented in Fig. 5.2a) for the case of waveguide sizes much smaller than the wavelength.

Additionally, such large waveguide arrangements can still be used as XUV filters, and the attenuation and diffraction effects on the XUV-SXR will be even less since the difference of the wavelength and the waveguide size is large, more than three orders of magnitude in this case. Similar approaches were proposed as diffractive XUV filters in Ref. [270] 55 years ago, where a tunable slit provides transmission characteristics similar to the waveguide presented in Fig. 5.2. XUV filters consisting of a microchannel plate have been used for the separation of IR and XUV-SXR in Refs. [271,272]. Microchannel plates share similar properties with the metallic waveguides discussed here, but they are made from lead glass and have the holey structure fabricated at an angle to their front face [273]. In the experiment, I could not demonstrate that a microchannel plate withstands the high average power of the laser, whereas the metal mesh filters did.

However, the occurrence of surface (plasmon) or Zenneck waves can lead to transmission through the mesh filter for wavelengths longer than the cut-off wavelength as propagating surface waves couple incident light to the backside of the metal mesh [263,264,274]. The corresponding inhomogeneities in the transmission curve, similar to Wood's anomalies [274, 275], must be considered.

Making use of such methods, the filter properties can not only be tuned, but the diffractive parts can be used for diagnostics without the insertion of any beamsplitter that introduces material dispersion and/or absorption of short wavelengths. This is the main motivation for using free-standing metal grids for filtering IR and XUV-SXR as they provide a reference beam. The importance of the reference is the typical time resolved experiment, which requires interferometric scanning of the delay between the XUV-SXR and another beam, usually derived from the driving laser via a Mach-Zehnder interferometer.

In addition to high-pass filters, spatial filter methods can be used, such as a pinhole that separates different spectral components based on the different divergence angles of the IR and the XUV/SXR. Such approaches have been employed since the beginning of attosecond science [62] and can now be used to reduce the power load on the filtering techniques described above.

5.2 General setup, interferometer and spectrometer

Summarizing the constraints described in the introduction, the beamline must provide solutions for power handling and proper filtering but also provide high XUV-SXR transmission. Starting with the latter, the consequence is that the number of optics in the short wavelength part of the beamline must be reduced to the bare minimum, that is a single focusing element, and its reflectivity must be enhanced. Since the reflectivity of typical mirror coatings, see Fig. 5.1b), is only high for grazing incidence, the XUV-SXR beampath can only be deflected by a few degrees. Consequently, toroidal or elliptical mirrors designed for such grazing angles must be used for focusing the short wavelength beam. The

drawback of such a setup is the low flexibility with the delay line: Attempts to split-off and recombine the driving laser after the HHG, e.g., as in Ref. [276], are hindered by the low deflection angle of the XUV. Therefore, the IR laser for the pump probe experiments has to be separated before HHG which extends the arm length of the interferometer by a significant amount.

In Fig. 5.3, the general setup of the XUV-SXR beamline is presented. In brief, the beamline is split into several UHV chambers, each of which fulfills a different task. The first one, the incoupling chamber, splits the driving laser beam (the OPA output of the HORUS laser, see Sec. 4.3.1) into a strong portion used for the HHG process and a weak portion that is from now on referred to as "bypass" (arm). The latter contains a telescope made from OAPs that contains a chopper near the focus for repetition rate reduction, which is equivalent to an amplitude modulation for future lock-in detection measurements. The chopper is mounted from the chamber wall and is therefore decoupled from the optical breadboards as those are vibrationally isolated by UHV edge-welded bellows. The strong portion is sent to the HHG chamber, generating HHs in a conversion cell made from Markor, see Fig. 5.6a), which can be backed with different gases at controlled pressures. All chambers are equipped with turbomolecular pumps. The small connectors between the chambers allow to reduce the pressure towards the experiment to below 1×10^{-8} mbar while the HHG chamber is at 1×10^{-3} mbar due to the high gas load of the target. The gas pressure is below 1×10^{-8} mbar in the HHG chamber and downstream when idle.

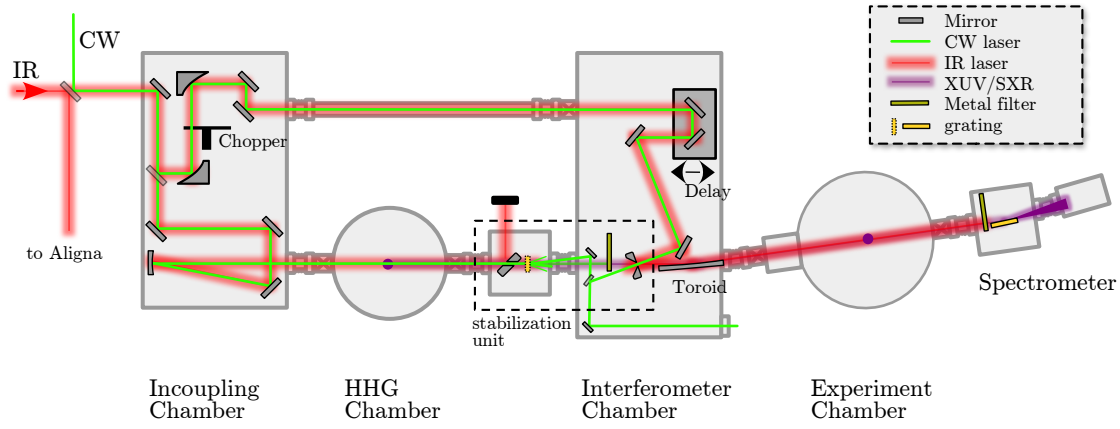

Figure 5.3: Sketch of the XUV-SXR beamline. Each chamber is equipped with a turbomolecular pump (not shown).

After HHG, the driving laser and the generated XUV and SXR radiation propagate towards the interferometer chamber, which is used for recombination of the bypass laser with the XUV-SXR. A variable temporal delay can be introduced via a piezo retroreflector in the bypass arm. Bypass beam and XUV-SXR are recombined, and the optical path is controlled in the stabilization unit, which additionally serves as filter unit for suppression of the driving IR laser, see below. Both the bypass laser beam and the attosecond pulses are sent via a toroidal mirror to the experimental chamber for ultrafast light-matter interaction studies and further downstream to an XUV-SXR spectrometer for characterization. Details on the spectrometer are presented below and in Appendix D.

The stabilization and filter unit is the core element for any subsequent time-resolved measurement. A detailed sketch can be found in Fig. 5.4. The incoming laser co-propagates with the generated XUV-SXR. The different divergence of both beams [5] is exploited in a first perforated mirror that spatially filters a significant portion of the driving IR laser. After the residual IR and the less divergent XUV/SXR are transmitted through the aperture, a metallic grating acts as filter element similar to that presented in the

introduction. The metal mesh is square shaped with a period of 51 µm as determined by the diffraction pattern of a CW laser. Its open area of 57 % corresponds to an XUV transmission that is comparable to a 200 nm Zr filter. Subsequent thin metal foils allow for additional contrast enhancement and spectral selection of the desired part of transmitted XUV/SXR light. By means of a second perforated mirror, it is collinearly recombined with the bypass arm laser beam. Note that a metal filter foil alone could not withstand the laser power, making the mesh filter a necessary component. A CW laser can be collinearly coupled into the beamline and serve as a reference.

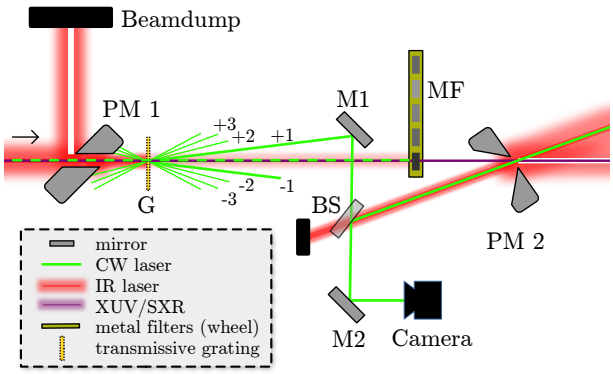

Figure 5.4: PM 1,2: perforated mirror 1,2; G: grating; M1,2: mirrors; BS: beamsplitter; the numbers $-3, \ldots, +3$ enumerate diffraction orders.

Overlapping one diffraction order of the grating with the leakage of the bypass arm beam through the perforated mirror forms a reference interferometer that allows for control of the optical path length difference between both arms of the interferometer. Since the interferometric distance between the XUV/SXR and the reference interferometer is small (few cm) compared to the size of the total interferometer (several meters of arm length), the reference is measuring the stability of the main interferometer in good approximation. A detailed presentation of the principle and achievable performance as well as a discussion of bottlenecks and capabilities is presented below in Section 5.4.

The characterization of the generated HHs requires a spectrometer capable of resolving the full bandwidth while being compatible with the UHV environment. Basic development of such a device has been performed by Kilian Unterguggenberger in his BSc thesis [277], Shubhadeep Biswas and Sambit Mitra. Their first prototype was capable of measuring HH spectra in a limited range, since the detector was fixed and could therefore not resolve the complete signal range. Thus, a technical development that allows to scan the detector under UHV conditions is required. With the help of the MPQ technician Andreas Küchler, I developed such a UHV compatible spectrometer with a variable detector based on the previous design. A 3D view of the device can be found in Fig. 5.5, and a more detailed sketch with a description of the individual components is presented in Appendix D. There, more information on the resolution, wavelength calibration and software is presented. The spectrometer is used for characterization of the generated HHs as presented in the next section.

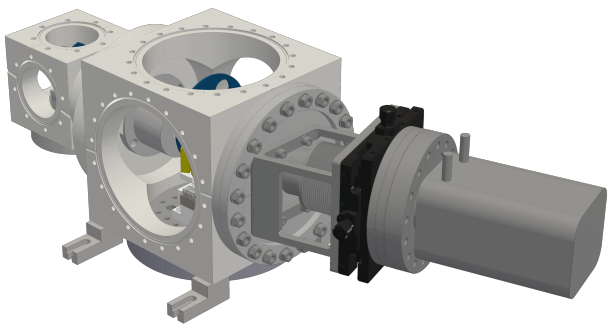

Figure 5.5: 3D view of the XUV spectrometer. The setup is entirely UHV compatible. The core element is the movable detector that travels across the entire image plane while being under UHV conditions.

5.3 High-harmonic generation

For the generation of HH with more than 35 W of average power, gas conversion cells made from Markor are used, see Fig. 5.6a). The cell is backed with 10 to 100 mbar of Argon for initial tests. The corresponding XUV beamprofile at the exit of the beamline is shown in Fig. 5.6b). It is taken with the spectrometer camera after the grating is replaced by a plane gold-coated mirror. The round aperture is caused by the perforated mirrors, whereas the fine linear sub-structures in the beam are caused by the metal mesh filter.

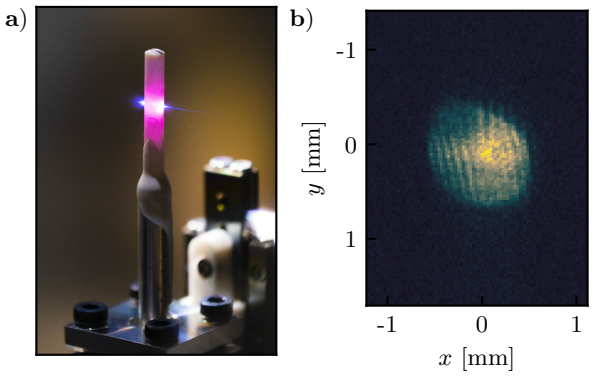

Figure 5.6: **a)** HHG conversion cell filled with Argon driven by the SWIR laser. **b)** XUV beamprofile measured with the spectrometer camera.

The spectral data of the HH generated are shown in Fig. 5.7. For calibration, characteristic features of Zr, Pd and Mo filters are used to determine wavelength reference points to which the grating equation can be fitted [277], see Appendix D. The observed cut-off is in the region where the transmission through the Zr filter and over the gold coated toroidal mirror drops significantly but reaches 200 eV in Argon. The incident intensity on the HHG target is reduced with a 56% transmission filter (Lasnix Mod. 102-C option 2.5-3.6-4.3-5-10 dB) for best conversion efficiency. Scaling for even higher cut-off energies with higher ionization potential gases, such as Neon or Helium, is therefore possible since the intensity can be increased without decreasing the focal volume.

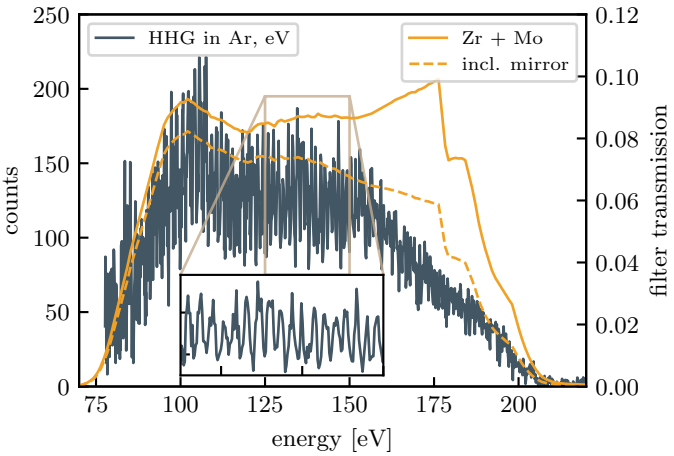

Figure 5.7: XUV spectrum of HH after passing through a 500 nm Zr and 150 nm Mo filter. The filter curves do not include the grating efficiency.

To determine the focal size, a knife edge is scanned through the focus at the experimental site. Assuming a Gaussian beamprofile of the XUV in the focus defined by Eq. 2.9, and an infinitely sharp edge, the resulting signal can be modeled as

$$S(x_0) = \int_{-\infty}^{\infty} \mathrm{d}y \int_{-\infty}^{x_0} \mathrm{d}x I_0 \exp\left(-\frac{2(x^2+y^2)}{w_0^2}\right) \tag{5.1}$$

$$= I_0 \frac{w_0^2 \pi}{4} \left[\mathrm{erf}\left(\frac{\sqrt{2}}{w_0} x_0\right) + 1\right]. \tag{5.2}$$

A least-squares fit to the experimental data, see Fig. 5.8 taken at different positions along the propagation direction yields a beam waist of $w_0 = 42\,\mu\text{m}$.

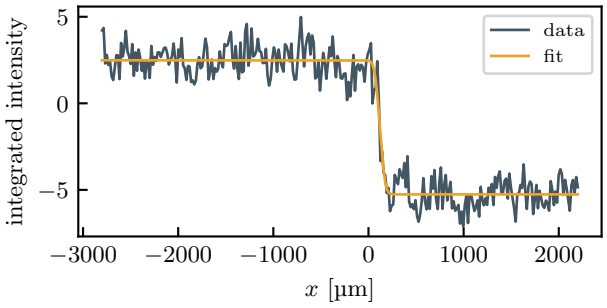

Figure 5.8: Knife edge measurement and fit yielding an XUV beam waist of 42 µm.

5.4 Characterization of the interferometric stability

For precision experiments aiming to resolve shortest timescales, the interferometric stability is the key parameter for their success. There are three main aspects characterizing the novel stabilization approach: First, the passive stability in a free-running scenario without active stabilization of the optical path length for both the reference and the SWIR beam path; second, the stability of the actively stabilized interferometer, both in an in-loop and out-of-loop measurement; and third, the correlation between the in and out-of-loop measurement. All of them are investigated and quantized in this section after an introduction of the detection scheme in general.

5.4.1 Optical setup of the detection scheme

To characterize the interferometric stability of the main interferometer, the SWIR laser beam after the toroidal mirror is detected in an out-of-loop measurement. The interference pattern is shown in Fig. 5.9a). For its detection, the recombination mirror (PM 2 in Fig. 5.4) is slightly tilted to generate a stripe-like pattern instead of a perfectly concentered one. Since the detected wavelength lies far outside the silicon detection range, a microbolometer camera (Swiss Terahertz Rigi) has to be used. Its automatic shutter moves every 300 s such that data for around one second has to be removed for every shutter event from the long-term scans.

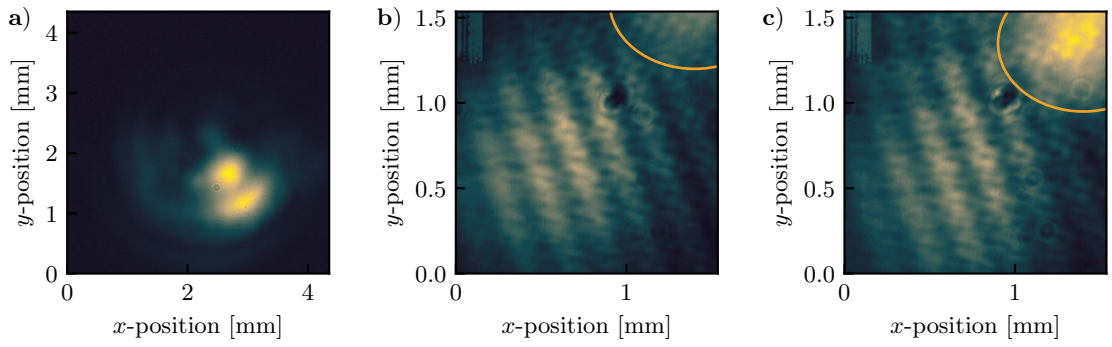

Figure 5.9: **a)** Interference pattern of the SWIR laser beam measured after the toroidal mirror. **b)** Interference pattern of the CW laser. The marked spot shows the position of the SWIR laser beam coming from the bypass arm. **c)** Interference pattern as in b) after the measurement. The position of the SWIR beam has drifted. The delay value is not the same and thus the interference pattern is not expected to be similar in b) and c).

The in-loop camera is used for the generation of the feedback signal to the actuator and placed as indicated in Fig. 5.4. For generation of the interference pattern, a stabilized CW

laser diode with long coherence length (LD-PD INC PL-LN-1064-B-A81-PA) with 1 MHz linewidth at 1064 nm wavelength is coupled into the interferometer and co-propagates to the pulsed SWIR beam. The fringe pattern (Fig. 5.9b)) is detected on a silicon camera (IDS Imaging UI122xLE). The beamsplitter (BS in Fig. 5.4) is again slightly tilted to generate several interference fringes.

Both cameras allow to select a region of interest, which is set to 256×256 pixels to profit from the performance of a fast Fourier transform (FFT) algorithm (FFTW [278]). The latter comes into play for the real-time analysis of the data. Each image retrieved from the camera is Fourier-transformed for the extraction of the delay, as described in Sec. 2.7. Extraction of the phase at the spatial frequency corresponding to the fringe pattern yields the relative optical path of the beam in radians of the central wavelength. It is beneficial to have more than two full periods of the interference fringes such that their spatial frequency is well-defined and not a broad range. In fact, if there is less than one period of the fringes, the spatial frequency of interest in Fourier space might change with delay making this method inapplicable. Nevertheless, this approach is more robust than the detection of the intensity of the interference pattern at a single point in space with a photodiode, since it can detect the phase in a $[0; 2\pi]$ interval and is insensitive to amplitude changes since they don't influence the phase value.

On the other hand, similar to a photodiode, the beam position on the sensor does influence the detected phase, such that pointing instabilities couple to detected phase value and therefore to the optical path length. This property is particularly important for long-term stability measurements, since in the experiment, the relative position between the CW and the SWIR laser is suspect to drifts, as apparent when comparing the beam position (Fig. 5.9) before and after the measurements presented below in Fig. 5.11. The SWIR beam exhibits a drift of a few hundred microns over a period of several hours. Such a drift can be perpendicular to the plane the interferometer arms define, such that it does not affect the optical path length in the same amount. However, if it is an angular drift or within the plane of the interferometer, a change of the optical path length is expected.

The origin of the drift is most likely a thermal one since the amount of movement is close to the expected value for a thermal wedge in the incoupling setup before the vacuum chambers, but after the beamstabilization detectors. There, the beam with diameter 15 mm propagates for around 20 cm in a closed box of 10 cm in height. Assuming that the box heats up to 25 °C on the top side, whereas the bottom side is at 22 °C, a deflection of the beam of 4.5×10^{-5} rad towards the downside direction can be estimated. Here, the temperature dependence of the refractive index of humid air from Ref. [279] entered and a temperature difference from the lower side of the beam to the upper one of 0.6 K is assumed. After a propagation of 4 m, which is roughly the distance to the camera, a beam position change of 184 µm is expected. The refractive index for warm air is lower than for cold one [279], therefore, a deflection to the upwards direction is expected. However, the telescope in the bypass arm flips this to a downwards direction. Note that even though an angular change by the air wedge is expected, it basically appears as positional translation due to the small angle and the large distance. Another possible reason is a drift of the OPA alignment, which can change the beamprofile of the SWIR output and therefore its center of mass. The beam stabilization system, on the other hand, regulates on the center of mass and thus the beam position can shift if the beamprofile changes its shape.

5.4.2 Feedback signal generation

For the generation of a feedback signal, a software PID control is implemented. It compares the retrieved phase value ϕ with a setpoint ϕ_{set} and calculates the feedback f to the piezo

controller via the well-known relation

$$f = k_\mathrm{p} \cdot m_\mathrm{p} + k_\mathrm{i} \cdot m_\mathrm{i} + k_\mathrm{d} \cdot m_\mathrm{p}, \tag{5.3}$$

where p, i and d denote the proportional, integral and derivative contribution, respectively. The k parameters describe the behavior of the regulation loop and need to be adapted once. The m values, on the other hand, are calculated for each newly retrieved phase value ϕ_l for the l-th regulation cycle according to the following expressions, where $\Delta\phi_l = \phi_\mathrm{set} - \phi_l$ denotes the current regulation error:

$$m_\mathrm{p} = \Delta\phi_l, \tag{5.4}$$

$$m_\mathrm{i} = \sum_{j=l-N}^{l} \Delta\phi_j \cdot \mathrm{d}t_j, \tag{5.5}$$

$$m_\mathrm{d} = (\Delta\phi_l - \Delta\phi_{l-1}) \,/\, \mathrm{d}t_l, \tag{5.6}$$

where N is the number of previous phase values to take into account in the integral part, $\mathrm{d}t_l = t_l - t_{l-1}$ is the time interval. To prevent phase jumps larger than 2π, the maximum value of $|f|$ is restricted such that the piezo driver does not perform a sudden movement that cannot be tracked.

Potential limitations on the maximum regulation frequency arise from several aspects: Firstly, the mechanical eigenfrequency of the piezo-driven retroreflector, which depends on the mass of the assembly; secondly, the capacitance of the piezo actor and the maximum current of the power supply; thirdly, the speed of the interface to the power supply; fourthly, the frame rate of the camera; and finally, the speed of the software routine.

The latter is benchmarked with pre-defined image data and a feedback to the device by a simple function call, not waiting for any response from the device. A cycle time of $\approx 150\,\mu\mathrm{s}$ is easily possible using an image size of 256×256 pixels, corresponding to more than 6 kHz regulation frequency. This time interval basically covers the time needed for the FFT, phase extraction and calculation of the error signal according to Eq. (5.3). Thus, the software part is comparatively fast.

The frame rate of the camera depends on various settings, such as the exposure time or the region of interest. This limits the regulation speed to more than 10 ms, since the camera could not be operated faster at sufficient signal level.

The serial interface to the piezo controller, supporting only up to 19200 Baud (and a minimum command length of 13 characters), does not allow any communication faster than ≈ 0.8 ms. The internal processing in the device (Piezosystem EDA 4) could not even process the commands at that speed, such that an additional delay had to be added to the regulation loop.

The mechanical properties of the piezo mirror (128 g for the mirror mount, 2 mirrors with 19 g each [280]) influence the unloaded resonance frequency of the piezo (295 Hz [281]) such that it is reduced finally. In addition, the capacitance of the piezo (13.6 µF [281]) limits the maximum frequency since the current the power supply can provide is limited to 40 mA. As an example, for a voltage step of 5 V, the frequency is limited to roughly 150 Hz.

The frame rate of the camera, the piezo driver, and the communication in combination, limit the maximum cycle time to a bit less than $\bar{\mathrm{d}t} \approx 19$ ms, corresponding to a regulation frequency $f_\mathrm{reg} = 1/\bar{\mathrm{d}t} \approx 53$ Hz. Since the mechanical limitations of the piezo are less than one order of magnitude larger, this regulation frequency is close to the maximum possible. Enhancing the regulation speed is possible regarding the camera speed, but more complicated measures are required for the mechanical properties of the piezo and its control. To speed up the piezo response, both its capacitance and the weight of the

attached mirror setup have to be reduced. A reduction in capacitance transfers to a lower travel range (currently 400 µm), where 200 µm with an actor of the series would have 2.5 µF and a resonance frequency of 625 Hz [281], thus a factor of two to five improvement. In addition, a more powerful power supply would improve the dynamic capabilities by the maximum current it can provide. However, with the setup presented here, a voltage step of 2 mV (from 150 V) in total could be clearly detected, thus the noise level of the power supply is crucial. High-current power supplies are noisier in general; therefore, the choice is a trade-off between speed and precision. The noise level of the device used is 0.3 mV [282], which corresponds to 1.6 nm precision and is therefore not yet a limitation.

5.4.3 Benchmarking of the stabilization performance

The stability of the interferometer is founded on passive stability by the design of the setup and on active stabilization via fast detection and feedback to the delay line. The design of the setup with isolated optical breadboards in all chambers reduces vibrations from pumps or the optical copper since they are mounted to the vacuum chamber itself. The chambers are decoupled and stand on separate metal frames on the floor without any mechanical contact to the optical setup except via the edge welded bellows required for keeping the vacuum.

In the following, I focus on the active stabilization and compare it to the free-running case without stabilization. In all measurements, the CW laser (used as in-loop feedback if needed) and an out-of-loop reference measurement with the pulsed SWIR laser are detected. The SWIR laser is sent into the beamline at full power (≈ 40 W). In Fig. 5.10a), the open-loop measurement (i.e., without feedback from the CW measurement applied to the delay line) is presented, revealing two main characteristics: Firstly, both the in- and out-of-loop evolution of the interferometer shows a correlated drift of the absolute position x_{abs} of the order of a few microns. Although this drift might seem small, it corresponds to a drift of the delay line of nearly 7 fs, which is the duration of an optical cycle of the SWIR laser. Secondly, the in- and out-of-loop measurements drift with respect to each other, as shown in Fig. 5.10b). The relative drift Δx is strongest at the beginning of the measurement, where possible thermalization processes take place. After this initial warm-up phase, the drift between in- and out-of-loop measurement is smaller, as confirmed below.

When stabilizing the interferometer, see Fig. 5.10c), the in-loop stability is 5.53 nm and the out-of-loop stability amounts to 11.75 nm on a one-minute time scale. Without the feedback loop, the stability is worse even on such short time scales, see Fig. 5.10d), which yields standard deviations of 21.63 and 28.19 nm for the in- and out-of-loop measurement, respectively. The stabilized precision in timing jitter is thus 18.4 as in-loop and 39.2 as out-of-loop.

To demonstrate the capabilities of the stabilization scheme in long-term stabilization, the interference fringes are detected and stabilized over a time of 4 h after the initial warm-up phase, see Fig. 5.11. The achieved in-loop stability is 5.58 nm, which is similar to the short-term stability and confirms that the stabilization scheme does not suffer from any restrictions on the measurement time. The out-of-loop measurement exhibits a standard deviation of 85.01 nm, slightly larger than shown above for a short interval of time. The reason for this difference is the continuing drift between in- and out-of-loop measurement, which was identified above and is caused by a positional movement of the SWIR laser, see Fig. 5.9. The regulation speed of the in-loop stabilization is 18.6 ms per cycle, whereas the out-of-loop measurement cycle takes 20.0 ms. The latter is slower due to camera limitations, even though no communication to a piezo hindered the speed.

Until now, all data relies on the assumption that the in- and out-of-loop measurements both detect the very same drift of the optical path length. To confirm that both measure-

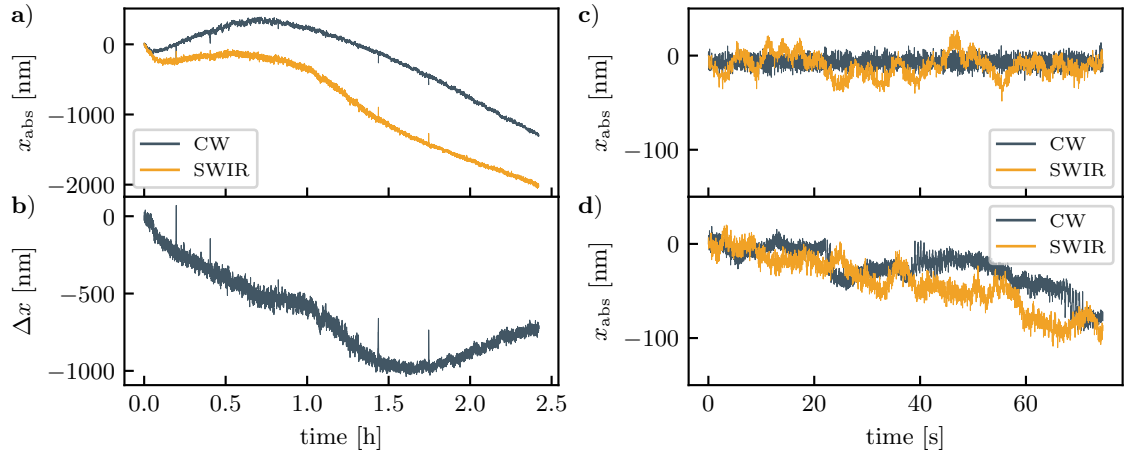

Figure 5.10: **a)** Free-running interferometer evolution. **b)** The in- and out-of-loop measurement drift relative to each other by up to 1 µm. **c)** Short-term closed-loop stability in an in- (CW) and out-of-loop (SWIR) measurement. The in-loop stability is 5.53 nm in contrast to 11.75 nm out-of-loop. **d)** Free-running scenario, the standard deviations are 21.63 nm and 28.19 nm for the CW and SWIR signal, respectively.

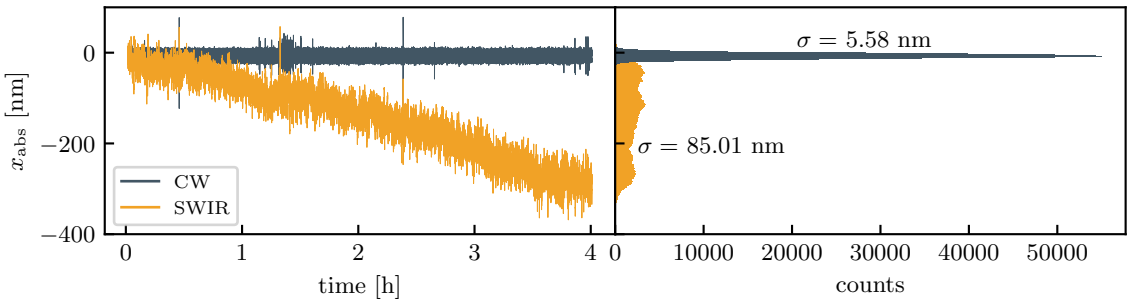

Figure 5.11: Long-term measurement of the interferometric stability. The in-loop standard deviation is 5.58 nm, corresponding to 19 as, whereas the out-of-loop measurement yields 85.01 nm. Here, a slow drift is present.

ments are indeed detecting the same quantity, the set point of the in-loop stabilization is scanned, and the correlation between both detection sites is investigated, yielding a measure for the dynamic response of the stabilization. As shown in Fig. 5.12a), both the in- and out-of-loop measurements follow the set point decently. Even larger steps in the set point are adequately reproduced, yielding an overall correlation of 0.999. In all cases, the deviation between the in-loop and out-of-loop measurement is smaller than 100 nm, see Fig. 5.12b). The residual differences are founded in the detection of the SWIR laser as the number of detected fringes is low, and therefore the FFT detection scheme operates at the edge of its possibilities. Additionally, the coherence length of the SWIR source is only of the order of $5 - 10\,\mu m$ and therefore the fringe contrast varies with delay. Fortunately, both restrictions do not apply to the CW measurement. Thus, having a better out-of-loop detection could yield higher short-term and dynamic stability. Nonetheless, the long-term drift would still be present.

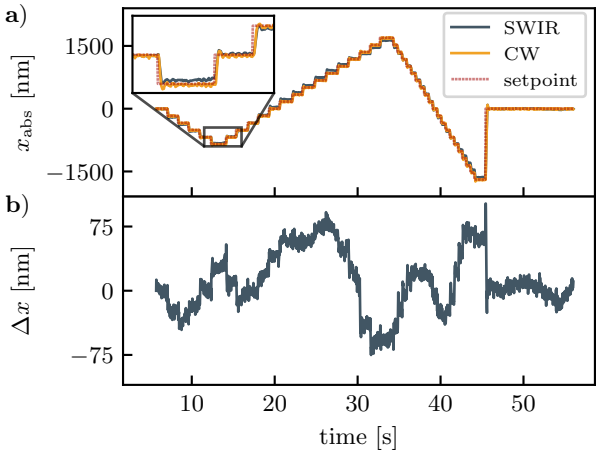

Figure 5.12: **a)** Scanning the set-point of the optical path length demonstrates dynamic performance of the stabilization. **b)** The detected difference between the in- and out-of-loop measurement is always smaller than 100 nm.

5.5 Discussion and conclusion

Since the advent of attosecond science, the interferometric stability of interferometric attosecond experiments has been the key for highest precision [5–7, 283]. Attosecond beamlines, where such experiments are conducted, typically follow one of two major interferometer schemes: The first kind is a collinear interferometer, using either a segmented mirror following the HHG, where different coatings reflect the XUV or the driving laser [190, 284–290], or using time plates [291]. The other common method is a Mach-Zehnder-interferometer, where a part of the driving laser is split of before or after the HHG and then recombined [258, 276, 292–311]. While the first method profits from compactness and the stability related to the small setup, it suffers from a severe drawback: the reflection of XUV or even SXR radiation under a small angle of incidence (i.e., a large grazing angle). There, the reflectivity drops drastically for high energy photons. Even specialized dielectric coatings can only reach the water window energies under grazing incidence [260], which complicates the interferometric setup.

Figure 5.13 compares related attosecond beamlines regarding their interferometric stability as well as average power to the achieved values of 18.4 as in-loop and 39.2 as out-of-loop and the average power of 40 W. The achieved stability in the out-of-loop measurement is among the best values reported. Most references, however, only specify the in-loop stability of their interferometers, where the stabilization scheme can definitely compete, even though there are systems with better stability - but at much lower average power. In particular, Refs. [309, 310] achieve very good values. Ref. [309] employs a comparable detection scheme with a camera, but their filter consists of a metal-foil mounted on a fused

silica substrate. The in-loop data there yields 13 as precision, whereas the fast out-of-loop data results in 50 as up to a kilohertz scale [309]. Ref. [310] achieves a resolution of 13 as as well; however, the rms value is taken over a moving window of 1000 points (1.4 min), such that the long-term drifts of up to 10 fs were not accounted for. Interestingly, Wanie et al. [310] observe a correlation between the slow drift of the interferometer and the ambient temperature. In particular, they found that a temperature drift within 0.6 °C is directly related to the total drift of 10 fs of the interferometer. This finding can also be transferred to the observations made above, where a comparable amount of long-term drift was discovered.

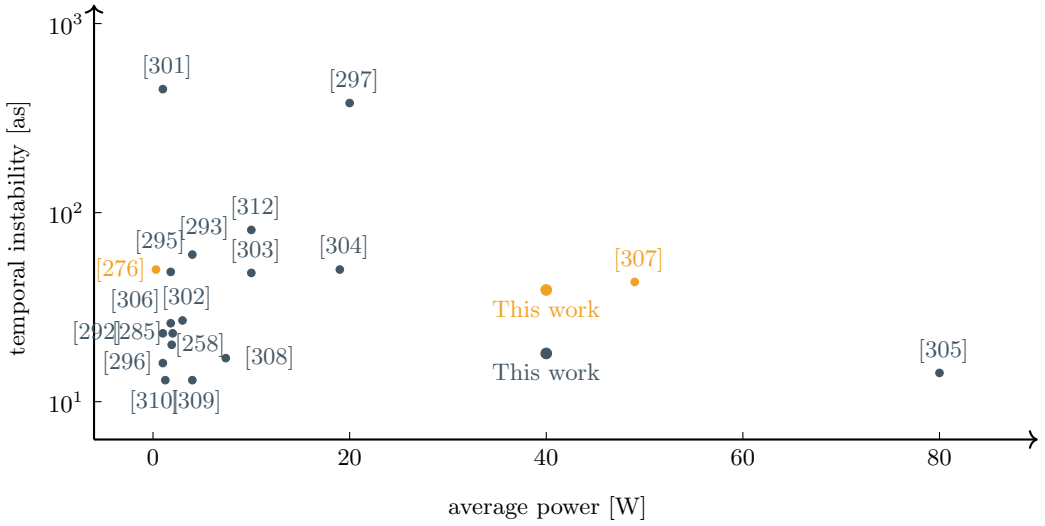

Figure 5.13: Overview of the performance of state-of-the-art beamline stabilization schemes. All except the yellow dots are in-loop measurements.

There are only few beamlines operated with more than 20 W of average power, along with the work presented here, there is a 100 kHz, 80 W system at ELI ALPS (Ref. [305]) and one by a group from Heidelberg using a 49 kHz, 1 mJ system [307]. Both works use a holey mirror in combination with a metallic foil as IR filter technique. The combination of high average power and high stability represents a major challenge since the high average power obstructs the compactness of the setup and, therefore, the passive stability. In addition, the design for high cut-off energies prevents the use of retro-reflecting segmented mirrors for the time-delay scan. Thus, increasingly large setups are required. With a total arm length of around 2.4 m, the presented interferometer is kept as compact as possible while preventing damage to optics subsequent to HHG. Increasing the size could reduce the power load at the metal filters, a major problem in the experiment, since the divergence of driving laser and XUV-SXR is different [5]. At a larger distance, the power content of the IR within the beam size of the XUV-SXR drops. This scaling law is a potential explanation for why the metallic filter technique is sufficient for other groups [305, 307].

The stabilization scheme implemented in the presented apparatus captivates with the entirely collinear CW laser for stabilization, which measures the exact optical beam path of the IR laser. The concept of using an infrared high-pass filter that acts as filter for the short-wavelengths generated and provides the reference for the interferometric stabilization has, to the best of my knowledge, not yet been reported in the literature. Such filter elements have a very high damage threshold, up to 200 W in CW or a fluence of 20 J/cm^2 [313]. In addition, following discussions with F. Keilmann, several metal meshes can be stacked with aligned patterns, such that the diffractive effects attenuating the IR increase, whereas the XUV transmission, which is proportional to the open area, stays the same. This scaling is to some extent equivalent to extending the length of the waveguide, which

increases its attenuation. However, diffractive effects can be enhanced for a multi-grating stack. Thus, the contrast of the filter technique can be controlled and enhanced. Even if the IR transmission is reduced so much that not even the diffraction orders have enough energy for forming the reference interferometer, the back-reflection of the very first element can still be used.

A limiting factor for SXR attosecond beamlines is the reflectivity of the toroidal mirror and the accompanying spectral selection. Since its only purpose is focusing the XUV-SXR, it can be replaced by novel approaches, such as XUV metalenses [314]. Such devices exploit vacuum guiding, i.e., waveguide effects of small structures. However, since the refractive index of the material is smaller than unity for short wavelengths, such devices effectively act as a high-index waveguide in a low-index substrate. A combination of the focusing properties of such a Fresnel-like lens with the filter properties of the metal mesh filters discussed here would thus not only solve the filtering problem but also eliminate the need for a toroidal mirror.

In addition, the XUV-SXR divergence can be manipulated with multi grating stacks. As an example, a collimator setup can be found that limits diffractive effects of the XUV and creates a strong angle dependence, such that only rays parallel to the optical axis transmit [315].

The generation of isolated attosecond pulses, that is, a single HH emission event per laser pulse, is crucial for time-resolved spectroscopy. In the last decades various methods, referred to as gating techniques, have been introduced [5]. The most prominent ones are amplitude gating [63], polarization gating [316, 317] and its variants [286, 318, 319], or ionization gating [320].

For amplitude gating, the different field strengths of neighboring half-cycles in a (near) single-cycle pulse imprint on the energy of the emitted photon, and therefore, highest energies are only emitted for the strongest half-cycle [63]. The cutoff is thus isolated in time, provided that the pulses are short enough for a broad cutoff. The required short pulse duration can only be provided by the frequency broadened HORUS, as presented in Chapter 4. Thus, a combination of both of the single-cycle pulses and the presented beamline promises to become a unique XUV-SXR table-top source with isolated attosecond pulses.

Polarization gating, on the other hand, is a temporal gating technique that makes use of the strong reduction of the recombination probability of an electron with increasing ellipticity of the laser field [316, 321, 322]. Thus, temporally-shaped laser fields that have a time-dependent ellipticity can confine the recombination process, thus HH emission, to a sub-cycle time interval. Consequently, an isolated attosecond pulse can be emitted. In particular, for harmonic emission, the ellipticity ϵ has to be below $\epsilon = 0.2$ for Ti:Sa laser systems [286], but even below 0.1 for long wavelength drivers due to the longer excursion time of the electron [323]. The generation of such polarization states typically consists of a time plate and a quarter-wave plate [316, 317], which result in a time-dependent ellipticity [324]. Its implementation seems straightforward, but since the leading and the trailing edge of the pulse are not contributing to the HHG, the available pulse energy for conversion is less than for amplitude gating where the same pulse energy is confined in a shorter pulse.

Chapter 6

Conclusion and perspective

In summary, I have demonstrated cutting-edge techniques pushing the three main aspects of modern attosecond metrology: the control and manipulation of both light-fields and charge-carriers, and the stability of delay lines in time-resolved experiments. Petahertz electronics-based techniques in the gas hereby serve as carrier-envelope phase diagnostics. Solitons in hollow-core fibers have shown their outstanding properties in ultrashort pulse compression and demonstrated sub-cycle electron control. The stabilization approach integrated into the attosecond beamline offers new possibilities for high-power driven table-top extreme ultraviolet and soft X-ray sources. These three key elements form a basis for future high-precision time-resolved spectroscopy.

In detail, I demonstrated that laser-induced currents in the gas phase enable single-shot tagging of the CEP with long-term stability and good precision. The performance of the petahertz electronics device is found to be best in a confined intensity region around the point of saturation of ionization. The saturation initially boosts the net momentum imprinted on the free charges, but this effect is counteracted by the spatial intensity profile resulting in a confined intensity region of a net boost in signal. The presented method is a direct competitor to the spectral interference phasemeter and to the stereo-ATI phasemeter and can replace the latter regarding the required pulse energy and achievable precision. Compared to other developments in petahertz electronics, the presented scheme requires more pulse energy due to the lack of local field enhancement but comes with a vast wavelength independence of the detector setup.

The spectral broadening of the Horus based on a higher-order soliton in a hollow waveguide generated single-cycle pulses at a high repetition rate with more than 2 mJ pulse energy. Its peak power of 0.26 TW makes it the most intense light source of its class, accompanied by an outstanding CEP and power stability. Therefore, the light source is an excellent driver for strong field experiments like HHG. As first application of the waveform stability, the CEP-dependent spectral response of Tiptoe was investigated. The characteristic amplitude modulations in the spectrum at the second harmonic of the fundamental frequency could be resolved owing to the large spectral bandwidth. In particular, the data revealed that the waveform change with CEP alters the ionization dynamics by confining the ionization event to either one predominant half-cycle or to several of them. Thus, the detectable spectral bandwidth varied and an in-situ absolute CEP calibration was possible, up to the pre-sign of the waveform.

The characterization of the attosecond beamline, especially regarding the stability of the delay line, showed that a highly stable and yet high average power and high pulse energy driven setup is feasible. Decent stability values could be achieved grace to the filter mesh that provides both IR attenuation and separation from the XUV. By exploiting the wavelength dependence of the propagation through the metal mesh, a reference can be split off without diffracting the XUV transmission. The achieved stability is competitive

with others, especially for systems with comparable average power. The detection of the phase of the interference pattern of the stabilization emerged as robust and versatile, whereas the mechanical properties limited the dynamic capabilities of the stabilization loop. The generated HHs were characterized with an in-house developed spectrometer and the harmonic comb was observed, confirming that the resolution and bandwidth of the device are high enough (below 0.25 eV) and that the presented imaging conditions of the grating are fulfilled. The cut-off energies in Argon exceed 200 eV (6.2 nm), confirming that the approach using a SWIR driving laser is fruitful.

Future combination of the presented CEP detection scheme, the soliton propagation-based spectral broadening scheme and the high-power XUV-SXR beamline promises to be an excellent experimental apparatus for attosecond science. It offers accurate control over the waveform, provides high peak intensity, is well characterized, and thus forms an ideal basis for possible experiments ranging from transient absorption spectroscopy [325, 326], ultrafast magnetism [327], time-resolved photoelectron spectroscopy [5], nanoplasmonics [17], attosecond transient reflection spectroscopy [328], and many others [329]. The generation of attosecond pulses with solitons was demonstrated recently using a combination of fiber and gas target HHG [330] as well as the same approach in addition to a fully fiber-based one [331]. With the parameters of the laser source presented here, such combination seems thus promising in pushing the flux of the generated high-energy radiation. The single-cycle pulses provided by the self-compressing broadening scheme enable the manipulation of charge carrier dynamics on sub-cycle timescales, as demonstrated by the observed CEP effects. Other experiments, such as HHG, can profit from this precision as well, e.g., for amplitude gating [63]. The novel stabilization scheme for the attosecond beamline impresses with its excellent power-handling capabilities and long-term precision. It promises further scalability, e.g., to higher repetition rates and thus a higher thermal load.

An extension of the spectral coverage of the entire system towards the UV is possible when launching resonant dispersive waves in fibers [41, 42, 51]. The large driving pulse energy would allow the generation of a powerful UV source and to close the spectral gap between the supercontinuum generated from 750 nm to 3 µm and the harmonics in the XUV. Potential scalability of the cut-off energies to the water window and beyond is possible with different gas types, such as Neon or Helium [1, 65]. Other groups have shown that, for the driving wavelength used here, cut-off energies as high as 700 eV (1.8 nm) are possible [1, 332]. Thus, the presented methods would constitute a tunable supercontinuum source spanning a frequency range starting from 0.1 PHz (3 µm) towards more than 160 PHz (1.9 nm), therefore, a spectral coverage exceeding 3 orders of magnitude at petahertz frequencies.

The self-compressing broadening scheme allows for the temporal compression of arbitrarily polarized laser pulses, such as vortex beams. The high peak power approaches the relativistic limit at a high repetition rate and promises to become a successful candidate in the generation of tesla-scale magnetic fields via laser-induced ring currents in plasmas [27, 333]

The simplicity and wavelength independence of the presented phasemeter make it an ideal CEP tagging tool for future coincidence measurements, as desired in (atto-) COLTRIMS measurements [146, 293, 334, 335]. It is especially useful for facilities operating at various central wavelengths or with tunable systems, guaranteeing single-shot CEP over a wide range.

Appendix A

Mathematical helpers

A.1 Relation between pulse energy and peak power

Different pulse shapes in time alter the conversion from pulse energy to peak power, and therefore the conversion to intensity, knowing the focal profile. Here, the two most common cases are considered, Gaussian and sech^2 temporal beam profiles.

sech^2 pulse in time First, if the laser pulse is described by a sech^2 power profile, expressed via the FWHM pulse duration, the profile reads

$$P(t) = P_0 \mathrm{sech}^2\left(2\ln(\sqrt{2}+1)\frac{t}{\tau_{\mathrm{fwhm}}}\right). \tag{A.1}$$

If $t = \tau_{\mathrm{fwhm}}/2$, $\mathrm{sech}^2(\ln(\sqrt{2}+1)) \approx \mathrm{sech}^2(0.88) \approx 0.5$. The pulse energy then reads

$$\mathcal{E} = \int_{\mathbb{R}} P(t)\,\mathrm{d}t = P_0 \int_{\mathbb{R}} \mathrm{sech}^2\left(2\ln(\sqrt{2}+1)\frac{t}{\tau_{\mathrm{fwhm}}}\right)\mathrm{d}t \tag{A.2}$$

$$\overset{t'=2\ln(\sqrt{2}+1)\frac{t}{\tau_{\mathrm{fwhm}}}}{=} P_0 \frac{\tau_{\mathrm{fwhm}}}{2\ln(\sqrt{2}+1)} \int_{\mathbb{R}} \mathrm{sech}^2(t')\,\mathrm{d}t' \tag{A.3}$$

$$= P_0 \frac{\tau_{\mathrm{fwhm}}}{2\ln(\sqrt{2}+1)} \tanh(t)\Big|_{-\infty}^{\infty} = P_0 \frac{\tau_{\mathrm{fwhm}}}{\ln(\sqrt{2}+1)} \approx P_0 \frac{\tau_{\mathrm{fwhm}}}{0.88} \tag{A.4}$$

Consequently, $P_0 \approx 0.88 \frac{\mathcal{E}}{\tau_{\mathrm{fwhm}}}$.

Gaussian pulse in time Analogously to above, for a Gaussian pulse in time

$$P(t) = P_0 \exp\left[-4\ln(2)\frac{t^2}{\tau_{\mathrm{fwhm}}^2}\right], \tag{A.5}$$

which transfers to a pulse energy of

$$\mathcal{E} = P_0 \int_{\mathbb{R}} \exp\left[-4\ln(2)\frac{t^2}{\tau_{\mathrm{fwhm}}^2}\right] = P_0 \sqrt{\frac{\pi\tau_{\mathrm{fwhm}}^2}{4\ln(2)}} \approx P_0 \frac{\tau_{\mathrm{fwhm}}}{0.94}, \tag{A.6}$$

and therefore, $P_0 \approx 0.94 \frac{\mathcal{E}}{\tau_{\mathrm{fwhm}}}$.

A.2 Ponderomotive potential

Given an electric field $E(t) = E_0 \cos(\omega t)$, the average kinetic energy of a free electron, the ponderomotive potential, is

$$U_{\mathrm{P}} = \frac{1}{2} m_{\mathrm{e}} \langle v^2 \rangle. \tag{A.7}$$

With the velocity

$$v = -\frac{e}{m_\mathrm{e}} \int_{t_0}^{t_1} E(t)\,\mathrm{d}t \tag{A.8}$$

$$= -\frac{eE_0}{m_\mathrm{e}} \int_{t_0}^{t_1} \cos(\omega t)\,\mathrm{d}t, \tag{A.9}$$

$$\tag{A.10}$$

the average kinetic energy

$$U_\mathrm{P} = \frac{e^2E_0^2}{2m_\mathrm{e}} \frac{1}{T} \int_t^{t+T} \left[\int_0^t \cos(\omega\tilde{t})\,\mathrm{d}\tilde{t}\right]^2 \mathrm{d}t \tag{A.11}$$

$$= \frac{e^2E_0^2}{2m_\mathrm{e}\omega^2} \frac{1}{T} \int_t^{t+T} \sin(\omega t)^2\,\mathrm{d}t \tag{A.12}$$

$$= \frac{e^2E_0^2}{2m_\mathrm{e}\omega^3} \frac{1}{T} \int_\omega^{\omega+2\pi} \sin(t')^2\,\mathrm{d}t' \tag{A.13}$$

$$= \frac{e^2E_0^2}{2m_\mathrm{e}\omega^3 2\pi/\omega}\pi = \frac{e^2E_0^2}{4m_\mathrm{e}\omega^2} \tag{A.14}$$

is determined. This expression is the ponderomotive potential.

A.3 Definition of the TIPTOE response function

According to Eq. (2.46), the charge modulation is

$$\Delta Q \approx \int \left.\frac{\partial w(E)}{\partial E}\right|_{E_\mathrm{Pump}(t)} \cdot E_\mathrm{Signal}(t+\tau)\,\mathrm{d}t = \int f(t)g(t+\tau)\,\mathrm{d}t. \tag{A.15}$$

Its Fourier transform reads

$$\mathcal{FT}(\Delta Q) = \int_\mathbb{R} \mathrm{d}\tau \int_\mathbb{R} \mathrm{d}t f(t)g(t+\tau) \exp(-i\omega\tau) \tag{A.16}$$

$$= \int_\mathbb{R} \mathrm{d}t' \int_\mathbb{R} \mathrm{d}t f(t)g(t') \exp\left(-i\omega(t'-t)\right) \tag{A.17}$$

$$= \int_\mathbb{R} \mathrm{d}t f(t) \exp(+i\omega t) \int_\mathbb{R} \mathrm{d}t' g(t') \exp\left(-i\omega t'\right) \tag{A.18}$$

$$= \mathcal{FT}^*\left[f(t)\right] \cdot \mathcal{FT}\left[g(t)\right], \tag{A.19}$$

which is Eq. (2.47).

Comment on the sign of the response phase

Concluding from Fig. 2.13b) and Eq. (2.47), it might appear that the phase of $H(f) \cdot E_\mathrm{Signal}(f)$ is exactly twice the CEP and rather than zero when both pump and signal beam are CEP modulated in the same way. At first, this may seem contradictory; however, the CEP as introduced in Eq. (2.6) transfers to Fourier space with an additional minus sign, ultimately yielding a cancellation of the response phase. This cancellation can be shown by explicit calculation. Assuming a field analogously to Eq. (2.6) defined by $E(t) =$

$\cos(\omega_0 t - \varphi_{\mathrm{CEP}})$, the Fourier transform reads

$$E(\omega) = \frac{1}{\sqrt{2\pi}} \int_{\mathbb{R}} \cos(\omega_0 t - \varphi_{\mathrm{CEP}}) \exp(-i\omega t)\, \mathrm{d}t \tag{A.20}$$

$$= \frac{1}{2\sqrt{2\pi}} \left[\int_{\mathbb{R}} \exp\left(+i\omega_0 t - i\omega t - i\varphi_{\mathrm{CEP}}\right)\right) \mathrm{d}t + \int_{\mathbb{R}} \exp\left(-i\omega_0 t - i\omega t + i\varphi_{\mathrm{CEP}}\right)\right) \mathrm{d}t \Bigg] \tag{A.21}$$

$$= \frac{1}{2\sqrt{2\pi}} \big[\exp(-i\varphi_{\mathrm{CEP}})\delta(\omega - \omega_0) + \exp(i\varphi_{\mathrm{CEP}})\delta(\omega + \omega_0) \big]. \tag{A.22}$$

The first term accounts for the positive frequency components, and therefore, the CEP enters as $\exp(-i\varphi_{\mathrm{CEP}})$. The phase of the response function $\phi = \angle H(f)$ is defined as by $\exp(+i\phi)$, therefore, the CEP appears in the Fourier transform with a different sign than that of the spectral response function. Consequently, cancellation occurs, which is in agreement with the experiment in Chapter 4.

Response of the holey mirror interferometer

For the TIPTOE measurements, an interferometer with a perforated mirror for splitting the beam is used. Since the holey mirror is placed in the collimated beam, it selects the central part only, and therefore the selected spectral components differ from the ones of the entire beam (see, for example, the beam profiles with color filters in Fig. 4.11). Under the assumption that the fiber is equivalent to a source of radius a_{eff}, which is related to the effective mode area $A_{\mathrm{eff}} \approx \frac{3a^2}{2}$ for the ground mode [51], with fiber radius a, via $a_{\mathrm{eff}} = a\sqrt{\frac{3}{2\pi}}$, the collimated beam forms an Airy pattern that favors a wavelength dependence. For each spectral component with wavelength λ, the intensity distribution is

$$I(r) = I_0(\lambda) \left[\frac{2J_1\left(\frac{2\pi a_{\mathrm{eff}}}{\lambda} \frac{r}{\sqrt{r^2+L^2}}\right)}{\frac{2\pi a_{\mathrm{eff}}}{\lambda} \frac{r}{\sqrt{r^2+L^2}}} \right]^2, \tag{A.23}$$

where L is the distance of the collimation mirror to the fiber exit, 1 m in this case, and $a_{\mathrm{eff}} = 242\,\mu\mathrm{m}$, J_1 is the first Bessel function. The energy transmitted through the hole (radius $\tilde{R}$), $\mathcal{E}_{\mathrm{in}}$, is

$$\mathcal{E}_{\mathrm{in}} = \int_0^{2\pi} \mathrm{d}\phi \int_0^{\tilde{R}} \mathrm{d}r \quad r I_0(\lambda) \left[\frac{2J_1\left(\frac{2\pi a_{\mathrm{eff}}}{\lambda} \frac{r}{\sqrt{r^2+L^2}}\right)}{\frac{2\pi a_{\mathrm{eff}}}{\lambda} \frac{r}{\sqrt{r^2+L^2}}} \right]^2. \tag{A.24}$$

For the total energy $\mathcal{E}_{\mathrm{tot}}$, the second integral is extended to ∞. Comparison of both values yields a ratio of transmitted energy to total energy for each wavelength of

$$\frac{\mathcal{E}_{\mathrm{in}}}{\mathcal{E}_{\mathrm{tot}}} = \frac{\displaystyle\int_0^{\tilde{R}} \mathrm{d}r \quad \frac{r^2+L^2}{r} \left[J_1\left(\frac{2\pi a_{\mathrm{eff}}}{\lambda} \frac{r}{\sqrt{r^2+L^2}}\right)\right]^2}{\displaystyle\int_0^{\infty} \mathrm{d}r \quad \frac{r^2+L^2}{r} \left[J_1\left(\frac{2\pi a_{\mathrm{eff}}}{\lambda} \frac{r}{\sqrt{r^2+L^2}}\right)\right]^2}. \tag{A.25}$$

Since the electric field scales with the square root of the energy, a field response function

$$|H_{\mathrm{mirror}}| = \sqrt{\frac{\mathcal{E}_{\mathrm{in}}}{\mathcal{E}_{\mathrm{tot}}}}, \tag{A.26}$$

can be defined, which is shown for a hole diameter of 1 mm and the experimental parameters in Fig. A.1.

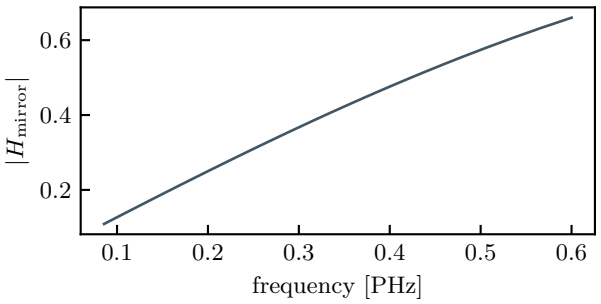

Figure A.1: Relative spectral selection by the holey mirror.

With this definition, the experimentally determined overall spectral amplitude response $|H_{\text{exp}}|$ can now be decomposed as $|H_{\text{exp}}| = |H_{\text{mirror}}| \cdot |H_{\text{TIPTOE}}|$. Alternatively, the experimentally determined TIPTOE response function given by $|H^{\text{exp}}_{\text{TIPTOE}}| = |H_{\text{exp}}|/|H_{\text{mirror}}|$ can be compared to the theoretically expected value, see Fig. 4.16.

A.4 Losses in curved waveguides

Following Ref. [132], the losses of the EH_{nm} mode in a curved waveguide are (Eq. (2.55) and notation from Sec. 2.6)

$$\alpha_{nm}(R) = \alpha_{nm}(\infty) + \frac{a^3}{\lambda^2 R^2} \Re V_{nm}(\nu) \tag{A.27}$$

with the loss term of a straight waveguide $\alpha_{nm}(\infty)$ and

$$V_{nm} = \frac{4}{3} \frac{\nu^2+1}{2\sqrt{\nu^2-1}} \left(\frac{2\pi}{u_{nm}}\right)^2 \cdot \left[1 - \frac{n(n-2)}{u_{nm}^2} + \frac{3}{4}\delta_n(\pm 1) \left(\frac{\nu^2-1}{\nu^2+1}\right) \cos(2\theta_0)\right], \tag{A.28}$$

with $\delta_n(\pm 1) = 1$ for $n = \pm 1$ and 0 else. As an example, for a FS waveguide with refractive index $\nu = 1.4366$ [79], an EH_{11} mode and $u_{11} = 2.4048$,

$$V_{11} = 13.52\,[1.42 + 0.26\cos(2\theta_0)]\,. \tag{A.29}$$

Now, if the laser is polarized in the plane of curvature, i.e. $\theta_0 = 0$, the attenuation is larger than for perpendicular polarization $\theta_0 = \pm\frac{\pi}{2}$ [132]. The attenuation constants then are

$$\alpha_{nm}(R) = \alpha_{nm}(\infty) + 22.08 \cdot \frac{a^3}{\lambda^2 R^2} \quad \text{and} \tag{A.30}$$

$$\alpha_{nm}(R) = \alpha_{nm}(\infty) + 15.68 \frac{a^3}{\lambda^2 R^2}. \tag{A.31}$$

Appendix B

Circuit diagram for the carrier-envelope-phase detector

The essential part of the detection electronics for the phasemeter is outlined in Fig. B.1. It consists of a timing circuitry that produces the integration and reset windows required for the gated integrator. The circuits producing the time windows were provided by Harald Haas; one of them (the integration one) is shown in Fig. B.1. It takes a trigger input (flag `TRG_IN`) on the Schmitt-triggered input pin 2. The delay and pulse width value of the generated pulse are set via a digital potentiometer (`MCP42100`), which is controlled by a serial-peripheral-interface from a microcontroller. The time constants of `C2` and `R2` as well as of `C3` and `R3` define delay and pulse width, respectively.

The signal coming from the TIA is fed into the `IVC102` gated integrator (`Signal In` flag). The `RSTpulse` and `INTpulse` flags indicate the inputs from the timing circuits. The output (`Out_SIG1`) is then digitized and captured for each laser shot. In total, two such integrators are used, synchronously controlled by one timing circuit for the integration window and one timing circuit for the reset time window. The minimum reset window length of 10 µs [336] limits the maximum repetition rate, which can be resolved, to around 50 kHz. Similar performance as compared to the SRS SR250 boxcar averager is observed in the experiment. The capacitors `C1`,`C4`,`C5`, and `C6` are decoupling the power supply.

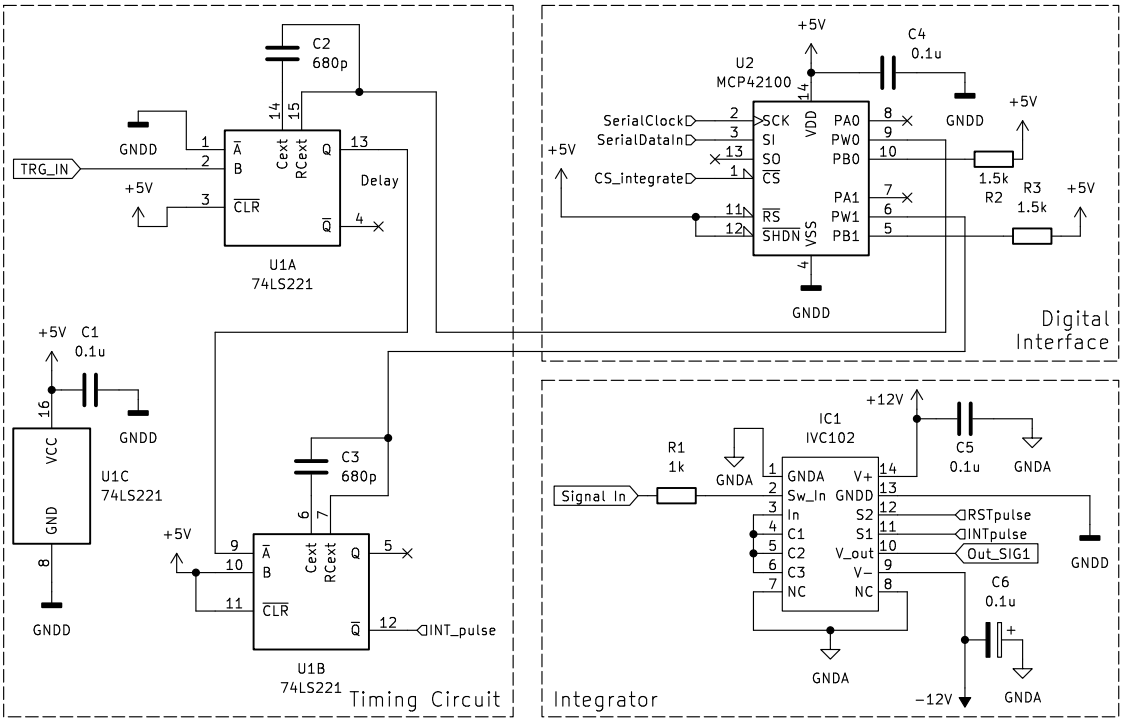

Figure B.1: The main parts of the electronic circuitry are two timing units (one of them is shown, the other one is similar), a digital interface accessing each of them by setting a resistive value controlled from a microcontroller and the analog integrator based on the `IVC102`.

Appendix C

Spectrometer calibration

The spectral detection of multi-octave spanning supercontinua demands for equally broadband detectors. Grating-based spectrometers therefore only cover a limited range, for example, the Silicon range from the VIS to NIR. For longer wavelengths, Indium-Gallium-Arsenide detectors are suitable (up to 2.5 µm wavelength), and for the mid to far-IR, Leadsulfite or Leadselenide detetors can be used, among others.

The detection setup used for the spectrometer data presented in Fig. 4.14b) is outlined in Fig. C.1. The laser beam is focused into a ZrF_4 fiber and sent to a free-space splitting unit. There, the beam is collimated and refocused into three different fibers by means of OAPs and beamsplitters for specific wavelength regions. In addition, wavelength selective filters can be placed in the specific beams.

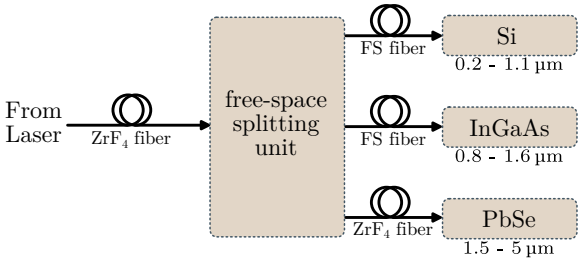

Figure C.1: Schematic drawing of the spectral detection setup. The laser or the calibration lamp is focused into the first fiber. The free space splitting unit consists of wavelength selective beamsplitters and filters as well as focusing optics for subsequent fiber coupling.

For calibration, a black-body lamp ($T = 2800\,\mathrm{K}$) is focused into the very same input fiber, and the spectrum of all three spectrometers is captured for the same configuration. The integration times are set to exploit the maximum dynamic range. Importantly, the splitting setup and the spectrometer settings are not changed after taking the black body lamp spectrum, such that subsequent measurements can be amplitude calibrated with that dataset. Using this scheme, all wavelength-dependent reflection or transmission properties of all optical elements are calibrated and therefore compensated for as well.

Having captured spectral data with different devices for different wavelength regions, the construction of the total spectrum requires some processing. Firstly, the black body spectrum [337, 338],

$$I_{\mathrm{blackbody}}(f) \propto \frac{f^3}{c^2} \frac{1}{\exp\left[\frac{hf}{k_\mathrm{B}T}\right] - 1}, \tag{C.1}$$

$$I_{\mathrm{blackbody}}(\lambda) \propto \frac{c^2}{\lambda^5} \frac{1}{\cdot \exp\left[\frac{hf}{k_\mathrm{B}T}\right] - 1}, \tag{C.2}$$

is used to calculate an amplitude correction factor for each individual device. Here, all pre-factors have been dropped since the measurement devices deliver only integer values

from the analog-to-digital converter; h denotes Planck's constant and k_B denotes Boltzmann's constant. Secondly, the correction factor is applied to all spectral data for each device individually. Thirdly, since devices with overlapping spectral coverage are chosen, the overlap regions need to be corrected. Having spectral overlap between the individual detectors allows for better compensation of the non-uniform response curve, which typically drops towards the edges of their spectral range. In this way, the very edges of each individual detector range are not needed as they can be replaced with more reliable data from another detector. To be precise, the silicon detector data is used in a range up to 1000 nm, the InGaAs data in a range from 880 to 1600 nm and the PbSe data from 1550 nm on. Note that the InGaAs detector response curve is not found to drop at 1600 nm since the detection range of the material could in principle be larger. In the residual overlap regions, the data of both devices is averaged after interpolation of all data to an equal wavelength axis.

Appendix D

Design of an XUV spectrometer

Design criteria for a spectrometer to be used with the presented beamline are the vacuum compatibility, the spectral range from 60 to 600 eV, and a resolution that allows the observation of the harmonic comb, that is at least 0.5 eV or below. Such devices use a diffractive element, typically a grating, to spatially disperse the incident radiation. For high precision, an entrance slit is imaged onto the detector, either by external focusing elements or by a curved grating [277]. The precision of such devices depends on imaging properties; the image plane can be cylindrical for gratings with spherical shape and uniform line-space grooves [339]. Since typical detectors are linear, a linear image plane is desired and can be achieved by using curved varied-line-space gratings [339]. The spectral range and resolution additionally depend on the geometry of the device, specifically the choice of the grating and the detector resolution. The coordinates used for the description of the spectrometer are defined in Fig. D.1. Important parameters are the slit to grating distance r, the grating to image distance r', as well as the incident angle α and the exit angle β. The detector is placed at a distance x_d and y_d, which mark the center of the detector plane. The extension of the image is L. The angular dependence of incident and exit beam is defined by the grating equation

$$\sin(\alpha) - \sin(\beta) = mN\lambda, \tag{D.1}$$

where m is the diffraction order, N the groove density and λ the wavelength.

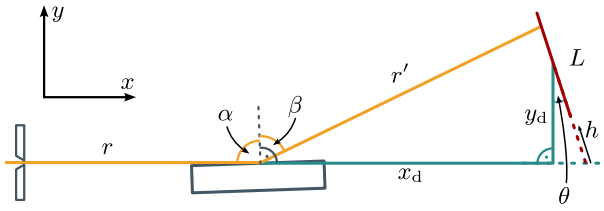

Figure D.1: Coordinates for the description of the grating parameters. Adapted from [277].

Following Refs. [277, 339], the focal curve of a varied-line-space grating parametrized by a b_2 parameter describing the space variation of the grooves is

$$r' = \frac{rR\cos^2\beta}{r\left[\cos\alpha + \cos\beta - 2\left(\sin\alpha - \sin\beta\right)b_2\right] - R\cos^2\alpha}. \tag{D.2}$$

Here, R is the radius of curvature of the grating, and b_2 relates to the groove spacing σ via

$$\sigma = \frac{\sigma_0}{1 + \frac{2b_2}{R}\tilde{x}}, \tag{D.3}$$

where σ_0 is the groove spacing at the center of the grating, $\tilde{x}$ the spatial coordinate on the grating. Equation (D.2) is taken from Ref. [339] but with a different sign in front of $\sin(\beta)$. This change is necessary to reproduce the results in Refs. [277, 339].

Unterguggenberger [277] showed that the grating 30-001 from Shimadzu [340] can be used for the detection of the given wavelength range above, if the design complies with the following geometrical constraints: The extension of the flat-field image is $L = 50\,\mathrm{mm}$ for $x_\mathrm{d} = 236\,\mathrm{mm}$ and $y_\mathrm{d} = 55\,\mathrm{mm}$. The inclination angle $\theta = 16°$. The distance of the slit to the grating is $r = 237\,\mathrm{mm}$ and $\alpha = 88.37°$, or $\alpha = 88.04°$ without slit. Under these circumstances, the image plane of the flat-field grating is in the described detector plane, thus the values of θ, x_d and y_d define the optical setup. The angle α has to be matched rather precisely, since a deviation of 0.5° already shifts the image plane significantly [277, Fig. 3.4]. The large image extension of 50 mm requires a detector of similar size or a movable one. This feature was implemented to the device by me and the according technical drawings for the fabrication were created by Andreas Küchler.

The vacuum compatibility is fulfilled by the usage of UHV components, which is not yet standard in commercially available products and manifests as an additional cost factor. From a mechanical point of view, the movable detector under such conditions has to be connected with an edge-welded bellow allowing for sufficient travel range. Here, a custom-made product from Metallic Flex GmbH is used. Figure D.2 a) shows a 3D model of the device including the movable detector. It is implemented in the laboratory in exactly the same way. A sketch of the laser beam propagation through the device is shown in Fig. D.2b). The main components are: the entrance slit; a filter wheel for thin metal foil used for calibration of the device, see below; a grating mount that can be rotated and displaced in x and y direction and carry up to three gratings; an additional filter in front of the detector for stray light suppression; and the movable detector part with the CCD camera (Andor Newton DO920P-BEN).

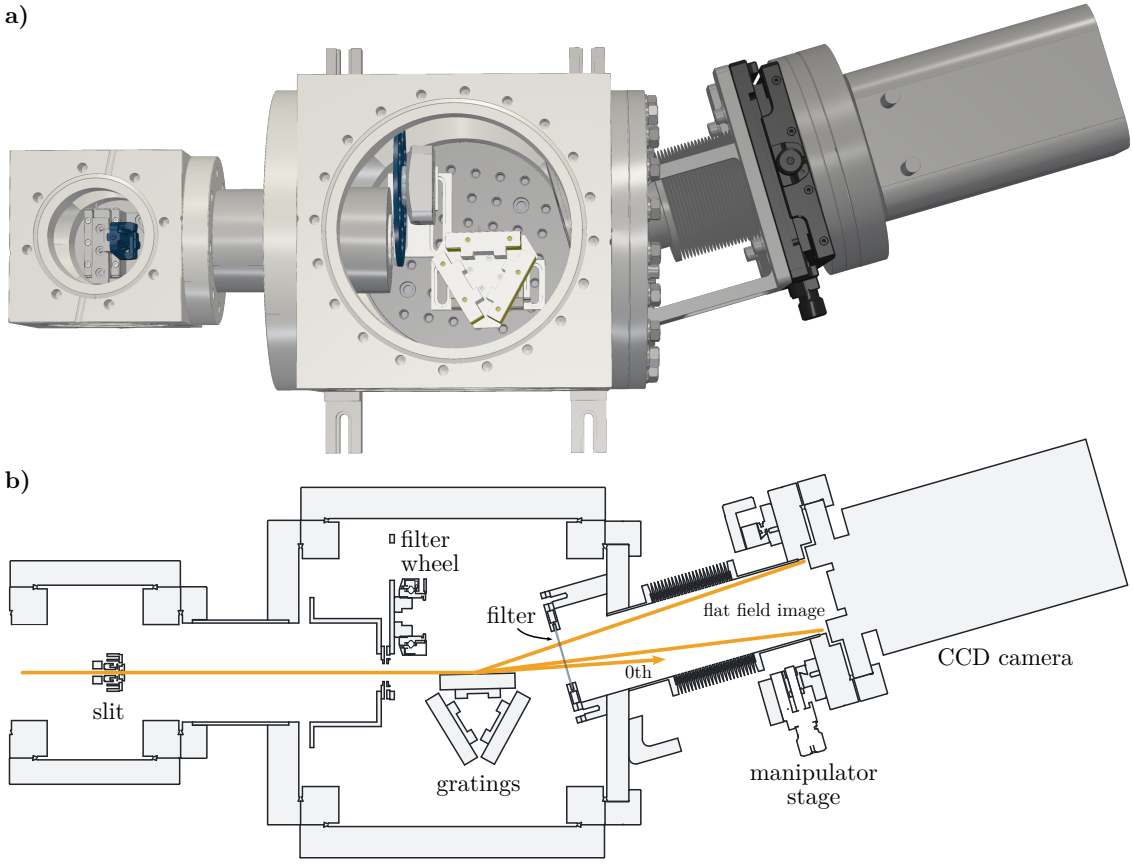

Figure D.2: a) 3D view from the top **b)** Cut-view at the plane where the radiation propagates. The XUV-SXR beam is drawn in orange. The detector can be moved through the entire image plane by ±12.5 mm.

Calibration For calibration, a mapping of pixel number on the detector to wavelength or energy has to be found. In theory, if all parameters are known, Eq. (D.2) provides such a function. In reality, parameters entering this equation are either not precisely known or inaccessible, therefore, an approximation has to be found [277]. Before that, we consider the position on the detector and connect it to the wavelength by its dependence on the angle β. Assuming the device images according to Fig. D.1, the parameter h can be expressed via the position on the detector s [277]

$$h(s) = \frac{y_\mathrm{d}}{\cos(\theta)} + \frac{L}{2} - s \tag{D.4}$$

In addition, the following relations hold according to the law of cosines and the law of sines (c.f. Ref. [277]):

$$r'^2 = h^2(s) + x_0^2 - 2h(s)x_0\cos(90^\circ - \theta) \tag{D.5}$$

$$x_0 = x_\mathrm{d} + \tan(\theta)y_\mathrm{d} \tag{D.6}$$

and

$$\frac{h(s)}{\sin(180^\circ - \alpha - \beta)} = \frac{r'}{\sin(90^\circ - \theta)}. \tag{D.7}$$

Solving Eq. (D.7) for β and using Eq. (D.5) yields

$$\beta = \arcsin\left[\frac{\cos(\theta)}{\sqrt{h^2(s) + x_0^2 - 2h(s)x_0\sin(\theta)}}h(s)\right]. \tag{D.8}$$

With the grating equation Eq. (D.2), the wavelength λ can be linked to a postion h on the detector

$$\lambda(h(s)) = \frac{1}{mN}\left\{\sin(\alpha) - \sin\left[\arcsin\left(\frac{h(s)\cos(\theta)}{\sqrt{h^2(s) + x_0^2 - 2h(s)x_0\sin(\theta)}}\right) - \alpha\right]\right\} \tag{D.9}$$

This equation maps a signal on a specific point on the detector to a wavelength. However, it requires a precise knowledge of α, θ, x_d and y_d, thus the precise geometry of the device. Eq. (D.9) can be approximated with polynomial or exponential functions [277, 341], e.g. as

$$\lambda(s) = a_0 + a_1\exp(a_2 s), \tag{D.10}$$

with parameters a_1, a_2 and a_3. With this equation and several precisely known wavelength references, the spectrometer can be calibrated. More precisely, for a fixed detector position, characteristic spectral features have to be identified, e.g. characteristic filter edges. Such features can be connected to a known wavelength, and therefore, the best fitting parameters in Eq. (D.10) can be determined. Following this procedure, each position on the detector can be mapped to a specific wavelength. If the detector is moved, calibration has to be repeated. Alternatively, the movement Δs can be tracked and accounted for by shifting $\lambda(s) \to \lambda(s + \Delta s)$. This feature, however, is not implemented in the current version of the device.

Other aspects, such as the achievable wavelength precision and the free spectral range are discussed in Ref. [277] to which the interested reader is referred. The control software for the spectrometer is written in C++ and controls the camera as well as the placement of slit and grating.

Appendix E

Data archive

The experimental data as well as all the scripts for generating the figures are stored on servers of the Laboratory for Attosecond Physics at the Max Planck Institute of Quantum Optics. The root folder contains a readme file that describes which script was used for which figure. In addition, it lists the datasets used. The responsible person for any inquiry is Vladislav Yakovlev.

References

[1] Zenghu Chang, Li Fang, Vladimir Fedorov, Chase Geiger, Shambhu Ghimire, Christian Heide, Nobuhisa Ishii, Jiro Itatani, Chandrashekhar Joshi, Yuki Kobayashi, Prabhat Kumar, Alphonse Marra, Sergey Mirov, Irina Petrushina, Mikhail Polyanskiy, David A. Reis, Sergei Tochitsky, Sergey Vasilyev, Lifeng Wang, Yi Wu and Fangjie Zhou. *Intense infrared lasers for strong-field science.* Adv. Opt. Photon., **Vol. 14**, No. 4: pp. 652–782, 2022. URL http://dx.doi.org/10.1364/AOP.454797.

[2] Matthias F Kling, Carmen S Menoni, Cameron Geddes, Almantas Galvanauskas, Felicie Albert, Leily Kiani, Michael Chini, L Robert Baker, Keith A Nelson, Linda Young, Jeffrey Moses, Sergio Carbajo, Stavros G Demos, Franklin Dollar, Douglass Schumacher, Janet Y Tsai, Alan R Fry and Jonathan D Zuegel. *Roadmap on basic research needs for laser technology.* Journal of Optics, **Vol. 27**, No. 1: p. 013002, 2024. URL http://dx.doi.org/10.1088/2040-8986/ad8458.

[3] Hanieh Fattahi, Helena G. Barros, Martin Gorjan, Thomas Nubbemeyer, Bidoor Alsaif, Catherine Y. Teisset, Marcel Schultze, Stephan Prinz, Matthias Haefner, Moritz Ueffing, Ayman Alismail, Lénárd Vámos, Alexander Schwarz, Oleg Pronin, Jonathan Brons, Xiao Tao Geng, Gunnar Arisholm, Marcelo Ciappina, Vladislav S. Yakovlev, Dong-Eon Kim, Abdallah M. Azzeer, Nicholas Karpowicz, Dirk Sutter, Zsuzsanna Major, Thomas Metzger and Ferenc Krausz. *Third-generation femtosecond technology.* Optica, **Vol. 1**, No. 1: pp. 45–63, 2014. URL http://dx.doi.org/10.1364/OPTICA.1.000045.

[4] P. B. Corkum and Ferenc Krausz. *Attosecond science.* Nature Physics, **Vol. 3**, No. 6: pp. 381–387, 2007. ISSN 1745-2481. URL http://dx.doi.org/10.1038/nphys620.

[5] Ferenc Krausz and Misha Ivanov. *Attosecond physics.* Rev. Mod. Phys., **Vol. 81**, No. 1: pp. 163–234, 2009. URL http://dx.doi.org/10.1103/RevModPhys.81.163.

[6] Ferenc Krausz and Mark I. Stockman. *Attosecond metrology: from electron capture to future signal processing.* Nature Photonics, **Vol. 8**, No. 3: pp. 205–213, 2014. ISSN 1749-4893. URL http://dx.doi.org/10.1038/nphoton.2014.28.

[7] Francesca Calegari, Giuseppe Sansone, Salvatore Stagira, Caterina Vozzi and Mauro Nisoli. *Advances in attosecond science.* Journal of Physics B: Atomic, Molecular and Optical Physics, **Vol. 49**, No. 6: p. 062001, 2016. URL http://dx.doi.org/10.1088/0953-4075/49/6/062001.

[8] Keisuke Kaneshima, Yuki Ninota and Taro Sekikawa. *Time-resolved high-harmonic spectroscopy of ultrafast photoisomerization dynamics.* Opt. Express, **Vol. 26**, No. 23: pp. 31039–31054, 2018. URL http://dx.doi.org/10.1364/OE.26.031039.

[9] Matthias F. Kling and Marc J.J. Vrakking. *Attosecond Electron Dynamics*. Annual Review of Physical Chemistry, **Vol. 59**, No. Volume 59, 2008: pp. 463–492, 2008. ISSN 1545-1593. URL http://dx.doi.org/https://doi.org/10.1146/annurev.physchem.59.032607.093532.

[10] Mauro Nisoli, Piero Decleva, Francesca Calegari, Alicia Palacios and Fernando Martín. *Attosecond Electron Dynamics in Molecules*. Chemical Reviews, **Vol. 117**, No. 16: pp. 10760–10825, 2017. PMID: 28488433, URL http://dx.doi.org/10.1021/acs.chemrev.6b00453.

[11] Mark I. Stockman, Matthias F. Kling, Ulf Kleineberg and Ferenc Krausz. *Attosecond nanoplasmonic-field microscope*. Nature Photonics, **Vol. 1**, No. 9: pp. 539–544, 2007. ISSN 1749-4893. URL http://dx.doi.org/10.1038/nphoton.2007.169.

[12] Frederik Süssmann and Matthias F. Kling. *Attosecond nanoplasmonic streaking of localized fields near metal nanospheres*. Phys. Rev. B, **Vol. 84**: p. 121406, 2011. URL http://dx.doi.org/10.1103/PhysRevB.84.121406.

[13] M F Ciappina, J A Pérez-Hernández, A S Landsman, W A Okell, S Zherebtsov, B Förg, J Schötz, L Seiffert, T Fennel, T Shaaran, T Zimmermann, A Chacón, R Guichard, A Zaïr, J W G Tisch, J P Marangos, T Witting, A Braun, S A Maier, L Roso, M Krüger, P Hommelhoff, M F Kling, F Krausz and M Lewenstein. *Attosecond physics at the nanoscale*. Reports on Progress in Physics, **Vol. 80**, No. 5: p. 054401, 2017. URL http://dx.doi.org/10.1088/1361-6633/aa574e.

[14] Agustin Schiffrin, Tim Paasch-Colberg, Nicholas Karpowicz, Vadym Apalkov, Daniel Gerster, Sascha Mühlbrandt, Michael Korbman, Joachim Reichert, Martin Schultze, Simon Holzner, Johannes V. Barth, Reinhard Kienberger, Ralph Ernstorfer, Vladislav S. Yakovlev, Mark I. Stockman and Ferenc Krausz. *Optical-field-induced current in dielectrics*. Nature, **Vol. 493**, No. 7430: pp. 70–74, 2013. ISSN 1476-4687. URL http://dx.doi.org/10.1038/nature11567.

[15] Tim Paasch-Colberg, Agustin Schiffrin, Nicholas Karpowicz, Stanislav Kruchinin, Özge Sağlam, Sabine Keiber, Olga Razskazovskaya, Sascha Mühlbrandt, Ali Alnaser, Matthias Kübel, Vadym Apalkov, Daniel Gerster, Joachim Reichert, Tibor Wittmann, Johannes V. Barth, Mark I. Stockman, Ralph Ernstorfer, Vladislav S. Yakovlev, Reinhard Kienberger and Ferenc Krausz. *Solid-state light-phase detector*. Nature Photonics, **Vol. 8**, No. 3: pp. 214–218, 2014. ISSN 1749-4893. URL http://dx.doi.org/10.1038/nphoton.2013.348.

[16] M. Garg, M. Zhan, T. T. Luu, H. Lakhotia, T. Klostermann, A. Guggenmos and E. Goulielmakis. *Multi-petahertz electronic metrology*. Nature, **Vol. 538**, No. 7625: pp. 359–363, 2016. ISSN 1476-4687. URL http://dx.doi.org/10.1038/nature19821.

[17] J. Schoetz, Z. Wang, E. Pisanty, M. Lewenstein, M. F. Kling and M. F. Ciappina. *Perspective on Petahertz Electronics and Attosecond Nanoscopy*. ACS Photonics, **Vol. 6**, No. 12: pp. 3057–3069, 2019. https://doi.org/10.1021/acsphotonics.9b01188, URL http://dx.doi.org/10.1021/acsphotonics.9b01188.

[18] Christian Heide, Phillip D. Keathley and Matthias F. Kling. *Petahertz electronics*. Nature Reviews Physics, **Vol. 6**, No. 11: pp. 648–662, 2024. ISSN 2522-5820. URL http://dx.doi.org/10.1038/s42254-024-00764-7.

[19] Péter Dombi, Zsuzsanna Pápa, Jan Vogelsang, Sergey V. Yalunin, Murat Sivis, Georg Herink, Sascha Schäfer, Petra Gross, Claus Ropers and Christoph Lienau. *Strong-field nano-optics*. Rev. Mod. Phys., **Vol. 92**, No. 2: p. 025003, 2020. URL http://dx.doi.org/10.1103/RevModPhys.92.025003.

[20] Björn Piglosiewicz, Slawa Schmidt, Doo Jae Park, Jan Vogelsang, Petra Gross, Cristian Manzoni, Paolo Farinello, Giulio Cerullo and Christoph Lienau. *Carrier-envelope phase effects on the strong-field photoemission of electrons from metallic nanostructures*. Nature Photonics, **Vol. 8**, No. 1: pp. 37–42, 2014. ISSN 1749-4893. URL http://dx.doi.org/10.1038/nphoton.2013.288.

[21] Dominik Hoff, Michael Krüger, Lothar Maisenbacher, A. M. Sayler, Gerhard G. Paulus and Peter Hommelhoff. *Tracing the phase of focused broadband laser pulses*. Nature Physics, **Vol. 13**, No. 10: pp. 947–951, 2017. ISSN 1745-2481. URL http://dx.doi.org/10.1038/nphys4185.

[22] Yujia Yang, Marco Turchetti, Praful Vasireddy, William P. Putnam, Oliver Karnbach, Alberto Nardi, Franz X. Kärtner, Karl K. Berggren and Phillip D. Keathley. *Light phase detection with on-chip petahertz electronic networks*. Nature Communications, **Vol. 11**, No. 1: p. 3407, 2020. ISSN 2041-1723. URL http://dx.doi.org/10.1038/s41467-020-17250-0.

[23] Tobias Boolakee, Christian Heide, Antonio Garzón-Ramírez, Heiko B. Weber, Ignacio Franco and Peter Hommelhoff. *Light-field control of real and virtual charge carriers*. Nature, **Vol. 605**, No. 7909: pp. 251–255, 2022. ISSN 1476-4687. URL http://dx.doi.org/10.1038/s41586-022-04565-9.

[24] Felix Ritzkowsky, Matthew Yeung, Engjell Bebeti, Thomas Gebert, Toru Matsuyama, Matthias Budden, Roland E. Mainz, Huseyin Cankaya, Karl K. Berggren, Giulio Maria Rossi, Phillip D. Keathley and Franz X. Kärtner. *On-chip petahertz electronics for single-shot phase detection*. Nature Communications, **Vol. 15**, No. 1: p. 10179, 2024. ISSN 2041-1723. URL http://dx.doi.org/10.1038/s41467-024-53788-z.

[25] Václav Hanus, Beatrix Fehér, Viktória Csajbók, Péter Sándor, Zsuzsanna Pápa, Judit Budai, Zilong Wang, Pallabi Paul, Adriana Szeghalmi and Péter Dombi. *Carrier-envelope phase on-chip scanner and control of laser beams*. Nature Communications, **Vol. 14**, No. 1: p. 5068, 2023. ISSN 2041-1723. URL http://dx.doi.org/10.1038/s41467-023-40802-z.

[26] Seung Beom Park, Kyungseung Kim, Wosik Cho, Sung In Hwang, Igor Ivanov, Chang Hee Nam and Kyung Taec Kim. *Direct sampling of a light wave in air*. Optica, **Vol. 5**, No. 4: pp. 402–408, 2018. URL http://dx.doi.org/10.1364/OPTICA.5.000402.

[27] Shawn Sederberg, Fanqi Kong and Paul B. Corkum. *Tesla-Scale Terahertz Magnetic Impulses*. Phys. Rev. X, **Vol. 10**: p. 011063, 2020. URL http://dx.doi.org/10.1103/PhysRevX.10.011063.

[28] Mina R. Bionta, Felix Ritzkowsky, Marco Turchetti, Yujia Yang, Dario Cattozzo Mor, William P. Putnam, Franz X. Kärtner, Karl K. Berggren and

Phillip D. Keathley. *On-chip sampling of optical fields with attosecond resolution.* Nature Photonics, **Vol. 15**, No. 6: pp. 456–460, 2021. ISSN 1749-4893. URL http://dx.doi.org/10.1038/s41566-021-00792-0.

[29] Yangyang Liu, Shima Gholam-Mirzaei, John E. Beetar, Jonathan Nesper, Ahmed Yousif, M. Nrisimhamurty and Michael Chini. *All-optical sampling of few-cycle infrared pulses using tunneling in a solid.* Photon. Res., **Vol. 9**, No. 6: pp. 929–936, 2021. URL http://dx.doi.org/10.1364/PRJ.420916.

[30] Yangyang Liu, John E. Beetar, Jonathan Nesper, Shima Gholam-Mirzaei and Michael Chini. *Single-shot measurement of few-cycle optical waveforms on a chip.* Nature Photonics, **Vol. 16**, No. 2: pp. 109–112, 2022. ISSN 1749-4893. URL http://dx.doi.org/10.1038/s41566-021-00924-6.

[31] Johannes Blöchl, Johannes Schötz, Ancyline Maliakkal, Natālija Šreibere, Zilong Wang, Philipp Rosenberger, Peter Hommelhoff, Andre Staudte, Paul B. Corkum, Boris Bergues and Matthias F. Kling. *Spatiotemporal sampling of near-petahertz vortex fields.* Optica, **Vol. 9**, No. 7: pp. 755–761, 2022. URL http://dx.doi.org/10.1364/OPTICA.459612.

[32] Dmitry A. Zimin, Vladislav S. Yakovlev and Nicholas Karpowicz. *Ultrabroadband all-optical sampling of optical waveforms.* Science Advances, **Vol. 8**, No. 51: p. eade1029, 2022. https://www.science.org/doi/pdf/10.1126/sciadv.ade1029, URL http://dx.doi.org/10.1126/sciadv.ade1029.

[33] Najd Altwaijry, Muhammad Qasim, Mikhail Mamaikin, Johannes Schötz, Keyhan Golyari, Michael Heynck, Enrico Ridente, Vladislav S. Yakovlev, Nicholas Karpowicz and Matthias F. Kling. *Broadband Photoconductive Sampling in Gallium Phosphide.* Advanced Optical Materials, **Vol. 11**, No. 9: p. 2202994, 2023. https://advanced.onlinelibrary.wiley.com/doi/pdf/10.1002/adom.202202994, URL http://dx.doi.org/https://doi.org/10.1002/adom.202202994.

[34] Yangyang Liu, Shima Gholam-Mirzaei, Dipendra Khatri, Tran-Chau Truong, Troie D. Journigan, Christian Cabello, Christopher Lantigua, André Staudte, Paul B. Corkum and Michael Chini. *Field-resolved space–time characterization of few-cycle structured light pulses.* Optica, **Vol. 11**, No. 6: pp. 846–851, 2024. URL http://dx.doi.org/10.1364/OPTICA.521764.

[35] M. Nisoli, S. De Silvestri, O. Svelto, R. Szipöcs, K. Ferencz, Ch. Spielmann, S. Sartania and F. Krausz. *Compression of high-energy laser pulses below 5 fs.* Opt. Lett., **Vol. 22**, No. 8: pp. 522–524, 1997. URL http://dx.doi.org/10.1364/OL.22.000522.

[36] Mauro Nisoli. *Hollow Fiber Compression Technique: A Historical Perspective.* IEEE Journal of Selected Topics in Quantum Electronics, **Vol. 30**, No. 6: Advances and Applications of Hollow-Core Fibers: pp. 1–14, 2024. ISSN 1558-4542. URL http://dx.doi.org/10.1109/JSTQE.2024.3373174.

[37] Peter Simon Tamas Nagy and Laszlo Veisz. *High-energy few-cycle pulses: post-compression techniques.* Advances in Physics: X, **Vol. 6**, No. 1: p. 1845795, 2020. https://doi.org/10.1080/23746149.2020.1845795, URL http://dx.doi.org/10.1080/23746149.2020.1845795.

[38] Anne-Lise Viotti, Marcus Seidel, Esmerando Escoto, Supriya Rajhans, Wim P. Leemans, Ingmar Hartl and Christoph M. Heyl. *Multi-pass cells for post-compression of ultrashort laser pulses.* Optica, **Vol. 9**, No. 2: pp. 197–216, 2022. URL http://dx.doi.org/10.1364/OPTICA.449225.

[39] Robert Szipöcs, Kárpát Ferencz, Christian Spielmann and Ferenc Krausz. *Chirped multilayer coatings for broadband dispersion control in femtosecond lasers.* Opt. Lett., **Vol. 19**, No. 3: pp. 201–203, 1994. URL http://dx.doi.org/10.1364/OL.19.000201.

[40] R. Szipőcs and A. Kőházi-Kis. *Theory and design of chirped dielectric laser mirrors.* Applied Physics B, **Vol. 65**, No. 2: pp. 115–135, 1997. ISSN 1432-0649. URL http://dx.doi.org/10.1007/s003400050258.

[41] John C. Travers. *Optical solitons in hollow-core fibres.* Optics Communications, **Vol. 555**: p. 130191, 2024. ISSN 0030-4018. URL http://dx.doi.org/https://doi.org/10.1016/j.optcom.2023.130191.

[42] Christian Brahms and John C. Travers. *HISOL: High-energy soliton dynamics enable ultrafast far-ultraviolet laser sources.* APL Photonics, **Vol. 9**, No. 5: p. 050901, 2024. ISSN 2378-0967. https://pubs.aip.org/aip/app/article-pdf/doi/10.1063/5.0206108/19946861/050901_1_5.0206108.pdf, URL http://dx.doi.org/10.1063/5.0206108.

[43] J Scott Russell. *Report on Waves, 14th Meeting of the British Association for the Advancement of Science*, 1844.

[44] Akira Hasegawa and Frederick Tappert. *Transmission of stationary nonlinear optical pulses in dispersive dielectric fibers. I. Anomalous dispersion.* Applied Physics Letters, **Vol. 23**, No. 3: pp. 142–144, 1973. ISSN 0003-6951. https://pubs.aip.org/aip/apl/article-pdf/23/3/142/18428001/142_1_online.pdf, URL http://dx.doi.org/10.1063/1.1654836.

[45] Akira Hasegawa and Frederick Tappert. *Transmission of stationary nonlinear optical pulses in dispersive dielectric fibers. II. Normal dispersion.* Applied Physics Letters, **Vol. 23**, No. 4: pp. 171–172, 1973. ISSN 0003-6951. https://pubs.aip.org/aip/apl/article-pdf/23/4/171/18428166/171_1_online.pdf, URL http://dx.doi.org/10.1063/1.1654847.

[46] L. F. Mollenauer, R. H. Stolen and J. P. Gordon. *Experimental Observation of Picosecond Pulse Narrowing and Solitons in Optical Fibers.* Phys. Rev. Lett., **Vol. 45**: pp. 1095–1098, 1980. URL http://dx.doi.org/10.1103/PhysRevLett.45.1095.

[47] Dimitre G. Ouzounov, Faisal R. Ahmad, Dirk Müller, Natesan Venkataraman, Michael T. Gallagher, Malcolm G. Thomas, John Silcox, Karl W. Koch and Alexander L. Gaeta. *Generation of megawatt optical solitons in hollow-core photonic band-gap fibers.* Science, **Vol. 301**, No. 5640: p. 1702 – 1704, 2003. URL http://dx.doi.org/10.1126/science.1088387.

[48] N. Y. Joly, J. Nold, W. Chang, P. Hölzer, A. Nazarkin, G. K. L. Wong, F. Biancalana and P. St. J. Russell. *Bright Spatially Coherent Wavelength-Tunable Deep-UV Laser Source Using an Ar-Filled Photonic Crystal Fiber.* Phys. Rev. Lett., **Vol. 106**: p. 203901, 2011. URL http://dx.doi.org/10.1103/PhysRevLett.106.203901.

[49] K.F. Mak, J.C. Travers, N.Y. Joly, A. Abdolvand and P.St.J. Russell. *Two techniques for temporal pulse compression in gas-filled hollow-core kagomé photonic crystal fiber.* Optics Letters, **Vol. 38**, No. 18: p. 3592 – 3595, 2013. URL http://dx.doi.org/10.1364/OL.38.003592.

[50] T. Balciunas, C. Fourcade-Dutin, G. Fan, T. Witting, A. A. Voronin, A. M. Zheltikov, F. Gerome, G. G. Paulus, A. Baltuska and F. Benabid. *A strong-field driver in the single-cycle regime based on self-compression in a kagome fibre.* Nature Communications, **Vol. 6**, No. 1: p. 6117, 2015. ISSN 2041-1723. URL http://dx.doi.org/10.1038/ncomms7117.

[51] John C. Travers, Teodora F. Grigorova, Christian Brahms and Federico Belli. *High-energy pulse self-compression and ultraviolet generation through soliton dynamics in hollow capillary fibres.* Nature Photonics, **Vol. 13**, No. 8: pp. 547–554, 2019. ISSN 1749-4893. URL http://dx.doi.org/10.1038/s41566-019-0416-4.

[52] Tamas Nagy, Michael Forster and Peter Simon. *Flexible hollow fiber for pulse compressors.* Appl. Opt., **Vol. 47**, No. 18: pp. 3264–3268, 2008. URL http://dx.doi.org/10.1364/AO.47.003264.

[53] A. Wirth, M. Th. Hassan, I. Grguraš, J. Gagnon, A. Moulet, T. T. Luu, S. Pabst, R. Santra, Z. A. Alahmed, A. M. Azzeer, V. S. Yakovlev, V. Pervak, F. Krausz and E. Goulielmakis. *Synthesized Light Transients.* Science, **Vol. 334**, No. 6053: pp. 195–200, 2011. https://www.science.org/doi/pdf/10.1126/science.1210268, URL http://dx.doi.org/10.1126/science.1210268.

[54] Shu-Wei Huang, Giovanni Cirmi, Jeffrey Moses, Kyung-Han Hong, Siddharth Bhardwaj, Jonathan R. Birge, Li-Jin Chen, Enbang Li, Benjamin J. Eggleton, Giulio Cerullo and Franz X. Kärtner. *High-energy pulse synthesis with sub-cycle waveform control for strong-field physics.* Nature Photonics, **Vol. 5**, No. 8: pp. 475–479, 2011. ISSN 1749-4893. URL http://dx.doi.org/10.1038/nphoton.2011.140.

[55] C. Manzoni, S.-W. Huang, G. Cirmi, P. Farinello, J. Moses, F. X. Kärtner and G. Cerullo. *Coherent synthesis of ultra-broadband optical parametric amplifiers.* Opt. Lett., **Vol. 37**, No. 11: pp. 1880–1882, 2012. URL http://dx.doi.org/10.1364/OL.37.001880.

[56] Giulio Maria Rossi, Roland E. Mainz, Yudong Yang, Fabian Scheiba, Miguel A. Silva-Toledo, Shih-Hsuan Chia, Phillip D. Keathley, Shaobo Fang, Oliver D. Mücke, Cristian Manzoni, Giulio Cerullo, Giovanni Cirmi and Franz X. Kärtner. *Sub-cycle millijoule-level parametric waveform synthesizer for attosecond science.* Nature Photonics, **Vol. 14**, No. 10: pp. 629–635, 2020. ISSN 1749-4893. URL http://dx.doi.org/10.1038/s41566-020-0659-0.

[57] N. H. Burnett, H. A. Baldis, M. C. Richardson and G. D. Enright. *Harmonic generation in CO2 laser target interaction.* Applied Physics Letters, **Vol. 31**, No. 3: pp. 172–174, 1977. ISSN 0003-6951. https://pubs.aip.org/aip/apl/article-pdf/31/3/172/18435123/172_1_online.pdf, URL http://dx.doi.org/10.1063/1.89628.

[58] A. McPherson, G. Gibson, H. Jara, U. Johann, T. S. Luk, I. A. McIntyre, K. Boyer and C. K. Rhodes. *Studies of multiphoton production of vacuum-ultraviolet radiation in the rare gases.* J. Opt. Soc. Am. B, **Vol. 4**, No. 4: pp. 595–601, 1987. URL http://dx.doi.org/10.1364/JOSAB.4.000595.

[59] M Ferray, A L'Huillier, X F Li, L A Lompre, G Mainfray and C Manus. *Multiple-harmonic conversion of 1064 nm radiation in rare gases.* Journal of Physics B: Atomic, Molecular and Optical Physics, **Vol. 21**, No. 3: p. L31, 1988. URL http://dx.doi.org/10.1088/0953-4075/21/3/001.

[60] P. B. Corkum. *Plasma perspective on strong field multiphoton ionization.* Phys. Rev. Lett., **Vol. 71**, No. 13: pp. 1994–1997, 1993. URL http://dx.doi.org/10.1103/PhysRevLett.71.1994.

[61] M. Lewenstein, Ph. Balcou, M. Yu. Ivanov, Anne L'Huillier and P. B. Corkum. *Theory of high-harmonic generation by low-frequency laser fields.* Phys. Rev. A, **Vol. 49**: pp. 2117–2132, 1994. URL http://dx.doi.org/10.1103/PhysRevA.49.2117.

[62] P. M. Paul, E. S. Toma, P. Breger, G. Mullot, F. Augé, Ph. Balcou, H. G. Muller and P. Agostini. *Observation of a Train of Attosecond Pulses from High Harmonic Generation.* Science, **Vol. 292**, No. 5522: pp. 1689–1692, 2001. https://www.science.org/doi/pdf/10.1126/science.1059413, URL http://dx.doi.org/10.1126/science.1059413.

[63] M. Hentschel, R. Kienberger, Ch. Spielmann, G. A. Reider, N. Milosevic, T. Brabec, P. Corkum, U. Heinzmann, M. Drescher and F. Krausz. *Attosecond metrology.* Nature, **Vol. 414**, No. 6863: pp. 509–513, 2001. ISSN 1476-4687. URL http://dx.doi.org/10.1038/35107000.

[64] E. Goulielmakis, M. Uiberacker, R. Kienberger, A. Baltuska, V. Yakovlev, A. Scrinzi, Th. Westerwalbesloh, U. Kleineberg, U. Heinzmann, M. Drescher and F. Krausz. *Direct Measurement of Light Waves.* Science, **Vol. 305**, No. 5688: pp. 1267–1269, 2004. ISSN 0036-8075. https://science.sciencemag.org/content/305/5688/1267.full.pdf, URL http://dx.doi.org/10.1126/science.1100866.

[65] Xiaoming Ren, Jie Li, Yanchun Yin, Kun Zhao, Andrew Chew, Yang Wang, Shuyuan Hu, Yan Cheng, Eric Cunningham, Yi Wu, Michael Chini and Zenghu Chang. *Attosecond light sources in the water window.* Journal of Optics, **Vol. 20**, No. 2: p. 023001, 2018. URL http://dx.doi.org/10.1088/2040-8986/aaa394.

[66] P. Colosimo, G. Doumy, C. I. Blaga, J. Wheeler, C. Hauri, F. Catoire, J. Tate, R. Chirla, A. M. March, G. G. Paulus, H. G. Muller, P. Agostini and L. F. DiMauro. *Scaling strong-field interactions towards the classical limit.* Nature Physics, **Vol. 4**, No. 5: pp. 386–389, 2008. ISSN 1745-2481. URL http://dx.doi.org/10.1038/nphys914.

[67] K. Schiessl, K. L. Ishikawa, E. Persson and J. Burgdörfer. *Quantum Path Interference in the Wavelength Dependence of High-Harmonic Generation.* Phys. Rev. Lett., **Vol. 99**: p. 253903, 2007. URL http://dx.doi.org/10.1103/PhysRevLett.99.253903.

[68] M. V. Frolov, N. L. Manakov and Anthony F. Starace. *Wavelength Scaling of High-Harmonic Yield: Threshold Phenomena and Bound State Symmetry Dependence.* Phys. Rev. Lett., **Vol. 100**: p. 173001, 2008. URL http://dx.doi.org/10.1103/PhysRevLett.100.173001.

[69] A. D. Shiner, C. Trallero-Herrero, N. Kajumba, H.-C. Bandulet, D. Comtois, F. Légaré, M. Giguère, J-C. Kieffer, P. B. Corkum and D. M. Villeneuve. *Wavelength Scaling of High Harmonic Generation Efficiency.* Phys.

Rev. Lett., **Vol. 103**: p. 073902, 2009. URL http://dx.doi.org/10.1103/PhysRevLett.103.073902.

[70] K. L. Ishikawa, K. Schiessl, E. Persson and J. Burgdörfer. *Fine-scale oscillations in the wavelength and intensity dependence of high-order harmonic generation: Connection with channel closings.* Phys. Rev. A, **Vol. 79**: p. 033411, 2009. URL http://dx.doi.org/10.1103/PhysRevA.79.033411.

[71] Johannes Blöchl, Maximilian F. Seeger, Hartmut Schröder, Minjie Zhan, Alexander Guggenmos, Thomas Nubbemeyer, Matthias F. Kling and Boris Bergues. *Ionization effects in single-shot carrier-envelope phase detection with gas-gap devices.* Applied Physics Letters, **Vol. 126**, No. 13: p. 131106, 2025. ISSN 0003-6951. https://pubs.aip.org/aip/apl/article-pdf/doi/10.1063/5.0246794/20471935/131106_1_5.0246794.pdf, URL http://dx.doi.org/10.1063/5.0246794.

[72] James Clerk Maxwell. *VIII. A dynamical theory of the electromagnetic field.* Philosophical Transactions of the Royal Society of London, **Vol. 155**: pp. 459–512, 1865. https://royalsocietypublishing.org/doi/pdf/10.1098/rstl.1865.0008, URL http://dx.doi.org/10.1098/rstl.1865.0008.

[73] John David Jackson. *Klassische Elektrodynamik.* De Gruyter, Berlin, Boston, 2014. ISBN 9783110334470. URL http://dx.doi.org/doi:10.1515/9783110334470.

[74] Stefan Karsch. *Generation of ultraintense Laserpulses - Lecture Notes*, 2017.

[75] Johannes Blöchl. *Laser field sampling with attosecond and nanometer precision.* Masters's thesis, Ludwig-Maximilians-Universität München, München, 2021.

[76] Wolfgang Zinth and Ursula Zinth. *Optik - Lichtstrahlen-Wellen-Photonen.* Oldenbourg, München, 4. edition, 2013. ISBN 978-3-486-72136-2.

[77] Sellmeier. *Zur Erklärung der abnormen Farbenfolge im Spectrum einiger Substanzen.* Annalen der Physik, **Vol. 219**, No. 6: pp. 272–282, 1871. https://onlinelibrary.wiley.com/doi/pdf/10.1002/andp.18712190612, URL http://dx.doi.org/https://doi.org/10.1002/andp.18712190612.

[78] W. Sellmeier. *Ueber die durch die Aetherschwingungen erregten Mitschwingungen der Körpertheilchen und deren Rückwirkung auf die ersteren, besonders zur Erklärung der Dispersion und ihrer Anomalien.* Annalen der Physik, **Vol. 223**, No. 11: pp. 386–403, 1872. https://onlinelibrary.wiley.com/doi/pdf/10.1002/andp.18722231105, URL http://dx.doi.org/https://doi.org/10.1002/andp.18722231105.

[79] I. H. Malitson. *Interspecimen Comparison of the Refractive Index of Fused Silica∗,†.* J. Opt. Soc. Am., **Vol. 55**, No. 10: pp. 1205–1209, 1965. URL http://dx.doi.org/10.1364/JOSA.55.001205.

[80] H. H. Li. *Refractive index of alkaline earth halides and its wavelength and temperature derivatives.* Journal of Physical and Chemical Reference Data, **Vol. 9**, No. 1: pp. 161–290, 1980. ISSN 0047-2689. https://pubs.aip.org/aip/jpr/article-pdf/9/1/161/11502934/161_1_online.pdf, URL http://dx.doi.org/10.1063/1.555616.

[81] Heinrich Hertz. *Über einen Einfluss des ultravioletten Lichtes auf die electrische Entladung.* Annalen der Physik, **Vol. 267**, No. 8: pp. 983–1000, 1887.

[82] Wilhelm Hallwachs. *Über den Einfluss des Lichtes auf electrostatisch geladene Körper*. Annalen der Physik, **Vol. 269**, No. 2: pp. 301–312, 1888.

[83] A. Einstein. *Über einen die Erzeugung und Verwandlung des Lichtes betreffenden heuristischen Gesichtspunkt*. Annalen der Physik, **Vol. 322 (17. Band d. 4. Folge)**: pp. 132–148, 1905.

[84] L. V. Keldysh. *Ionization in the Field of a Strong Electromagnetic Wave*. Soviet Physics JETP, **Vol. 20**, No. 5: pp. 1307–1314, 1965. URL `http://www.jetp.ac.ru/cgi-bin/e/index/e/20/5/p1307?a=list`.

[85] F A Ilkov, J E Decker and S L Chin. *Ionization of atoms in the tunnelling regime with experimental evidence using Hg atoms*. Journal of Physics B: Atomic, Molecular and Optical Physics, **Vol. 25**, No. 19: p. 4005, 1992. URL `http://dx.doi.org/10.1088/0953-4075/25/19/011`.

[86] Gennady L. Yudin and Misha Yu. Ivanov. *Nonadiabatic tunnel ionization: Looking inside a laser cycle*. Phys. Rev. A, **Vol. 64**: p. 013409, 2001. URL `http://dx.doi.org/10.1103/PhysRevA.64.013409`.

[87] N. B. Delone and V. P. Krainov. *Tunneling and barrier-suppression ionization of atoms and ions in a laser radiation field*. Phys. Usp., **Vol. 41**, No. 5: pp. 469–485, 1998. URL `http://dx.doi.org/10.1070/PU1998v041n05ABEH000393`.

[88] Armin Scrinzi, Michael Geissler and Thomas Brabec. *Ionization Above the Coulomb Barrier*. Phys. Rev. Lett., **Vol. 83**: pp. 706–709, 1999. URL `http://dx.doi.org/10.1103/PhysRevLett.83.706`.

[89] X M Tong and C D Lin. *Empirical formula for static field ionization rates of atoms and molecules by lasers in the barrier-suppression regime*. Journal of Physics B: Atomic, Molecular and Optical Physics, **Vol. 38**, No. 15: p. 2593, 2005. URL `http://dx.doi.org/10.1088/0953-4075/38/15/001`.

[90] R. H. Fowler and L. Nordheim. *Electron Emission in Intense Electric Fields*. Proc. R. Soc. Lond. A, **Vol. 119**, No. 781: pp. 173–181, 1928. URL `http://dx.doi.org/10.1098/rspa.1928.0091`.

[91] A. M. Perelomov, V. S. Popov and M. V. Terent'ev. *Ionization of Atoms in an Alternating Electric Field*. Sov. Phys. JETP, **Vol. 23**, No. 5: pp. 924–934, 1966. URL `http://jetp.ac.ru/cgi-bin/e/index/e/23/5/p924?a=list`.

[92] A. M. Perelomov, V. S. Popov and M. V. Terent'ev. *Ionization of Atoms in an Alternating Electric Field: II*. Sov. Phys. JETP, **Vol. 24**, No. 1: p. 207, 1967. URL `http://jetp.ac.ru/cgi-bin/e/index/e/24/1/p207?a=list`.

[93] A. M. Perelomov and V. S. Popov. *Ionization of Atoms in an Alternating Electric Field. III*. Sov. Phys. JETP, **Vol. 25**, No. 2: p. 336, 1967. URL `http://jetp.ac.ru/cgi-bin/e/index/e/25/2/p336?a=list`.

[94] M. V. Ammosov, N. B. Delone and V. P. Krainov. *Tunnel ionization of complex atoms and of atomic ions in an alternating electromagnetic field*. Sov. Phys. JETP, **Vol. 64**, No. 6: p. 1191, 1986. URL `http://jetp.ac.ru/cgi-bin/e/index/e/64/6/p1191?a=list`.

[95] Vladimir S Popov. *Tunnel and multiphoton ionization of atoms and ions in a strong laser field (Keldysh theory)*. Physics-Uspekhi, **Vol. 47**, No. 9: pp. 855–885, 2004. URL `http://dx.doi.org/10.1070/pu2004v047n09abeh001812`.

[96] X. M. Tong, Z. X. Zhao and C. D. Lin. *Theory of molecular tunneling ionization.* Phys. Rev. A, **Vol. 66**: p. 033402, 2002. URL http://dx.doi.org/10.1103/PhysRevA.66.033402.

[97] Vladimir P. Krainov, Howard R. Reiss and Boris M. Smirnov. *Radiative Processes in Atomic Physics - Appendix I: Atomic Units and Measures of Intensity*, pp. 269–272. John Wiley & Sons, Ltd, 1997. ISBN 9783527605606. https://onlinelibrary.wiley.com/doi/pdf/10.1002/3527605606.app9, URL http://dx.doi.org/https://doi.org/10.1002/3527605606.app9.

[98] J. Tate, T. Auguste, H. G. Muller, P. Salières, P. Agostini and L. F. DiMauro. *Scaling of Wave-Packet Dynamics in an Intense Midinfrared Field.* Phys. Rev. Lett., **Vol. 98**: p. 013901, 2007. URL http://dx.doi.org/10.1103/PhysRevLett.98.013901.

[99] C. J. G. J. Uiterwaal, C. R. Gebhardt, H. Schröder and K.-L. Kompa. *Predicting intense-field photoionization of atoms and molecules from their linear photoabsorption spectra in the ionization continuum.* The European Physical Journal D - Atomic, Molecular, Optical and Plasma Physics, **Vol. 30**, No. 3: pp. 379–392, 2004. ISSN 1434-6079. URL http://dx.doi.org/10.1140/epjd/e2004-00102-7.

[100] Lu Yan, Fadia Cudry, Wen Li and Arthur G. Suits. *Isomer-Specific Mass Spectrometric Detection Via "Semisoft" Strong-Field Ionization.* The Journal of Physical Chemistry A, **Vol. 117**, No. 46: pp. 11890–11895, 2013. PMID: 23614669, https://doi.org/10.1021/jp403118c, URL http://dx.doi.org/10.1021/jp403118c.

[101] Fadia Cudry, James M. Oldham, Steven Lingenfelter and Arthur G. Suits. *Strong-Field Ionization of Flash Pyrolysis Reaction Products.* The Journal of Physical Chemistry A, **Vol. 119**, No. 3: pp. 460–467, 2015. PMID: 25517403, https://doi.org/10.1021/jp510552a, URL http://dx.doi.org/10.1021/jp510552a.

[102] Franz E Haniel, Hartmut Schröder, Subhendu Kahaly, Arjun Nayak, Mathieu Dumergue, Sudipta Mondal, Filus Zoltán, Roland Flender, Máté Kurucz, Ludovit Haizer, Bálint Kiss, Dimitris Charalambidis, Matthias F Kling, Paraskevas Tzallas and Boris Bergues. *Saturating multiple ionization in intense mid-infrared laser fields.* New Journal of Physics, **Vol. 23**, No. 5: p. 053026, 2021. URL http://dx.doi.org/10.1088/1367-2630/abf583.

[103] Johannes Schötz. *Field-resolved studies of ultrafast light-matter interaction.* Ph.D. thesis, Ludwig-Maximilians-Universität München, München, 2021. URL http://nbn-resolving.de/urn:nbn:de:bvb:19-295851.

[104] Johannes Schötz, Ancyline Maliakkal, Johannes Blöchl, Dmitry Zimin, Zilong Wang, Philipp Rosenberger, Meshaal Alharbi, Abdallah M. Azzeer, Matthew Weidman, Vladislav S. Yakovlev, Boris Bergues and Matthias F. Kling. *The emergence of macroscopic currents in photoconductive sampling of optical fields.* Nature Communications, **Vol. 13**, No. 1: p. 962, 2022. ISSN 2041-1723. URL http://dx.doi.org/10.1038/s41467-022-28412-7.

[105] W. Shockley. *Currents to Conductors Induced by a Moving Point Charge.* Journal of Applied Physics, **Vol. 9**, No. 10: pp. 635–636, 1938. ISSN 0021-8979. https://pubs.aip.org/aip/jap/article-pdf/9/10/635/18304047/635_1_online.pdf, URL http://dx.doi.org/10.1063/1.1710367.

[106] S. Ramo. *Currents Induced by Electron Motion*. Proceedings of the IRE, **Vol. 27**, No. 9: pp. 584–585, 1939. URL http://dx.doi.org/10.1109/JRPROC.1939.228757.

[107] Zhong He. *Review of the Shockley–Ramo theorem and its application in semiconductor gamma-ray detectors*. Nuclear Instruments and Methods in Physics Research Section A: Accelerators, Spectrometers, Detectors and Associated Equipment, **Vol. 463**, No. 1: pp. 250–267, 2001. ISSN 0168-9002. URL http://dx.doi.org/https://doi.org/10.1016/S0168-9002(01)00223-6.

[108] W. Riegler. *An application of extensions of the Ramo–Shockley theorem to signals in silicon sensors*. Nuclear Instruments and Methods in Physics Research Section A: Accelerators, Spectrometers, Detectors and Associated Equipment, **Vol. 940**: pp. 453–461, 2019. ISSN 0168-9002. URL http://dx.doi.org/https://doi.org/10.1016/j.nima.2019.06.056.

[109] Homer Reid. *scuff-static implementation of scuff-em*. Accessed online on 2 May 2025, URL https://github.com/HomerReid/scuff-em.

[110] Christophe Geuzaine and Jean-François Remacle. *Gmsh: A 3-D finite element mesh generator with built-in pre- and post-processing facilities*. International Journal for Numerical Methods in Engineering, **Vol. 79**, No. 11: pp. 1309–1331, 2009. https://onlinelibrary.wiley.com/doi/pdf/10.1002/nme.2579, URL http://dx.doi.org/https://doi.org/10.1002/nme.2579.

[111] A.M. Velasco and C. Lavín. *Photoionization cross sections and asymmetry parameters for ethanol. A theoretical study*. Journal of Quantitative Spectroscopy and Radiative Transfer, **Vol. 169**: pp. 122–126, 2016. ISSN 0022-4073. URL http://dx.doi.org/https://doi.org/10.1016/j.jqsrt.2015.10.010.

[112] John L Holmes, Mervin Fingas and FP Lossing. *Towards a general scheme for estimating the heats of formation of organic ions in the gas phase. Part I. Odd-electron cations*. Canadian Journal of Chemistry, **Vol. 59**, No. 1: pp. 80–93, 1981.

[113] A. Ansari, M. Kumar, H. Singhal and J. A. Chakera. *Spatiotemporal reshaping of femtosecond laser pulses on interaction with gas sheath at ionization saturation intensity regime*. Journal of Applied Physics, **Vol. 135**, No. 14: p. 143103, 2024. ISSN 0021-8979. https://pubs.aip.org/aip/jap/article-pdf/doi/10.1063/5.0198038/19874722/143103_1_5.0198038.pdf, URL http://dx.doi.org/10.1063/5.0198038.

[114] J. Itatani, F. Quéré, G. L. Yudin, M. Yu. Ivanov, F. Krausz and P. B. Corkum. *Attosecond Streak Camera*. Phys. Rev. Lett., **Vol. 88**: p. 173903, 2002. URL http://dx.doi.org/10.1103/PhysRevLett.88.173903.

[115] Kyung Taec Kim, Chunmei Zhang, Andrew D. Shiner, Bruno E. Schmidt, François Légaré, D. M. Villeneuve and P. B. Corkum. *Petahertz optical oscilloscope*. Nature Photonics, **Vol. 7**, No. 12: pp. 958–962, 2013. ISSN 1749-4893. URL http://dx.doi.org/10.1038/nphoton.2013.286.

[116] Keyhan Golyari. *Linear-Petahertz-PhotoConductive switching*. Ph.D. thesis, Ludwig-Maximilians-Universität München, 2022. URL http://nbn-resolving.de/urn:nbn:de:bvb:19-308263.

[117] Shawn Sederberg, Dmitry Zimin, Sabine Keiber, Florian Siegrist, Michael S. Wismer, Vladislav S. Yakovlev, Isabella Floss, Christoph Lemell, Joachim Burgdörfer, Martin Schultze, Ferenc Krausz and Nicholas Karpowicz. *Attosecond optoelectronic field measurement in solids.* Nature Communications, **Vol. 11**, No. 1: p. 430, 2020. ISSN 2041-1723. URL http://dx.doi.org/10.1038/s41467-019-14268-x.

[118] Dmitry Zimin, Matthew Weidman, Johannes Schötz, Matthias F. Kling, Vladislav S. Yakovlev, Ferenc Krausz and Nicholas Karpowicz. *Petahertz-scale nonlinear photoconductive sampling in air.* Optica, **Vol. 8**, No. 5: pp. 586–590, 2021. URL http://dx.doi.org/10.1364/OPTICA.411434.

[119] A. Korobenko, K. Johnston, M. Kubullek, L. Arissian, Z. Dube, T. Wang, M. Kübel, A. Yu. Naumov, D. M. Villeneuve, M. F. Kling, P. B. Corkum, A. Staudte and B. Bergues. *Femtosecond streaking in ambient air.* Optica, **Vol. 7**, No. 10: pp. 1372–1376, 2020. URL http://dx.doi.org/10.1364/OPTICA.398846.

[120] Enrico Ridente, Mikhail Mamaikin, Najd Altwaijry, Dmitry Zimin, Matthias F. Kling, Vladimir Pervak, Matthew Weidman, Ferenc Krausz and Nicholas Karpowicz. *Electro-optic characterization of synthesized infrared-visible light fields.* Nature Communications, **Vol. 13**, No. 1: p. 1111, 2022. ISSN 2041-1723. URL http://dx.doi.org/10.1038/s41467-022-28699-6.

[121] Maximilian Kubullek, Miguel A. Silva-Toledo, Roland E. Mainz, Fabian Scheiba, Rafael de Q. Garcia, Felix Ritzkowsky, Giulio Maria Rossi and Franz X. Kärtner. *Complete Electric Field Characterization of Ultrashort Multicolor Pulses.* Ultrafast Science, **Vol. 5**: p. 0081, 2025. https://spj.science.org/doi/pdf/10.34133/ultrafastscience.0081, URL http://dx.doi.org/10.34133/ultrafastscience.0081.

[122] Nariyuki Saito, Nobuhisa Ishii, Teruto Kanai and Jiro Itatani. *All-optical characterization of the two-dimensional waveform and the Gouy phase of an infrared pulse based on plasma fluorescence of gas.* Opt. Express, **Vol. 26**, No. 19: pp. 24591–24601, 2018. URL http://dx.doi.org/10.1364/OE.26.024591.

[123] Wosik Cho, Sung In Hwang, Chang Hee Nam, Mina R. Bionta, Philippe Lassonde, Bruno E. Schmidt, Heide Ibrahim, François Légaré and Kyung Taec Kim. *Temporal characterization of femtosecond laser pulses using tunneling ionization in the UV, visible, and mid-IR ranges.* Scientific Reports, **Vol. 9**, No. 1: p. 16067, 2019. ISSN 2045-2322. URL http://dx.doi.org/10.1038/s41598-019-52237-y.

[124] Sung In Hwang, Seung Beom Park, Jehoi Mun, Wosik Cho, Chang Hee Nam and Kyung Taec Kim. *Generation of a single-cycle pulse using a two-stage compressor and its temporal characterization using a tunnelling ionization method.* Scientific Reports, **Vol. 9**, No. 1: p. 1613, 2019. ISSN 2045-2322. URL http://dx.doi.org/10.1038/s41598-018-38220-z.

[125] J. Shin, I. Ivanov, W. Cho, R. Shrestha and K. T. Kim. *Temporal characterization of a two-color laser field using tunneling ionization.* Opt. Express, **Vol. 30**, No. 16: pp. 28686–28695, 2022. URL http://dx.doi.org/10.1364/OE.464586.

[126] Pei Huang, Hao Yuan, Huabao Cao, Hushan Wang, Xianglin Wang, Yishan Wang, Wei Zhao and Yuxi Fu. *Direct sampling of ultrashort laser pulses using third-harmonic generation with perturbation in ambient air.* Opt. Lett., **Vol. 48**, No. 8: pp. 2154–2157, 2023. URL http://dx.doi.org/10.1364/OL.485665.

[127] Ming-Shian Tsai, An-Yuan Liang, Chia-Lun Tsai, Po-Wei Lai, Ming-Wei Lin and Ming-Chang Chen. *Nonlinear compression toward high-energy single-cycle pulses by cascaded focus and compression.* Science Advances, **Vol. 8**, No. 31: p. eabo1945, 2022. https://www.science.org/doi/pdf/10.1126/sciadv.abo1945, URL http://dx.doi.org/10.1126/sciadv.abo1945.

[128] Johannes Blöchl, Maximilian F. Kuthe, Hartmut Schröder, Abdallah M. Azzeer, Thomas Nubbemeyer and Matthias F. Kling. *Multi-millijoule hollow-core fiber compression of short-wave infrared pulses to a single cycle.* Opt. Express, **Vol. 33**, No. 13: pp. 28071–28080, 2025. URL http://dx.doi.org/10.1364/OE.564364.

[129] Robert R. Alfano (Editor). *The supercontinuum laser source: the ultimate white light.* Springer Nature, 2023. ISBN 978-3-031-06197-4. URL http://dx.doi.org/https://doi.org/10.1007/978-3-031-06197-4.

[130] Govind P. Agrawal (Editor). *Nonlinear Fiber Optics (Fifth Edition).* Academic Press, Elsevier, Boston, fifth edition edition, 2013. ISBN 978-0-12-397023-7. URL http://dx.doi.org/https://doi.org/10.1016/C2011-0-00045-5.

[131] Govind P. Agrawal. *Nonlinear fiber optics: its history and recent progress - Invited.* J. Opt. Soc. Am. B, **Vol. 28**, No. 12: pp. A1–A10, 2011. URL http://dx.doi.org/10.1364/JOSAB.28.0000A1.

[132] E. A. J. Marcatili and R. A. Schmeltzer. *Hollow Metallic and Dielectric Waveguides for Long Distance Optical Transmission and Lasers.* Bell System Technical Journal, **Vol. 43**, No. 4: pp. 1783–1809, 1964. https://onlinelibrary.wiley.com/doi/pdf/10.1002/j.1538-7305.1964.tb04108.x, URL http://dx.doi.org/https://doi.org/10.1002/j.1538-7305.1964.tb04108.x.

[133] Keiji Kataoka. *Estimation of coupling efficiency of optical fiber by far-field method.* Optical Review, **Vol. 17**, No. 5: pp. 476–480, 2010. ISSN 1349-9432. URL http://dx.doi.org/10.1007/s10043-010-0086-4.

[134] Robert W. Boyd. *Nonlinear Optics.* Elsevier Inc., Burlington San Diego London, 3. edition, 2008. ISBN 978-0-12-369470-6.

[135] Johannes Blöchl. *Erzeugung von ultrakurzen nah-UV Laserpulsen und Charakterisierung mittels Transient-Grating-Dispersions-Scan [Generation of Ultrashort Near-UV Laserpulses and Characterisation by a Transient-Grating-Dispersion-Scan].* Bachelor's thesis, Ludwig-Maximilians-Universität München, München, 2019.

[136] John M. Dudley, Goëry Genty and Stéphane Coen. *Supercontinuum generation in photonic crystal fiber.* Rev. Mod. Phys., **Vol. 78**: pp. 1135–1184, 2006. URL http://dx.doi.org/10.1103/RevModPhys.78.1135.

[137] A. A. Voronin and A. M. Zheltikov. *Subcycle solitonic breathers.* Phys. Rev. A, **Vol. 90**: p. 043807, 2014. URL http://dx.doi.org/10.1103/PhysRevA.90.043807.

[138] Christian Brahms, Federico Belli and John C. Travers. *Infrared attosecond field transients and UV to IR few-femtosecond pulses generated by high-energy soliton self-compression.* Phys. Rev. Res., **Vol. 2**: p. 043037, 2020. URL http://dx.doi.org/10.1103/PhysRevResearch.2.043037.

[139] Amelie M. Heinzerling, Francesco Tani, Manoram Agarwal, Vladislav S. Yakovlev, Ferenc Krausz and Nicholas Karpowicz. *Field-resolved attosecond solitons*. Nature Photonics, **Vol. 19**, No. 7: pp. 772–777, 2025. ISSN 1749-4893. URL http://dx.doi.org/10.1038/s41566-025-01658-5.

[140] Chia-Ming Chen and Paul L. Kelley. *Nonlinear pulse compression in optical fibers: scaling laws and numerical analysis*. J. Opt. Soc. Am. B, **Vol. 19**, No. 9: pp. 1961–1967, 2002. URL http://dx.doi.org/10.1364/JOSAB.19.001961.

[141] Daniel Schade, Felix Köttig, Johannes R. Koehler, Michael H. Frosz, Philip St. J. Russell and Francesco Tani. *Scaling rules for high quality soliton self-compression in hollow-core fibers*. Opt. Express, **Vol. 29**, No. 12: pp. 19147–19158, 2021. URL http://dx.doi.org/10.1364/OE.426307.

[142] Christian Brahms and John C. Travers. *Luna.jl*, 2023. Version v0.4.3, URL http://dx.doi.org/10.5281/zenodo.10323704.

[143] Boris Bergues. *The circular-polarization phase-meter*. Opt. Express, **Vol. 20**, No. 23: pp. 25317–25324, 2012. URL http://dx.doi.org/10.1364/OE.20.025317.

[144] M. Kubullek, Z. Wang, K. von der Brelje, D. Zimin, P. Rosenberger, J. Schötz, M. Neuhaus, S. Sederberg, A. Staudte, N. Karpowicz, M. F. Kling and B. Bergues. *Single-shot carrier–envelope-phase measurement in ambient air*. Optica, **Vol. 7**, No. 1: pp. 35–39, 2020. URL http://dx.doi.org/10.1364/OPTICA.7.000035.

[145] Szczepan Chelkowski, André D. Bandrauk and Alexander Apolonski. *Phase-dependent asymmetries in strong-field photoionization by few-cycle laser pulses*. Phys. Rev. A, **Vol. 70**: p. 013815, 2004. URL http://dx.doi.org/10.1103/PhysRevA.70.013815.

[146] T Rathje, Nora G Johnson, M Möller, F Süssmann, D Adolph, M Kübel, R Kienberger, M F Kling, G G Paulus and A M Sayler. *Review of attosecond resolved measurement and control via carrier–envelope phase tagging with above-threshold ionization*. Journal of Physics B: Atomic, Molecular and Optical Physics, **Vol. 45**, No. 7: p. 074003, 2012. URL http://dx.doi.org/10.1088/0953-4075/45/7/074003.

[147] M. Mehendale, S. A. Mitchell, J.-P. Likforman, D. M. Villeneuve and P. B. Corkum. *Method for single-shot measurement of the carrier envelope phase of a few-cycle laser pulse*. Opt. Lett., **Vol. 25**, No. 22: pp. 1672–1674, 2000. URL http://dx.doi.org/10.1364/OL.25.001672.

[148] P Dombi, A Apolonski, Ch Lemell, G G Paulus, M Kakehata, R Holzwarth, Th Udem, K Torizuka, J Burgdörfer, T W Hänsch and F Krausz. *Direct measurement and analysis of the carrier-envelope phase in light pulses approaching the single-cycle regime*. New Journal of Physics, **Vol. 6**, No. 1: p. 39, 2004. URL http://dx.doi.org/10.1088/1367-2630/6/1/039.

[149] Masayuki Kakehata, Hideyuki Takada, Yohei Kobayashi, Kenji Torizuka, Yoshihiko Fujihira, Tetsuya Homma and Hideo Takahashi. *Single-shot measurement of carrier-envelope phase changes by spectral interferometry*. Opt. Lett., **Vol. 26**, No. 18: pp. 1436–1438, 2001. URL http://dx.doi.org/10.1364/OL.26.001436.

[150] Xiaoming Ren, A M Summers, Kanaka Raju P, Aram Vajdi, Varun Makhija, C W Fehrenbach, Nora G Kling, K J Betsch, Z Wang, M F Kling, K D Carnes, I Ben-Itzhak, Carlos Trallero-Herrero and Vinod Kumarappan. *Single-shot carrier-envelope-phase tagging using an f–2f interferometer and a phase meter: a comparison.* Journal of Optics, **Vol. 19**, No. 12: p. 124017, 2017. URL http://dx.doi.org/10.1088/2040-8986/aa9865.

[151] C. Feng, J.-F. Hergott, P.-M. Paul, X. Chen, O. Tcherbakoff, M. Comte, O. Gobert, M. Reduzzi, F. Calegari, C. Manzoni, M. Nisoli and G. Sansone. *Complete analog control of the carrier-envelope-phase of a high-power laser amplifier.* Opt. Express, **Vol. 21**, No. 21: pp. 25248–25256, 2013. URL http://dx.doi.org/10.1364/OE.21.025248.

[152] Chen Guo, Miguel Miranda, Ann-Kathrin Raab, Anne-Lise Viotti, Paulo Tiago Guerreiro, Rosa Romero, Helder Crespo, Anne L'Huillier and Cord L. Arnold. *Single-shot, high-repetition rate carrier-envelope-phase detection of ultrashort laser pulses.* Opt. Lett., **Vol. 48**, No. 20: pp. 5431–5434, 2023. URL http://dx.doi.org/10.1364/OL.498664.

[153] Simon Maier, Manuel Meierhofer, Ignaz Laepple, Katharina Glöckl, Christoph Tresp, Matthias Hohenleutner, Markus A. Huber and Rupert Huber. *Fast and compact four-quadrant CEP detection with f-2f polarization interferometry.* Opt. Express, **Vol. 33**, No. 12: pp. 25221–25232, 2025. URL http://dx.doi.org/10.1364/OE.545392.

[154] Máté Kurucz, Szabolcs Tóth, Roland Flender, Ludovít Haizer, Bálint Kiss, Benjamin Persielle and Eric Cormier. *Single-shot CEP drift measurement at arbitrary repetition rate based on dispersive Fourier transform.* Opt. Express, **Vol. 27**, No. 9: pp. 13387–13399, 2019. URL http://dx.doi.org/10.1364/OE.27.013387.

[155] Cristian Manzoni, Michael Först, Henri Ehrke and Andrea Cavalleri. *Single-shot detection and direct control of carrier phase drift of midinfrared pulses.* Opt. Lett., **Vol. 35**, No. 5: pp. 757–759, 2010. URL http://dx.doi.org/10.1364/OL.35.000757.

[156] G. G. Paulus, W. Nicklich, Huale Xu, P. Lambropoulos and H. Walther. *Plateau in above threshold ionization spectra.* Phys. Rev. Lett., **Vol. 72**: pp. 2851–2854, 1994. URL http://dx.doi.org/10.1103/PhysRevLett.72.2851.

[157] G. G. Paulus, F. Lindner, H. Walther, A. Baltuška, E. Goulielmakis, M. Lezius and F. Krausz. *Measurement of the Phase of Few-Cycle Laser Pulses.* Phys. Rev. Lett., **Vol. 91**: p. 253004, 2003. URL http://dx.doi.org/10.1103/PhysRevLett.91.253004.

[158] G. G. Paulus, F. Lindner, H. Walther, A. Baltuška and F. Krausz. *Measurement of the phase of few-cycle laser pulses.* Journal of Modern Optics, **Vol. 52**, No. 2-3: pp. 221–232, 2005. https://doi.org/10.1080/09500340412331283651, URL http://dx.doi.org/10.1080/09500340412331283651.

[159] T. Wittmann, B. Horvath, W. Helml, M. G. Schätzel, X. Gu, A. L. Cavalieri, G. G. Paulus and R. Kienberger. *Single-shot carrier–envelope phase measurement of few-cycle laser pulses.* Nature Physics, **Vol. 5**, No. 5: pp. 357–362, 2009. ISSN 1745-2481. URL http://dx.doi.org/10.1038/nphys1250.

[160] A. M. Sayler, Tim Rathje, Walter Müller, Klaus Rühle, R. Kienberger and G. G. Paulus. *Precise, real-time, every-single-shot, carrier-envelope phase measurement of ultrashort laser pulses.* Opt. Lett., **Vol. 36**, No. 1: pp. 1–3, 2011. URL http://dx.doi.org/10.1364/OL.36.000001.

[161] M Kübel, K J Betsch, Nora G Johnson, U Kleineberg, R Moshammer, J Ullrich, G G Paulus, M F Kling and B Bergues. *Carrier-envelope-phase tagging in measurements with long acquisition times.* New Journal of Physics, **Vol. 14**, No. 9: p. 093027, 2012. URL http://dx.doi.org/10.1088/1367-2630/14/9/093027.

[162] Yinyu Zhang, Philipp Kellner, Daniel Adolph, Danilo Zille, Philipp Wustelt, Daniel Würzler, Slawomir Skruszewicz, Max Möller, A. Max Sayler and Gerhard G. Paulus. *Single-shot, real-time carrier-envelope phase measurement and tagging based on stereographic above-threshold ionization at short-wave infrared wavelengths.* Opt. Lett., **Vol. 42**, No. 24: pp. 5150–5153, 2017. URL http://dx.doi.org/10.1364/OL.42.005150.

[163] Dominik Hoff, Federico J. Furch, Tobias Witting, Klaus Rühle, Daniel Adolph, A. Max Sayler, Marc J. J. Vrakking, Gerhard G. Paulus and Claus Peter Schulz. *Continuous every-single-shot carrier-envelope phase measurement and control at 100 kHz.* Opt. Lett., **Vol. 43**, No. 16: pp. 3850–3853, 2018. URL http://dx.doi.org/10.1364/OL.43.003850.

[164] M Kübel, M Arbeiter, C Burger, Nora G Kling, T Pischke, R Moshammer, T Fennel, M F Kling and B Bergues. *Phase- and intensity-resolved measurements of above threshold ionization by few-cycle pulses.* Journal of Physics B: Atomic, Molecular and Optical Physics, **Vol. 51**, No. 13: p. 134007, 2018. URL http://dx.doi.org/10.1088/1361-6455/aac584.

[165] Bin Kim, Jeong uk Shin, Wosik Cho, Yang Hwan Kim, Kyung Hoon Yeom and Kyung Taec Kim. *Single-shot carrier-envelope-phase detection using tunneling ionization in ambient air.* Opt. Express, **Vol. 32**, No. 19: pp. 33795–33802, 2024. URL http://dx.doi.org/10.1364/OE.530546.

[166] C. Lemell, X.-M. Tong, F. Krausz and J. Burgdörfer. *Electron Emission from Metal Surfaces by Ultrashort Pulses: Determination of the Carrier-Envelope Phase.* Phys. Rev. Lett., **Vol. 90**: p. 076403, 2003. URL http://dx.doi.org/10.1103/PhysRevLett.90.076403.

[167] Tobias Rybka, Markus Ludwig, Michael F. Schmalz, Vanessa Knittel, Daniele Brida and Alfred Leitenstorfer. *Sub-cycle optical phase control of nanotunnelling in the single-electron regime.* Nature Photonics, **Vol. 10**, No. 10: pp. 667–670, 2016. ISSN 1749-4893. URL http://dx.doi.org/10.1038/nphoton.2016.174.

[168] P. D. Keathley, W. P. Putnam, P. Vasireddy, R. G. Hobbs, Y. Yang, K. K. Berggren and F. X. Kärtner. *Vanishing carrier-envelope-phase-sensitive response in optical-field photoemission from plasmonic nanoantennas.* Nature Physics, **Vol. 15**, No. 11: pp. 1128–1133, 2019. ISSN 1745-2481. URL http://dx.doi.org/10.1038/s41567-019-0613-6.

[169] Markus Ludwig, Andrey K. Kazansky, Garikoitz Aguirregabiria, Dana Codruta Marinica, Matthias Falk, Alfred Leitenstorfer, Daniele Brida, Javier Aizpurua and Andrei G. Borisov. *Active control of ultrafast electron dynamics in plasmonic gaps using an applied bias.* Phys. Rev. B, **Vol. 101**, No. 24: p. 241412, 2020. URL http://dx.doi.org/10.1103/PhysRevB.101.241412.

[170] Markus Ludwig, Garikoitz Aguirregabiria, Felix Ritzkowsky, Tobias Rybka, Dana Codruta Marinica, Javier Aizpurua, Andrei G. Borisov, Alfred Leitenstorfer and Daniele Brida. *Sub-femtosecond electron transport in a nanoscale gap*. Nature Physics, **Vol. 16**, No. 3: pp. 341–345, 2020. ISSN 1745-2481. URL http://dx.doi.org/10.1038/s41567-019-0745-8.

[171] Andrea Rossetti, Matthias Falk, Alfred Leitenstorfer, Daniele Brida and Markus Ludwig. *Gouy phase effects on photocurrents in plasmonic nanogaps driven by single-cycle pulses*. Nanophotonics, **Vol. 13**, No. 15: pp. 2803–2809, 2024. URL http://dx.doi.org/doi:10.1515/nanoph-2023-0897.

[172] Michael Krüger, Markus Schenk and Peter Hommelhoff. *Attosecond control of electrons emitted from a nanoscale metal tip*. Nature, **Vol. 475**, No. 7354: pp. 78–81, 2011. ISSN 1476-4687. URL http://dx.doi.org/10.1038/nature10196.

[173] L. Wimmer, G. Herink, D. R. Solli, S. V. Yalunin, K. E. Echternkamp and C. Ropers. *Terahertz control of nanotip photoemission*. Nature Physics, **Vol. 10**, No. 6: pp. 432–436, 2014. ISSN 1745-2481. URL http://dx.doi.org/10.1038/nphys2974.

[174] Sebastian Thomas, Georg Wachter, Christoph Lemell, Joachim Burgdörfer and Peter Hommelhoff. *Large optical field enhancement for nanotips with large opening angles*. New Journal of Physics, **Vol. 17**, No. 6: p. 063010, 2015. URL http://dx.doi.org/10.1088/1367-2630/17/6/063010.

[175] Michael Krüger, Christoph Lemell, Georg Wachter, Joachim Burgdörfer and Peter Hommelhoff. *Attosecond physics phenomena at nanometric tips*. Journal of Physics B: Atomic, Molecular and Optical Physics, **Vol. 51**, No. 17: p. 172001, 2018. URL http://dx.doi.org/10.1088/1361-6455/aac6ac.

[176] M. Garg and K. Kern. *Attosecond coherent manipulation of electrons in tunneling microscopy*. Science, **Vol. 367**, No. 6476: pp. 411–415, 2020. ISSN 0036-8075. https://science.sciencemag.org/content/367/6476/411.full.pdf, URL http://dx.doi.org/10.1126/science.aaz1098.

[177] Christian Burger. *Laser-induced nuclear dynamics in hydrocarbons*. Ph.D. thesis, Ludwig-Maximilians-Universität München, München, 2018. URL http://nbn-resolving.de/urn:nbn:de:bvb:19-223296.

[178] Sebastian Koke, Christian Grebing, Harald Frei, Alexandria Anderson, Andreas Assion and Günter Steinmeyer. *Direct frequency comb synthesis with arbitrary offset and shot-noise-limited phase noise*. Nature Photonics, **Vol. 4**, No. 7: pp. 462–465, 2010. ISSN 1749-4893. URL http://dx.doi.org/10.1038/nphoton.2010.91.

[179] Fabian Lücking, Andreas Assion, Alexander Apolonski, Ferenc Krausz and Günter Steinmeyer. *Long-term carrier-envelope-phase-stable few-cycle pulses by use of the feed-forward method*. Opt. Lett., **Vol. 37**, No. 11: pp. 2076–2078, 2012. URL http://dx.doi.org/10.1364/OL.37.002076.

[180] H. R. Telle, G. Steinmeyer, A. E. Dunlop, J. Stenger, D. H. Sutter and U. Keller. *Carrier-envelope offset phase control: A novel concept for absolute optical frequency measurement and ultrashort pulse generation*. Applied Physics B, **Vol. 69**, No. 4: pp. 327–332, 1999. ISSN 1432-0649. URL http://dx.doi.org/10.1007/s003400050813.

[181] Henry Timmers, Yuki Kobayashi, Kristina F. Chang, Maurizio Reduzzi, Daniel M. Neumark and Stephen R. Leone. *Generating high-contrast, near single-cycle waveforms with third-order dispersion compensation.* Opt. Lett., **Vol. 42**, No. 4: pp. 811–814, 2017. URL http://dx.doi.org/10.1364/OL.42.000811.

[182] Miguel Miranda, Cord L. Arnold, Thomas Fordell, Francisco Silva, Benjamín Alonso, Rosa Weigand, Anne L'Huillier and Helder Crespo. *Characterization of broadband few-cycle laser pulses with the d-scan technique.* Opt. Express, **Vol. 20**, No. 17: pp. 18732–18743, 2012. URL http://dx.doi.org/10.1364/OE.20.018732.

[183] Esmerando Escoto, Ayhan Tajalli, Tamas Nagy and Günter Steinmeyer. *Advanced phase retrieval for dispersion scan: a comparative study.* J. Opt. Soc. Am. B, **Vol. 35**, No. 1: pp. 8–19, 2018. URL http://dx.doi.org/10.1364/JOSAB.35.000008.

[184] FEMTO Messtechnik GmbH, Klosterstr. 64, 10179 Berlin, Germany. *Datasheet DLPCA-200*, 2019. Version: DE-DLPCA-200_R19/JM/02JAN2019, 2019.

[185] Ryuji Itakura, Kaoru Yamanouchi, Takasumi Tanabe, Tatsuyoshi Okamoto and Fumihiko Kannari. *Dissociative ionization of ethanol in chirped intense laser fields.* The Journal of Chemical Physics, **Vol. 119**, No. 8: pp. 4179–4186, 2003. ISSN 0021-9606. https://pubs.aip.org/aip/jcp/article-pdf/119/8/4179/19235477/4179_1_online.pdf, URL http://dx.doi.org/10.1063/1.1592504.

[186] T Ikuta, K Hosaka, H Akagi, A Yokoyama, K Yamanouchi, F Kannari and R Itakura. *Separation of ionization and subsequent electronic excitation for formation of electronically excited ethanol cation in intense laser fields.* Journal of Physics B: Atomic, Molecular and Optical Physics, **Vol. 44**, No. 19: p. 191002, 2011. URL http://dx.doi.org/10.1088/0953-4075/44/19/191002.

[187] Koji Sugioka and Ya Cheng. *Ultrafast lasers—reliable tools for advanced materials processing.* Light: Science & Applications, **Vol. 3**, No. 4: pp. e149–e149, 2014. ISSN 2047-7538. URL http://dx.doi.org/10.1038/lsa.2014.30.

[188] Mangirdas Malinauskas, Albertas Žukauskas, Satoshi Hasegawa, Yoshio Hayasaki, Vygantas Mizeikis, Ričardas Buividas and Saulius Juodkazis. *Ultrafast laser processing of materials: from science to industry.* Light: Science & Applications, **Vol. 5**, No. 8: pp. e16133–e16133, 2016. ISSN 2047-7538. URL http://dx.doi.org/10.1038/lsa.2016.133.

[189] Lucas Eisenbach, Ziyao Wang, Jan Schulte, Tobias Heuermann, Peter Russbüldt, Rudolf Meyer, Philipp Gierschke, Mathias Lenski, Muneo Sugiura, Koichi Tamura, Jens Limpert and Constantin Häfner. *Highly efficient nonlinear compression of mJ pulses at 2 μm wavelength to 20 fs in a gas-filled multi-pass cell.* Journal of Physics: Photonics, **Vol. 6**, No. 3: p. 035015, 2024. URL http://dx.doi.org/10.1088/2515-7647/ad4cc4.

[190] E. Goulielmakis, V. S. Yakovlev, A. L. Cavalieri, M. Uiberacker, V. Pervak, A. Apolonski, R. Kienberger, U. Kleineberg and F. Krausz. *Attosecond Control and Measurement: Lightwave Electronics.* Science, **Vol. 317**, No. 5839: pp. 769–775, 2007. https://www.science.org/doi/pdf/10.1126/science.1142855, URL http://dx.doi.org/10.1126/science.1142855.

[191] Shih-Hsuan Chia, Giovanni Cirmi, Shaobo Fang, Giulio M. Rossi, Oliver D. Mücke and Franz X. Kärtner. *Two-octave-spanning dispersion-controlled precision optics for sub-optical-cycle waveform synthesizers.* Optica, **Vol. 1**, No. 5: pp. 315–322, 2014. URL http://dx.doi.org/10.1364/OPTICA.1.000315.

[192] Ayman Alismail, Haochuan Wang, Gaia Barbiero, Najd Altwaijry, Syed Ali Hussain, Volodymyr Pervak, Wolfgang Schweinberger, Abdallah M. Azzeer, Ferenc Krausz and Hanieh Fattahi. *Multi-octave, CEP-stable source for high-energy field synthesis.* Science Advances, **Vol. 6**, No. 7: p. eaax3408, 2020. https://www.science.org/doi/pdf/10.1126/sciadv.aax3408, URL http://dx.doi.org/10.1126/sciadv.aax3408.

[193] Z. Pi, H. Y. Kim and E. Goulielmakis. *Synthesis of single-cycle pulses based on a Yb:KGW laser amplifier.* Optica, **Vol. 12**, No. 3: pp. 296–301, 2025. URL http://dx.doi.org/10.1364/OPTICA.544731.

[194] Guan Gui, Amitava Adak, Manika Dandapat, Daniel Carlson, Drew Morrill, Alexander Guggenmos, Henry Kapteyn, Margaret Murnane, Vladimir Pervak and Chen-Ting Liao. *Measurement and control of optical nonlinearities in dispersive dielectric multilayers.* Opt. Express, **Vol. 29**, No. 4: pp. 4947–4957, 2021. URL http://dx.doi.org/10.1364/OE.409216.

[195] Nicholas L. Wagner, Emily A. Gibson, Tenio Popmintchev, Ivan P. Christov, Margaret M. Murnane and Henry C. Kapteyn. *Self-Compression of Ultrashort Pulses through Ionization-Induced Spatiotemporal Reshaping.* Phys. Rev. Lett., **Vol. 93**: p. 173902, 2004. URL http://dx.doi.org/10.1103/PhysRevLett.93.173902.

[196] Andrea Blanco-Redondo, C. Martijn de Sterke, Chris Xu, Stefan Wabnitz and Sergei K. Turitsyn. *The bright prospects of optical solitons after 50 years.* Nature Photonics, **Vol. 17**, No. 11: pp. 937–942, 2023. ISSN 1749-4893. URL http://dx.doi.org/10.1038/s41566-023-01307-9.

[197] F. Köttig, D. Novoa, F. Tani, M. C. Günendi, M. Cassataro, J. C. Travers and P. St.J. Russell. *Mid-infrared dispersive wave generation in gas-filled photonic crystal fibre by transient ionization-driven changes in dispersion.* Nature Communications, **Vol. 8**, No. 1: p. 813, 2017. ISSN 2041-1723. URL http://dx.doi.org/10.1038/s41467-017-00943-4.

[198] John C. Travers, Wonkeun Chang, Johannes Nold, Nicolas Y. Joly and Philip St. J. Russell. *Ultrafast nonlinear optics in gas-filled hollow-core photonic crystal fibers - Invited.* J. Opt. Soc. Am. B, **Vol. 28**, No. 12: pp. A11–A26, 2011. URL http://dx.doi.org/10.1364/JOSAB.28.000A11.

[199] P. St. J. Russell, P. Hölzer, W. Chang, A. Abdolvand and J. C. Travers. *Hollow-core photonic crystal fibres for gas-based nonlinear optics.* Nature Photonics, **Vol. 8**, No. 4: pp. 278–286, 2014. ISSN 1749-4893. URL http://dx.doi.org/10.1038/nphoton.2013.312.

[200] Christos Markos, John C. Travers, Amir Abdolvand, Benjamin J. Eggleton and Ole Bang. *Hybrid photonic-crystal fiber.* Rev. Mod. Phys., **Vol. 89**: p. 045003, 2017. URL http://dx.doi.org/10.1103/RevModPhys.89.045003.

[201] Ugaitz Elu, Matthias Baudisch, Hugo Pires, Francesco Tani, Michael H. Frosz, Felix Köttig, Alexey Ermolov, Philip St.J. Russell and Jens Biegert. *High*

average power and single-cycle pulses from a mid-IR optical parametric chirped pulse amplifier. Optica, **Vol. 4**, No. 9: pp. 1024–1029, 2017. URL http://dx.doi.org/10.1364/OPTICA.4.001024.

[202] I. V. Savitsky, E. A. Stepanov, A. A. Lanin, A. B. Fedotov and A. M. Zheltikov. *Single-Cycle, Multigigawatt Carrier–Envelope-Phase-Tailored Near-to-Mid-Infrared Driver for Strong-Field Nonlinear Optics.* ACS Photonics, **Vol. 9**, No. 5: pp. 1679–1690, 2022. https://doi.org/10.1021/acsphotonics.2c00072, URL http://dx.doi.org/10.1021/acsphotonics.2c00072.

[203] Kirk A. Larsen, Christopher Lantigua, Chelsea Kincaid, Felix Allum, Mathew Britton, José L. Godínez Castellanos, Brian Kaufman, Marcel Neuhaus, François Sylla, Kyung Taec Kim, Stephen E. Bradforth, Matthias F. Kling, Joseph S. Robinson, Christian Brahms, John C. Travers, Michael Chini, Matthew Bain and Ruaridh Forbes. *Characterizing few-cycle UV resonant dispersive waves through direct field sampling.* Opt. Lett., **Vol. 50**, No. 16: pp. 4962–4965, 2025. URL http://dx.doi.org/10.1364/OL.566906.

[204] Francesco Tani, John C. Travers and Philip St.J. Russell. *Multimode ultrafast nonlinear optics in optical waveguides: numerical modeling and experiments in kagomé photonic-crystal fiber.* J. Opt. Soc. Am. B, **Vol. 31**, No. 2: pp. 311–320, 2014. URL http://dx.doi.org/10.1364/JOSAB.31.000311.

[205] C. Vozzi, M. Nisoli, G. Sansone, S. Stagira and S. De Silvestri. *Optimal spectral broadening in hollow-fiber compressor systems.* Applied Physics B, **Vol. 80**, No. 3: pp. 285–289, 2005. ISSN 1432-0649. URL http://dx.doi.org/10.1007/s00340-004-1721-1.

[206] Kristina S. Zinchenko, Fernando Ardana-Lamas, Valentina Utrio Lanfaloni, Yoann Pertot, Tran Trung Luu and Hans Jakob Wörner. *Energy scaling of carrier-envelope-phase-stable sub-two-cycle pulses at 1.76 μm from hollow-core-fiber compression to 1.9 mJ.* Opt. Express, **Vol. 30**, No. 13: pp. 22376–22387, 2022. URL http://dx.doi.org/10.1364/OE.457477.

[207] Eduardo Granados, Li-Jin Chen, Chien-Jen Lai, Kyung-Han Hong and Franz X. Kärtner. *Wavelength scaling of optimal hollow-core fiber compressors in the single-cycle limit.* Opt. Express, **Vol. 20**, No. 8: pp. 9099–9108, 2012. URL http://dx.doi.org/10.1364/OE.20.009099.

[208] Nenad Milosevic, Gabriel Tempea and Thomas Brabec. *Optical pulse compression: bulk media versus hollow waveguides.* Opt. Lett., **Vol. 25**, No. 9: pp. 672–674, 2000. URL http://dx.doi.org/10.1364/OL.25.000672.

[209] Carsten Brée, Ayhan Demircan and Günter Steinmeyer. *Method for Computing the Nonlinear Refractive Index via Keldysh Theory.* IEEE Journal of Quantum Electronics, **Vol. 46**, No. 4: pp. 433–437, 2010. URL http://dx.doi.org/10.1109/JQE.2009.2031599.

[210] S. Zahedpour, J. K. Wahlstrand and H. M. Milchberg. *Measurement of the nonlinear refractive index of air constituents at mid-infrared wavelengths.* Opt. Lett., **Vol. 40**, No. 24: pp. 5794–5797, 2015. URL http://dx.doi.org/10.1364/OL.40.005794.

[211] Carsten Brée, Ayhan Demircan and Günter Steinmeyer. *Kramers-Kronig relations and high-order nonlinear susceptibilities.* Phys. Rev. A, **Vol. 85**: p. 033806, 2012. URL http://dx.doi.org/10.1103/PhysRevA.85.033806.

[212] Á. Börzsönyi, Z. Heiner, A.P. Kovács, M. P. Kalashnikov and K. Osvay. *Measurement of pressure dependent nonlinear refractive index of inert gases.* Opt. Express, **Vol. 18**, No. 25: pp. 25847–25854, 2010. URL http://dx.doi.org/10.1364/OE.18.025847.

[213] A. Börzsönyi, Z. Heiner, M. P. Kalashnikov, A. P. Kovács and K. Osvay. *Dispersion measurement of inert gases and gas mixtures at 800 nm.* Appl. Opt., **Vol. 47**, No. 27: pp. 4856–4863, 2008. URL http://dx.doi.org/10.1364/AO.47.004856.

[214] Maximilian F. Seeger, Dominik Kammerer, Johannes Blöchl, Marcel Neuhaus, Vladimir Pervak, Thomas Nubbemeyer and Matthias F. Kling. *49 W carrier-envelope-phase-stable few-cycle 2.1μm OPCPA at 10 kHz.* Opt. Express, **Vol. 31**, No. 15: pp. 24821–24834, 2023. URL http://dx.doi.org/10.1364/OE.493326.

[215] Maximilian Seeger. *Development of high power CEP-stable light sources.* Ph.D. thesis, Ludwig-Maximilians-Universität München, 2023. URL http://nbn-resolving.de/urn:nbn:de:bvb:19-326238.

[216] Thomas Nubbemeyer, Martin Kaumanns, Moritz Ueffing, Martin Gorjan, Ayman Alismail, Hanieh Fattahi, Jonathan Brons, Oleg Pronin, Helena G. Barros, Zsuzsanna Major, Thomas Metzger, Dirk Sutter and Ferenc Krausz. *1 kW, 200 mJ picosecond thin-disk laser system.* Opt. Lett., **Vol. 42**, No. 7: pp. 1381–1384, 2017. URL http://dx.doi.org/10.1364/OL.42.001381.

[217] D.J. Kane and R. Trebino. *Characterization of arbitrary femtosecond pulses using frequency-resolved optical gating.* IEEE Journal of Quantum Electronics, **Vol. 29**, No. 2: pp. 571–579, 1993. URL http://dx.doi.org/10.1109/3.199311.

[218] Rick Trebino and Daniel J. Kane. *Using phase retrieval to measure the intensity and phase of ultrashort pulses: frequency-resolved optical gating.* J. Opt. Soc. Am. A, **Vol. 10**, No. 5: pp. 1101–1111, 1993. URL http://dx.doi.org/10.1364/JOSAA.10.001101.

[219] Peter Simon and Tamas Nagy. Patent DE 10 2007 048 769 B3, assignee: Laser Laboratorium Göttingen e.V. 10.10.2007.

[220] Amir Abdolvand, Federico Belli, John Travers and Philip Russell. Patent US 9,160,137 B1, assignee: Max-Planck-Gesellschaft zur Förderung der Wissenschaften e.V. 9.5.2014.

[221] Riccardo Piccoli, Bruno E. Schmidt, Luca Razzari, Younggyn Jeong and Roberto Morandotti. Patent US 11,289,870 B2, assignee: Institut National de la Recherche Scientifique 7.2.2020.

[222] François Légaré, Reza Safaei Mohammadabadi and Guangyu Fan. Patent CA 3 180 870 A1, assignee: Institut National de la Recherche Scientifique 7.6.2021.

[223] Andreas Blumenstein. Patent DE 10 2021 103 097 B3, assignee: Institut für Nanophotonik Göttingen e.V. 10.2.2022.

[224] Mikalai Zhavarankau. Patent DE 10 2014 215 415 C5, assignee: Institut für Nanophotonik Göttingen e.V. 5.8.2014.

[225] Molex. *Data Sheet*, 2024. Polymicro flexible fused silica capillary tubing, Part no. 1068150029.

[226] Molex. *Data Sheet*, 2024. Polymicro flexible fused silica capillary tubing, Part no. 1068150028.

[227] Gutekunst Federn. *Datenblatt Zugfeder RZ-094AX*, 2025. URL https://www.federnshop.com/de/produkte/zugfedern/rz-094ax.html.

[228] Christian Brahms. *Effect of nonlinear lensing on the coupling of ultrafast laser pulses to hollow-core waveguides.* Opt. Express, **Vol. 31**, No. 5: pp. 7187–7199, 2023. URL http://dx.doi.org/10.1364/OE.482749.

[229] Arlee Smith. *SNLO classic (free version).* Downloaded 30 June 2025, URL https://as-photonics.com/products/snlo/.

[230] Gintaras Tamošauskas. *β-Barium Borate (BBO) Absorption in the 0.188-6.22 µm Range*, 2021. ArXiv, 2111.01212, URL https://arxiv.org/abs/2111.01212.

[231] Value provided by the supplier upon request.

[232] Benjamín Alonso, Miguel Miranda, Francisco Silva, Vladimir Pervak, Jens Rauschenberger, Julio San Román, Íñigo J. Sola and Helder Crespo. *Characterization of sub-two-cycle pulses from a hollow-core fiber compressor in the spatiotemporal and spatiospectral domains.* Applied Physics B, **Vol. 112**, No. 1: pp. 105–114, 2013. ISSN 1432-0649. URL http://dx.doi.org/10.1007/s00340-013-5406-5.

[233] P. Béjot, B. E. Schmidt, J. Kasparian, J.-P. Wolf and F. Legaré. *Mechanism of hollow-core-fiber infrared-supercontinuum compression with bulk material.* Phys. Rev. A, **Vol. 81**: p. 063828, 2010. URL http://dx.doi.org/10.1103/PhysRevA.81.063828.

[234] Bruno E. Schmidt, Pierre Béjot, Mathieu Giguère, Andrew D. Shiner, Carlos Trallero-Herrero, Éric Bisson, Jérôme Kasparian, Jean-Pierre Wolf, David M. Villeneuve, Jean-Claude Kieffer, Paul B. Corkum and François Légaré. *Compression of 1.8 µm laser pulses to sub two optical cycles with bulk material.* Applied Physics Letters, **Vol. 96**, No. 12: p. 121109, 2010. ISSN 0003-6951. https://pubs.aip.org/aip/apl/article-pdf/doi/10.1063/1.3359458/14663274/121109_1_online.pdf, URL http://dx.doi.org/10.1063/1.3359458.

[235] Guangyu Fan, Tadas Balčiūnas, Tsuneto Kanai, Tobias Flöry, Giedrius Andriukaitis, Bruno E. Schmidt, François Légaré and Andrius Baltuška. *Hollow-core-waveguide compression of multi-millijoule CEP-stable 3.2 µm pulses.* Optica, **Vol. 3**, No. 12: pp. 1308–1311, 2016. URL http://dx.doi.org/10.1364/OPTICA.3.001308.

[236] Kyung-Han Hong, Chien-Jen Lai, Jonathas P. Siqueira, Peter Krogen, Jeffrey Moses, Chun-Lin Chang, Gregory J. Stein, Luis E. Zapata and Franz X. Kärtner. *Multi-mJ, kHz, 2.1 µm optical parametric chirped-pulse amplifier and high-flux soft x-ray high-harmonic generation.* Opt. Lett., **Vol. 39**, No. 11: pp. 3145–3148, 2014. URL http://dx.doi.org/10.1364/OL.39.003145.

[237] Yanchun Yin, Jie Li, Xiaoming Ren, Kun Zhao, Yi Wu, Eric Cunningham and Zenghu Chang. *High-efficiency optical parametric chirped-pulse amplifier in BiB3O6 for generation of 3 mJ, two-cycle, carrier-envelope-phase-stable pulses at 1.7 µm.* Opt. Lett., **Vol. 41**, No. 6: pp. 1142–1145, 2016. URL http://dx.doi.org/10.1364/OL.41.001142.

[238] Yunpei Deng, Alexander Schwarz, Hanieh Fattahi, Moritz Ueffing, Xun Gu, Marcus Ossiander, Thomas Metzger, Volodymyr Pervak, Hideki Ishizuki, Takunori Taira, Takayoshi Kobayashi, Gilad Marcus, Ferenc Krausz, Reinhard Kienberger and Nicholas Karpowicz. *Carrier-envelope-phase-stable, 1.2 mJ, 1.5 cycle laser pulses at 2.1 µm*. Opt. Lett., **Vol. 37**, No. 23: pp. 4973–4975, 2012. URL http://dx.doi.org/10.1364/OL.37.004973.

[239] Tianli Feng, Anke Heilmann, Martin Bock, Lutz Ehrentraut, Tobias Witting, Haohai Yu, Holger Stiel, Stefan Eisebitt and Matthias Schnürer. *27 W 2.1 µm OPCPA system for coherent soft X-ray generation operating at 10 kHz*. Opt. Express, **Vol. 28**, No. 6: pp. 8724–8733, 2020. URL http://dx.doi.org/10.1364/OE.386588.

[240] Jan Heye Buss, Sebastian Starosielec, Michael Schulz, Robert Riedel, Filippo Campi, Carl Stefan Lehmann, Stefan Witte and Peter M. Kraus. *Mid-infrared optical parametric chirped-pulse amplifier at 50 W and 38 fs pumped by a high-power Yb-InnoSlab platform*. Opt. Express, **Vol. 32**, No. 21: pp. 36185–36192, 2024. URL http://dx.doi.org/10.1364/OE.539079.

[241] Simon Reiger, Mikhail Mamaikin, Dmitrii Kormin, Keyhan Golyari, Hadil Kassab, Maximilian Seeger, Volodymyr Pervak, Nicholas Karpowicz and Thomas Nubbemeyer. *Ultra-phase-stable infrared light source at the watt level*. Opt. Lett., **Vol. 49**, No. 4: pp. 1049–1052, 2024. URL http://dx.doi.org/10.1364/OL.509905.

[242] Daniel Walke, Azize Koç, Florian Gores, Minjie Zhan, Nicolas Forget, Raman Maksimenka and Iain Wilkinson. *High-average-power, few-cycle, 2.1 µm OPCPA laser driver for soft-X-ray high-harmonic generation*. Opt. Express, **Vol. 33**, No. 5: pp. 10006–10019, 2025. URL http://dx.doi.org/10.1364/OE.547689.

[243] Matthew K. R. Windeler, Katalin Mecseki, Alan Miahnahri, Joseph S. Robinson, James M. Fraser, Alan R. Fry and Franz Tavella. *100 W high-repetition-rate near-infrared optical parametric chirped pulse amplifier*. Opt. Lett., **Vol. 44**, No. 17: pp. 4287–4290, 2019. URL http://dx.doi.org/10.1364/OL.44.004287.

[244] Yariv Shamir, Jan Rothhardt, Steffen Hädrich, Stefan Demmler, Maxim Tschernajew, Jens Limpert and Andreas Tünnermann. *High-average-power 2 µm few-cycle optical parametric chirped pulse amplifier at 100 kHz repetition rate*. Opt. Lett., **Vol. 40**, No. 23: pp. 5546–5549, 2015. URL http://dx.doi.org/10.1364/OL.40.005546.

[245] M. Neuhaus, H. Fuest, M. Seeger, J. Schötz, M. Trubetskov, P. Russbueldt, H.D. Hoffmann, E. Riedle, Zs. Major, V. Pervak, M. F. Kling and P. Wnuk. *10 W CEP-stable few-cycle source at 2 µm with 100 kHz repetition rate*. Opt. Express, **Vol. 26**, No. 13: pp. 16074–16085, 2018. URL http://dx.doi.org/10.1364/OE.26.016074.

[246] Ziyao Wang, Tobias Heuermann, Martin Gebhardt, Mathias Lenski, Philipp Gierschke, Robert Klas, Jan Rothhardt, Cesar Jauregui and Jens Limpert. *Nonlinear pulse compression to sub-two-cycle, 1.3 mJ pulses at 1.9 µm wavelength with 132 W average power*. Opt. Lett., **Vol. 48**, No. 10: pp. 2647–2650, 2023. URL http://dx.doi.org/10.1364/OL.487587.

[247] Bruno E. Schmidt, Andrew D. Shiner, Philippe Lassonde, Jean-Claude Kieffer, Paul B. Corkum, David M. Villeneuve and François Légaré. *CEP stable 1.6*

cycle laser pulses at 1.8 μm. Opt. Express, **Vol. 19**, No. 7: pp. 6858–6864, 2011. URL http://dx.doi.org/10.1364/OE.19.006858.

[248] S. L. Cousin, F. Silva, S. Teichmann, M. Hemmer, B. Buades and J. Biegert. *High-flux table-top soft x-ray source driven by sub-2-cycle, CEP stable, 1.85-μm 1-kHz pulses for carbon K-edge spectroscopy.* Opt. Lett., **Vol. 39**, No. 18: pp. 5383–5386, 2014. URL http://dx.doi.org/10.1364/OL.39.005383.

[249] Tamas Nagy, Lorenz von Grafenstein, Dennis Ueberschaer and Uwe Griebner. *Femtosecond multi-10-mJ pulses at 2 μm wavelength by compression in a hollow-core fiber.* Opt. Lett., **Vol. 46**, No. 13: pp. 3033–3036, 2021. URL http://dx.doi.org/10.1364/OL.426340.

[250] Dane R. Austin, Tobias Witting, Sébastien J. Weber, Peng Ye, Thomas Siegel, Paloma Matía-Hernando, Allan S. Johnson, John W.G. Tisch and Jonathan P. Marangos. *Spatio-temporal characterization of intense few-cycle 2 μm pulses.* Opt. Express, **Vol. 24**, No. 21: pp. 24786–24798, 2016. URL http://dx.doi.org/10.1364/OE.24.024786.

[251] Chuang Li, Ding Wang, Liwei Song, Jun Liu, Peng Liu, Canhua Xu, Yuxin Leng, Ruxin Li and Zhizhan Xu. *Generation of carrier-envelope phase stabilized intense 1.5 cycle pulses at 1.75 μm.* Opt. Express, **Vol. 19**, No. 7: pp. 6783–6789, 2011. URL http://dx.doi.org/10.1364/OE.19.006783.

[252] Xun Gu, Gilad Marcus, Yunpei Deng, Thomas Metzger, Catherine Teisset, Nobuhisa Ishii, Takao Fuji, Andrius Baltuska, Rytis Butkus, Volodymyr Pervak, Hideki Ishizuki, Takunori Taira, Takayoshi Kobayashi, Reinhard Kienberger and Ferenc Krausz. *Generation of carrier-envelope-phase-stable 2-cycle 740-μJ pulses at 2.1-μm carrier wavelength.* Opt. Express, **Vol. 17**, No. 1: pp. 62–69, 2009. URL http://dx.doi.org/10.1364/OE.17.000062.

[253] Augustinas Petrulėnas, Paulius Mackonis and Aleksej M. Rodin. *High-efficiency bismuth borate-based optical parametric chirped pulse amplifier with approximately 2.1 mJ, 38 fs output pulses at approximately 2150 nm.* High Power Laser Science and Engineering, **Vol. 11**: p. e27, 2023. URL http://dx.doi.org/10.1017/hpl.2023.24.

[254] Fanqi Kong, Hugo Larocque, Ebrahim Karimi, P. B. Corkum and Chunmei Zhang. *Generating few-cycle radially polarized pulses.* Optica, **Vol. 6**, No. 2: pp. 160–164, 2019. URL http://dx.doi.org/10.1364/OPTICA.6.000160.

[255] Alba de las Heras, Franco P. Bonafé, Carlos Hernández-García, Angel Rubio and Ofer Neufeld. *Tunable Tesla-Scale Magnetic Attosecond Pulses through Ring-Current Gating.* The Journal of Physical Chemistry Letters, **Vol. 14**, No. 49: pp. 11160–11167, 2023. URL http://dx.doi.org/10.1021/acs.jpclett.3c02899.

[256] Yu Chen, Weiwei Li, Zilong Wang, Daniel Hahner, Matthias F. Kling and Vladimir Pervak. *Complementary dispersive mirror pair produced in one coating run based on desired non-uniformity.* Opt. Express, **Vol. 30**, No. 18: pp. 32074–32083, 2022. URL http://dx.doi.org/10.1364/OE.467664.

[257] Maciej Kowalczyk, Nathalie Nagl, Philipp Steinleitner, Nicholas Karpowicz, Vladimir Pervak, Aleksander Głuszek, Arkadiusz Hudzikowski, Ferenc Krausz, Ka Fai Mak and Alexander Weigel. *Ultra-CEP-stable single-cycle pulses at 2.2 μm.* Optica, **Vol. 10**, No. 6: pp. 801–811, 2023. URL http://dx.doi.org/10.1364/OPTICA.481673.

[258] Kristina S. Zinchenko, Fernando Ardana-Lamas, Valentina Utrio Lanfaloni, Tran Trung Luu, Yoann Pertot, Martin Huppert and Hans Jakob Wörner. *Apparatus for attosecond transient-absorption spectroscopy in the water-window soft-X-ray region*. Scientific Reports, **Vol. 13**, No. 1: p. 3059, 2023. ISSN 2045-2322. URL http://dx.doi.org/10.1038/s41598-023-29089-8.

[259] Johannes Blöchl, Maximilian F. Kuthe, Fritz Keilmann, Thomas E. Nubbemeyer and Matthias F. Kling. German patent application DE 10 2025 119 843.8, assignee: Ludwig-Maximilians-Universität München and Max-Planck-Gesellschaft zur Förderung der Wissenschaften e.V., 21.05.2025, patent filed.

[260] Alexander Guggenmos, Yang Cui, Stephan Heinrich and Ulf Kleineberg. *Attosecond Pulse Shaping by Multilayer Mirrors*. Applied Sciences, **Vol. 8**, No. 12, 2018. ISSN 2076-3417. URL http://dx.doi.org/10.3390/app8122503.

[261] C. Y. Ho, R. W. Powell and P. E. Liley. *Thermal Conductivity of the Elements*. Journal of Physical and Chemical Reference Data, **Vol. 1**, No. 2: pp. 279–421, 1972. ISSN 0047-2689. https://pubs.aip.org/aip/jpr/article-pdf/1/2/279/19140486/279_1_online.pdf, URL http://dx.doi.org/10.1063/1.3253100.

[262] B.L. Henke, E.M. Gullikson and J.C. Davis. *X-Ray Interactions: Photoabsorption, Scattering, Transmission, and Reflection at E = 50-30,000 eV, Z = 1-92*. Atomic Data and Nuclear Data Tables, **Vol. 54**, No. 2: pp. 181–342, 1993. ISSN 0092-640X. URL http://dx.doi.org/https://doi.org/10.1006/adnd.1993.1013.

[263] Fritz Keilmann. *Infrared high-pass filter with high contrast*. International Journal of Infrared and Millimeter Waves, **Vol. 2**, No. 2: pp. 259–272, 1981. ISSN 1572-9559. URL http://dx.doi.org/10.1007/BF01007034.

[264] Fritz Keilmann. *Precision Broadband Far-Infrared Attenuator*. In Jerald A. R. Izatt (Editor), *Far-Infrared Science and Technology*, Vol. 0666, pp. 213 – 218. International Society for Optics and Photonics, SPIE, 1986. URL http://dx.doi.org/10.1117/12.938837.

[265] Fritz Keilmann. *Nonlinear far-infrared spectroscopy of solids*. Infrared Physics, **Vol. 31**, No. 4: pp. 373–380, 1991. ISSN 0020-0891. URL http://dx.doi.org/https://doi.org/10.1016/0020-0891(91)90011-4.

[266] Wolfgang S. M. Werner, Kathrin Glantschnig and Claudia Ambrosch-Draxl. *Optical Constants and Inelastic Electron-Scattering Data for 17 Elemental Metals*. Journal of Physical and Chemical Reference Data, **Vol. 38**, No. 4: pp. 1013–1092, 2009. ISSN 0047-2689. https://pubs.aip.org/aip/jpr/article-pdf/38/4/1013/16152713/1013_1_online.pdf, URL http://dx.doi.org/10.1063/1.3243762.

[267] Shaista Babar and J. H. Weaver. *Optical constants of Cu, Ag, and Au revisited*. Appl. Opt., **Vol. 54**, No. 3: pp. 477–481, 2015. URL http://dx.doi.org/10.1364/AO.54.000477.

[268] Mark A. Ordal, Robert J. Bell, Ralph W. Alexander, Larry L. Long and Marvin R. Querry. *Optical properties of Au, Ni, and Pb at submillimeter wavelengths*. Appl. Opt., **Vol. 26**, No. 4: pp. 744–752, 1987. URL http://dx.doi.org/10.1364/AO.26.000744.

[269] Fritz Keilmann and Karl-Wilhelm Kussmaul. Patent US 4,561,721, assignee: Max-Planck-Gesellschaft zur Förderung der Wissenschaften e.V. 21 Dec 1983; priority date 23 Dec 1982.

[270] G. Schmidtke. *Diffraction Filters in XUV Spectroscopy.* Appl. Opt., **Vol. 9**, No. 2: pp. 447–450, 1970. URL http://dx.doi.org/10.1364/AO.9.000447.

[271] Qi Zhang, Kun Zhao, Jie Li, Michael Chini, Yan Cheng, Yi Wu, Eric Cunningham and Zenghu Chang. *Suppression of driving laser in high harmonic generation with a microchannel plate.* Opt. Lett., **Vol. 39**, No. 12: pp. 3670–3673, 2014. URL http://dx.doi.org/10.1364/OL.39.003670.

[272] Zenghu Chang, Qi Zhang and Kun Zhao. Patent US 9,158,176 B2, assignee: University of Central Florida Research Foundation, Inc. 14 Jan 2014.

[273] Joseph Ladislas Wiza. *Microchannel plate detectors.* Nuclear Instruments and Methods, **Vol. 162**, No. 1: pp. 587–601, 1979. ISSN 0029-554X. URL http://dx.doi.org/https://doi.org/10.1016/0029-554X(79)90734-1.

[274] Stefan Enoch and Nicolas Bonod. *Plasmonics: from basics to advanced topics*, Vol. 167 of *Springer Series in Optical Sciences.* Springer, Heidelberg, New York, Dordrecht, London, 2012. ISBN 978-3-642-28079-5. URL http://dx.doi.org/0.1007/978-3-642-28079-5.

[275] R W Wood. *On a Remarkable Case of Uneven Distribution of Light in a Diffraction Grating Spectrum.* Proceedings of the Physical Society of London, **Vol. 18**, No. 1: p. 269, 1902. URL http://dx.doi.org/10.1088/1478-7814/18/1/325.

[276] M. Fiess, M. Schultze, E. Goulielmakis, B. Dennhardt, J. Gagnon, M. Hofstetter, R. Kienberger and F. Krausz. *Versatile apparatus for attosecond metrology and spectroscopy.* Review of Scientific Instruments, **Vol. 81**, No. 9: p. 093103, 2010. ISSN 0034-6748. https://pubs.aip.org/aip/rsi/article-pdf/doi/10.1063/1.3475689/13707448/093103_1_online.pdf, URL http://dx.doi.org/10.1063/1.3475689.

[277] Kilian Unterguggenberger. *Development of an XUV/SXR Spectrometer for Applications in Attosecond Science.* Bachelor's thesis, Ludwig-Maximilians-Universität München, München, 2019.

[278] Matteo Frigo and Steven G. Johnson. *The Design and Implementation of FFTW3.* Proceedings of the IEEE, **Vol. 93**, No. 2: pp. 216–231, 2005. Special issue on "Program Generation, Optimization, and Platform Adaptation".

[279] Richard J Mathar. *Refractive index of humid air in the infrared: model fits.* Journal of Optics A: Pure and Applied Optics, **Vol. 9**, No. 5: p. 470, 2007. URL http://dx.doi.org/10.1088/1464-4258/9/5/008.

[280] Thorlabs Inc. *25.0 mm Silver coated right angle prism mirror AutoCAD PDF*, 2003,2022. Accessed 24 July 2025, URL https://www.thorlabs.com/_sd.cfm?fileName=7249-E0W.pdf&partNumber=MRA25-P01.

[281] piezosystem Jena. *PZ 400 SG OEM Datasheet*, 2017.

[282] piezosystem Jena. *ENT/ENV Manual, German version 30.03.2016 von AS*, 2016.

[283] Michael Chini, Kun Zhao and Zenghu Chang. *The generation, characterization and applications of broadband isolated attosecond pulses.* Nature Photonics, **Vol. 8**, No. 3: pp. 178–186, 2014. ISSN 1749-4893. URL http://dx.doi.org/10.1038/nphoton.2013.362.

[284] Markus Drescher, Michael Hentschel, Reinhard Kienberger, Gabriel Tempea, Christian Spielmann, Georg A. Reider, Paul B. Corkum and Ferenc Krausz. *X-ray Pulses Approaching the Attosecond Frontier.* Science, **Vol. 291**, No. 5510: pp. 1923–1927, 2001. https://www.science.org/doi/pdf/10.1126/science.1058561, URL http://dx.doi.org/10.1126/science.1058561.

[285] F. M. Böttcher, B. Manschwetus, H. Rottke, N. Zhavoronkov, Z. Ansari and W. Sandner. *Interferometric long-term stabilization of a delay line: a tool for pump–probe photoelectron–photoion-coincidence spectroscopy on the attosecond time scale.* Applied Physics B, **Vol. 91**, No. 2: pp. 287–293, 2008. ISSN 1432-0649. URL http://dx.doi.org/10.1007/s00340-008-2987-5.

[286] Ximao Feng, Steve Gilbertson, Hiroki Mashiko, He Wang, Sabih D. Khan, Michael Chini, Yi Wu, Kun Zhao and Zenghu Chang. *Generation of Isolated Attosecond Pulses with 20 to 28 Femtosecond Lasers.* Phys. Rev. Lett., **Vol. 103**: p. 183901, 2009. URL http://dx.doi.org/10.1103/PhysRevLett.103.183901.

[287] E. Magerl, S. Neppl, A. L. Cavalieri, E. M. Bothschafter, M. Stanislawski, Th. Uphues, M. Hofstetter, U. Kleineberg, J. V. Barth, D. Menzel, F. Krausz, R. Ernstorfer, R. Kienberger and P. Feulner. *A flexible apparatus for attosecond photoelectron spectroscopy of solids and surfaces.* Review of Scientific Instruments, **Vol. 82**, No. 6: p. 063104, 2011. ISSN 0034-6748. https://pubs.aip.org/aip/rsi/article-pdf/doi/10.1063/1.3596564/15894783/063104_1_online.pdf, URL http://dx.doi.org/10.1063/1.3596564.

[288] M. Schultze, A. Wirth, I. Grguras, M. Uiberacker, T. Uphues, A.J. Verhoef, J. Gagnon, M. Hofstetter, U. Kleineberg, E. Goulielmakis and F. Krausz. *State-of-the-art attosecond metrology.* Journal of Electron Spectroscopy and Related Phenomena, **Vol. 184**, No. 3: pp. 68–77, 2011. ISSN 0368-2048. Advances in Vacuum Ultraviolet and X-ray Physics, URL http://dx.doi.org/https://doi.org/10.1016/j.elspec.2011.01.003.

[289] Arohi Jain, Thomas Gaumnitz, Anatoli Kheifets and Hans Jakob Wörner. *Using a passively stable attosecond beamline for relative photoemission time delays at high XUV photon energies.* Opt. Express, **Vol. 26**, No. 22: pp. 28604–28620, 2018. URL http://dx.doi.org/10.1364/OE.26.028604.

[290] D. Greening, B. Weaver, A. J. Pettipher, D. J. Walke, E. W. Larsen, J. P. Marangos and J. W. G. Tisch. *Generation and measurement of isolated attosecond pulses with enhanced flux using a two colour synthesized laser field.* Opt. Express, **Vol. 28**, No. 16: pp. 23329–23337, 2020. URL http://dx.doi.org/10.1364/OE.396927.

[291] D. Ertel, M. Schmoll, S. Kellerer, A. Jäger, R. Weissenbilder, M. Moioli, H. Ahmadi, D. Busto, I. Makos, F. Frassetto, L. Poletto, C. D. Schröter, T. Pfeifer, R. Moshammer and G. Sansone. *Ultrastable, high-repetition-rate attosecond beamline for time-resolved XUV–IR coincidence spectroscopy.* Review of Scientific Instruments, **Vol. 94**, No. 7: p. 073001, 2023. ISSN 0034-6748. https://pubs.aip.org/aip/rsi/article-pdf/doi/10.1063/

5.0139496/18143666/073001_1_5.0139496.pdf, URL http://dx.doi.org/10.1063/5.0139496.

[292] Michael Chini, Hiroki Mashiko, He Wang, Shouyuan Chen, Chenxia Yun, Shane Scott, Steve Gilbertson and Zenghu Chang. *Delay control in attosecond pump-probe experiments.* Opt. Express, **Vol. 17**, No. 24: pp. 21459–21464, 2009. URL http://dx.doi.org/10.1364/OE.17.021459.

[293] M. Sabbar, S. Heuser, R. Boge, M. Lucchini, L. Gallmann, C. Cirelli and U. Keller. *Combining attosecond XUV pulses with coincidence spectroscopy.* Review of Scientific Instruments, **Vol. 85**, No. 10: p. 103113, 2014. ISSN 0034-6748. https://pubs.aip.org/aip/rsi/article-pdf/doi/10.1063/1.4898017/13625704/103113_1_online.pdf, URL http://dx.doi.org/10.1063/1.4898017.

[294] R. Locher, M. Lucchini, J. Herrmann, M. Sabbar, M. Weger, A. Ludwig, L. Castiglioni, M. Greif, M. Hengsberger, L. Gallmann and U. Keller. *Versatile attosecond beamline in a two-foci configuration for simultaneous time-resolved measurements.* Review of Scientific Instruments, **Vol. 85**, No. 1: p. 013113, 2014. ISSN 0034-6748. https://pubs.aip.org/aip/rsi/article-pdf/doi/10.1063/1.4862656/14775402/013113_1_online.pdf, URL http://dx.doi.org/10.1063/1.4862656.

[295] M. Huppert, I. Jordan and H. J. Wörner. *Attosecond beamline with actively stabilized and spatially separated beam paths.* Review of Scientific Instruments, **Vol. 86**, No. 12: p. 123106, 2015. ISSN 0034-6748. https://pubs.aip.org/aip/rsi/article-pdf/doi/10.1063/1.4937623/15837295/123106_1_online.pdf, URL http://dx.doi.org/10.1063/1.4937623.

[296] S. J. Weber, B. Manschwetus, M. Billon, M. Böttcher, M. Bougeard, P. Breger, M. Géléoc, V. Gruson, A. Huetz, N. Lin, Y. J. Picard, T. Ruchon, P. Salières and B. Carré. *Flexible attosecond beamline for high harmonic spectroscopy and XUV/near-IR pump probe experiments requiring long acquisition times.* Review of Scientific Instruments, **Vol. 86**, No. 3: p. 033108, 2015. ISSN 0034-6748. https://pubs.aip.org/aip/rsi/article-pdf/doi/10.1063/1.4914464/15818739/033108_1_online.pdf, URL http://dx.doi.org/10.1063/1.4914464.

[297] V Loriot, A Marciniak, L Quintard, V Despré, B Schindler, I Compagnon, B Concina, G Celep, C Bordas, F Catoire, E Constant and F Lépine. *Resolving XUV induced femtosecond and attosecond dynamics in polyatomic molecules with a compact attosecond beamline.* Journal of Physics: Conference Series, **Vol. 635**, No. 1: p. 012006, 2015. URL http://dx.doi.org/10.1088/1742-6596/635/1/012006.

[298] Emma R. Simpson, Alvaro Sanchez-Gonzalez, Thomas Siegel, Zsolt Diveki, Simon E. E. Hutchinson, Lukas Miseikis, Christian Strüber, Dane R. Austin and Jon P. Marangos. *A beamline for attosecond pump-probe experiments: towards tracking ultrafast electron dynamics in atoms and molecules.* In Zhiwen Liu (Editor), *Ultrafast Nonlinear Imaging and Spectroscopy III*, Vol. 9584, p. 958402. International Society for Optics and Photonics, SPIE, 2015. URL http://dx.doi.org/10.1117/12.2187269.

[299] Seth L. Cousin, Nicola Di Palo, Bárbara Buades, Stephan M. Teichmann, M. Reduzzi, M. Devetta, A. Kheifets, G. Sansone and Jens Biegert. *Attosecond Streaking in the Water Window: A New Regime of Attosecond Pulse Char-*

acterization. Phys. Rev. X, **Vol. 7**: p. 041030, 2017. URL http://dx.doi.org/10.1103/PhysRevX.7.041030.

[300] Hao Teng, Xin-Kui He, Kun Zhao and Zhi-Yi Wei. *Attosecond laser station**. Chinese Physics B, **Vol. 27**, No. 7: p. 074203, 2018. URL http://dx.doi.org/10.1088/1674-1056/27/7/074203.

[301] F. Schlaepfer, M. Volkov, N. Hartmann, A. Niedermayr, Z. Schumacher, L. Gallmann and U. Keller. *Phase stabilization of an attosecond beamline combining two IR colors*. Opt. Express, **Vol. 27**, No. 16: pp. 22385–22392, 2019. URL http://dx.doi.org/10.1364/OE.27.022385.

[302] Veit Stooss, Maximilian Hartmann, Paul Birk, Gergana D. Borisova, Thomas Ding, Alexander Blättermann, Christian Ott and Thomas Pfeifer. *XUV-beamline for attosecond transient absorption measurements featuring a broadband common beam-path time-delay unit and in situ reference spectrometer for high stability and sensitivity*. Review of Scientific Instruments, **Vol. 90**, No. 5: p. 053108, 2019. ISSN 0034-6748. https://pubs.aip.org/aip/rsi/article-pdf/doi/10.1063/1.5091069/14695868/053108_1_online.pdf, URL http://dx.doi.org/10.1063/1.5091069.

[303] Giacinto D. Lucarelli, Bruno Moio, Giacomo Inzani, Nicola Fabris, Liliana Moscardi, Fabio Frassetto, Luca Poletto, Mauro Nisoli and Matteo Lucchini. *Novel beamline for attosecond transient reflection spectroscopy in a sequential two-foci geometry*. Review of Scientific Instruments, **Vol. 91**, No. 5: p. 053002, 2020. ISSN 0034-6748. https://pubs.aip.org/aip/rsi/article-pdf/doi/10.1063/5.0005932/13637374/053002_1_online.pdf, URL http://dx.doi.org/10.1063/5.0005932.

[304] Mikhail Osolodkov, Federico J Furch, Felix Schell, Peter Šušnjar, Fabio Cavalcante, Carmen S Menoni, Claus P Schulz, Tobias Witting and Marc J J Vrakking. *Generation and characterisation of few-pulse attosecond pulse trains at 100 kHz repetition rate*. Journal of Physics B: Atomic, Molecular and Optical Physics, **Vol. 53**, No. 19: p. 194003, 2020. URL http://dx.doi.org/10.1088/1361-6455/aba77d.

[305] Peng Ye, Tamás Csizmadia, Lénárd Gulyás Oldal, Harshitha Nandiga Gopalakrishna, Miklós Füle, Zoltán Filus, Balázs Nagyillés, Zsolt Divéki, Tímea Grósz, Mathieu Dumergue, Péter Jójárt, Imre Seres, Zsolt Bengery, Viktor Zuba, Zoltán Várallyay, Balázs Major, Fabio Frassetto, Michele Devetta, Giacinto Davide Lucarelli, Matteo Lucchini, Bruno Moio, Salvatore Stagira, Caterina Vozzi, Luca Poletto, Mauro Nisoli, Dimitris Charalambidis, Subhendu Kahaly, Amelle Zaïr and Katalin Varjú. *Attosecond pulse generation at ELI-ALPS 100 kHz repetition rate beamline*. Journal of Physics B: Atomic, Molecular and Optical Physics, **Vol. 53**, No. 15: p. 154004, 2020. URL http://dx.doi.org/10.1088/1361-6455/ab92bf.

[306] Sara Mikaelsson, Jan Vogelsang, Chen Guo, Ivan Sytcevich, Anne-Lise Viotti, Fabian Langer, Yu-Chen Cheng, Saikat Nandi, Wenjie Jin, Anna Olofsson, Robin Weissenbilder, Johan Mauritsson, Anne L'Huillier, Mathieu Gisselbrecht and Cord L. Arnold. *A high-repetition rate attosecond light source for time-resolved coincidence spectroscopy*. Nanophotonics, **Vol. 10**, No. 1: pp. 117–128, 2021. URL http://dx.doi.org/doi:10.1515/nanoph-2020-0424.

[307] Hemkumar Srinivas, Farshad Shobeiry, Divya Bharti, Thomas Pfeifer, Robert Moshammer and Anne Harth. *High-repetition rate attosecond beamline for multi-particle coincidence experiments*. Opt. Express, **Vol. 30**, No. 8: pp. 13630–13646, 2022. URL http://dx.doi.org/10.1364/OE.454553.

[308] Mingxuan Li, Huiyong Wang, Xiaokai Li, Jun Wang, Jieda Zhang, Xinyue San, Pan Ma, Yongnan Lu, Zhang Liu, Chuncheng Wang, Yujun Yang, Sizuo Luo and Dajun Ding. *Stable attosecond beamline equipped with high resolution electron and XUV spectrometer based on high-harmonics generation*. Journal of Electron Spectroscopy and Related Phenomena, **Vol. 263**: p. 147287, 2023. ISSN 0368-2048. URL http://dx.doi.org/https://doi.org/10.1016/j.elspec.2023.147287.

[309] Sizuo Luo, Robin Weissenbilder, Hugo Laurell, Mattias Ammitzböll, Vénus Poulain, David Busto, Lana Neoričić, Chen Guo, Shiyang Zhong, David Kroon, Richard J Squibb, Raimund Feifel, Mathieu Gisselbrecht, Anne L'Huillier and Cord L Arnold. *Ultra-stable and versatile high-energy resolution setup for attosecond photoelectron spectroscopy*. Advances in Physics: X, **Vol. 8**, No. 1: p. 2250105, 2023. https://doi.org/10.1080/23746149.2023.2250105, URL http://dx.doi.org/10.1080/23746149.2023.2250105.

[310] V. Wanie, S. Ryabchuk, L. Colaizzi, M. Galli, E. P. Månsson, A. Trabattoni, A. B. Wahid, J. Hahne, A. Cartella, K. Saraswathula, F. Frassetto, D. P. Lopes, R. Martínez Vázquez, R. Osellame, L. Poletto, F. Légaré, M. Nisoli and F. Calegari. *A flexible beamline combining XUV attosecond pulses with few-femtosecond UV and near-infrared pulses for time-resolved experiments*. Review of Scientific Instruments, **Vol. 95**, No. 8: p. 083004, 2024. ISSN 0034-6748. https://pubs.aip.org/aip/rsi/article-pdf/doi/10.1063/5.0190889/20119447/083004_1_5.0190889.pdf, URL http://dx.doi.org/10.1063/5.0190889.

[311] Tamás Csizmadia, Lénárd Gulyás Oldal, Barnabás Gilicze, Dániel Sándor Kiss, Tamás Bartyik, Katalin Varjú, Subhendu Kahaly and Balázs Major. *Active stabilization for ultralong acquisitions in an attosecond pump-probe beamline*, 2025. 2504.08448, URL https://arxiv.org/abs/2504.08448.

[312] Tamás Csizmadia, Lénárd Gulyás Oldal, Barnabás Gilicze, Dániel Kiss, Tamás Bartyik, Katalin Varjú, Subhendu Kahaly and Balázs Major. *Active stabilization for ultralong acquisitions in an attosecond pump–probe beamline*. APL Photonics, **Vol. 10**, No. 8: p. 080803, 2025. ISSN 2378-0967. https://pubs.aip.org/aip/app/article-pdf/doi/10.1063/5.0273558/20657004/080803_1_5.0273558.pdf, URL http://dx.doi.org/10.1063/5.0273558.

[313] Lasnix. *Step Attenuators for Infrared Laser Beams Datasheet*, 2015. Accessed 5 August 2025, URL http://www.lasnix.com/datasheets/step-attenuator.pdf.

[314] Marcus Ossiander, Maryna Leonidivna Meretska, Hana Kristin Hampel, Soon Wei Daniel Lim, Nico Knefz, Thomas Jauk, Federico Capasso and Martin Schultze. *Extreme ultraviolet metalens by vacuum guiding*. Science, **Vol. 380**, No. 6640: pp. 59–63, 2023. https://www.science.org/doi/pdf/10.1126/science.adg6881, URL http://dx.doi.org/10.1126/science.adg6881.

[315] Robert L. Lucke and Stefan E. Thonnard. *Stacked-grid collimators described with dimensionless parameters*. Appl. Opt., **Vol. 37**, No. 4: pp. 616–621, 1998. URL http://dx.doi.org/10.1364/AO.37.000616.

[316] O. Tcherbakoff, E. Mével, D. Descamps, J. Plumridge and E. Constant. *Time-gated high-order harmonic generation.* Phys. Rev. A, **Vol. 68**: p. 043804, 2003. URL http://dx.doi.org/10.1103/PhysRevA.68.043804.

[317] I. J. Sola, E. Mével, L. Elouga, E. Constant, V. Strelkov, L. Poletto, P. Villoresi, E. Benedetti, J.-P. Caumes, S. Stagira, C. Vozzi, G. Sansone and M. Nisoli. *Controlling attosecond electron dynamics by phase-stabilized polarization gating.* Nature Physics, **Vol. 2**, No. 5: pp. 319–322, 2006. ISSN 1745-2481. URL http://dx.doi.org/10.1038/nphys281.

[318] Zenghu Chang. *Controlling attosecond pulse generation with a double optical gating.* Phys. Rev. A, **Vol. 76**: p. 051403, 2007. URL http://dx.doi.org/10.1103/PhysRevA.76.051403.

[319] Henry Timmers, Mazyar Sabbar, Johannes Hellwagner, Yuki Kobayashi, Daniel M. Neumark and Stephen R. Leone. *Polarization-assisted amplitude gating as a route to tunable, high-contrast attosecond pulses.* Optica, **Vol. 3**, No. 7: pp. 707–710, 2016. URL http://dx.doi.org/10.1364/OPTICA.3.000707.

[320] Mark J. Abel, Thomas Pfeifer, Phillip M. Nagel, Willem Boutu, M. Justine Bell, Colby P. Steiner, Daniel M. Neumark and Stephen R. Leone. *Isolated attosecond pulses from ionization gating of high-harmonic emission.* Chemical Physics, **Vol. 366**, No. 1: pp. 9–14, 2009. ISSN 0301-0104. Attosecond Molecular Dynamics, URL http://dx.doi.org/https://doi.org/10.1016/j.chemphys.2009.09.016.

[321] K. S. Budil, P. Salières, Anne L'Huillier, T. Ditmire and M. D. Perry. *Influence of ellipticity on harmonic generation.* Phys. Rev. A, **Vol. 48**: pp. R3437–R3440, 1993. URL http://dx.doi.org/10.1103/PhysRevA.48.R3437.

[322] Max Möller, Yan Cheng, Sabih D. Khan, Baozhen Zhao, Kun Zhao, Michael Chini, Gerhard G. Paulus and Zenghu Chang. *Dependence of high-order-harmonic-generation yield on driving-laser ellipticity.* Phys. Rev. A, **Vol. 86**: p. 011401, 2012. URL http://dx.doi.org/10.1103/PhysRevA.86.011401.

[323] Jie Li, Xiaoming Ren, Yanchun Yin, Yan Cheng, Eric Cunningham, Yi Wu and Zenghu Chang. *Polarization gating of high harmonic generation in the water window.* Applied Physics Letters, **Vol. 108**, No. 23: p. 231102, 2016. ISSN 0003-6951. https://pubs.aip.org/aip/apl/article-pdf/doi/10.1063/1.4953402/13465156/231102_1_online.pdf, URL http://dx.doi.org/10.1063/1.4953402.

[324] Bing Shan, Shambhu Ghimire and Zenghu Chang. *Generation of the attosecond extreme ultraviolet supercontinuum by a polarization gating.* Journal of Modern Optics, **Vol. 52**, No. 2-3: pp. 277–283, 2005. https://doi.org/10.1080/09500340410001729573, URL http://dx.doi.org/10.1080/09500340410001729573.

[325] Aditi Bhattacherjee and Stephen R. Leone. *Ultrafast X-ray Transient Absorption Spectroscopy of Gas-Phase Photochemical Reactions: A New Universal Probe of Photoinduced Molecular Dynamics.* Accounts of Chemical Research, **Vol. 51**, No. 12: pp. 3203–3211, 2018. PMID: 30462481, https://doi.org/10.1021/acs.accounts.8b00462, URL http://dx.doi.org/10.1021/acs.accounts.8b00462.

[326] Romain Geneaux, Hugo J. B. Marroux, Alexander Guggenmos, Daniel M. Neumark and Stephen R. Leone. *Transient absorption spectroscopy using high harmonic generation: a review of ultrafast X-ray dynamics in molecules and*

solids. Philosophical Transactions of the Royal Society A: Mathematical, Physical and Engineering Sciences, **Vol. 377**, No. 2145: p. 20170463, 2019. https://royalsocietypublishing.org/doi/pdf/10.1098/rsta.2017.0463, URL http://dx.doi.org/10.1098/rsta.2017.0463.

[327] Florian Siegrist, Julia A. Gessner, Marcus Ossiander, Christian Denker, Yi-Ping Chang, Malte C. Schröder, Alexander Guggenmos, Yang Cui, Jakob Walowski, Ulrike Martens, J. K. Dewhurst, Ulf Kleineberg, Markus Münzenberg, Sangeeta Sharma and Martin Schultze. *Light-wave dynamic control of magnetism*. Nature, **Vol. 571**, No. 7764: pp. 240–244, 2019. ISSN 1476-4687. URL http://dx.doi.org/10.1038/s41586-019-1333-x.

[328] Matteo Lucchini, Shunsuke A. Sato, Giacinto D. Lucarelli, Bruno Moio, Giacomo Inzani, Rocío Borrego-Varillas, Fabio Frassetto, Luca Poletto, Hannes Hübener, Umberto De Giovannini, Angel Rubio and Mauro Nisoli. *Unravelling the intertwined atomic and bulk nature of localised excitons by attosecond spectroscopy*. Nature Communications, **Vol. 12**, No. 1: p. 1021, 2021. ISSN 2041-1723. URL http://dx.doi.org/10.1038/s41467-021-21345-7.

[329] Lukas Gallmann, Claudio Cirelli and Ursula Keller. *Attosecond Science: Recent Highlights and Future Trends*. Annual Review of Physical Chemistry, **Vol. 63**, No. Volume 63, 2012: pp. 447–469, 2012. ISSN 1545-1593. URL http://dx.doi.org/https://doi.org/10.1146/annurev-physchem-032511-143702.

[330] Jacob P. Lee, Timur Avni, Oliver Alexander, Marios Maimaris, Haoqing Ning, Artem A. Bakulin, Philippe G. Burden, Evangelos Moutoulas, Dimitra G. Georgiadou, Christian Brahms, John C. Travers, Jon P. Marangos and Clément Ferchaud. *Few-femtosecond soft X-ray transient absorption spectroscopy with tuneable DUV-Vis pump pulses*. Optica, **Vol. 11**, No. 9: pp. 1320–1323, 2024. URL http://dx.doi.org/10.1364/OPTICA.530964.

[331] Marina Fernández Galán, Javier Serrano, Enrique Conejero Jarque, Rocío Borrego-Varillas, Matteo Lucchini, Maurizio Reduzzi, Mauro Nisoli, Christian Brahms, John C. Travers, Carlos Hernández-García and Julio San Roman. *Robust Isolated Attosecond Pulse Generation with Self-Compressed Subcycle Drivers from Hollow Capillary Fibers*. ACS Photonics, **Vol. 11**, No. 4: pp. 1673–1683, 2024. https://doi.org/10.1021/acsphotonics.3c01897, URL http://dx.doi.org/10.1021/acsphotonics.3c01897.

[332] Seunghwoi Han, Jie Li, Zheyuan Zhu, Andrew Chew, Esben W. Larsen, Yi Wu, Shuo Sean Pang and Zenghu Chang. *Chapter One - Tabletop attosecond X-rays in the water window*. Vol. 69 of *Advances In Atomic, Molecular, and Optical Physics*, pp. 1–65. Academic Press, 2020. URL http://dx.doi.org/https://doi.org/10.1016/bs.aamop.2020.04.003.

[333] D Wu and J W Wang. *Magetostatic amplifier with tunable maximum by twisted-light plasma interactions*. Plasma Physics and Controlled Fusion, **Vol. 59**, No. 9: p. 095010, 2017. URL http://dx.doi.org/10.1088/1361-6587/aa77c5.

[334] Nora G. Johnson, O. Herrwerth, A. Wirth, S. De, I. Ben-Itzhak, M. Lezius, B. Bergues, M. F. Kling, A. Senftleben, C. D. Schröter, R. Moshammer, J. Ullrich, K. J. Betsch, R. R. Jones, A. M. Sayler, T. Rathje, K. Rühle, W. Müller and G. G. Paulus. *Single-shot carrier-envelope-phase-tagged ion-momentum imaging of nonsequential double ionization of argon in in-*

tense 4-fs laser fields. Phys. Rev. A, **Vol. 83**: p. 013412, 2011. URL http://dx.doi.org/10.1103/PhysRevA.83.013412.

[335] Boris Bergues, Matthias Kübel, Nora G. Johnson, Bettina Fischer, Nicolas Camus, Kelsie J. Betsch, Oliver Herrwerth, Arne Senftleben, A. Max Sayler, Tim Rathje, Thomas Pfeifer, Itzik Ben-Itzhak, Robert R. Jones, Gerhard G. Paulus, Ferenc Krausz, Robert Moshammer, Joachim Ullrich and Matthias F. Kling. *Attosecond tracing of correlated electron-emission in non-sequential double ionization*. Nature Communications, **Vol. 3**, No. 1: p. 813, 2012. ISSN 2041-1723. URL http://dx.doi.org/10.1038/ncomms1807.

[336] Burr-Brown and Texas Instruments. *Precision Switched Integrator Transimpedance Amplifier - Datasheet IVC102*, 1996. URL https://www.ti.com/de/lit/gpn/ivc102.

[337] Max Planck. *Faksimile Aus Den Verhandlungen Der Deutschen Physikalischen Gesellschaft 2 (1900) S. 237: Zur Theorie des Gesetzes der Energieverteilung im Normalspectrum; von M. Planck*. Physikalische Blätter, **Vol. 4**, No. 4: pp. 146–151, 1948. URL http://dx.doi.org/https://doi.org/10.1002/phbl.19480040404.

[338] Max Planck. *Zur Theorie der Wärmestrahlung*. Annalen der Physik, **Vol. 336**, No. 4: pp. 758–768, 1910. https://onlinelibrary.wiley.com/doi/pdf/10.1002/andp.19103360406, URL http://dx.doi.org/https://doi.org/10.1002/andp.19103360406.

[339] Tatsuo Harada, Kaoru Takahashi, Hideo Sakuma and Andrzej Osyczka. *Optimum design of a grazing-incidence flat-field spectrograph with a spherical varied-line-space grating*. Appl. Opt., **Vol. 38**, No. 13: pp. 2743–2748, 1999. URL http://dx.doi.org/10.1364/AO.38.002743.

[340] Shimadzu Corporation. *Laminar-type Replica Diffraction Gratings for VUV/Soft X-ray Region*, 2025. Accessed online 7 August 2025, URL https://www.shimadzu.com/opt/products/dif/o-k25cur0000006zd0.html.

[341] Gang Xiong, Jiyan Zhang, Guohong Yang, Jiamin Yang, Hang Li, Zhimin Hu, Yang Zhao, Minxi Wei and Tao Yi. *Different approaches to precise wavelength calibration of a flat-field grating spectrometer for laser-produced plasmas **. Physica Scripta, **Vol. 89**, No. 6: p. 065005, 2014. URL http://dx.doi.org/10.1088/0031-8949/89/6/065005.

Acknowledgements

I would like to express my gratitude to my supervisor, Matthias Kling, for giving me the great opportunity to contribute to science, for his supervision, and for providing a friendly and inspiring work environment. I thank my local supervisor, Thomas Nubbemeyer, for his constant support in all matters, fruitful discussions, and guidance – thank you very much. I also appreciate the supervision from Boris Bergues during the phasemeter project and his passion for CEP detection. I thank Hartmut Schröder for his support and all the discussions we had over the last few years. Your dedication to science continues to inspire me.

I want to thank Maximilian Kuthe for teaching me how the laser system works, for being a great office mate, and for sharing my coffee addiction. I also appreciate the exchange with the rest of the group, particularly with Weiwei Li and Najd Altwaijry. I want to thank my former colleagues, especially Philipp Rosenberger, Johannes Schötz and Zilong Wang. I value the interactions with other members of the Krausz group, including Keyhan Goliary, Simon Reiger, Marco Dassie, Amelie Heinzerling, Mikhail Mamaikin, Dmitrii Kormin, Nick Karpowicz, Vladislav Yakovlev, and many others.

The collaboration with UltraFast Innovations has always been synergistic. I appreciate the exchange and mutual support. I thank the MPQ technicians for their assistance. I am grateful to Michael Rogg and his team for their excellent work and positive feedback on all mechanical matters. I thank Fritz Keilmann for sharing his expertise on grating filters and for providing filter samples at no cost. I appreciate the support from the Max Planck School of Photonics (MPSP). Finally, I want to thank my friends and family for their ongoing encouragement and unwavering support.